Universitetet
i Stavanger

UNIVERSITY OF STAVANGER

FACULTY OF SCIENCE AND TECHNOLOGY

DEPARTMENT OF MATHEMATICS AND PHYSICS

PH.D. THESIS IN INFORMATICS, MATHEMATICS AND PHYSICS

Signal analysis in gravitational wave data

Candidate : Paolo Marcoccia
Supervisor : Prof. Germano Nardini
Co-Supervisor : Prof. Alex B. Nielsen

University of Stavanger
NO-4036 Stavanger
NORWAY
wwww.uis.no

ISBN: 978-82-8439-212-7

ISSN: 1890-1387
PhD: Thesis UiS No. 740

It's easy to think of ourselves as separated from everything, but this is not true. We are as much the Universe as a neutron star or a black hole or a nebula. Even better, actually, we are its thinking and feeling part: the central organs of the universe.

We are truly free in a universe-sized playground, so we might as well aim to be happy and to build some kind of utopia in the stars.

Kurzgesagt, Optimistic Nihilism

PREFACE

This thesis is submitted in partial fulfillment of the requirements for the degree of Philosophiae Doctor (Ph.D.) at the University of Stavanger, Faculty of Science and Technology, Norway. The presented research has been carried out at the University of Stavanger from May 2019 to May 2023. In this document, we are going to investigate the effects of gravitational wave signals from compact objects on present-stage and future detectors. We are going to consider both the case of single resolvable sources and the stochastic background noise coming from the superposition of all the unresolvable sources. The thesis is based on 3 papers, of which 2 are published and 1 will appear in the coming weeks. Further articles, such as [1] and [2], have been published during my research period. These articles are however omitted from this document as, either my contribution was minimal, or the topic was not closely related to the main theme presented in this thesis. The original work carried out in the papers will be presented in Chapter {3} to Chapter {5}.

We will start the document with some brief introductory chapters, to guide the reader through some of the main concepts and tools required in the analysis of the presented papers. In detail, this thesis will be structured as follows:

- In Chapter {1} we are going to introduce some elementary tools coming from *General Relativity*, that lead to the definitions of gravitational waves and black holes. In particular, we will define the *Einstein equations* and their components in order to introduce the Schwarzschild and Kerr solutions. The *Schwarzschild solution* naturally leads to the concept of *Black Hole*, while the *Kerr metric* is, to date, the best description for the black holes in our Universe. We will also present the geodesic equation and deviation, to understand the motion of particles in the General Relativity framework. The aforementioned, in particular, will be needed to define the gravitational wave's polarization states and, in general, how the signal coming from an inspiralling event in our Universe will appear in a physical detector. To conclude, in the last part of this section, we are going to discuss two of the main black hole formation channels, *i.e. Stellar Origin Binary Black Holes*, which are the main component for black holes of astrophysical origin, and *Primordial Black Holes*. The differences between the expected behavior, as a function of redshift, of these two considered populations is the main reason that led to the study performed in our third paper.

- In Chapter {2} we introduce the concept of *Gravitational Wave*, and to this extent, we define them by perturbing the *Einstein equations*. Through this process, we are going to both present the equations that need to be integrated to

obtain the numerical waveforms used in the presented papers, as well as introduce some of the key features and assumptions in gravitational wave theory, such as polarization states, the TT-gauge and the Quadrupole Moment Tensor. Starting from these general results, we then consider the Newtonian circular-orbit approximation in order to obtain an analytical solution to the waveform coming from an inspiralling binary system. This result, although coming from a rough approximation, has a two-fold relevance for this document: on one hand, this approximation will always be valid for stellar-mass black holes in the LISA frequency range, on the other, it is the starting point for all the phenomenological waveforms that will be adopted in the presented articles, which generally only differ from this results for some Post-Newtonian corrections. We conclude this section by considering the evolution of a binary inspiralling system due to gravitational wave emission from an energy point of view. This result, in particular, will become useful when discussing the LISA Stochastic Gravitational Wave Background in the second and third papers of this thesis.

- In Chapter {3} we present an article published in *JCAP* ***11*** *(2020) 043*, where we analyze the first four LIGO gravitational wave detections using a *Pearson Cross-Correlation* analysis. This work was motivated as a follow-up to some studies carried out by a group at the Niels-Bohr Institute. In their works, they tried to reproduce the detections claimed by the LIGO collaboration using matched filtering, through the use of a more agnostic method such as the Pearson cross-correlation. This led them to discover that the waveforms used by the LIGO collaboration in their subtractions were not optimal, as some of the signal remained buried in the detector noise after the subtraction, and led them to raise some doubts about the LIGO claims. In the paper that we present in this chapter, we used different waveforms obtained through maximum-likelihood, and we demonstrate that the residual signal found in the noise was just a consequence of the choice of waveforms. Such signal, buried in the residual detector noise, can hence be removed by using a more accurate waveform description. Furthermore, we show that the LIGO results can be reproduced with statistical significance even by using the Pearson cross-correlation method, even though with this approach the statistical significance will be slightly lower compared to the results obtained using matched filtering.

- In Chapter {4} we present an article published in *JCAP* ***08*** *(2023) 034*, where we analyze the *Stochastic Gravitational Wave Background* predicted on the LISA detector. To this extent, we use the results coming from the latest LVK population inference paper to produce catalogs representing a Stellar-Origin Black Hole population in our Universe. The Stochastic Gravitational Wave Background is then computed by adopting four different methods, that in order of complexity, range from a simple analytical evaluation to estimating the real detector strain after synthesizing a black hole population and iteratively subtracting all the resolvable sources. We find that, when the assumed SNR threshold is high enough to keep the number of resolvable sources small (~ 10 over 4 years of observation),

all the methods give results well in agreement with each other. This implies that, when working with LISA data, it is possible to use the fast analytical estimation for the stochastic noise component with a small loss of precision. On the other hand, the use of more complex methods like the iterative subtraction of a synthesized population, despite naturally requiring numerical cuts in the population generation phase due to its computational cost, can present both the value of the Stochastic Gravitational Wave Background amplitude as well as the resolvable sources predicted on the LISA strain at the same time. It can hence be useful when both these quantities need to be taken into account in a particular study.

- In Chapter {5} we present an article where we investigate the prospects of identifying potential *Primordial Black Hole Binary* populations over the astrophysical *Stellar-Origin Black Hole Binary* population of our Universe. To this extent, once again we assume that our fiducial population follows the latest LVK GWTC-3 inference paper results, and we forecast our analysis on the next generation of gravitational wave detectors. We consider different possibilities both for the merger rate and mass function of the studied Primordial Black Hole subpopulations, and we perform our analysis by focusing on the signatures at higher redshifts than the current LVK detection horizon. We exploit the fact that the astrophysical black holes of our universe are supposed to follow a distribution as a function of redshift closely related to the Star Formation Rate, which is supposed to peak and then slowly die off. At distances beyond the peak of the stellar formation rate, the Stellar-Origin Binary Black Hole contribution will hence become negligible, whereas Primordial Black Hole models predict many sources and will dominate. We generally find that Earth-based and space-based detectors work synergistically, and the value of the Stochastic Gravitational Wave Background measured by LISA will generally be able to improve constraining the presence of additional sub-populations compared to the case when only Earth-based detector observations are considered.

- We summarize the results obtained through the articles, and conclude the document in Chapter {6}.

ACKNOWLEDGEMENT

I wish to dedicate this thesis to my granny Maria, who made me understand the importance of aiming high in life. I know that she would be proud to see how far I got from the rebel high schooler she used to know so well. I also wish to dedicate this document to my mother Gina and father Sergio, who despite not being perfect, never failed to show me love and support toward my life choices. For my sister Annalisa, I place my flag here, I trust that you won't disappoint me and do better as you always were the serious one ;3. I also wish to thank my girlfriend Kristine with whom I shared most of my life in Stavanger, and led me to the first small steps toward stability in my life. I appreciate your efforts and support even though I rarely say so. My thanks also go to the University of Stavanger and my supervisors Germano and Alex, for trusting me and giving me this first big opportunity to develop my personal career. Further thanks to Germano for surviving through my hardest moments on the path of suffering that is a Ph.D. (you will still miss me!), and Alex for being an inspirational figure and showing me the positive sides of life in academia [1]. A special thank also goes to Bjørn, for being a figure of reference for all the troubles I had during my years at the University of Stavanger, and all my Ph.D. colleagues, with whom I share nice memories involving overpriced alcohol in the Stavanger city center. Additional thanks also go to my research group within the LISA collaboration, with whom I worked for the second paper presented in this document. In particular, I wish to thank Mauro and Jesus, who were my mentors for all the software-related problems that I had during the research projects. I also wish to point out that the third paper would probably not be in this thesis without all the last-minute help that Mauro provided me. A special thank also goes to the American Physical Society and Kurzgesagt studio, for allowing me to re-use the images on the cover and page 2 of this document respectively. The COST organization also deserves some special thanks for supporting my short-term scientific missions in Paris and London, which respectively led to the second and third papers that we presented in this document. To conclude, I wish to thank all the friends I met throughout my lifetime, both present and gone. Even if we might have enjoyed little time together, all the interactions I had with you made me the one I am now. In particular, a special thanks goes to my friends in Veroli, who even after I left always made me feel like nothing had changed every time I went back there for holidays.

[1] I still wish to leave Academia after my Ph.D., but looking at how you approached work was one of the few things that weighed on the other side of the scale.

Contents

Chapter 1

Basics of General Relativity and Black Holes populations

Gravitational Waves (GWs) were first discovered theoretically by perturbing the metric in the *Einstein equations of General Relativity* [3–6]. It hence makes sense to begin this document by briefly introducing them and the components that are involved, *i.e.* the *Ricci tensor* and the *stress-energy tensor* [7, 8]. While discussing these basic quantities of *General Relativity (GR)*, we will naturally incur into the concepts of metrics, geodesic equations, and geodesic deviation, which are to date still very relevant in gravitational waves astronomy. The geodesic equation, for example, describes the motion of a gravitational wave (or any generic particle) from its source to the observer in an assumed universe, while the geodesic deviation will be used in sec. {2.1.3} to describe the polarization states of gravitational waves, and is the quantity that is measured in all interferometer detectors in order to claim a gravitational wave detection [9–12]. By imposing spherical symmetry on our metric, it is instead possible to obtain the *Schwarzschild solution* of the Einstein equations [13, 14], which led through the properties of its singularities to the concepts of event horizons and *Black Holes (BHs)*. The derivation of the results will follow the approach presented in [8, 15, 16].

In this text, we are going to use metric signature $(-,+,+,+)$, and we will use Greek indices for the space-time coordinates (*i.e.* $\mu,\nu = 0,1,2,3$) where 0 represents the time component, while we will use Latin indices for the purely spatial 3-metric ($i,j = 1,2,3$). The chapter is organized as follows: In sec. {1.1} we describe the *Einstein equations* and its components, this is the starting point to discuss all the other tools that we will need in order to present the work of our articles. In sec. {1.2} we discuss the motion of particles in the GR framework by introducing the geodesic equation and deviation. Even though some alternatives were proposed to the Einstein standard framework (see *e.g.* refs. [17–19]) there is still no evidence to prefer a particular modified theory over the base GR [20–22]. Standard GR is hence to date the main framework in gravitational wave astronomy, due to its simplicity with respect to the one derivated from more complicated theories. In sec. {1.3} we introduce the Schwarzschild and Kerr solutions to the *Einstein equations*. In particular, we use the *Schwarzschild*

solution to analyze the surface properties of its singularities and introduce the concepts of event horizon and black holes in correspondence of the *Schwarzschild radius*. This will be the starting point to discuss black hole populations later on in this chapter, as well as to introduce the Kerr solution for rotating compact objects, that is to date the best description for the black holes that we observed in our Universe (see *e.g.* ref. [23]) and is the model that we assumed in all the papers presented in this document. We conclude in sec. {1.4} by briefly discussing black hole populations. However, we limit our discussion to the case of stellar-origin and *Primordial Black Holes (PBHs)*. The first of the two considered populations is considered to be the main formation channel for all the black holes observed by the LVK collaboration to date [24, 25], and is the main target of the study that we performed in the article in sec. {4}. Primordial black holes are instead interesting since events involving these objects are supposed to be observed more densely at higher values of redshift, while we know that black holes coming from stellar origin are supposed to disappear after the peak of the star formation rate. Possible models describing PBHs are hence the main targets of the analysis presented in Chapter {5}.

1.1 The Einstein's equations of gravitation

One of the greatest contributions that A. Einstein gave to the world of physics, is the modern description of gravitational phenomena through the *Theory of General Relativity* [3, 6]. In this framework, gravity can be described in terms of curved space-times [26], where the amount of curvature is directly proportional to the amount of mass and energy in the considered space. This relation is described by the *Einstein equations*, which read as

$$G_{\mu\nu} = R_{\mu\nu} - \frac{1}{2} g_{\mu\nu} R = \frac{8\pi G}{c^4} T_{\mu\nu}, \tag{1.1.1}$$

where $G_{\mu\nu}$ is the *Einstein tensor*, $R_{\mu\nu}$ and R are respectively the *Ricci tensor* and the *Ricci scalar*, and $T_{\mu\nu}$ is the *stress-energy tensor*. In the next subsections, we are going to briefly define all the quantities that are involved in (1.1.1).

1.1.1 The metric and Ricci curvature tensor on a space-time

To measure distances in a curved space we need to introduce the *metric tensor* $g_{\mu\nu}$, which given a differential line element ds, is defined such as the relation

$$ds^2 = g_{\mu\nu} dx^\mu dx^\nu \ : \ g_{\mu\nu} = g_{\nu\mu}, \tag{1.1.2}$$

holds. The easiest example of a *Lorentzian metric tensor* [27, 28] is the *Minkowski space-time*, which can be considered as a 4d generalization of the *Euclidian space*. It reads as

$$ds^2 = -c^2 dt^2 + dx^2 + dy^2 + dz^2, \tag{1.1.3}$$

where the first coordinate is a temporal coordinate and the other coordinates are the standard 3d *Euclidean space* coordinates. We can write the metric tensor components in matrix form as

$$g_{\mu\nu} = \eta_{\mu\nu} = \begin{bmatrix} -c^2 & 0 & 0 & 0 \\ 0 & 1 & 0 & 0 \\ 0 & 0 & 1 & 0 \\ 0 & 0 & 0 & 1 \end{bmatrix}. \tag{1.1.4}$$

If instead we consider a more complex case, for example, a 4d expanding homogeneous and isotropic space such as the case of the *FLRW* cosmology [29], the differential line element in spherical coordinates is given by

$$ds^2 = -c^2 dt^2 + a^2(t) \left[\frac{dr^2}{1 - kr^2} + r^2 d\theta^2 + r^2 \sin^2 \theta d\phi^2 \right], \tag{1.1.5}$$

with k a constant that describes the curvature of the space manifold. The metric tensor components for the *FLRW* cosmology, defined in eq. (1.1.5), may hence be represented in matrix form as follows:

$$g_{\mu\nu} = \begin{bmatrix} -c^2 & 0 & 0 & 0 \\ 0 & a^2(t)/(1 - kr^2) & 0 & 0 \\ 0 & 0 & r^2 a^2(t) & 0 \\ 0 & 0 & 0 & r^2 a^2(t) \sin^2 \theta \end{bmatrix}. \tag{1.1.6}$$

Once a metric is defined on our manifold, we can start to introduce metric connections [27] to compute derivatives and parallel transports in our space. If we introduce the notation $g_{\alpha\beta,\nu} = \mathrm{d}g_{\alpha\beta}/\mathrm{d}x^\nu$, we can write the *Christoffel symbols* [30] as

$$\Gamma^\mu_{\alpha\beta} = \frac{g^{\mu\nu}}{2} \left(g_{\alpha\nu,\beta} + g_{\beta\nu,\alpha} - g_{\alpha\beta,\nu} \right). \tag{1.1.7}$$

These terms will describe how the basis vector α of our space evolves when moved along the β direction. Using the Christoffel symbols we can define a quantity that measures the degree to which the geometry of a given metric tensor, differs locally from that of ordinary *Euclidean space*. This quantity is called the *Ricci curvature tensor* [30], and is the one that builds the left-hand side of the previously defined Einsteins's equations (1.1.1). The latter can be expressed in terms of the Christoffel symbols (1.1.7) as follows:

$$R_{\mu\nu} = \Gamma^\alpha_{\mu\nu,\alpha} - \Gamma^\alpha_{\mu\alpha,\nu} + \Gamma^\alpha_{\beta\alpha}\Gamma^\beta_{\mu\nu} - \Gamma^\alpha_{\beta\nu}\Gamma^\beta_{\mu\alpha}. \tag{1.1.8}$$

We can easily demonstrate that this tensor is symmetric, and hence satisfy the relation $R_{\mu\nu} = R_{\nu\mu}$. Analogously, the *Ricci curvature scalar* can be easily obtained as the trace of the tensor, i.e

$$R = g^{\mu\nu} R_{\mu\nu} = R^\mu_\mu, \tag{1.1.9}$$

with

$$g^{\mu\nu} \ : \ g^{\mu\nu}g_{\nu\gamma} = \delta^{\mu}_{\gamma}. \tag{1.1.10}$$

We finally have all the terms composing the Einstein tensor $G_{\mu\nu}$. This term will account for how the space-time geometry will be curved and shaped by the term in the right-hand side of the Einsteins's equations (1.1.1).

1.1.2 The stress-energy tensor

What is missing now is defining the *stress-energy tensor*. This term will account for the mass/energy content that is present in our space-time. To give a first general form for this quantity, let us start by considering a system of n relativistic non-interacting particles located at $\xi_n(t)$ and having relativistic momenta given by

$$p^{\mu} = m(c\gamma, \gamma\vec{v}) \ : \ \gamma = \frac{\mathrm{d}\xi_0}{\mathrm{d}\tau} = \frac{\mathrm{d}ct}{\mathrm{d}\tau}, \tag{1.1.11}$$

where τ is the *proper time* in the particle reference system [7, 28]. In this situation, following [8], we can express the Stress-Energy tensor as

$$g^{\alpha\mu}g^{\nu\beta}T_{\alpha\beta} = T^{\mu\nu} = c\sum_{n}\int p^{\mu}_{n}\frac{\mathrm{d}\xi^{\nu}_{n}}{\mathrm{d}\tau_n}\delta^4(\vec{\xi} - \vec{\xi}_n(\tau_n))\mathrm{d}\tau_n, \tag{1.1.12}$$

where we can divide its components such as

- the T^{00} component describes the *energy density* in the volume;
- $\frac{1}{c}T^{0i}$ is the *density of momentum*;
- T^{ij} represent the *current of momentum*.

Even this tensor, like the Einstein tensor, is symmetric. We can hence write the condition $T^{\mu\nu} = T^{\nu\mu}$. Furthermore, it can be demonstrated (see refs. [8, 31]) that it verifies the divergenceless equation

$$T^{\mu\nu}{}_{,\nu} = 0. \tag{1.1.13}$$

In practice, depending on the context, there are some well-known models for the Stress-Energy tensor. For example, in the cosmological case, we can use the approximation of *perfect fluid* [32, 33] to write

$$T_{\mu\nu} = (\rho + \frac{p}{c^2})u_{\mu}u_{\nu} - pg_{\mu\nu}, \tag{1.1.14}$$

where ρ is the density of the fluid, p is its pressure and u_{μ}, u_{ν} is the *4-velocity* [8, 28, 33] of the fluid.

1.2 Motion of particles and geodesic deviation

We now have to understand how to write the equation of motions for a body in a gravitational field in GR, to this extent, we can use the principle of *general covariance* [3, 8], which states that the form of physical laws is the same as seen by different observers. This implies that our problem of describing the motion of a particle in a curved space can be reduced to write the equation of motion in a *Locally Inertial Frame (LIF)*, which is a spacetime that locally behaves like a flat Minkowski (1.1.4), and then simply change the equations by doing a coordinate transformation.

If the particle has coordinates ξ^μ in the locally inertial frame, the inertial condition can be expressed as

$$\frac{\mathrm{d}^2\xi^\mu}{\mathrm{d}\tau^2} = 0. \tag{1.2.1}$$

We can now move into a new coordinate system, where the new coordinates are related to the old ones as $x^\mu = x^\mu(\xi^\mu)$. By defining $\Lambda^\mu_\alpha = \mathrm{d}\xi^\mu/\mathrm{d}x^\alpha$, we can express distances in the new reference frame as

$$ds^2 = \eta_{\mu\nu}\Lambda^\mu_\alpha\Lambda^\nu_\beta dx^\alpha dx^\beta = g_{\alpha\beta}dx^\alpha dx^\beta, \tag{1.2.2}$$

where the coordinate system is chosen in such a way that η is given by eq. (1.1.4). It is clear from eq. (1.2.2) that the new metric tensor is related to the old one through the transformation law $g_{\alpha\beta} = \eta_{\mu\nu}\Lambda^\mu_\alpha\Lambda^\nu_\beta$. In the same way, by replacing the new coordinates in eq. (1.2.1), we find that the equation on motion in the new frame is given by

$$\frac{\mathrm{d}^2x^\alpha}{\mathrm{d}\tau^2} + \left[\frac{\partial x^\alpha}{\partial\xi^\lambda}\frac{\partial^2\xi^\lambda}{\partial x^\mu\partial x^\nu}\right]\left[\frac{\mathrm{d}x^\mu}{\mathrm{d}\tau}\frac{\mathrm{d}x^\mu}{\mathrm{d}\tau}\right] = \frac{\mathrm{d}^2x^\alpha}{\mathrm{d}\tau^2} + \Gamma^\alpha_{\mu\nu}\left[\frac{\mathrm{d}x^\mu}{\mathrm{d}\tau}\frac{\mathrm{d}x^\mu}{\mathrm{d}\tau}\right] = 0, \tag{1.2.3}$$

where we introduced again the *Christoffel's symbols* in order to simplify the equation. It can be proved that the $\Gamma^\alpha_{\mu\nu}$ defined in (1.2.3) and in (1.1.7) are equivalent. Equation (1.2.3) is called the *geodesic equation*, and it describes a freely falling particle in an arbitrary coordinate frame. We can further observe that the geodesic equation, together with the gravitational force naturally contains all the *apparent forces* [34], like centrifugal, Coriolis, etc. By making an analogy with the *Newtonian law of gravitation* [35] we can observe that for a cartesian coordinate system, in the geodesic equation (1.2.3) the affine connections $\Gamma^\alpha_{\mu\nu}$ are the generalization of the Newtonian gravitational field, while the metric tensor $g_{\alpha\beta}$ is the generalization of the Newtonian gravitational potential.

1.2.1 The covariant derivative of vectors

In order to properly establish the nature of a force, we need to study the relative acceleration between two neighboring geodesics. To this extent, we need to introduce the concept of *geodesic deviation*, which is generally used to check for the presence of tidal gravitational force among geodesics at different points in space-time.

Let us start by defining with $x^\mu(\tau)$ and $x^\mu(\tau)+\delta x^\mu(\tau)$ two neighboring geodesics, where we introduced δx^μ as the coordinate separation among the two close geodesics, and τ is a generical affine parameter. The tangent vector to the geodesic, in this situation, is simply given by $t^\mu = dx^\mu/d\tau$. We can parameterize this problem as a 2-parameter family of geodesic given by

$$x^\mu(\tau, p) \; : \; \begin{cases} \delta x^\mu = \frac{\partial x^\mu}{\partial p} \\ \frac{\partial t^\mu}{\partial p} = \frac{\partial \delta x^\mu}{\partial \tau} \end{cases} \quad . \tag{1.2.4}$$

As we are considering different vectors in different points of the manifold, we need to introduce a derivative that is independent of the coordinate system and is hence valid for each vector basis. Once we choose a reference system, having basis vectors $\vec{e}_{(\mu)}$, we can express a vector $\vec{V}$ in a coordinate-independent form as

$$\vec{V} = V^\mu \vec{e}_{(\mu)}. \tag{1.2.5}$$

This implies that the coordinate-independent derivative can be found by derivating eq. (1.2.5):

$$\frac{\partial \vec{V}}{\partial x^\nu} = \frac{\partial V^\mu}{\partial x^\nu}\vec{e}_{(\mu)} + V^\mu \frac{\partial \vec{e}_\mu}{\partial x^\nu}. \tag{1.2.6}$$

The first term on the RHS is a derivative of a vector, and hence we know how to compute it. The second term instead requires us to subtract basis vectors applied in different points of the manifold, which is not obvious for curved geometries. In the case of the Minkowski space-time, we know that $\vec{e}_\mu(\mathbf{p}) = \vec{e}_\mu(\mathbf{q})$ for each point $\mathbf{p}, \mathbf{q}$ in the manifold. The condition implies that the derivative of the basis vectors will be 0 everywhere on the manifold. This is a good starting point, yet we still need to find the transformation rule for the basis vector under a coordinate change in order to use it in our favor. To this extent, we can use the invariant condition on eq. (1.2.5) together with the transformation rule under coordinate change for vectors introduced in eq. (1.2.2). When moving from a coordinate system μ to a new one α, we obtain

$$\vec{V} = V^\mu \vec{e}_{(\mu)} = V^\alpha \vec{e}_{(\alpha)} = V^\mu \Lambda^\alpha_\mu \Lambda^\mu_\alpha \vec{e}_{(\mu)}. \tag{1.2.7}$$

We hence shown that a basis vector transforms as $\vec{e}_{(\alpha)} = \Lambda^\mu_\alpha \vec{e}_{(\mu)}$. If we now use the condition that Minkowskian basis vectors $\vec{e}_{M(\alpha)}$ are constants, together with the transformation rule under coordinate change for basis vector, to find the general form for the derivative of basis vectors. We get

$$\frac{\partial \vec{e}_{M(\alpha)}}{\partial x^\nu} = 0 \quad \Rightarrow \quad \frac{\partial \vec{e}_\mu}{\partial x^\nu} = \left(\frac{\partial}{\partial x^\nu}\Lambda^\alpha_\mu\right)\vec{e}_{M(\alpha)}. \tag{1.2.8}$$

It can be demonstrated that $\partial/\partial x^\nu\ \Lambda^\alpha_\mu$ is equal to the Christoffel's symbol $\Gamma^\alpha_{\mu\nu}$ (1.1.7) (see refs. [8, 27]). Hence by plugging eq. (1.2.8) in (1.2.6) we obtain

$$\frac{\partial \vec{V}}{\partial x^\nu} = \frac{\partial V^\mu}{\partial x^\nu}\vec{e}_{(\mu)} + V^\mu \Gamma^\alpha_{\mu\nu}\vec{e}_{(\alpha)}. \tag{1.2.9}$$

Equation (1.2.9) is called *covariant derivative of a vector*, and describes how a vector changes on a manifold in any chosen system of reference. In the next sections, we are going to use the notation $V^\mu_{;\nu}$ to indicate the covariant derivative of a vector, such as $\partial\vec{V}/\partial x^\nu = V^\mu_{;\nu}\vec{e}_\mu$.

1.2.2 The geodesic deviation

The question of how the relative acceleration between two neighboring geodesics behaves can now be easily posed through the mean of the covariant derivative (1.2.9). Recalling the previously introduced family of geodesics (1.2.4), one first question we may ask ourselves is how the tangent vector to the geodesic evolves by moving along the direction of the displacement δx^μ for $\tau = constant$. We hence have to estimate

$$\delta x^\alpha t^\mu_{;\alpha} = \frac{\partial x^\alpha}{\partial p}\left[\frac{\partial t^\mu}{\partial x^\alpha} + \Gamma^\mu_{\alpha\beta}t^\beta\right] = \frac{\partial t^\mu}{\partial p} + \Gamma^\mu_{\alpha\beta}t^\beta\delta x^\alpha. \tag{1.2.10}$$

Analogously, we can be interested in how the separation vector δx^μ changes along the curve with $p = const$. This is equivalent to say

$$t^\alpha \delta x^\mu_{;\alpha} = \frac{\partial \delta x^\mu}{\partial \tau} + \Gamma^\mu_{\alpha\beta}\delta x^\beta t^\alpha. \tag{1.2.11}$$

By looking at eq. (1.2.4), and recalling the symmetry in the lower indices of $\Gamma^\mu_{\alpha\beta}$, it is easy to demonstrate that

$$\delta x^\alpha t^\mu_{;\alpha} = t^\alpha \delta x^\mu_{;\alpha}. \tag{1.2.12}$$

These quantities, however, only involve the affine connections $\Gamma^\mu_{\alpha\beta}$, and do not hold consequently any information regarding the gravitational field. We hence have to compute the second covariant derivative of δx^μ along the curve with $p = const$ in order to study the effects of the latter. By introducing the new notation

$$\frac{\mathrm{D}\delta x^\mu}{\mathrm{d}\tau} = t^\alpha \delta x^\mu_{;\alpha}, \tag{1.2.13}$$

we can express the second covariant derivative as

$$\frac{\mathrm{D}^2\delta x^\mu}{\mathrm{d}\tau^2} = t^\beta (t^\alpha \delta x^\mu_{;\alpha})_{;\beta}. \tag{1.2.14}$$

It can be proved (see ref. [8]) that the RHS of eq. (1.2.14) can be rewritten as

$$\frac{\mathrm{D}^2\delta x^\mu}{\mathrm{d}\tau^2} = R^\mu_{\alpha\beta\gamma}t^\alpha t^\beta \delta x^\gamma, \tag{1.2.15}$$

where $R^{\mu}_{\alpha\beta\gamma}$ is the *Riemann curvature tensor* [27] and read as

$$R^{\mu}_{\alpha\beta\gamma} = -\left[\Gamma^{\mu}_{\alpha\beta,\gamma} - \Gamma^{\mu}_{\alpha\gamma,\beta} + \Gamma^{\mu}_{\gamma\eta}\Gamma^{\eta}_{\alpha\beta} - \Gamma^{\mu}_{\beta\eta}\Gamma^{\eta}_{\alpha\gamma}\right]. \tag{1.2.16}$$

We can further demonstrate that the *Riemann tensor* (1.2.16) is closely related to the *Ricci Curvature Tensor* (1.1.8), and we can obtain the second from the first by simply contracting over the indices $R^{\alpha}_{\mu\alpha\nu} = R_{\mu\nu}$. Equation (1.2.15) is the equation of *geodesic deviation*, that describes the relative acceleration of nearby particles moving along neighboring geodesics. Since the *Riemann tensor* is zero if and only if the gravitational field is either zero or constant and uniform, the equation of the geodesic deviation can be used to test if any gravitational field is present in our space-time, as we will see later on in the context of gravitational waves (see sec. {2.1.3}).

1.3 The Schwarzschild and Kerr solutions

We are now going to derive a solution for the *Einstein equations* (1.1.1) that is *spherically symmetric* and *static*. This type of solution is the generalization of the *Newtonian potential* $V = -GM/r$ and can be used to describe the gravitational field exterior to a non-rotating compact body.

The assumption that this solution will be static implies that the metric will be independent on time and invariant under time reversal $t \to -t$ (see refs. [7, 8]). Under this assumption, we can choose the coordinates in such a way that $\vec{\xi} \to (1, 0, 0, 0)$ and the line element assumes the simplified form:

$$ds^2 = g_{00}(x^i)(dx^0)^2 + g_{kn}(x^i)dx^k dx^n \ : \ i, k, n \in [1, 3] \ , \ g_{00} = g(\vec{\xi}, \vec{\xi}) = \vec{\xi} \cdot \vec{\xi}. \tag{1.3.1}$$

The spherical symmetry can instead be imposed on the metric by "filling" the space with concentric spherical surfaces. For example, if we consider the $2-$sphere of radius a in flat space we can write

$$ds^2_{(2)} = g_{22}(dx^2)^2 + g_{33}(dx^3)^2 = a^2\left(d\theta^2 + \sin^2\theta d\phi^2\right). \tag{1.3.2}$$

It can be shown that these results will continue to hold even if $a = a(x^0, x^1)$. In our case, however, we already know that due to our static assumption, our metric will not depend on time. We can hence define $r = a(x^1)$ and rewrite eq. (1.3.2) as

$$ds^2_{(2)} = r^2\left(d\theta^2 + \sin^2\theta d\phi^2\right). \tag{1.3.3}$$

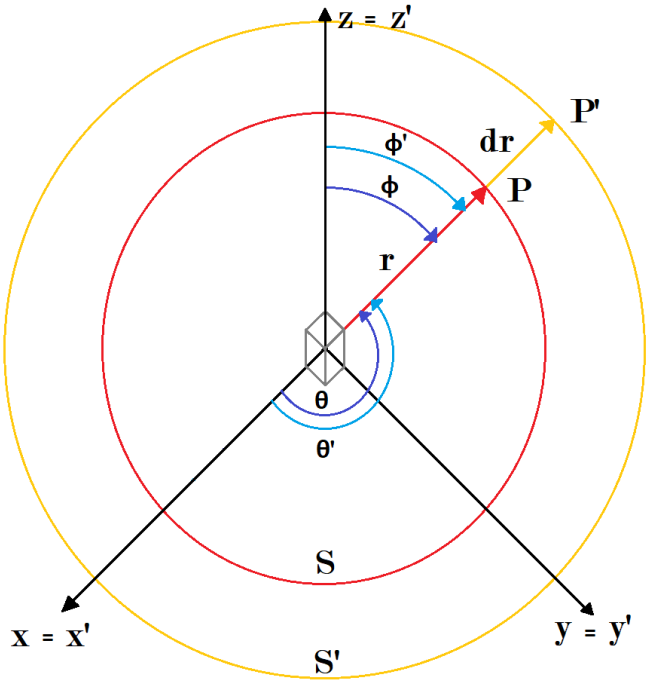

Figure 1.1. A set of concentric spheres with aligned poles. For these objects, it is possible to represent a point on the surface of each sphere at radius r using the same reference frame.

We have to emphasize that the radial coordinate r introduced in eq. (1.3.3) has nothing to do with the distance between the center of the sphere and the surface. By moving in our space to the next sphere at radius $r + dr$, we have in principle to define a new coordinate system for the angular coordinates on the second sphere given by (θ', ϕ'). Since we want angular coordinates (θ, ϕ) defined in a unique way on the whole set of spheres filling the space, we have to assume that the poles of the spheres are aligned, hence for all the spheres we have

$$\begin{cases} \frac{\vec{\partial}}{\partial r} = \vec{e}_{(r)} \\ \frac{\vec{\partial}}{\partial \theta} = \vec{e}_{(\theta)} \\ \frac{\vec{\partial}}{\partial \phi} = \vec{e}_{(\phi)} \end{cases} \xrightarrow{\text{orthogonality}} \begin{cases} \vec{e}_{(r)} \cdot \vec{e}_{(\theta)} = g_{r\theta} = 0 \\ \vec{e}_{(r)} \cdot \vec{e}_{(\phi)} = g_{r\phi} = 0 \end{cases} . \tag{1.3.4}$$

The situation is represented in fig. 1.1. Under these assumptions, we can rewrite the metric for the 3−space as

$$ds^2_{(3)} = g_{rr} dr^2 + r^2 \left(d\theta^2 + \sin^2 \theta d\phi^2 \right) , \tag{1.3.5}$$

while the one for the 4−dimensional space-time becomes:

$$ds^2 = g_{00} (dx^0)^2 + g_{rr} dr^2 + r^2 \left(d\theta^2 + \sin^2 \theta d\phi^2 \right) , \tag{1.3.6}$$

where we recall that, as by changing to a different angular coordinate system the two quantities g_{00} and g_{rr} should remain invariant and are not dependant on time, we can

only have $g_{00} = g_{00}(r)$ and $g_{rr} = g_{rr}(r)$. It is convenient to redefine

$$\begin{cases} g_{00}(r) = -e^{2\nu(r)} \\ g_{rr}(r) = e^{2\lambda(r)} \end{cases} . \tag{1.3.7}$$

We can now express the components of the *Einstein tensor* defined in (1.1.1), for the metric defined in (1.3.6),(1.3.7), we obtain the following non-zero components:

$$G_{00} = \frac{1}{r^2} e^{2\nu(r)} \frac{\mathrm{d}}{\mathrm{d}r} \left[r \left(1 - e^{-2\lambda(r)} \right) \right], \tag{1.3.8a}$$

$$G_{rr} = -\frac{1}{r^2} e^{2\lambda(r)} \left[\left(1 - e^{-2\lambda(r)} \right) \right] + \frac{2}{r} \nu_{,r}(r), \tag{1.3.8b}$$

$$G_{\theta\theta} = r^2 e^{-2\lambda(r)} \left[\nu_{,rr}(r) + \nu_{,r}^2(r) + \frac{\nu_{,r}(r)}{r} - \nu_{,r}(r)\lambda_{,r}(r) - \frac{\lambda_{,r}(r)}{r} \right], \tag{1.3.8c}$$

$$G_{\phi\phi} = \sin^2\theta \, G_{\theta\theta}. \tag{1.3.8d}$$

When looking for a solution in a vacuum, the *Einstein equations* becomes

$$G_{\mu\nu} = 0. \tag{1.3.9}$$

Equation (1.3.8a) implies

$$r \left(1 - e^{-2\lambda} \right) = r_s \quad \Rightarrow \quad e^{2\lambda} = \frac{1}{1 - \frac{r_s}{r}}, \tag{1.3.10}$$

where r_s, for now, is just an integration constant. The second equation (1.3.8b) will instead reduce to

$$\nu_{,r}(r) = \frac{1}{2} \frac{r_s}{r(r - r_s)} \quad \Rightarrow \quad \nu = \frac{1}{2} \log \left(1 - \frac{r_s}{r} \right) + \nu_0, \tag{1.3.11}$$

which implies that

$$e^{2\nu(r)} = \left(1 - \frac{r_s}{r} \right) e^{2\nu_0}. \tag{1.3.12}$$

The constant ν_0 introduced in eq. (1.3.12) can be removed by rescaling the time coordinate to $t \to e^{\nu_0} t$. We can hence rewrite it as

$$e^{2\nu(r)} = \left(1 - \frac{r_s}{r} \right). \tag{1.3.13}$$

By substituting the terms of eqs. (1.3.13) and (1.3.10) into the metric (1.3.6) we obtain

$$ds^2 = -\left(1 - \frac{r_s}{r} \right) c^2 dt^2 + \frac{1}{1 - \frac{r_s}{r}} dr^2 + r^2 \left(d\theta^2 + \sin^2\theta d\phi^2 \right). \tag{1.3.14}$$

The last thing that is missing is understanding what the integration constant r_s that we introduced in eq. (1.3.10) is. To this extent, we can use the *weak field limit* (see refs. [7, 8]) to impose that the geodesic equations of motion (1.2.3) reduce to the Newtonian equation of motions as

$$g_{00} \approx -\left(1 + \frac{2\Phi}{c^2}\right) = -\left(1 - \frac{2GM}{c^2 r}\right), \tag{1.3.15}$$

where we defined with $\Phi = -GM/r$ the Newtonian gravitational potential. By comparing with the g_{00} component defined in the Schwarzschild metric it is easy to demonstrate that

$$r_s = \frac{2GM}{c^2}. \tag{1.3.16}$$

Hence the quantity that we defined with r_s is simply the *Schwarzschild radius* [36], which as we are going to show in the next subsection, for a Schwarzschild black hole is located in correspondence of its event horizon.

1.3.1 Singularities of the Schwarzschild solution and Black Holes

The metric defined in eq. (1.3.14) is singular when $r = 0$ or $r = r_s$, while for $r \to \infty$ the metric reduces to that of a flat spacetime (*asymptotically flat*). We further observe that when $r \to 0$ we have $g_{00} \to \infty$ and $g_{rr} \to 0$. Analogously, when $r \to r_s = 2GM/c^2$ we have $g_{00} \to 0$ and $g_{rr} \to \pm\infty$ depending on whether r is approaching r_s from left or right respectively.

To check the nature of the previous singularities we have to compute the scalars of the *Riemann tensor* (1.2.16) and check if they diverge. By renormalizing the mass as $m = MG/c^2$, we have

$$R^t_{rtr} = -2\frac{m}{r^3}\left(1 - \frac{2m}{r}\right)^{-1}, \tag{1.3.17a}$$

$$R^t_{\theta t\theta} = \frac{1}{\sin^2\theta} R^t_{\phi t\phi} = \frac{m}{r^5}, \tag{1.3.17b}$$

$$R^\theta_{\phi\theta\phi} = 2\frac{m}{r^5}\sin^2\theta, \tag{1.3.17c}$$

$$R^r_{\theta r\theta} = \frac{1}{\sin^2\theta} R^r_{\phi r\phi} = -\frac{m}{r^5}. \tag{1.3.17d}$$

The *Kretschmann scalar* can be obtained as

$$K_{Scal} = R_{\alpha\beta\gamma\delta} R^{\alpha\beta\gamma\delta}. \tag{1.3.18}$$

We can demonstrate that the divergencies of this quantity will correspond to proper curvature singularities, while the others are just singularities induced by the choice of the coordinates (see ref. [27]). For the Schwarzschild metric we obtain

$$K^{Schw}_{Scal} = \frac{12 r_s^2}{r^6}, \tag{1.3.19}$$

which clearly diverges only for $r = 0$. We can hence conclude that the singularity in $r = 0$ is a true singularity for the Schwarzschild metric, in analogy with the one that we have for the classical Newtonian potential, while the one in $r = 2m$ is merely a coordinate singularity.

We will now try to describe better the properties of the hypersurface that lies in the coordinate singularity at $r = 2m$. Given a generic hypersurface $\Sigma(x^\mu)$, we can define the normal vector $\vec{n} : n_\alpha = \Sigma_{,\alpha}(x^\mu)$. Analogously, the tangent vector to the hypersurface can be defined as $t^\alpha = \mathrm{d}x^\alpha(\lambda)/\mathrm{d}\lambda$, with $x^\alpha(\lambda)$ a curve on the hypersurface $\Sigma(x^\mu)$. Using the orthogonality of the two quantities we get

$$t^\alpha n_\alpha = \frac{\mathrm{d}x^\alpha}{\mathrm{d}\lambda}\frac{\mathrm{d}\Sigma}{\mathrm{d}\lambda} = \frac{\mathrm{d}\Sigma}{\mathrm{d}\lambda} = 0. \tag{1.3.20}$$

If we now introduce a locally inertial frame at a point in the hypersurface in such a way that the coordinates of the normal vector $\vec{n}$ becomes $n^\alpha = (n^0, n^1, 0, 0)$: $n_\alpha n^\alpha = (n^1)^2 - (n^0)^2$, eq. (1.3.20) will become

$$t^\alpha n_\alpha = -n^0 t^0 + n^1 t^1 = 0 \quad \Rightarrow \quad \frac{t^0}{t^1} = \frac{n^1}{n^0}. \tag{1.3.21}$$

By looking at eq. (1.3.21), we can observe that the tangent vector $\vec{t}$ can be parametrized as a function of the normal vector $\vec{n}$ as

$$t^\alpha = \Lambda\left(n^1, n^0, a, b\right) \; : \; t_\alpha t^\alpha = \Lambda^2\left[-n_\alpha n^\alpha + (a^2 + b^2)\right], \tag{1.3.22}$$

with Λ, a, b constant and arbitrary. If we compare the disposition of the *light-cones* [7] with respect to the hypersurfaces, we have three possibilities:

- $n_\alpha n^\alpha < 0$: n^α is a *timelike* vector and the surface $\Sigma(x^\mu)$ is **spacelike** ;
- $n_\alpha n^\alpha > 0$: n^α is a *spacelike* vector and the surface $\Sigma(x^\mu)$ is **timelike** ;
- $n_\alpha n^\alpha = 0$: n^α is a *null* vector and the surface $\Sigma(x^\mu)$ is **null**.

Since we know that a massive particle that starts in **P** has to move inside the light cone, or on the light cone if the particle is massless, looking at the relative disposition of the two will give us information about how the world lines will behave when crossing the hypersurfaces. The situations can be as follows:

1) In the case where $n_\alpha n^\alpha < 0$ and $t_\alpha t^\alpha > 0$ the surface Σ is *spacelike*, the situation is shown in fig. 1.2. In this configuration, no tangent vector of Σ lies inside the light cone generated in **P**. This implies that a spacelike surface can only be crossed in one direction;

2) When $n_\alpha n^\alpha > 0$, by looking at eq. (1.3.22) we observe that $t_\alpha t^\alpha$ can be positive,

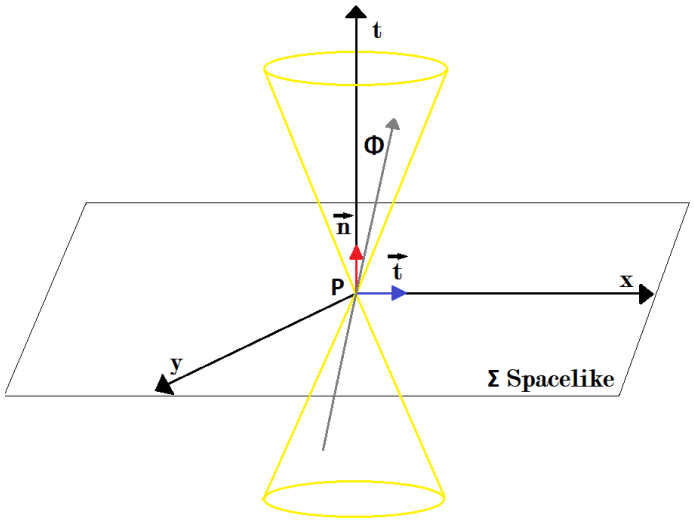

Figure 1.2. The surface Σ is *spacelike* with respect to the light-cone in **P**, it can hence be crossed by a world line Φ only in one direction. In the figure, we indicated with $\vec{n}$ the normal vector to the surface and with $\vec{t}$ its tangent vector.

negative, or null depending on the value of $a^2 + b^2$. Indeed in this case we will have tangent vectors that lies inside the light cone, and hence the surface can be crossed inward and outward several time during the path of a world line Φ. The situation is represented in fig. 1.3;

3) The last possibility is when $n_\alpha n^\alpha = 0$, in this case $t_\alpha t^\alpha \geq 0$, with $t_\alpha t^\alpha = 0 \iff a = b = 0$. In this case, only one tangent vector of Σ (and its multiples) will lie in the light cone at **P**, the situation is shown in fig. 1.4. Only massless particles can have a world line Φ parallel to the surface Σ in this configuration.

In the case of the Schwarzschild singularity at $r = 2m$ we can consider a surface $\Sigma = r - cost = 0$. The normal vector, by using the definition (1.3.20), will hence be given by

$$n_\alpha n^\alpha = g^{\alpha\beta}\Sigma_{,\alpha}\Sigma_{,\beta} = g^{rr}\Sigma_{,r}^2 = \left(1 - \frac{2m}{r}\right). \tag{1.3.23}$$

We observe that for

- $r > 2m \quad \rightarrow \quad n_\alpha n^\alpha > 0 \quad \rightarrow \quad \Sigma$ is *timelike* ;
- $r = 2m \quad \rightarrow \quad n_\alpha n^\alpha = 0 \quad \rightarrow \quad \Sigma$ is *null* ;

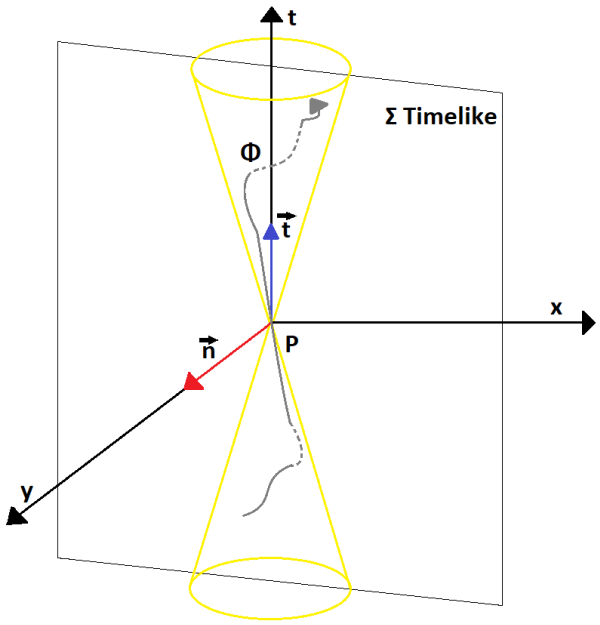

Figure 1.3. The surface Σ is *timelike* with respect to the light-cone in **P**, it can hence be crossed by a world line Φ both inward and outward several time. In the figure, we indicated with $\vec{n}$ the normal vector to the surface and with $\vec{t}$ its tangent vector.

- $r < 2m \quad \rightarrow \quad n_\alpha n^\alpha < 0 \quad \rightarrow \quad \Sigma$ is *spacelike*.

If we consider two different hypersurfaces Σ_{int} and Σ_{ext} respectively inside and outside the *horizon* at $r = 2m$, as shown in fig. 1.5. Signals starting at Σ_{ext} can be sent both toward the origin and outward, since this surface is timelike. In the case of signals generated at Σ_{int} instead, we observe that these signals must necessarily travel inward and be trapped in $r = 0$, as the surface Σ_{int} is spacelike. The *horizon* surface in $r = 2m$ instead is null, and works as a transition between the spacelike and timelike surfaces.

The *Schwarzschild solution* represents the gravitational field of a black hole [8, 37], and the hypersurface at $r = r_s = 2GM/c^2$ is called the *event horizon*. One of the reasons that led these objects to be called black holes is that if we estimate the *escape velocity* [34] for a compact object of mass M and we impose $v = c$, we obtain

$$\frac{1}{2}mc^2 = \frac{GmM}{r} \quad \Rightarrow \quad r_s = \frac{2GM}{c^2}. \tag{1.3.24}$$

In correspondence of the event horizon, the escape velocity becomes equivalent to the speed of light, and for a radius smaller than r_s, not even light has enough speed to counter the gravitational field and escape the object. This implies that no signal can escape the volume inside an event horizon, and we have no way of knowing what

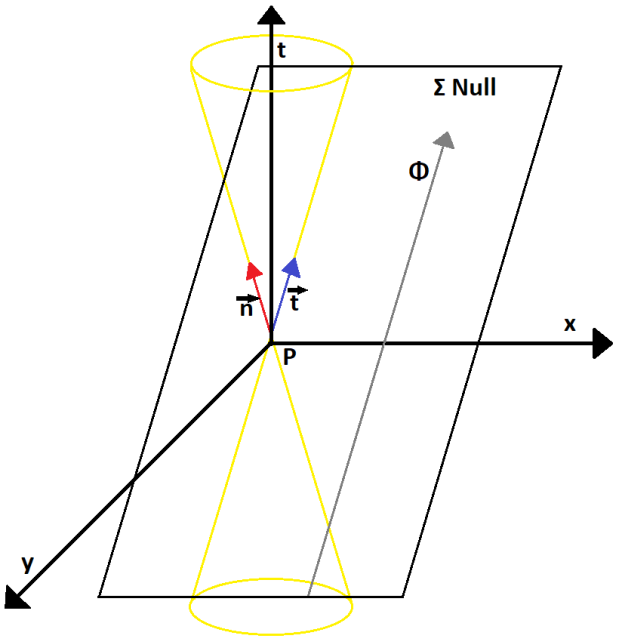

Figure 1.4. The surface Σ is *null* with respect to the light-cone in **P**, it can hence be parallel to a world line Φ only if the particle is massless. In the figure, we indicated with $\vec{n}$ the normal vector to the surface and with $\vec{t}$ its tangent vector.

happens inside of that. We can hence observe that General Relativity predicts the existence of singularities hidden behind a horizon.

1.3.2 The Kerr solution for rotating Black Holes

It is possible to find an exact solution of the *Einstein equations* (1.1.1) even for a spinning massive object, such a solution was first presented by Roy Kerr in [38, 39]. The *Kerr metric* is a solution of the *Einstein equations* in vacuum that describes a rotating, stationary, axially symmetric black hole. We emphasized that it describes a black hole because this solution describes the spacetime generated by a curvature singularity concealed by a horizon, and can hence be used only to describe the outside of these objects.

We can write the *Kerr metric* as

$$ds^2 = -dt^2 + \Sigma\left(\frac{dr^2}{\Delta} + d\theta^2\right) + \left(r^2 + a^2\right)\sin^2\theta d\phi^2 + \frac{2Mr}{\Sigma}\left(a\sin^2\theta d\phi - dt\right)^2, \quad (1.3.25)$$

where we introduced the quantities

$$\Delta(r) = r^2 - 2Mr + a^2, \quad (1.3.26a)$$
$$\Sigma(r,\theta) = r^2 + a^2\cos^2\theta. \quad (1.3.26b)$$

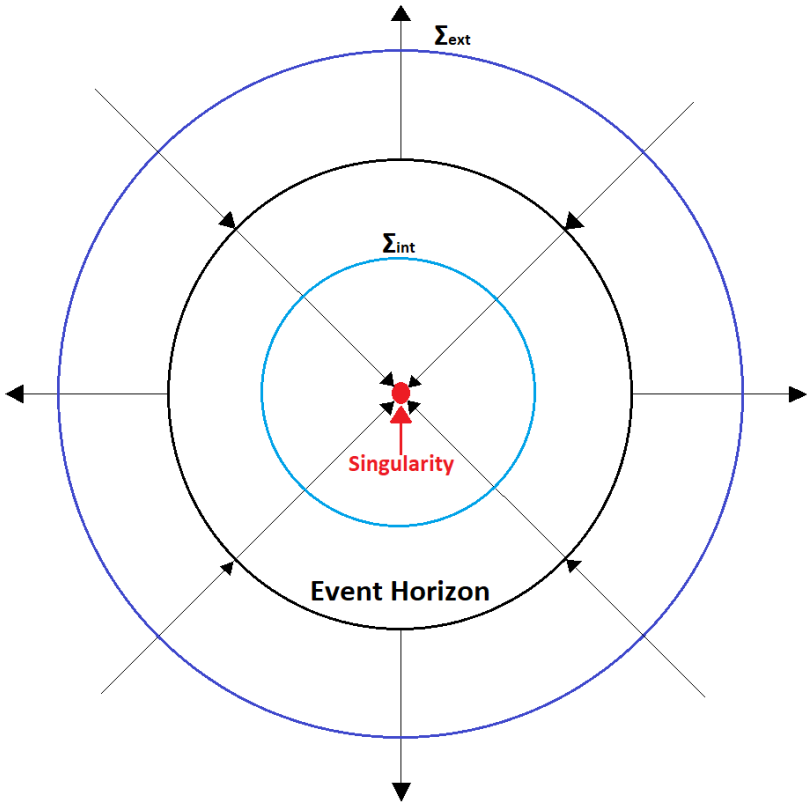

Figure 1.5. Behaviour of particles around the Schwarzschild event horizon surface. Particles that start at the surface Σ_{ext}, or generally outside the event horizon, are allowed to move both inward and outward. Particles starting at Σ_{int}, or inside the horizon are only allowed to move inward.

The metric described by eq. (1.3.25) assumes this form when using the *Boyer-Lindquist coordinates* [39]. The two parameters M and a on which the metric depends are respectively the black hole mass and its spin. We observe that we can express the angular momentum of the black hole simply as $|\vec{J}| = Ma$.

By further analyzing the line element defined in eq. (1.3.25), we can observe the following properties:

- It is not *static*, hence not invariant for time reversal $t \to -t$, it is however invaiant if we simulataneously invert $t \to -t,\ \phi \to -\phi$;
- It is *stationary*, hence it does not depend explicitly on time;
- It is *axisymmetric*, as it does not depend explicitly on the coordinate ϕ;
- In the limit $r \to \infty$, it reduces to the *Minkowski's metric* (1.1.3) in polar coordinates, hence the Kerr spacetime is *asymptotically flat*;

- In the limit $a \to 0$, if the mass $M \neq 0$, by looking at the two terms defined in eqs. (1.3.26a), (1.3.26b) we can show that the Kerr metric reduces to the *Schwarzschild metric* (1.3.14);
- In the limit $M \to 0$, if the spin $a \neq 0$, it reduces to

$$ds^2 = -dt^2 + \frac{r^2 + a^2\cos^2\theta}{r^2 + a^2}dr^2 + \left(r^2 + a^2\cos^2\theta\right)d\theta^2 + \left(r^2 + a^2\right)\sin^2\theta d\phi^2, \tag{1.3.27}$$

that is the metric of the flat spacetime in *spheroidal coordinates*

$$\begin{aligned} x =& \sqrt{r^2 + a^2}\sin\theta\cos\phi \\ y =& \sqrt{r^2 + a^2}\sin\theta\sin\phi \\ z =& r\cos\theta. \end{aligned} \tag{1.3.28}$$

For what concerns the singularities of the *Kerr metric* (1.3.25), we have a singularity in $\Delta = 0$ and one in $\Sigma = 0$, if we further look at the curvature invariants (1.3.18) we would obtain them regular on $\Delta = 0$ and singular in $\Sigma = 0$. We can hence say that the singularity in $\Delta = 0$ is a coordinate singularity while the one in $\Sigma = 0$ is a true singularity of the manifold. If we go to the Schwarzschild limit by imposing $a \to 0$, we would see that the two singularities converge to $\Sigma \approx r^2 = 0$ and $\Delta \approx r\,(r - 2M) = 0$. We can hence recover the two singularities of the Schwarzschild metric and, by comparing, we see that we have the black hole event horizon in $r = 2M$. The situation is indeed different if $a \neq 0$, as imposing $\Delta = 0 \;\Rightarrow\; r^2 - 2Mr + a^2 = 0$, which is a second order equation and hence has two solutions r_+, r_-. For a detailed description of the singularities of the *Kerr metric*, we invite the reader to see refs. [8, 39, 40].

We wish to emphasize that all astrophysical objects, to conserve angular momentum, are supposed to rotate. Hence even though most of the Black Hole observed in nature to date have a spin that is close to 0, we still expect it to be non-zero (see *e.g.* [41]), hence these objects should be described by the Kerr metric. From a theoretical point of view, we further know that when a black hole forms via gravitational collapse, gravitational wave emission, and other dissipative processes will dampen its violent oscillations and leave the remnant after some time in a *stationary* state. We have some remarkable theorems on stationary black holes, derived by S. Hawking, W. Israel, and B. Carter that prove that:

- A *stationary* black hole is *axially symmetric*;
- Any *stationary*, *axially symmetric* black hole with no electric charge is described by the *Kerr solution*;
- Any *stationary*, *axially symmetric* black hole with electric charge can be described using the *Kerr-Newmann solution*, which is a generalization of the *Kerr solution* characterized by the three parameters M, a and Q.

From the third point we see that all the other features that a star had before collapsing disappear once the final black hole is formed, this characteristic has been summarized with the sentence *"A Black Hole has no hair"* [42, 43], and for this reason, the theorems are defined as *No-Hair theorems*.

1.4 Black Holes formation channels and populations

The direct detection of gravitational waves by the LIGO-Virgo collaboration [44] opened a new era of scientific exploration, as gravitational-wave astronomy can allow us to test models of black hole formation, growth, and evolution [15]. To date, we now have officially around 90 detections [45], and this allowed us to start analyzing the population properties of the BHs that populate our Universe [46]. Among the main goals that we have for the next decades, we plan to understand better the formation channels [47] that led to the BHs population that we are observing in our Universe. Furthermore, it would be nice to understand if some of the observed ones come from a *non-astrophysical origin* [15, 48], *e.g.* the case of PBHs [49, 50]. To this extent, some studies were already performed with the latest LVK results [51, 52] and several analyses are planned for the next generation of detectors (see *e.g.* [25, 53–55]).

In the following sections, we are going to briefly describe BHs coming from *astrophysical origin* and PBHs. Rather than discussing in detail all the evolutionary processes involved that lead to the BHs that we can observe today, we are going to present how these objects are formed, in order to emphasize the difference that we expect among them. To begin, astrophysical black holes are more likely to form in rich environments where stars can form, and hence they can interact with their environment and increase their mass through *accretion*, *merger*, or both. Furthermore, we will try to highlight that while astrophysical black holes follow the cosmic history of our Universe, and as such are supposed to have a distribution in redshift that peaks around the *Star Formation Rate (SFR)* ($z \sim 2$) [56, 57]. The PBH formation mechanism allows them to form at any redshift in our Universe, and in particular, for these objects, we expect to have a *merger rate* that grows as a function of redshift. This main differentiation makes them an extremely interesting object for next-generation detectors like A^+ LIGO [58], LISA [59] and ET [60], which will be able to observe the Universe at much higher redshift compared to the present-stage detectors, and led to the study that we performed in the paper in Chapter {5}.

1.4.1 Stellar Origin Black Holes populations

As the name suggests, *Stellar Origin Black Holes (SOBHs)* are formed from the gravitational collapse of stars. The formation of BHs can both be achieved through the evolution of massive *single stars* [61–64], or as the end product of a *binary star system* [62, 65–67] or *multiple star system* [68–70]. When discussing star evolution, in particular, we can further differentiate between the evolution in *isolated environments* [71–73], or the *dynamical evolution* in dense stellar clusters [74–76].

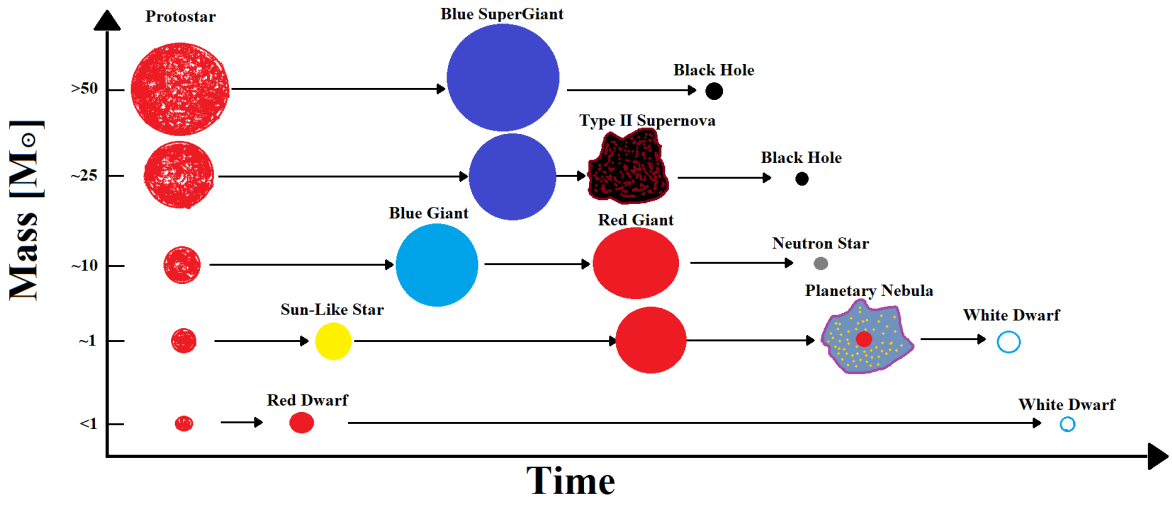

Figure 1.6. The evolution of single stars as a function of their mass. These results are indicative, as in principle they depend on several additional factors (*e.g.* chemical composition or potential accretions phenomena), and they are based on the figure presented in [77].

If we consider the simple case of a single star evolving in an isolated environment, we can assume that both *mass-transfers* and *accretion phenomena* are negligible. Under these circumstances, whether or not a star will create a black hole at the end of its life mainly depends on the initial mass of the progenitor star [77]. The situation is described in fig. 1.6, where we can observe that BHs usually form either from weak *supernovae* explosions, after some of the material that is initially ejected falls back and brings the core mass over the threshold. Alternatively, BHs can form without a supernova explosion at all, with what is called *direct collapse* [78, 79]. The description of fig. 1.6 is only indicative, as several additional factors need to be taken into account when properly estimating the evolution of stars. For example, the chemical composition, and in particular the *metallicity* [80–82], will influence the evolution of the considered star. This influence will be two-fold: the first one is direct, as the chemical composition of a star affects its life and evolution [81–83]. The reason is that stars balance the gravitational collapse and achieve hydrostatic equilibrium by means of nuclear reactions in their cores. The abundance of elements that are present in the stars are hence one of the main driving factors that will determine their life and evolution. Furthermore, the *stellar winds* intensity, and hence the mass-loss rates of stars, among other quantities, are also influenced by the metallicity of the considered star [84–87]. The second influence of metallicity over star evolution is instead indirect, and is related to the fact that the star metallicity can be directly linked with the cosmic history of our universe [80, 88]. We expect the first metal-free stars (also known as population III stars [72, 89]) to favor very high masses and appear in primordial isolated mini halos. As heavy elements are mainly produced throughout star Nucleosynthesis [90, 91], we expect these stars to appear at higher redshift ($z \gtrsim 15$), where the heavy elements were still rare. This also implies that these types of stars could,

in principle, have produced *Binary Black Hole (BBH)* mergers in the early Universe ($z \sim 10$) [92]. When considering the local Universe instead ($z < 2$), we mainly observe metal-rich population I and II stars [67, 93]. These stars are usually smaller compared to the old population III stars, but live in much richer environments where multiple star systems are more likely and dynamical evolution effects become relevant.

It's important to emphasize that the situation of fig. 1.6 deeply changes in the case of *binary or multiple star systems*. These systems, are also particularly relevant as the majority ($\sim 70\%$) of type O and B massive stars (see ref. [94] for details about this classification), which are the most likely progenitors of *Neutron Stars (NSs)* and BHs, are found in close binary systems [15, 95]. The main effects that will change the evolution of multiple star systems compared to isolated stars are the presence of *tidal forces* [96, 97] and *mass-transfers* [98–100] among the elements. We can further differentiate the *mass-transfer* phenomena among the involved stars as *stable* or *unstable* (also called *common-envelope phase*). During the *common envelope* stage, the BH from the more massive star (that is supposed to collapse first) and the core of the secondary star orbit inside a common envelope. Their separation will hence be reduced, while the residual orbital energy is given to the envelope, which is in turn expelled if said energy is high enough (see refs. [101–103] for further details about this phase). This phase is particularly relevant in GW astronomy as it will lead to BBHs with a reduced separation, which are hence more likely to merge in a Hubble time [104, 105]. Further difference from the single star evolution can also be found on the properties of the generated BHs, both on the resulting final mass and spin [62, 106, 107].

To conclude, we will briefly discuss the *dynamical effects* introduced by the environment in which the stars are born and evolve. As stars are formed from large clouds of dust and gas, the vast majority of the stars observed are found in clusters, which can contain from a few to several million of stars [108, 109]. When studying the evolution of a star system in a dense cluster, we can not neglect the dynamical effects that the environment will have on its evolution. The system will hence not be closed anymore, and exchanges of matter and energy with its surroundings will affect its resulting end-state [75, 110, 111]. Among the most relevant effects to consider when computing the dynamical evolution of stellar systems in dense environments, we have *stellar encounters and interactions* [76, 110, 112, 113], *mass segregation* [114–116], and the presence of *accretion disks* [83, 117, 118].

When taking into account all the second-order effects, observations and numerical simulations favor the formation of BHs with masses between $\sim [5, 50] M_\odot$ or masses above $\sim 135\, M_\odot$ [15]. For masses between $\sim [2, 5] M_\odot$, we have the *first mass gap* [119, 120], while for masses in $\sim [50, 135] M_\odot$ we have the *second gap*, which is supposed to arise from the occurrence of *Pair-Instability Supernovae (PISN)* [90, 121]. For a more detailed discussion on the processes and parameters involved in the evolution of single stars, we refer the reader to see *e.g.* refs. [122, 123], while for detailed numerical evolutionary simulations, we invite the reader to see refs. [63, 66, 124, 125].

In practice, we expect the merger rate of *SOBH* to follow (up to *time delays* [126, 127]) the *Star Formation Rate (SFR)* [56, 128]. The latter is phenomenological, and can be estimated from observations knowing that

$$L_{UV} \sim C_{IMF} SFR, \tag{1.4.1}$$

with L_{UV} representing the luminosity flux in the UV spectrum and C_{IMF} is a constant depending on the choice of the stellar *Initial Mass Function (IMF)*. Observations suggest that the *SFR* is supposed to have an initial power-law growth as a function of redshift until it reaches a peak. After the peak, the *SFR* will then dampen off with a different power-law behavior [129]. This result was used in refs. [56, 130] to estimate the *BBH merger* rate in our Universe, and will be used in the articles in sec. {4.2.2} and app. {5.6} to extend the BHs population synthesis at values greater than the volume of Universe observed by our present-stage detectors.

1.4.2 Primordial Black Holes

Among the most interesting formation channels for black holes we have the *Primordial Black Holes* [49, 50]. These compact objects gained over the last years an increasing relevance in literature as PBHs could explain both some of the signals from binary black hole mergers observed in gravitational wave detectors (especially the high z component and the black holes in the predicted stellar mass gaps) [131, 132], and an important component of the dark matter in the Universe [133, 134]. The idea that black holes could have formed in the early Universe dates back to the $60s$ [135, 136], even though it started to gain importance only later when it started to become the main suspect for the dark matter component of our Universe (see refs. [137, 138]). This belief reached its peak around the $90s$, when the results of the MACHO surveys were released (see refs. [139, 140]). However, later studies made by [141–143] imposed much more stringent limits to the PBHs abundancy, making them capable of accounting only for a small component of the dark matter observed in our Universe. Research in PBHs got lit up again by the first detection of gravitational waves in our Universe [44], as recent observations of black holes in the first, second, and third observing runs of LIGO/Virgo [45, 144] present events that could be of primordial origin. Furthermore, the analysis of the *Stochastic Gravitational Wave Background (SGWB)* [145, 146] in the context of LISA [1] and NANOGrav [147], will shed further light on the mechanisms and constraints that generate BHs of primordial origin.

We can now describe the theory behind the process of formation of primordial black holes. Generally speaking, they form after cosmological perturbations re-enter the cosmological horizon. The mechanisms that may generate the initial cosmological perturbations are several, and will generate highly different results both in terms of PBH abundancy and mass range. In the following, we are hence going to describe the general process of formation rather than focus on any particular perturbation formation mechanism; we leave the reader to more detailed PBH reviews such as

[16, 50, 132, 134, 148] for details about the latter.

When assuming spherical symmetry on superhorizon scales, we can write the metric for the local region of the Universe describing such perturbations in the following asymptotic form:

$$ds^2 = -dt^2 + a^2(t)\left[\frac{dr^2}{1-K(r)r^2} + r^2 d\Omega^2\right] = -dt^2 + a^2(t)e^{2\xi(\hat{r})}\left[d\hat{r}^2 + \hat{r}^2 d\Omega^2\right], \quad (1.4.2)$$

where $a(t)$ is the scale factor, while $K(r)$ and $\xi(\hat{r})$ are the conserved comoving curvature perturbations. These perturbations are defined on a super-Hubble scale and converge to zero at infinity, where we assume the Universe to be unperturbed and spatially flat. By equating the radial and angular parts of the two forms of the metric presented in (1.4.2), we obtain

$$\begin{cases} r = \hat{r}e^{\xi(\hat{r})} \\ \frac{dr}{\sqrt{1-K(r)r^2}} = e^{\xi(\hat{r})}d\hat{r} \end{cases} . \quad (1.4.3)$$

The difference between the two Lagrangian coordinates r and $\hat{r}$ is hence given by the parametrization of the comoving coordinate, fixed by a curvature perturbation chosen in the metric $K(r)$ or $\xi(\hat{r})$. This can be geometrically interpreted as the coordinate $\hat{r}$ considering the perturbed region as a local *Lemaitre-Tolman-Bondi (LTB)* universe (see refs. [17, 149] for further details about this metric) with the curvature perturbation $\xi(\hat{r})$ modifying the local expansion. The curvature profile $K(r)$ is defined with respect to the background *FLRW* solution (given by the condition $K = 0$) and measures more directly the spatial geometry of space-time. We can relate the two radial functions on superhorizon scales, where the curvature profile is time-independent, as

$$K(r)r^2 = -\hat{r}\xi'(\hat{r})\left[2 + \hat{r}\xi'(\hat{r})\right]. \quad (1.4.4)$$

In this regime, we can also expand the time-dependent variables (such as energy density and velocity profiles) as power series of a small parameter ϵ up to the first non-zero order, where we identify ϵ with the ratio between the *Hubble radius* and the length scale of the perturbation. This approximation is called *gradient Expansion* and is equivalent to saying that in this regime pressure gradients are negligible, hence the perturbation evolution grows with the universe expansion in a self-similar way. Further details on this approach can be found in [150, 151]. Using this approximation, we can follow [152, 153] to write the energy density profile as

$$\begin{aligned} \frac{\delta\rho}{\rho_b} &= \frac{\rho(r,t) - \rho_b(t)}{\rho_b(t)} = \frac{1}{a^2H^2}\frac{3(1+w)}{5+3w}\frac{[K(r)r^3]'}{3r^2} \\ &= -\frac{1}{a^2H^2}\frac{4(1+w)}{5+3w}e^{-5\xi(\hat{r})/2}\nabla^2 e^{\xi(\hat{r})/2}, \end{aligned} \quad (1.4.5)$$

where $H(t) = \dot{a}(t)/a(t)$ is the *Hubble parameter*, w is the coefficient of the equation of state $p = w\rho$ and ρ_b is the *background density*. The latter can be estimated with the

standard formula for homogeneous and isotropic universes, and scales as $\rho_b \propto 1/a^3$. For $\xi(\hat{r}) \ll 1$, we are in the linear regime, and eq. (1.4.5) can be rewritten as

$$\frac{\delta\rho}{\rho_b} = -\frac{1}{a^2H^2}\frac{2(1+w)}{5+3w}\nabla^2\xi(\hat{r}) \overset{\text{FT}}{\approx} -\frac{k^2}{a^2H^2}\frac{2(1+w)}{5+3w}\xi_k. \tag{1.4.6}$$

In the linear regime, there is hence a simple one-to-one mapping between the real space, where the perturbations collapse, and the Fourier space where the power spectrum of cosmological perturbations is defined. If we consider a Gaussian curvature perturbation ξ, the density contrast given by eq. (1.4.6) has also a Gaussian distribution within the linear regime. It has however to be emphasized that the *treshold amplitude* δ_c, that defines when a primordial perturbation will collapse into a PBH, has a non-linear behaviour. The linear regime does not hence give an accurate description of the statistics of the density contrast. For this reason, in the next subsection, we are going to define the amplitude of a perturbation δ_m, so that we can estimate the PBHs formation as a function of the number of perturbations that surpass the threshold amplitude δ_c.

1.4.3 Primordial perturbation amplitude and threshold for PBH formation

In order to describe the amplitude of primordial cosmological perturbations, it is useful to define the *compaction function* [153, 154]:

$$C(r,t) = 2\frac{\delta M(r,t)}{R(r,t)}, \tag{1.4.7}$$

where we defined with $R(r,t) = a(t)r$ the areal radius. The term $\delta M(r,t)$ is instead given by the difference between the *Misner-Sharp mass* $M_{MS} = R(r,t)^3 R_{\theta\phi\theta\phi}/2$ [155, 156] within a sphere of radius $R(r,t)$ and the background mass $M_b(r,t) = 4\pi\rho_b(r,t)R^3(r,t)/3$ calculated with respect to a spatially flat *FLRW* metric. In the superhorizon regime, the compaction function is time-independent and can be rewritten as

$$C(r) = \frac{3(1+w)}{5+3w}K(r)r^2, \tag{1.4.8}$$

which is directly dependent on the curvature profile $K(r)$ and can be rewritten as a function of $\xi(\hat{r})$ using eq. (1.4.4). We can define the comoving length scale of the perturbation simply by considering the distance at which the compact function reaches its peak, which will be a maximum for a positive perturbation and vice versa, this value will be denoted as $r = r_m \ : \ C'(r_m) = 0$. The value of r_m can hence be easily obtained from eq. (1.4.8) once the function $K(r)$ or $\xi(\hat{r})$ are defined, this can be done simply by imposing

$$\begin{cases} K(r_m) + \frac{r_m}{2}K'(r_m) = 0 \\ \xi'(\hat{r}_m) + \hat{r}_m\xi''(\hat{r}_m) = 0 \end{cases}. \tag{1.4.9}$$

From the definition of the curvature profile, we can also find the parameter ϵ used in the gradient expansion. In terms of the areal radius scales it reads as

$$\epsilon = \frac{R_H(t)}{R_b(r_m, t)} = \frac{1}{a(t)Hr_m} = \frac{1}{a(t)H\hat{r}_m e^{\xi(\hat{r}_m)}}, \tag{1.4.10}$$

where we defined with $R_H(t) = 1/H$ the *cosmological horizon* and with $R_b(r,t)$ the background component of the areal radius. We can observe that for values of $\epsilon \ll 1$ eq. (1.4.5) is valid.

Finally, we can now give a consistent definition of the *perturbation amplitude*, this can be defined as the mass excess of the energy density within the scale r_m when $\epsilon = 1$, or analogously $a(t)Hr_m = 1$. We are hence implicitly defining the *horizon crossing time* t_H with a linear extrapolation from the superhorizon regime. This assumption is not very accurate, but it still provides on one hand a well-defined criterion to measure and compare consistently the amplitude of different perturbations, and on the other hand to understand how the threshold varies with respect to the initial curvature profiles. We will hence define the perturbation amplitude measured at time t_H, which we are going to refer as $\delta_m = \delta(r_m, t_H)$, as

$$\delta_m = \frac{4\pi}{VR_m}\int_0^{R_m} \frac{\delta\rho}{\rho_b} R^2 dR = \frac{3}{r_m^3}\int_0^{R_m} \frac{\delta\rho}{\rho_b} r^2 dr, \tag{1.4.11}$$

where we can define the volume at the lenght scale R_m as $V_{R_m} = 4\pi R_m^3/3$, and the second equality comes from the approximation $R_m \approx a(t)r_m$.
If we now introduce eq. (1.4.5) into eq. (1.4.11), we can obtain an equation for $\delta_m \sim C(r_m)$. This can be further simplified as shown in ref. [153] to get the fundamental relation:

$$\delta_m = 3\frac{\delta\rho}{\rho_b}(r_m, t_H), \tag{1.4.12}$$

which shows that at the scale r_m the perturbation amplitude is independent of the location at which it is measured.

What is left is just to define a threshold δ_c such that PBHs will form when the perturbation amplitude is $\delta_m > \delta_c$. We emphasize that the value of the threshold δ_c is not constant, as should be dependent on the shape of the energy density profile and the equation of state. In literature, it is shown by refs. [153, 157] that for a *radiation-dominated* universe, where the equation of state read as $P = \rho/3$, we have the parameter δ_c in the range $2/5 \leq \delta_c \leq 2/3$. We can hence show that in this situation, the shape of the cosmological perturbation is simply related to one dimensionless parameter corresponding to the width of the peak of the compaction function. This parameter is defined as

$$\alpha = -\frac{C''(r_m)r_m^2}{4C(r_m)}. \tag{1.4.13}$$

The threshold value δ_c can now be defined as a function of α simply as

$$\delta_c \approx \frac{4}{15} e^{-1/\alpha} \frac{\alpha^{1-\frac{5}{2\alpha}}}{\Gamma\left(\frac{5}{2\alpha}\right) - \Gamma\left(\frac{5}{2\alpha}, \frac{1}{\alpha}\right)}, \tag{1.4.14}$$

where the Γ are the *special Gamma functions*. Analogously, the mass of the generated PBHs can be described as a function of its perturbation amplitude compared to the critical threshold as

$$m_{PBH} = \mathcal{K}(\delta - \delta_c)^{\eta} M_H. \tag{1.4.15}$$

In the last equation, we defined with η the *critical Exponent*, which depends only on the equation of state (*e.g.* for a radiation-dominated universe we have $\eta \approx 0.36$). We also introduced the quantity $\mathcal{K}$ that, as for δ_c, depends on the initial configuration of the energy density profile, and can roughly vary in the range $[1, 10]$.

We finally have all the tools we need to estimate the primordial component of BHs in our Universe. To this extent, we have to choose from theory a mechanism for the formation of the initial primordial perturbation and its relative shape for the functions $K(r)$ and $\xi(\hat{r})$. It has to be emphasized however that eq. (1.4.15) only describes the mass with good accuracy in the regime $m_{PBH} \leq M_H$. Furthermore, the non-linear relation between the curvature perturbation and the density contrast in eq. (1.4.5) introduces non-Gaussianity of the density contrast, even when assuming a Gaussian primordial initial condition (see refs. [153, 158, 159]). To conclude, it is important to take into account that several phenomena happen in our Universe from the formation of PBHs to how we observe them today. Rigorous analysis of this BH formation channel hence requires taking into account for *accretion phenomena* [51, 160] and potential *clustering effects* [161, 162].

Chapter 2

An introduction to Gravitational Waves

The *Einstein equations* (1.1.1) describe the gravitational field generated in a space-time by its matter-energy content. In stationary conditions, there are no big questions arising on the behavior of such a field. The situation however gets a bit more complicated in the real scenario, where massive objects will move around and eventually merge and change the spatial distribution of masses in the region. Indeed we expect that if one region of space-time becomes overdense compared to others, the gravitational field close to that region will become naturally stronger. What is not so straightforward is understanding how the information of the new field will be delivered to the affected bodies, and also, how the gravitational field generally propagates in space. We know that one of the main pillars on which *Einstein's special relativity* is built is the fact that the *speed of light* is absolute [28], and is the maximum speed that can be reached by bodies in a vacuum. This assumption also ensures that in GR the *causality* [8, 33] of events is respected. It is only natural hence to expect that variations in the gravitational field would not be delivered instantly to all the bodies affected by it, but will instead propagate in space at a speed lower or equal to the speed of light through some sort of carrier.

In this chapter, we are hence going to introduce the concept of *Gravitational Wave* [5], both to discuss how the gravitational field propagates into space and also as a means to observe *"dark objects"* such as *Black Holes* [15]. The derivation of the results will follow the approach of [8, 31], while the chapter is organized as follows: In sec. {2.1} we follow the standard approach of perturbing the *Minkowski metric* (see ref. [8] for the full calculation) in order to obtain the *Gravitational Waves equations on a flat space-time*. Through this process, we will discuss some useful concepts such as the *TT-gauge* and the *polarization states* of a gravitational wave. The second in particular, will be implicitly used in all the papers presented in this thesis when the incoming signal needs to be converted into strain in a particular detector (for further details see sec. {5.3.1}). We continue in sec. {2.2} with the gravitational wave theory by introducing the *quadrupole moment tensor* and the *Transverse-Traceless (TT) projector*. These quantities are extremely important in the context of *numerical*

waveforms [163, 164], and will lead at the end of subsection {2.2.1} to the *numerical waveform equation* (2.2.8). On one hand, this equation is in principle the most accurate description we have for gravitational wave phenomena, and was used to build the *LIGO Gravitational Waves Template Bank* as shown in refs. [165–167]. On the other hand, integrating the full *Einstein equations* has a very high computational cost, especially when they have to be computed for all the possible event parameters that could happen in our Universe. This drawback led hence to either try to reduce the density of points in the template bank (*e.g.* refs. [168–170]) at the cost of loss of representation quality of incoming signals (see the article in Chapter {3}), or to use approximated *phenomenological waveforms* to describe at least the pre-coalescence part of the signal (see *e.g.* waves of the class *IMRPhenomD* [171, 172] or *IMRPhenomXHM* [173]). In section {2.2.2} we present the analytical result of eq. (2.2.8) when assuming a *circular orbit approximation*. This result in its simplicity, is both relevant as a starting point to the development of Phenomenological waveforms, and because it is a very good approximation for nearly monochromatic events that are far away from merging in the LISA frequency band. To conclude, in sec. {2.3} we discuss the energy emitted from a system in the form of gravitational waves. We start by introducing the *stress-energy pseudotensor* and the *gauge-invariant energy density*. Through these quantities, after defining a waveform model we will be able to describe the GW energy emitted as a function of time (eq. (2.3.17)), surface (eq. (2.3.18)) or frequency (eq. (2.3.19)). The energy emitted as a function of time will then be used in sec. {2.3.2} to extend the regime of validity of the analytical result presented in sec. {2.2.2} to the so-called *adiabatic approximation* [174], which describes inspiralling objects that slowly evolve in time through semi-circular orbits. This approximation allows us to introduce several of the parameters that will then be used throughout this document to describe our waveforms, and are a step closer to the real phenomenological waveforms that we used, which can be obtained from these results through the use of *Post-Newtonian (PN)* corrections [175, 176]. The energy emitted through gravitational waves as a function of frequency will instead be used whenever we need to compute the *Stochastic Gravitational Wave Background* in the LISA detector (see for example the papers at sec. {4.3.1} and app. {5.10}).

2.1 Gravitational Waves theory

The metric tensor defined in eq. (1.1.2) has somehow a twofold nature: we know by definition that it defines how to measure distance in a space-time, however, due to the role that it assumes in GR and, in particular, in the *Einstein equations*, it can also be linked with the gravitational potential [8]. A consequence of this dual nature of the metric tensor is that we expect the carrier of the gravitational field, which from now on will be called *Gravitational Wave*, to behave as a *metric wave*, *i.e.* the propagation of such an object will affect the geometry and, in particular, the proper distance between space-time points in time.

The easiest way to study the properties of gravitational waves is by following a perturbative approach on a known solution of the *Einstein equations*. Let us consider for example a perturbation on the *Minkowski metric* (1.1.4), such as

$$g_{\mu\nu} = \eta_{\mu\nu} + h_{\mu\nu} \ : \ |h_{\mu\nu}| \ll |\eta_{\mu\nu}|. \tag{2.1.1}$$

This defines an inverse metric tensor that reads as

$$g^{\mu\nu} = \eta^{\mu\nu} - h^{\mu\nu} + O(h^2), \tag{2.1.2}$$

where the indices of $h^{\mu\nu}$ have been raised using the unperturbed metric. In order to find the equations that describe the behavior of $h_{\mu\nu}$, we will now try to solve the *Einstein equations* written in the following analogous form:

$$R_{\mu\nu} = \frac{8\pi G}{c^4}\left(T_{\mu\nu} - \frac{1}{2}g_{\mu\nu}T^{\lambda}_{\lambda}\right), \tag{2.1.3}$$

where even our $T_{\mu\nu} = T^0_{\mu\nu} + T^{pert}_{\mu\nu}$, with the first term of the RHS associated to our background metric and the second term associated to our perturbation term. By recalling the definitions of section sec. {1.1}, and by using the fact that the zero-order term of the *Einstein equations* is assumed to be a known solution of the latter, *i.e.*

$$R_{\mu\nu}(\eta) = \frac{8\pi G}{c^4}\left(T^0_{\mu\nu} - \frac{1}{2}\eta_{\mu\nu}T^0\right), \tag{2.1.4}$$

we can solve eq. (2.1.3) by keeping only first order terms and get

$$\begin{aligned}&\Gamma^{\alpha}_{\mu\nu,\alpha}(h) - \Gamma^{\alpha}_{\mu\alpha,\nu}(h) + \Gamma^{\alpha}_{\sigma\alpha}(\eta)\Gamma^{\sigma}_{\mu\nu}(h) + \Gamma^{\alpha}_{\sigma\alpha}(h)\Gamma^{\sigma}_{\mu\nu}(\eta)\\ -&\Gamma^{\alpha}_{\sigma\nu}(\eta)\Gamma^{\sigma}_{\mu\alpha}(h) - \Gamma^{\alpha}_{\sigma\nu}(h)\Gamma^{\sigma}_{\mu\alpha}(\eta) = \frac{8\pi G}{c^4}\left(T^{pert}_{\mu\nu} - \frac{1}{2}g_{\mu\nu}T^{pert}\right),\end{aligned} \tag{2.1.5}$$

that is linear in $h_{\mu\nu}$. We can observe that this formula is valid for any space-time metric that has a well-defined solution of the *Einstein equations* $g^0_{\mu\nu}$, as long as we replace the terms of the background metric $\eta_{\mu\nu} \to g^0_{\mu\nu}$. The situation, however, can easily become very complicated to calculate, and often, no analytical solution will be available for the chosen metric.

2.1.1 Gravitational Waves on a flat space-time

Choosing the *Minkowski spacetime* allows us to simplify even further eq. (2.1.5) and obtain an analytic solution, this is mainly because for a *Minkowski metric* we have $\Gamma^{\alpha}_{\mu\nu}(\eta) = 0$ as the metric is constant. By imposing this condition the LHS of eq. (2.1.5) simply reduces to:

$$\Gamma^{\alpha}_{\mu\nu,\alpha} - \Gamma^{\alpha}_{\mu\alpha,\nu} + O(h^2) = \frac{1}{2}\left\{-\Box_F h_{\mu\nu} + \left[h^{\lambda}_{\nu,\lambda\mu} + h^{\lambda}_{\mu,\lambda\nu} - h^{\lambda}_{\lambda,\mu\nu}\right]\right\} + O(h^2), \tag{2.1.6}$$

where the operator $\Box_F$ is the *D'Alembertian* in flat spacetime and read as

$$\Box_F = \eta^{\alpha\beta}\frac{\partial}{\partial x^{\alpha}}\frac{\partial}{\partial x^{\beta}} = -\frac{\partial^2}{c^2\partial t^2} + \nabla^2. \tag{2.1.7}$$

We can finally rewrite the *Einstein equations* (2.1.5) for a flat space-time as

$$\left\{\Box_F h_{\mu\nu} - \left[h^{\lambda}_{\nu,\lambda\mu} + h^{\lambda}_{\mu,\lambda\nu} - h^{\lambda}_{\lambda,\mu\nu}\right]\right\} = -\frac{16\pi G}{c^4}\left(T^{pert}_{\mu\nu} - \frac{1}{2}\eta_{\mu\nu}T^{pert}\right). \tag{2.1.8}$$

The solutions of eq. (2.1.8) are not uniquely determined, as if we make a coordinate transformation the transformed metric tensor will still be a solution, describing the same physical situation as seen from a different frame [8]. Indeed, in order to respect the weak field assumption, we have to choose a coordinate transformation such that the new perturbation on the metric tensor $h^{'}_{\mu\nu}$ respect the condition $|h^{'}_{\mu\nu}| \ll 1$. The usual choice is a coordinate system that satisfies the *harmonic gauge* condition, which can be expressed as

$$g^{\mu\nu}T^{\lambda}_{\mu\nu} = 0 \quad \Rightarrow \quad h^{\mu}_{\nu,\mu} = \frac{1}{2}h^{\mu}_{\mu,\nu}. \tag{2.1.9}$$

By imposing this condition, the terms in square bracket of eq. (2.1.8) vanish, and what is left of the *Einstein equations* is a simple wave equation with an additional constrain term:

$$\begin{cases} \Box_F h_{\mu\nu} = -\frac{16\pi G}{c^4}\left(T^{pert}_{\mu\nu} - \frac{1}{2}\eta_{\mu\nu}T^{pert}\right) \\ h^{\mu}_{\nu,\mu} = \frac{1}{2}h^{\mu}_{\mu,\nu} \end{cases}. \tag{2.1.10}$$

This equation can be simplified even further by defining the new tensor $\bar{h}_{\mu\nu} = h_{\mu\nu} - 1/2\eta_{\mu\nu}h$, and by moving far away from the source (void limit) where we have the condition $T_{\mu\nu} = 0$. Under these assumptions, we can write

$$\begin{cases} \Box_F \bar{h}_{\mu\nu} = 0 \\ \bar{h}^{\mu}_{\nu,\mu} = 0 \end{cases}. \tag{2.1.11}$$

From the last equation, it appears clear that a perturbation of a flat space-time propagates as a wave traveling at the speed of light, and that Einstein's theory of gravity predicts the existence of gravitational waves. The situation will change a bit in the case of curved spaces, where the curvature will act as a potential barrier and the final equation will become a Schrodinger-like equation (see ref. [37] for further details).

2.1.2 Plane Gravitational Waves solution and TT-gauge

The simplest solution to eq. (2.1.11) is a *monochromatic plane wave*, it can be written as

$$\bar{h}_{\mu\nu} = \mathcal{R}\left\{A_{\mu\nu}e^{ik_\alpha x^\alpha}\right\}, \tag{2.1.12}$$

where we defined with $A_{\mu\nu}$ the polarization tensor, which describes the wave amplitude along the various directions, and k_α is the wave vector. Constraints on both these variables can be found simply by plugging eq. (2.1.12) into eq. (2.1.11). We then obtain the following conditions:

$$\begin{cases} \eta^{\mu\nu}k_\mu k_\nu = 0 \\ \eta^{\mu\alpha}A_{\alpha\nu}k_\mu = 0 \quad \Rightarrow \quad k_\mu A^{\mu}_{\nu} = 0 \end{cases}. \tag{2.1.13}$$

The first constraint of eq. (2.1.13) requires k to be a null vector, and hence the carrier has to be massless. The second constraint instead expresses orthogonality between the wave vector k_μ and of the polarization tensor $A_{\mu\nu}$. This is equivalent to what happens for an electromagnetic wave where the field will be orthogonal to the direction of propagation of the wave. In analogy with electromagnetism, we can hence describe the wavefront equation by parameterizing the wave vector as

$$k_\mu = \left(\frac{\omega}{c}, \vec{k}\right). \tag{2.1.14}$$

The null vector condition will hence imply

$$-k_0^2 + k_x^2 + k_y^2 + k_z^2 = 0 \quad \Rightarrow \quad \omega = ck_0 = c\sqrt{k_x^2 + k_y^2 + k_z^2}. \tag{2.1.15}$$

What is left is just understanding how many of the 10 components of $A_{\mu\nu}$ have a proper physical meaning. This is equivalent to studying the polarization modes of a gravitational wave. To this extent, let us consider the case of a wave propagating in flat space-time along the x direction in our reference frame. Our $\bar{h}_{\mu\nu}$ will be independent of y and z, and in particular, due to the null vector condition it will only depend on $t \pm x/c$. By integrating eq. (2.1.11), and after setting to 0 the integration constants to consider only the time-dependent part, we obtain the following relations among the components of the perturbation tensor:

$$\begin{aligned} \bar{h}^t_t &= \bar{h}^x_t, & \bar{h}^t_y &= \bar{h}^x_y, \\ \bar{h}^t_x &= \bar{h}^x_x, & \bar{h}^t_z &= \bar{h}^x_z. \end{aligned} \tag{2.1.16}$$

These constraints can be used to set to 0 some of the components of our polarization tensor by means of a new coordinate transformation. In particular, we can use the 4 functions of the coordinates to set to zero the following quantities:

$$\bar{h}^t_x = \bar{h}^t_y = \bar{h}^t_z = \bar{h}^y_y = \bar{h}^z_z = 0. \tag{2.1.17}$$

Using eq. (2.1.16), this will naturally imply

$$\bar{h}^x_x = \bar{h}^x_y = \bar{h}^x_z = \bar{h}^t_t = 0. \tag{2.1.18}$$

The remaining non-vanishing components are hence given by $\bar{h}^z_y$ and $\bar{h}^y_y - \bar{h}^z_z$, we can observe that under these conditions, we get

$$\bar{h}^\mu_\mu = \bar{h}^t_t + \bar{h}^x_x + \bar{h}^y_y + \bar{h}^z_z = 0. \tag{2.1.19}$$

This greatly simplifies the form of our wave tensor $h_{\mu\nu}$ as

$$\bar{h}^\mu_\mu = h^\mu_\mu - 2h^\mu_\mu = -h^\mu_\mu = 0 \quad \Rightarrow \quad \bar{h}^\mu_\nu = h^\mu_\nu. \tag{2.1.20}$$

We hence proved that in this gauge $\bar{h}^{\mu}_{\nu}$ and h^{μ}_{ν} coincide and are traceless. Furthermore, we observed from eqs. (2.1.16), (2.1.17) and (2.1.18) that a plane wave propagating along the x direction will only depend on the two functions $\bar{h}^{z}_{y}$ and $\bar{h}^{y}_{y} - \bar{h}^{z}_{z}$. These two conditions together name the gauge *TT-gauge*, where TT stands for *Transverse-Traceless*. To conclude, the dependence on barely two functions implies that a gravitational wave only has two degrees of freedom which correspond to two polarization states, and we will see in detail how they behave in the TT-gauge in the next section.

2.1.3 Gravitational Waves polarization states

In order to understand how the 2 polarization states behave, we need to estimate how a gravitational wave would affect the motion of particles. We can start with the simple case of a single particle at rest in a flat space-time. If we set an inertial frame for this particle with x axis coincident with the direction of propagation of the incoming TT-wave, we can impose the geodesic equation (1.2.3) to check the effect of the incoming gravitational wave on its motion. The particle equation of motion will be written as

$$\frac{\mathrm{d}^2 x^{\mu}}{\mathrm{d}\tau^2} + \Gamma^{\mu}_{\alpha\beta}\frac{\mathrm{d}x^{\alpha}}{\mathrm{d}\tau}\frac{\mathrm{d}x^{\beta}}{\mathrm{d}\tau} = \frac{\mathrm{d}U^{\mu}}{\mathrm{d}\tau} + \Gamma^{\mu}_{\alpha\beta}U^{\alpha}U^{\beta}, \tag{2.1.21}$$

where U^{μ} is the particle 4-velocity. At $t = 0$ the particle is at rest, and hence $U^{\mu} = U^{0} = 1$. The particle acceleration will be given by

$$\left(\frac{\mathrm{d}U^{\mu}}{\mathrm{d}\tau}\right)_{t=0} = -\Gamma^{\mu}_{00} = -\frac{1}{2}\eta^{\mu\nu}\left[h_{\nu 0,0} + h_{0\nu,0} - h_{00,\nu}\right] \overset{\mathrm{TT}}{=} 0. \tag{2.1.22}$$

Thus, in the TT-gauge, the 4-velocity U^{μ} remains constant even when an incoming gravitational wave perturbs the metric. This implies that the study of the motion of a single particle is not sufficient to detect a gravitational wave.

Additional information can be obtained by studying the relative motion of particles induced by a gravitational wave. Let us assume to have two neighboring particles A and B at rest in a certain frame, with their coordinates denoted as x^{μ}_{A} and x^{μ}_{B}. The two particles will be reached at $t = 0$ by a plane-fronted gravitational wave propagating along the x axis. In the TT-frame, the metric will read as

$$ds^2 = g_{\mu\nu}dx^{\mu}dx^{\nu} = \left(\eta_{\mu\nu} + h^{TT}_{\mu\nu}\right)dx^{\mu}dx^{\nu}, \tag{2.1.23}$$

where we can recall that $g_{00} = \eta_{00} = -1$. Hence both particles have proper time $\tau = ct$. As the two particles are at rest, by using eq. (2.1.22) we can prove that they will remain at a constant coordinate position even when the wave arrives, and the same will be true for their coordinate separation $\delta x^{\mu} = x^{\mu}_{B} - x^{\mu}_{A}$. Since the metric (2.1.23) changes, however, the proper distance among them will change, and this can be studied using the previously introduced concept of *geodesic deviation* {1.2.2}.

Let us start by moving into a LIF with coordinates x^{μ}_{A} centered on the geodesic of the particle A. We can show that the following relations are true when considering

the particle A:

$$\left.\frac{\mathrm{d}x^\mu_A}{\mathrm{d}\tau}\right|_A = (1,0,0,0) \;:\; t_A = \frac{\tau}{c}, \tag{2.1.24}$$

$$g_{\mu\nu}|_A = \eta_{\mu\nu} \quad \Rightarrow \quad g_{\mu\nu,\alpha}|_A = 0 \quad (i.e\ \ \Gamma^\alpha_{\mu\nu}\big|_A = 0), \tag{2.1.25}$$

where the symbol $|_A$ means that the quantity is computed along the geodesic of the particle A. It is also easy to demonstrate that, in this frame, the components of the separation vector δx^μ_A satisfy the criterion $\delta x^\mu_A = x^\mu_A|_B$, which means that the separation vector will always be equal to the coordinates of particle B. The geodesic deviation for the latter will read as

$$\frac{\mathrm{D}^2\delta x^\mu_A}{\mathrm{d}\tau^2} = R^\mu_{\alpha\beta\gamma}\frac{\mathrm{d}x^\alpha_A}{\mathrm{d}\tau}\frac{\mathrm{d}x^\beta_A}{\mathrm{d}\tau}\delta x^\gamma_A. \tag{2.1.26}$$

If we evaluate eq. (2.1.26) along the geodesic of particle A, recalling the condition (2.1.24), we obtain

$$\frac{\mathrm{d}^2\delta x^i_A}{\mathrm{d}t^2} = R^i_{00j}\delta x^j_A, \tag{2.1.27}$$

where the two index $i, j \in [1,3]$, and hence are purely spatial index. The *Riemann curvature tensor* can be obtained using eq. (1.2.16). By keeping a first-order approximation and using the TT-gauge condition, we get

$$R^i_{00j} = \eta^{ik}R_{k00j} \overset{\mathrm{TT}}{=} \frac{1}{2}\eta^{ik}\frac{\partial^2 h^{TT}_{kj}}{c^2\partial t^2}. \tag{2.1.28}$$

By plugging in eq. (2.1.28), the equation of geodesic deviation (2.1.27) becomes

$$\frac{\mathrm{d}^2\delta x^i_A}{\mathrm{d}t^2} = \frac{1}{2}\eta^{ik}\frac{\partial^2 h^{TT}_{kj}}{c^2\partial t^2}\delta x^j_A. \tag{2.1.29}$$

We now have to make some considerations on the boundary conditions of the equation presented in eq. (2.1.29). Indeed we know that before the arrival of the GW($t<0$), the two particles A and B are at rest, and hence we have $\delta x^i_A(t<0) = \delta x^i_A(t=0) = const$. Under these circumstances, the derivative of eq. (2.1.29) will just result in

$$\frac{\mathrm{d}^2\delta x^i_A(t\le 0)}{\mathrm{d}t^2} = 0. \tag{2.1.30}$$

For $t>0$, instead, the $h_{\mu\nu}$ will infinitesimally perturb the metric. We can hence approximate the separation vector at later times as $\delta x^i_A(t>0) = \delta x^i_A(t=0) + \tilde{\delta} x^i_A(t>0)$, with $\tilde{\delta} x^i_A$ a small perturbation with respect to the original position $\delta x^i_A(t=0)$. If we substitute the last expansion in (2.1.29), the term $\delta x^i_A(t=0) = const$ will become null on the LHS of eq. (2.1.29), as shown in eq. (2.1.30). By retaining only first-order terms in h, the perturbation term $\tilde{\delta} x^i_A$ will instead evolve with time as

$$\frac{\mathrm{d}^2\tilde{\delta} x^i_A(t>0)}{\mathrm{d}t^2} = \frac{1}{2}\eta^{ik}\frac{\partial^2 h^{TT}_{kj}}{c^2\partial t^2}\delta x^j_A(t=0). \tag{2.1.31}$$

This equation can be integrated, by doing so we will obtain the following general solution for the coordinates of the separation vector:

$$\delta x^i(t) = \delta x^i(t=0) + \frac{1}{2}\eta^{ik} h^{TT}_{kj} \delta x^j(t=0). \tag{2.1.32}$$

Being in the TT-gauge, we know that the only non-zero components of the perturbation tensor $h_{\mu\nu}$ are $h_{22} = -h_{33}$ and $h_{23} = h_{32}$. We can hence rewrite eq. (2.1.32) for the only two components that would not remain constant during the wave propagation. We get

$$\begin{cases} \delta x^2(t) = \delta x^2(t=0) + \frac{1}{2}\left(h^{TT}_{22}\delta x^2(t=0) + h^{TT}_{23}\delta x^3(t=0)\right) \\ \delta x^3(t) = \delta x^3(t=0) + \frac{1}{2}\left(h^{TT}_{32}\delta x^2(t=0) + h^{TT}_{33}\delta x^3(t=0)\right) \end{cases} . \tag{2.1.33}$$

We can finally study the two *polarization states* of gravitational waves. To this extent, let us assume that the two modes are defined as

$$\begin{cases} h_{yy} = -h_{zz} = 2\mathcal{R}\left\{A_+ e^{i\omega\left(t-\frac{x}{c}\right)}\right\} & (+\ Polarization) \\ h_{yz} = \ \ h_{zy} = 2\mathcal{R}\left\{A_\times e^{i\omega\left(t-\frac{x}{c}\right)}\right\} & (\times\ Polarization) \end{cases} . \tag{2.1.34}$$

It is also convenient to redefine the wave phase as $\theta(t) = \omega\left(t - \frac{x}{c}\right)$. The effects of the GWpolarization modes can be studied by using eq. (2.1.33) on a ring of particles having unitary radius and centered in the origin in the assumed reference frame. We can start by looking at the + polarization state simply by assuming $A_+ = 0.5,\ A_\times = 0$, the situation is shown in fig. 2.1. Analogously, the $\times$ polarization state can be studied by imposing $A_+ = 0,\ A_\times = 0.5$. The results are shown in fig. 2.2.

2.2 Gravitational Waves from inspiralling compact objects

In order to compute the gravitational wave emitted by a gravitating system evolving with time, it is convenient to introduce the *quadrupole moment tensor* formalism (see refs. [8, 31] for a detailed description). This tensor describes the spatial distribution of mass/energy in the volume as a function of time, and can be built recalling the definition of the T^{00} component of the stress-energy tensor (1.1.12). We have

$$q^{ij}(t) = \frac{1}{c^2}\int_V T^{00}(t, x^k) x^i x^j d^3x^k \ \ :\ \ i,j,k \in [1,3], \tag{2.2.1}$$

while the other components of the stress-energy tensor can be related to eq. (2.2.1) through the *tensor virial theorem* (see ref. [8]) as

$$\int_V T^{ij}(t, x^k) d^3x^k = \frac{1}{2}\frac{\mathrm{d}^2}{\mathrm{d}t^2} q^{ij}(t). \tag{2.2.2}$$

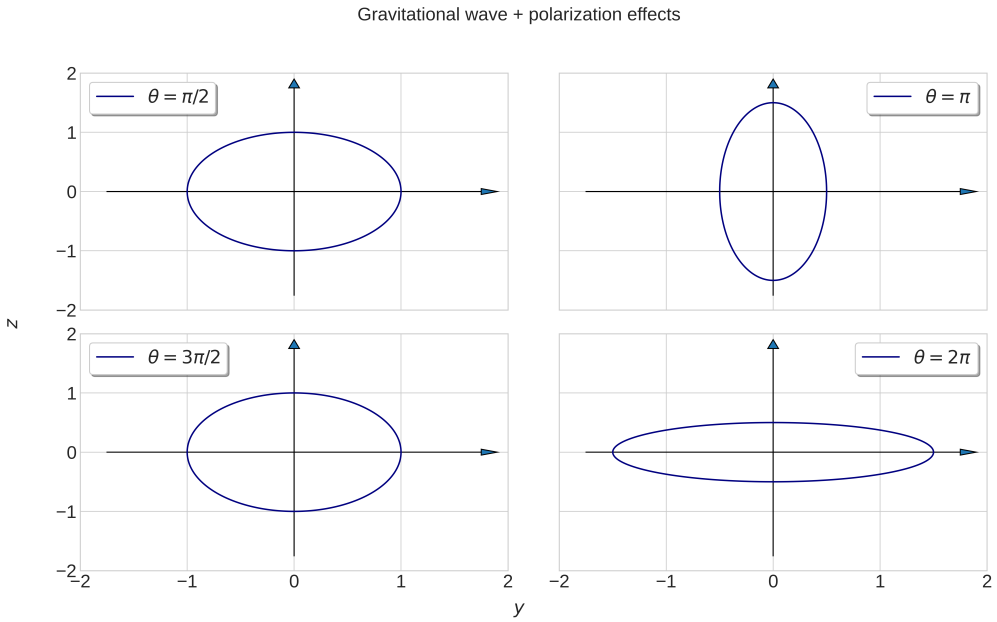

Figure 2.1. Gravitational wave effects due to the + polarization mode on a unitary ring of particles. The parameter *theta* is the phase of the incoming gravitational wave, and is given by $\theta(t) = \omega\left(t - \frac{x}{c}\right)$.

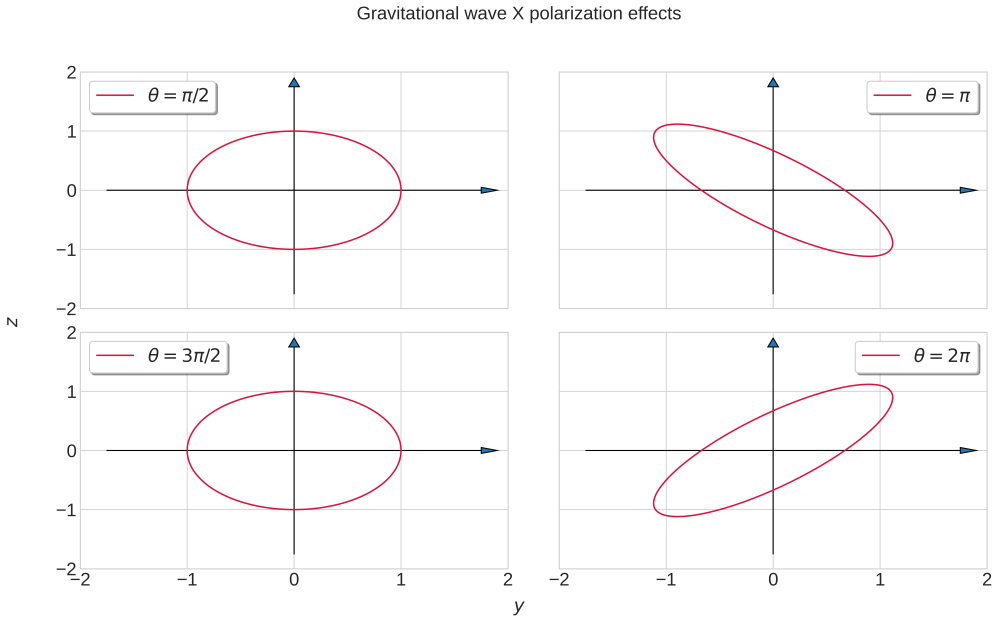

Figure 2.2. Gravitational wave effects due to the × polarization mode on a unitary ring of particles. The parameter *theta* is the phase of the incoming gravitational wave, and is given by $\theta(t) = \omega\left(t - \frac{x}{c}\right)$.

It can be demonstrated that, by assuming polar coordinates centered on the source of the gravitational waves, eq. (2.1.11) can be rewritten in terms of the quadrupole moment tensor (2.2.1) as

$$\begin{cases} \bar{h}^{\mu 0} = 0 \ : \ \mu \in [0,3] \\ \bar{h}^{ij}(t,r) = \frac{2G}{c^4 r}\left[\frac{\mathrm{d}^2}{\mathrm{d}t^2} q^{ij}\left(t - \frac{r}{c}\right)\right] \end{cases} . \tag{2.2.3}$$

This equation describes the gravitational waves emitted as a function of time by any gravitating system, regardless of the number of involved masses/energies and their time evolution. It has to be emphasized that eq. (2.2.3) implies that gravitational waves have a quadrupole nature, they do not have dipole contributions. For a spherical or axisymmetric stationary distribution of matter (or energy), the quadrupole moment will be a constant (even if the body is rotating), implying these bodies do not emit gravitational waves. Analogously, a star that collapses in a perfectly spherically symmetric way has a vanishing derivative of the quadrupole moment and does not emit gravitational waves. To produce these waves, we hence need a certain degree of asymmetry, as it occurs for instance in the non-radial pulsations of stars, in a non-spherical gravitational collapse, in the coalescence of massive bodies, etc...

2.2.1 The Transverse-Traceless projector

Equations (2.2.3) still have to be transformed in the TT-gauge in order to explicitly manifest the physical degrees of freedom. By writing eqs. (2.2.3) into the TT-gauge, we are imposing the two following conditions on the perturbation tensor $\bar{h}^{\mu\nu}$:

$$\begin{cases} \bar{h}^{TT}_{\mu\nu} n^\nu = 0 & (\textit{transverse wave condition}) \\ \bar{h}^{TT}_{\mu\nu} \delta^{\mu\nu} = 0 & (\textit{vanishing trace}) \end{cases} , \tag{2.2.4}$$

where n^ν is the unit vector parallel to the direction of propagation of the wavefront. We will now describe a procedure to project a gravitational wave in the TT-gauge. In the following, we will work in the 3-dimensional *Euclidean space* with metric δ_{ij}. This implies that there will be no difference between upper and lower indices. The described procedure is equivalent to performing a coordinate transformation, and we will hence start by defining an operator that projects a vector into the plane orthogonal to the direction of another vector $\vec{n}$. This can be defined as

$$P_{ij} = \delta_{ij} - n_i n_j. \tag{2.2.5}$$

It is easy to verify that for any vector V^j, the projection $P_{ij}V^j$ is orthogonal to n^i, hence $(P_{ij}V^j)n^i = 0$. Furthermore, we can easily demonstrate that P_{ij} is symmetric, and verifies the condition $P^i_j P^j_k = P^i_k$. The *TT-projector* can hence be defined as follows:

$$P_{ijkl} = P_{ik}P_{jl} - \frac{1}{2}P_{ij}P_{kl}. \tag{2.2.6}$$

This projector extracts the TT-part of a $\binom{0}{2}$ tensor, and we can demonstrate from its definition that the following properties are verified:

- $P_{ijkl} = P_{klij}$;
- $P_{ijkl} = P_{jilk}$;
- $P_{ijmn}P_{mnkl} = P_{ijkl}$;
- it is transverse on all the indices, *i.e.* $n^x P_{ijkl} = 0$ for $x = [i, j, k, l]$;
- it is traceless on the first and second couple of indices, *i.e.* $\delta^{ij}P_{ijkl} = \delta^{kl}P_{ijkl} = 0$.

We can finally transform our perturbation tensor into the TT-gauge simply by applying

$$h_{ij}^{TT} = P_{ijmn}h_{mn} = P_{ijmn}\bar{h}_{mn}, \tag{2.2.7}$$

where we used eq. (2.1.20) to impose the last equivalence. The equations (2.2.3) become

$$\begin{cases} h_{\mu 0}^{TT} = 0 \ : \ \mu \in [0, 3] \\ h_{ij}^{TT}(t, r) = \frac{2G}{c^4 r}\left[\frac{\mathrm{d}^2}{\mathrm{d}t^2}Q_{ij}^{TT}\left(t - \frac{r}{c}\right)\right] \end{cases}, \tag{2.2.8}$$

with

$$Q_{ij}^{TT} = P_{ijmn}q_{mn}. \tag{2.2.9}$$

It is sometime useful to define the *reduced quadrupole moment* Q_{ij}:

$$Q_{ij} = q_{ij} - \frac{1}{3}\delta_{ij}q \quad \Rightarrow \quad \delta^{ij}Q_{jk} = 0, \tag{2.2.10}$$

which by definition is traceless. This is related to the quadrupole tensor in TT-gauge as

$$Q_{ij}^{TT} = P_{ijmn}q_{mn} = P_{ijmn}Q_{mn}. \tag{2.2.11}$$

Equation (2.2.8) is to date the best representation we have for gravitational waves and was used to build the LIGO template bank [165–167]. However, integrating the full *Einstein equations* is usually highly computationally expendious. This led to the development of approximated phenomenological waveforms, by using approximations such as the one that we are going to introduce in the next subsection.

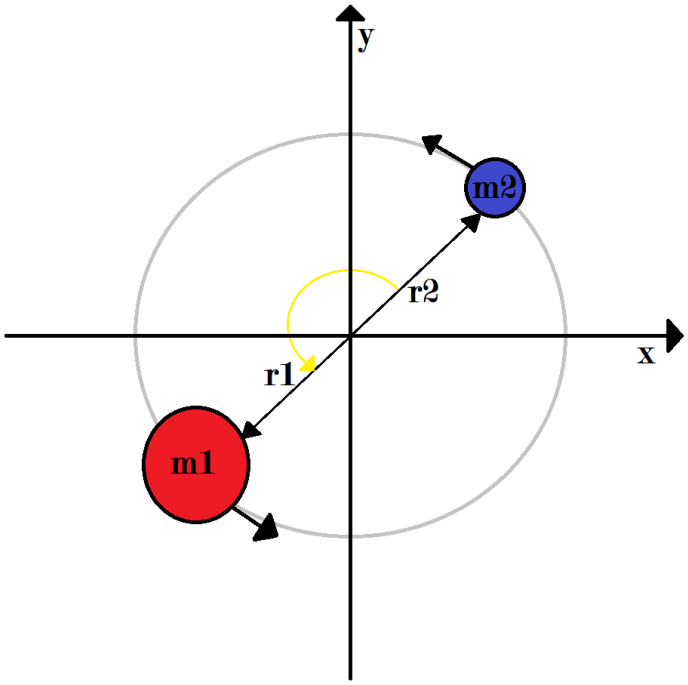

Figure 2.3. Scheme of the binary system with the two compact objects inspiralling around each other in circular orbit .

2.2.2 Gravitational Waves emitted by inspiralling binary compact objects

We will now compute the gravitational wave generated by a binary system of two compact objects inspiralling in a circular orbit around their center of mass. This will be a good first approximation to understand how the GW spectrum coming from a general inspiralling system, will look like. The two compact objects will be assumed as point-like masses having mass m_1 and m_2, where, by convention, we usually indicate with m_1 the most massive object. The situation is shown in fig. 2.3. At any time, the orbital separation among the two objects will be denoted with $l(t) = r_1 + r_2$, such that for a constant circular orbit we will have $l(t) = l(t = 0) = l_0$. It is also useful to define the *total mass* of the system $M = m_1 + m_2$ and the *reduced mass* $\mu = m_1 m_2/M$. To conclude, we will work in a reference frame centered in the center of mass of the system.

By using the previously defined quantities and assumptions, the following relations will hold:

$$\begin{cases} r_1 = \frac{m_2 l_0}{M} \\ r_1 = \frac{m_1 l_0}{M} \end{cases} . \tag{2.2.12}$$

The orbital frequency of the system can be found from *Kepler's law* [177, 178], and is given by

$$\frac{G m_1 m_2}{l_0^2} = m_1 \omega_k^2 \frac{m_2 l_0}{M} = m_2 \omega_k^2 \frac{m_1 l_0}{M} \quad \Rightarrow \quad \omega_K = \sqrt{\frac{GM}{l_0^3}}, \tag{2.2.13}$$

where the subscript k in ω_K is to denote the *Keplerian frequency*. The coordinates of the masses in the orbital plane can be written as a function of the latter, and read as

$$\begin{cases} x_i = \frac{m_i}{M} l_0 \cos \omega_K t \\ y_i = \frac{m_i}{M} l_0 \sin \omega_K t \end{cases} , \tag{2.2.14}$$

with $i = 1, 2$ an index for the two masses.

Assuming that the orbit of the bodies is on the $x - y$ plane (as shown in fig. 2.3), the 00 component of the stress-energy tensor (1.1.12) for this system is given by

$$T^{00} = c^2 \sum_{i=1}^{2} m_i \delta(x - x_i)\delta(y - y_i)\delta(z). \tag{2.2.15}$$

This implies that we have the following non-zero components for the quadrupole moment tensor (2.2.1):

$$\begin{aligned} q_{xx} =& \sum_{i=1}^{2} m_i \int_V x^2 \delta(x - x_i)\delta(y - y_i)\delta(z) = \sum_{i=1}^{2} m_i x_i^2 = \\ =& \mu l_0^2 \ \cos^2 \omega_K t = \frac{\mu}{2} l_0^2 \ \cos 2\omega_K t + c_1, \end{aligned} \tag{2.2.16}$$

$$\begin{aligned} q_{yy} =& \sum_{i=1}^{2} m_i \int_V y^2 \delta(x - x_i)\delta(y - y_i)\delta(z) = \sum_{i=1}^{2} m_i y_i^2 = \\ =& \mu l_0^2 \ \sin^2 \omega_K t = -\frac{\mu}{2} l_0^2 \ \cos 2\omega_K t + c_2, \end{aligned} \tag{2.2.17}$$

$$\begin{aligned} q_{xy} =& \sum_{i=1}^{2} m_i \int_V xy \delta(x - x_i)\delta(y - y_i)\delta(z) = \sum_{i=1}^{2} m_i x_i y_i = \\ =& \mu l_0^2 \ \cos \omega_K t \ \sin \omega_K t = \frac{\mu}{2} l_0^2 \ \sin 2\omega_K t, \end{aligned} \tag{2.2.18}$$

where c_1, c_2 are constant terms. We can observe that the trace of the quadrupole moment tensor will be given by

$$q = \eta^{ij} q_{ij} = q_{xx} + q_{yy} = constant, \tag{2.2.19}$$

and hence the *reduced quadrupole moment* (2.2.10) will share the same time evolution of the quadrupole moment tensor given by eqs. (2.2.16),(2.2.17) and (2.2.18). Such a time evolution can be represented through the use of a time-dependent matrix A_{ij} given by

$$A_{ij}(t) = \begin{pmatrix} \cos \ 2\omega_K t & \sin \ 2\omega_K t & 0 \\ \sin \ 2\omega_K t & -\cos \ 2\omega_K t & 0 \\ 0 & 0 & 0 \end{pmatrix}. \tag{2.2.20}$$

We can hence write

$$q_{ij} = \frac{\mu}{2} l_0^2 A_{ij} + constant. \tag{2.2.21}$$

The wave will be emitted along the direction $\vec{n}$, and in the TT-gauge, the wave equations will be given by eqs. (2.2.8) and (2.2.11). For this particular system, we can recall the definition of (2.2.13) to write

$$h_{ij}^{TT} = -\frac{2G}{rc^4}\frac{\mu}{2} l_0^2 (2\omega_K)^2 \left[P_{ijkl} A_{kl}\right] = -\frac{4\mu M G^2}{r l_0 c^4}\left[P_{ijkl} A_{kl}\right]. \tag{2.2.22}$$

The wave amplitude can be redefined as

$$h_0 = -\frac{4\mu M G^2}{r l_0 c^4}, \tag{2.2.23}$$

and hence eq. (2.2.22) can be rewritten in terms of h_0 as

$$h_{ij}^{TT} = -h_0 A_{ij}^{TT}\left(t - \frac{r}{c}\right) \ : \ A_{ij}^{TT}\left(t - \frac{r}{c}\right) = \left[P_{ijkl} A_{kl}\left(t - \frac{r}{c}\right)\right]. \tag{2.2.24}$$

The calculations shown in this section can be generalized to the case of non-circular orbits simply by replacing eqs. (2.2.14) with the proper equation of motion for the two masses. These may depend on the eccentricity of the orbit and the spins of the two bodies, and can generally complicate eqs. (2.2.22) to the point that no analytical solution can be found. This approach is what is usually followed when developing *phenomenological waveforms models*, like when considering *IMRPhenomD* waveforms [171, 172] or *IMRPhenomXHM* waveforms [173]. Even though eq. (2.2.24) can seem like a rough approximation, it works very well for events that are far away from coalescence, and have low eccentricity and approximately equal mass. A first-hand example that we are going to use in this thesis is the nearly monochromatic sources that can be found in the LISA frequency range. Furthermore, these results were used in 1975 to estimate the amplitude of the binary system *PSR 1913 + 16* [179]. The system is composed of two inspiralling neutron stars orbiting at a very short distance from each other, and the results presented in ref. [179] can be considered one of the first indirect detection of gravitational waves from an inspiralling binary system.

2.3 Energy carried by Gravitational Waves

When a system emits gravitational waves, a part of its internal energy gets radiated, and this energy loss will by itself contribute to the evolution, and final configuration of said system. If we wish to estimate the energy contribution dissipated through gravitational waves, we need to define a quantity able to describe the energy and momentum content of a gravitational field. This quantity is supposed to behave like a

tensor, but we will see in the following that it will not be possible to define a quantity as such under a generical coordinate transformation. By limiting ourselves to linear coordinate transformations, we can instead define a quantity that fulfills our needings, this is referred in literature as the *stress-energy pseudotensor of the gravitational field.*

Let us start by moving in a LIF. By recalling eq. (1.1.13), we need to find a quantity $\Phi^{\alpha\beta\gamma}$ that verifies

$$T^{\alpha\beta} = \Phi^{\alpha\beta\gamma}{}_{,\gamma}. \tag{2.3.1}$$

If the previous condition is verified, assuming that $\Phi^{\alpha\beta\gamma}$ is antisymmetric on the indices β, γ automatically implies that the condition (1.1.13) is verified. In order to find an explicit expression for $\Phi^{\alpha\beta\gamma}$, we can start by rewriting eq. (1.1.1) as follows:

$$T^{\alpha\beta} = \frac{c^4}{8\pi G}\left(R^{\alpha\beta} - \frac{1}{2}g^{\alpha\beta}R\right). \tag{2.3.2}$$

Since we are in a LIF, we can set all the first derivatives of the metric tensor to 0. This implies that all the $\Gamma^{\alpha}_{\mu\nu}$ that appear in the definition of the *Ricci tensor* (1.1.8), will vanish, and only the terms composed by second derivatives of the metric tensor will appear on the right-hand side of equation (2.3.2). After some calculations, we obtain the following relation for the stress-energy tensor:

$$T^{\alpha\beta} = \left\{\frac{c^4}{16\pi G}\frac{1}{(-g)}\left[(-g)\left(g^{\alpha\beta}g^{\gamma\sigma} - g^{\alpha\gamma}g^{\beta\sigma}\right)\right]_{,\sigma}\right\}_{,\gamma}. \tag{2.3.3}$$

We can observe that the term in parentheses is antisymmetric in the two indices β, γ. Furthermore, by direct comparison with eq. (2.3.1) it is easy to understand that we have

$$\Phi^{\alpha\beta\gamma}{}_{,\gamma} = \frac{c^4}{16\pi G}\frac{1}{(-g)}\left[(-g)\left(g^{\alpha\beta}g^{\gamma\sigma} - g^{\alpha\gamma}g^{\beta\sigma}\right)\right]_{,\sigma}. \tag{2.3.4}$$

As we are in a LIF, we also know that

$$\frac{\partial}{\partial x^{\sigma}}\frac{1}{(-g)} = 0, \tag{2.3.5}$$

and this implies that we can define the new quantity $\bar{\Phi}^{\alpha\beta\gamma} = (-g)\Phi^{\alpha\beta\gamma}$, and rewrite eq. (2.3.3) as

$$\bar{\Phi}^{\alpha\beta\gamma}{}_{,\gamma} = (-g)\,T^{\alpha\beta}. \tag{2.3.6}$$

It has to be emphasized that eq. (2.3.6) was derived in a LIF, where all first derivatives of the metric tensor vanish. In any other frame, this will not be true, as the presence of a gravitational field will account for a curvature on the latter. The correction due to the gravitational field on the stress-energy tensor will be indicated

with $t^{\alpha\beta}$. This quantity can be used to rewrite eq. (2.3.6) in a generical reference frame as:

$$(-g)\, t^{\alpha\beta} = \bar{\Phi}^{\alpha\beta\gamma}{}_{,\gamma} - (-g)\, T^{\alpha\beta} \quad \Rightarrow \quad (-g)\left(t^{\alpha\beta} + T^{\alpha\beta}\right) = \bar{\Phi}^{\alpha\beta\gamma}{}_{,\gamma}. \tag{2.3.7}$$

It can be observed that $t^{\alpha\beta}$ is symmetric as both $T^{\alpha\beta}$ and $\bar{\Phi}^{\alpha\beta\gamma}{}_{,\gamma}$ are symmetric in the two indices α, β. This quantity is called the *stress-energy pseudotensor of the gravitational field*. Its expression in an arbitrary reference frame can be found by substituting eqs. (1.1.8), (2.3.2), (2.3.4) and (2.3.6), into eq. (2.3.7). It can also be demonstrated (see ref. [31]) that $t_{\alpha\beta}$ can be written in compact form as

$$t_{\alpha\beta} = \frac{c^4}{32\pi G} \left\langle h_{\mu\nu,\alpha} h^{\mu\nu}{}_{,\beta} \right\rangle, \tag{2.3.8}$$

where we indicated with $\langle\rangle$ a spatial averaging for the quantity in the brackets. Indeed the quantity defined in (2.3.8) depends only on the physical modes h_{ij}^{TT}, as the energy flux emitted by a source should be the same for different observers. We can hence define the *gauge-invariant energy density* as

$$t^{00} = \frac{c^4}{32\pi G} \left\langle h_{ij,0}^{TT} h_{ij,0}^{TT} \right\rangle = \frac{c^4}{16\pi G} \left\langle h_{+,0}^2 + h_{\times,0}^2 \right\rangle, \tag{2.3.9}$$

where the Einstein's notation for sums was omitted in the second term of eq. (2.3.9) to avoid confusion among indices and superscripts. Thus, from now on we will have $h_{ij,0}^{TT} h_{ij,0}^{TT} = h_{ij,0}^{TT} \eta^{in} \eta^{jm} h_{nm,0}^{TT}$.

To conclude, we can observe that by using the *Bianchi identity* $T^{\alpha\beta}{}_{,\alpha} = 0$ together with the antisymmetry of $\Phi^{\alpha\beta\gamma}$ in α, γ defined in (2.3.4), we can obtain the following conservation law out of (2.3.7) simply by differentiating both terms in x^α. We get

$$\left[(-g)\left(t^{\alpha\beta} + T^{\alpha\beta}\right)\right]_{,\alpha} = 0. \tag{2.3.10}$$

2.3.1 The Gravitational Waves energy flux

Now that we have defined the energy-momentum tensor for the gravitational waves, we can easily express the corresponding energy flux. We can start by writing explicitly the conservation law of the energy-momentum tensor (2.3.10) for the stress-energy pseudotensor $t^{\alpha\beta}$, where the latter can be written as follows:

$$\int_V d^3x \left(t_0^{00} + t_i^{i0}\right) = 0, \tag{2.3.11}$$

with V being the spatial volume bounded by a surface S. Recalling the definition of the *gauge-invariant energy density* (2.3.9), we can define the gravitational wave energy inside a volume V as

$$E_V = \int_V d^3x t^{00}. \tag{2.3.12}$$

This implies that we can rewrite eq. (2.3.11) as

$$\frac{1}{c}\frac{\mathrm{d}E_V}{\mathrm{d}t} = -\int_V d^3x t_i^{0i} = -\int_S dA \hat{n}_i t^{0i}. \tag{2.3.13}$$

In the last equation, $\hat{n}_i$ is the versor normal to the surface and we used the *Stokes Theorem* [180] to transform the volume integral over V into a surface one over S.

Let us now move to spherical coordinates, where $dA = r^2 d\Omega$ and $\hat{n} = \hat{r}$. If we assume that we are at a large distance from the source, we can impose the TT-gauge. By doing so, we can rewrite eq. (2.3.12) using the definition (2.3.8) as

$$\frac{\mathrm{d}E_V}{\mathrm{d}t} = -c \int_S dA t^{0r} \ : \ t^{0r} = \frac{c^4}{32\pi G} \left\langle h^{TT}_{ij,0} h^{TT}_{ij,r} \right\rangle . \tag{2.3.14}$$

Recalling eq. (2.1.34), we know that the gravitational wave equation can be written in terms of *retarded times* $h^{TT}_{ij}(t - \vec{k}/c)$, where $\vec{k}$ is the vector parallel to the direction of propagation of the wavefront. In spherical coordinates, the wave equation will hence be a function of $h^{TT}_{ij} = h^{TT}_{ij}(t - \vec{r}/c)$. It is easy to demonstrate (see ref. [31]) that for these kind of functions we have $h^{TT}_{ij,r} \approx h^{TT}_{ij,0} + O(1/r^2)$. Far away from the source, we can hence approximate eq. (2.3.14) as

$$\frac{\mathrm{d}E_V}{\mathrm{d}t} = -c \int_S dA t^{00}. \tag{2.3.15}$$

The negative sign of eq. (2.3.15) implies that the gravitational waves emitted will carry energy away from the considered volume. It is sometimes useful to rewrite the wave energy flux as

$$\frac{\mathrm{d}E}{\mathrm{d}A\mathrm{d}t} = ct^{00} = \frac{c^5}{32\pi G} \left\langle h^{TT}_{ij,0} h^{TT}_{ij,0} \right\rangle = \frac{c^5}{16\pi G} \left\langle h^2_{+,0} + h^2_{\times,0} \right\rangle , \tag{2.3.16}$$

where we used eq. (2.3.9) to write the last equivalence.

We can finally compute some of the fundamental quantities that are used every day in GW science. To begin, the energy emitted as a function of time can be obtained simply by integrating eq. (2.3.16) in dA. When using spherical coordinates, we obtain

$$\frac{\mathrm{d}E}{\mathrm{d}t} = \frac{c^5 r^2}{32\pi G} \int d\Omega \left\langle h^{TT}_{ij,0} h^{TT}_{ij,0} \right\rangle = \frac{c^5 r^2}{16\pi G} \int d\Omega \left\langle h^2_{+,0} + h^2_{\times,0} \right\rangle . \tag{2.3.17}$$

The energy density emitted per unit area instead can be obtained by integrating eq. (2.3.16) in dt:

$$\frac{\mathrm{d}E}{\mathrm{d}A} = \frac{c^5}{32\pi G} \int dt \left\langle h^{TT}_{ij,0} h^{TT}_{ij,0} \right\rangle = \frac{c^5}{16\pi G} \int dt \left\langle h^2_{+,0} + h^2_{\times,0} \right\rangle , \tag{2.3.18}$$

while by Fourier expanding eq. (2.3.17) (see refs. [31, 181]), we can also express the energy emitted per unit of frequency:

$$\frac{\mathrm{d}E}{\mathrm{d}f} = \frac{\pi c^3}{2G} f^2 r^2 \int d\Omega \left(\left| \tilde{h}_+(f) \right|^2 + \left| \tilde{h}_\times(f) \right|^2 \right) . \tag{2.3.19}$$

To conclude, we can recall that using eq. (2.2.8), it is also possible to express the energy flux of gravitational waves in terms of the quadrupole moment (2.2.9). By direct substitution into eq. (2.3.16) we obtain

$$\frac{\mathrm{d}E}{\mathrm{d}A\mathrm{d}t} = \frac{G}{8\pi r^2 c^5}\left\langle \frac{\mathrm{d}^3 Q_{ij}^{TT}}{\mathrm{d}t^3}\frac{\mathrm{d}^3 Q_{ij}^{TT}}{\mathrm{d}t^3}\right\rangle. \tag{2.3.20}$$

2.3.2 Time evolution of inspiralling binary systems due to GW energy emission

The energy emitted from a binary inspiralling system due to gravitational waves will indeed affect the motion of its bodies and, in particular, can be measured by looking at the evolution over time of its orbital period $\mathrm{d}P/\mathrm{d}t$. Emitting energy in the form of GW, in fact speeds up the process of bringing the two inspiralling bodies closer to their center of mass, hence decreasing the time required to coalescence of the system. In this section, we are going to reuse all the results obtained when discussing inspiralling compact objects in sec. {2.2.2}. In particular, the terms in brackets on the right-hand side of eq. (2.3.16) can be computed in the circular-orbit approximation using the quadrupole moment defined in (2.2.21). Using this substitution, we get

$$\left\langle \frac{\mathrm{d}^3 Q_{ij}^{TT}}{\mathrm{d}t^3}\frac{\mathrm{d}^3 Q_{ij}^{TT}}{\mathrm{d}t^3}\right\rangle = \left\langle \frac{\mathrm{d}^3 Q_{ij}^{TT}}{\mathrm{d}t^3}\eta^{im}\eta^{jn}\frac{\mathrm{d}^3 Q_{mn}^{TT}}{\mathrm{d}t^3}\right\rangle = 32\mu^2 l_0^4 \omega_K^6 = \frac{32\mu^2 M^3 G^3}{l_0^5}. \tag{2.3.21}$$

The energy emitted per unit of time will hence be given by

$$\frac{\mathrm{d}E_{GW}}{\mathrm{d}t} = \frac{32G^4\mu^2 M^3}{5c^5 l_0^5}. \tag{2.3.22}$$

Equation (2.3.22) is valid in the regime where the orbital parameters of the inspiralling system do not vary significantly when averaged over several periods of the orbit, such as the case for systems that are several years away from coalescence. This assumption is called in literature as *adiabatic approximation*. In the adiabatic regime, the system has enough time to adjust the orbit to compensate for the energy lost due to gravitational wave emission. We can hence write down the equation for the evolution of the orbital energy as

$$\frac{\mathrm{d}E_{Orb}}{\mathrm{d}t} = -\frac{\mathrm{d}E_{GW}}{\mathrm{d}t} \;:\; E_{Orb} = E_K + U, \tag{2.3.23}$$

where we introduced E_{Orb} to define the orbital energy of the system, and we imposed that equal to the sum of the kinetic energy E_K plus the potential energy U. These quantities will be given by

$$E_K = \frac{1}{2}\omega_K^2\left(m_1 r_1^2 + m_2 r_2^2\right) = \frac{1}{2}\omega_K^2 \mu l_0^2 = \frac{1}{2}\frac{G\mu M}{l_0}, \tag{2.3.24}$$

$$U = -\frac{Gm_1m_2}{l_0} = -\frac{G\mu M}{l_0}. \tag{2.3.25}$$

We hence obtain

$$E_{Orb} = -\frac{1}{2}\frac{G\mu M}{l_0} \quad \Rightarrow \quad \frac{\mathrm{d}E_{Orb}}{\mathrm{d}t} = -E_{Orb}\left(\frac{1}{l_0}\frac{\mathrm{d}l_0}{\mathrm{d}t}\right). \tag{2.3.26}$$

Equation (2.2.13) can be used to express the derivative in l_0 as a function of ω_K, and we then get

$$\omega_K^2 = GMl_0^{-3} \quad \Rightarrow \quad 2\ln\,\omega_K = \ln\,GM - 3\ln\,l_0 \quad \Rightarrow \quad \frac{1}{\omega_K}\frac{\mathrm{d}\omega_K}{\mathrm{d}t} = -\frac{3}{2}\frac{1}{l_0}\frac{\mathrm{d}l0}{\mathrm{d}t}, \tag{2.3.27}$$

implying that eq. (2.3.26) can be rewritten as

$$\frac{\mathrm{d}E_{Orb}}{\mathrm{d}t} = \frac{2}{3}\frac{E_{Orb}}{\omega_K}\frac{\mathrm{d}\omega_K}{\mathrm{d}t}. \tag{2.3.28}$$

Since $\omega_K = 2\pi/P$, where P is the period of the orbit, we can also find

$$\frac{1}{\omega_K}\frac{\mathrm{d}\omega_K}{\mathrm{d}t} = -\frac{1}{P}\frac{\mathrm{d}P}{\mathrm{d}t}, \tag{2.3.29}$$

which implies that the period of the orbit will change due to gravitational wave emission as follows:

$$\frac{\mathrm{d}E_{Orb}}{\mathrm{d}t} = -\frac{2}{3}\frac{E_{Orb}}{P}\frac{\mathrm{d}P}{\mathrm{d}t} \quad \Rightarrow \quad \frac{\mathrm{d}P}{\mathrm{d}t} = -\frac{3}{2}\frac{P}{E_{Orb}}\frac{\mathrm{d}E_{Orb}}{\mathrm{d}t}. \tag{2.3.30}$$

The knowledge of the energy dissipated by the system allows us also to estimate how the orbital separation will evolve as a function of time. To this extent, we can use eq. (2.3.26) to write down

$$\frac{1}{l_0}\frac{\mathrm{d}l_0}{\mathrm{d}t} = -\frac{1}{E_{Orb}}\frac{\mathrm{d}E_{Orb}}{\mathrm{d}t} = -\left(\frac{64G^3\mu M^2}{5c^5}\right)\frac{1}{l_0^4}. \tag{2.3.31}$$

If we assume that at some initial time $t = 0$ we have $l_0(t = 0) = l_0^{in}$, we can integrate eq. (2.3.31) and get

$$l_0^4(t) = (l_0^{in})^4 - \frac{256G^3\mu M^2}{5c^5}t. \tag{2.3.32}$$

We can now introduce the *time to coalescence* t_{coal}, which describes the residual time left to reach the coalescence for the binary system, as

$$t_{coal} = \frac{5c^5(l_0^{in})^4}{256G^3\mu M^2}, \tag{2.3.33}$$

and rewrite eq. (2.3.32) in terms of the latter:

$$l_0(t) = l_0^{in}\left[1 - \frac{t}{t_{coal}}\right]^{1/4}. \tag{2.3.34}$$

It can be observed that when $t = t_{coal}$, the orbital separation goes to zero. This is a consequence of the assumption that the two bodies are point masses. Indeed in physics, both stars and black holes have finite sizes, and therefore their effective coalescence will happen before this estimated value of t_{coal}. It has to be emphasized, however, that when the distance between the two objects becomes close enough, both the *slow-motion* approximation and *weak-field* assumption would fail anyway, making the quadrupole approximation that was used to derive this results not valid. Nevertheless, for systems that are far away from coalescence, the quantity defined in eq. (2.3.33) serves as a very good approximation for the effective time to coalescence.

By using eq. (2.3.34) in eq. (2.2.13), we can obtain the time evolution for the orbital frequency ω_K:

$$\omega_K(t) = \sqrt{\frac{GM}{l_0^3(t)}} = \omega_K^{in}\left(1 - \frac{t}{t_{coal}}\right)^{-3/8} \; : \; \omega_K^{in} = \sqrt{\frac{GM}{(l_0^{in})^3}}, \tag{2.3.35}$$

which implies a frequency or the emitted wave given by

$$\nu_{GW}(t) = \frac{\omega_K(t)}{\pi} = \nu_{GW}^{in}\left(1 - \frac{t}{t_{coal}}\right)^{-3/8} \; : \; \nu_{GW}^{in} = \frac{1}{\pi}\sqrt{\frac{GM}{(l_0^{in})^3}}. \tag{2.3.36}$$

By considering eq. (2.2.23) we can also redefine the time-dependant wave amplitude as

$$h_0(t) = \frac{4\mu MG^2}{rl_0(t)c^4} = \frac{4\mu MG^2}{rc^4}\frac{\omega_K^{2/3}(t)}{G^{1/3}M^{1/3}}. \tag{2.3.37}$$

If we now introduce the *chirp mass* as

$$\mathcal{M} = \mu^{3/5}M^{2/5} \Rightarrow \mathcal{M}^{5/3} = \mu M^{2/3}, \tag{2.3.38}$$

we can rewrite eq. (2.3.37) as

$$h_0(t) = \frac{4\pi^{2/3}G^{5/3}\mathcal{M}^{5/3}}{c^4 r}\nu_{GW}^{2/3}(t). \tag{2.3.39}$$

The reason why $\mathcal{M}$ is called *chirp mass* is that, by looking at both eqs. (2.3.36) and (2.3.39), we can observe that both the frequency and amplitude for the emitted gravitational wave waveform increase with time, like the chirp of a bird.

Finally, we can define an approximate waveform for the binary system by slightly modifying eq. (2.2.24). To this extent, we can use an integrated phase for the term $A_{ij}^{TT}(t - r/c)$. The integrated phase will take into account the frequency evolution in time of the emitted waveform, and can be defined as

$$\Phi(t) = \int_0^t 2\omega_K(t)dt = \int_0^t 2\pi\nu_{GW}(t)dt + \Phi_{in} \ : \ \Phi_{in} = \Phi(t=0), \tag{2.3.40}$$

since

$$\nu_{in}t_{coal}^{3/8} = (5^{3/8})\frac{1}{8}\left(\frac{c^3}{G\mathcal{M}}\right)^{5/8} \Rightarrow \nu_{GW}(t) = \frac{1}{8\pi}\left(\frac{c^3}{G\mathcal{M}}\right)^{5/8}\left(\frac{5}{t_{coal}-t}\right)^{3/8}, \tag{2.3.41}$$

and eq. (2.3.40) can be integrated giving

$$\Phi(t) = -2\left[\frac{c^3(t_{coal}-t)}{5G\mathcal{M}}\right]^{5/8} + \Phi_{in}. \tag{2.3.42}$$

The signal emitted during the inspiralling can hence be written as

$$h_{ij}^{TT} = \frac{4\pi^{2/3}G^{5/3}\mathcal{M}^{5/3}}{rc^4}\nu_{GW}^{2/3}(t)\left[P_{ijkl}A_{kl}\left(t - \frac{r}{c}\right)\right], \tag{2.3.43}$$

with

$$A_{ij}(t) = \begin{pmatrix} \cos\Phi(t) & \sin\Phi(t) & 0 \\ \sin\Phi(t) & -\cos\Phi(t) & 0 \\ 0 & 0 & 0 \end{pmatrix}. \tag{2.3.44}$$

It has to be emphasized that all the results of this section are valid only as first approximations, as they are based on several assumptions that are not generally satisfied by all inspiralling binaries. For example, the adiabatic approximation is only valid when the orbital evolution of the binary is slow, and by looking at eqs. (2.3.34) and (2.3.35) it appears clear that this condition is not satisfied when the binary is close to coalescence and hence its orbital separation is small. Furthermore, the adiabatic approximation assumes that the binary will evolve through semi-stable circular orbits, which is a condition that is not fulfilled in any part of the binary evolution if the *eccentricity* of the orbit is not neglectable. Nevertheless, these results are widely used in literature and are particularly useful when considering systems that are far away from the coalescence, with masses that are approximately comparable and low eccentricity and spin amplitudes for the involved objects. This is usually the case for SMBBH in the LISA frequency range [182]. In principle, if we wish to study systems that do not respect the previously mentioned conditions, the right approach would be to solve (either analytically or numerically) the wave equations defined in (2.2.8). It is however possible to find better approximations than the one proposed in this section that are obtained through the use of additional *Post-Newtonian expansion* terms [31, 175].

Chapter 3

Article: Pearson cross-correlation in the first four black hole binary mergers

Published in JCAP 11 (2020) 043, DOI:10.1088/1475-7516/2020/11/043

Paolo Marcoccia[a], Felicia Fredriksson[b], Alex B. Nielsen[a,c], and Germano Nardini[a]

[a]Department of Mathematics and Physics, University of Stavanger, NO-4036 Stavanger, Norway

[b]Department of Physics and Astronomy, Uppsala University, Box 516, SE-75120 Uppsala, Sweden

[c]Max Planck Institute for Gravitational Physics, 38 Callin Street, D-30167 Hanover, Germany

E-mail: paolo.marcoccia@uis.no, felicia.fredriksson.7699@student.uu.se, alex.b.nielsen@uis.no, germano.nardini@uis.no

Abstract. We adopt the Pearson cross-correlation measure to analyze the LIGO Hanford and LIGO Livingston detector data streams around the events GW150914, GW151012, GW151226 and GW170104. We find that the Pearson cross-correlation method is sensitive to these signals, with correlations peaking when the black hole binaries reconstructed by the LIGO Scientific and Virgo Collaborations, are merging. We compare the obtained cross-correlations with the statistical correlation fluctuations arising in simulated Gaussian noise data and in LIGO data at times when no event is claimed. Our results for the significance of the observed cross-correlations are broadly consistent with those announced by the LIGO Scientific and Virgo Collaborations based on matched-filter analysis. In the same data, if we subtract the maximum likelihood waveforms corresponding to the announced signals, no residual cross-correlations persist at a statistically significant level.

3.1 Introduction

The detection of gravitational waves by LIGO was a major milestone in the history of astronomy [44]. Achieving the necessary strain sensitivity of the instruments was a memorable technological accomplishment [183], while determining the required waveforms was an astonishing success of the physics community [184]. Despite these great achievements, the detection of the signals remains a challenge: the signals are still at low signal-to-noise ratios and must be extracted from the data using advanced statistical techniques and signal processing.

The most sensitive gravitational wave data searches rely on *matched-filtering* techniques [185–187]. These are based on comparing the data with a class of signals determined in a specified theory. Such techniques are robust and very sensitive if the source waveform is accurately predicted. For signals with uncertain modelling, more model-independent, although less sensitive, searches are necessary [21, 188–192]. The coherent wave approach is particularly suitable in these cases. Its flexibility enables it to identify signals that deviate from model expectations. There are still some intrinsic assumptions in the coherent wave method (such as the waves being plane waves traveling at the speed of light with the polarisation behavior of GR waves), so that more agnostic techniques are required to rule out or discover (unexpected) signals not fulfilling these assumptions. Searching for statistically significant correlations in the data of noise-uncorrelated detectors, with as few as possible biases on the signal structure, is poorly efficient in terms of reconstruction power and computing resources but is an option that still deserves some attention. Moreover, the same searches applied to the data streams where the reconstructed signal is subtracted, are a powerful tool to quantify the quality of the reconstructions and the possibility of incoherent detector noise.

Matched-filtering searches typically assume Einstein's theory of General Relativity. This theory is the standard paradigm for gravity, having passed all tests in the Solar System with flying colors. Gravitational wave observations can be used to test this theory in different systems. Neutron star binary systems have been observed via gravitational waves and other astronomical messengers. These observations are already raising questions about our theoretical understanding of neutron star populations [193, 194]. On the other hand, black hole binaries, triplets, and other "dark" systems can be currently discovered only by means of gravitational wave observations. Robust confidence in the analysis of gravitational wave data is thus of key importance for the exact interpretation of the observations. This requires comprehending many aspects, for instance how deviations from expected models might manifest themselves in the data [195], and how to be sensitive to the unexpected.

Monitoring the correlation in the data collected by independent interferometers constitutes an interesting method to test the unexpected. Some publications have explored this direction by analyzing the LIGO data streams with known events [196–201]. It turns out that several subtleties jeopardize the reliability of such a test [202]. For instance, after supposedly subtracting the GW150914, GW151012, and GW151226 signals from the corresponding data streams, refs. [196, 197, 200] find some anomalies that could potentially be ascribed to a sizable mismatch between the detected signals and the general-relativity waveforms that best fit these signals. However, ref. [199] concludes that this mismatch for GW150914 is not statistically significant once one takes care of subtleties, such as whitening versus notching or discrepancies in the best-fit waveforms. Still, some debate remains over the exact size of the statistical significance [200, 201].

The question of whether the anomalies claimed in ref. [197] for GW151226 and GW170104 are actually caused by similar subtleties, has not been fully addressed yet. In the present paper, we tackle this question, and for completeness we run our tests also on GW151012, a black hole merger detected in the first observing run, that was initially classified as marginal but has now been promoted to a confident detection by several groups [144, 203, 204].[1] We believe that our results help to clarify several aspects that can guide the community in future implementations of correlation-based searches for new physics, in the presence and in the lack of a signal model.

This manuscript is organized as follows. Section {3.2} details how we preprocess the data and apply the *Pearson cross-correlation* measure. Section {3.3} contains the results and comments on them. Finally, sec. {3.4} is devoted to our main conclusions and outlook.

3.2 Methodology

Our methodology follows closely the approach presented in ref. [199] which itself is designed to scrutinize the claimed anomalous correlations in the GW150914 data from refs. [196, 197]. The approach in ref. [199] is thus tuned to work on the features of the GW150914 signal. To extend it beyond GW150914, we need to decide some criteria aimed at generalizing this procedure to other events.

In brief, the procedure we adopt is the following: we take the GWOSC calibrated gravitational wave strain data of LIGO Hanford and LIGO Livingston around the events GW150914, GW151012, GW151226, and GW170104; we whiten and bandpass the data of each event and each detector individually; we calculate the Pearson

[1] We restrict our analysis to the events GW150914, GW151012, GW151226 and GW170104 as their LIGO data can be easily handled by means of the Gravitational Wave Open Science Centre (GWOSC) toolbox [205]. The GWOSC webpage indeed provides several numerical tools already tuned for the analyses of these four events. There is no conceptual obstacle in analyzing other events in the way we present here.

cross-correlation between the data streams of the detectors before and after subtracting best-fit GR waveforms; and we check the statistical significance of the obtained correlations with the statistical fluctuations arising in pure noise. We now describe the choices of these steps and their reasons.

We choose here to whiten the data, rather than notch them with a list of frequency lines. This simplifies our analysis, providing a unique criterion applicable to every event without requiring a complete list of individual lines to be notched. Such a list, varying from event to event, does not exist in general and would need to be generated by hand with some judgment (we note that ref. [197] also uses whitening for their analysis of GW151226 and GW170104). This generalization of the analysis leads to a change in spectrum of both noise and templates. In particular, the whitening reduces the contribution of low frequencies to the residuals and cross-correlations. Whitening the data also more closely follows the practice in the wider gravitational wave literature; *e.g.* ref. [202]. We refer to ref. [199] for details on the whitening process we employ.

We apply a bandpass to the data filtering frequency ranges that vary for each event. The chosen ranges loosely follow those considered in the GWOSC webpage [205] which itself does not necessarily implement the values used in the published LIGO-Virgo Collaborations (LVC) analyses, but provides a convenient guide for our investigation. The high-pass frequency adopted in GWOSC is 43 Hz but the data at frequencies $35-60$ Hz are usually highly dominated by seismic noise. We then round the high pass frequency to 50 Hz for all events but the first one, for which we keep the choice adopted in ref. [199] to facilitate the comparison between our findings and those previously obtained. For the low-pass frequencies, we typically use lower frequencies than those chosen by GWOSC, which are 300 Hz for GW150914, 400 Hz for GW151012 and 800 Hz for GW151226 and GW170104.[2] We in fact take a low-pass frequency not smaller than $200-300$ Hz for these frequencies in order to be free of seismic and thermal noise, and sufficiently below the violin frequency disturbances at around 500 Hz.[3]

It is of course essential to not cut out the dominant frequencies associated with the binary coalescence. Indeed a cross-correlation analysis, as opposed to an extended matched-filter, appears to be more sensitive to the signals around their peak of strain. For a binary merger, it is hence weakly impacted by the low-frequency strain at the start of the inspiral phase whereas it is dominated by the higher-frequency strain around the coalescence stage. Table [3.1] shows the specific values of the low and high bandpasses we implement.[4] These values are in part determined by the inferred properties of the signal and thus further investigations with truly blind searches would be required to

[2] These values correspond to the option 'fband' in the JSON files of the GWOSC webpage [205].

[3] We ran some tests on power spectral density at about the time of the GW151226 event. For a low pass of 480 Hz or larger, the data at high frequencies are still very noisy due to contamination at the violin frequencies.

[4] As a consistency check, for the GW151012 event we ran our analysis with different choices of high- and low-pass frequencies. For variations of about ± 5 Hz, the findings do not qualitatively change.

test the capabilities of the Pearson correlation search method for unknown signals.

To construct the data sets of the residuals, we subtract best-fit GR waveforms. As shown in ref. [199], for GW150914 the *maximum likelihood waveform* produces cleaner residual data than the numerical relativity waveform released on GWOSC. In our analysis here we subtract maximum likelihood waveforms, specifically the one provided in ref. [206] for GW170104 and those available in ref. [207] for the other three events.

To measure the cross-correlations between the Hanford and Livingston data sets, we apply a Pearson cross-correlation measurement. The Pearson cross-correlation is given by

$$R(\tau, t, \omega) = \int_t^{t+\omega} \frac{H(t'+\tau)}{\sigma_H} \frac{L(t')}{\sigma_L} dt' \ , \tag{3.2.1}$$

where $H(t)$ and $L(t)$ are respectively the data in Hanford and Livingston (with or without the signal subtracted) at the time t set in Hanford, σ_H and σ_L are the standard deviations of the Hanford and Livingston data respectively, and ω is the time window in which the correlation is measured. The quantity τ is the time lag between the signal arrival times in Hanford and Livingston (positive if the signal reaches Livingston first). Unfortunately, in most of the realistic cases, τ comes with an important uncertainty $\Delta\tau$ that eq. (3.2.1) does not take into account. We thus need to modify the measure R, and define the (improved) cross-correlation measure

$$C(\tau, \Delta\tau, t, \omega) = \max_{\bar{\tau}} R(\bar{\tau}, t, \omega) \ : \ |\bar{\tau} - \tau| \leq \Delta\tau \ . \tag{3.2.2}$$

Due to computational limitations, we have not performed a complete multivariate analysis on t and τ. We instead prefer to analyze the t dependence of C along a strip $\tau_p \pm \Delta\tau_p$ — with τ_p and $\Delta\tau_p$ taken from refs. [197, 208], and identify the time $t = t_p$ at which $|C(\tau_p, \Delta\tau_p, t, \omega)|$ is maximal. This facilitates comparison with existing results in the literature and makes manifest the impact of some subtleties such as different bandpasses, whitening, and subtracted waveforms. On the other hand, the data preprocessing in refs. [197, 199] and in ours differs in several aspects, so that it is not guaranteed that taking $\tau = \tau_p$ is a valid assumption. For this reason, we perform some consistency checks, and test a posteriori that at $t = t_p$ no higher cross-correlations arise when moving τ outside the strip $\tau_p \pm \Delta_p$.

To identify t_p, it is important to evaluate C in a t interval including the merger time around which the maximal cross-correlation is expected in the data before subtracting the reconstructed signal. In principle the length of this interval should mildly affect the findings, however, an appropriate interval helps avoid statistical artifacts and include relevant signal data.

For concreteness, we take $t \in [t_r - 0.1\,\mathrm{s}, t_r + 0.1\,\mathrm{s}]$, with t_r being the arrival time (rounded at the first decimal digit) of the maximal signal strain in Hanford as esti-

Event Name	Bandpass range (Hz)	H-L time $\tau_p \pm \Delta\tau_p$ (ms)	Reference time t_r (s)	Window ω (ms)
GW150914	35-350	6.9 ± 0.5	1126259462.4	0.4
GW151012	50-230	-0.6 ± 0.6	1128678900.4	0.4
GW151226	50-460	1.1 ± 0.3	1135136350.6	0.4
GW170104	50-230	-3.0 ± 0.5	1167559936.6	0.4

Table 3.1. The values of the input parameters for the analysis of each event.

mated in the GWOSC analysis [205]. For τ and $\Delta\tau$ we adopt the values obtained in refs. [197, 208]), while for ω we consider the time window $\omega = 40$ ms which corresponds to four cycles of a gravitational wave of 100 Hz. As a consistency check, we allow τ to move from -10 to 10 ms. Such an analysis is performed for both the data sets with the signals and those with only the residuals. Table [3.1] summarizes the inputs we adopt in our analysis.

Lastly, we analyze the cross-correlation among the detectors for pure noise by estimating the backgrounds, following the procedure described in ref. [199]. However, our analysis differs from ref. [199] in some technical points. While in ref. [199] the residual data was used for background times, we preferred to use the original data strain in a time interval far away from the coalescence, where no event was declared. In particular, the time interval was chosen to start 12 minutes away from the coalescence time.

We generate several pairs of data sets, each pair consists of a set of mock data of simulated pure Gaussian noise and a set of LIGO data at times away from any claimed event. These pairs are then treated in exactly the same way as the event data we consider. We thus whiten and bandpass them, and run the C estimator over them according to table [3.1]. This tells us how often a given cross-correlation value arises as a statistical fluctuation in background noise, and furnishes a probability estimate for the maximal correlations we find in our analysis to occur by chance in pure noise.

The code with the implementation of our analysis is public [209]. We refer the reader to this for further details on the preprocessing of the data and their analysis.

3.3 Results

In this section, we discuss our main results. We start by presenting the t dependence of C in the strip $\tau_p \pm \Delta\tau_p$, and then show the consistency check previously described. At the end, we quantify the statistical significance of the identified cross-correlations before and after subtracting the maximum-likelihood waveforms of the reconstructed signals.

3.3.1 Cross-correlation: t dependence

We run the cross-correlation measure C over the time series around the GW150910, GW151012, GW151226 and GW170104 LIGO data, preprocessed as explained in Section {3.2}. The resulting t dependence is plotted in the upper panels of figs. 3.1–3.4, where the time variable is shifted by $t_0 \equiv t_r - 0.1$ for clarity. In each figure, each one dealing with a different event, the blue solid and dashed orange lines represent the t evolution of C in the data, respectively before and after subtracting the maximum likelihood waveforms of the reconstructed signals. The red vertical line marks t_p, the maximal (in absolute value) correlation time found in the data before the waveform subtraction. The green vertical line instead highlights t_d, the time at which subtracting the waveform signal leads to the maximal difference in the correlation between the original data and the residuals. The waveform signals that are subtracted are depicted in the lower panels of the figures. They are shown after being whitened, bandpassed and, for the waveform measured in Livingston, shifted by the value of τ reported in table [3.1]. In each of these lower panels, the yellow region highlights the time frame $\omega = 40$ms for the peak correlation value of $C(t_p, \tau_p, \Delta\tau_p, \omega)$ for the considered event. By construction, such a time frame contains the data that the LIGO Hanford and LIGO Livingston detectors collect at the times $t \in [t_p, t_p + \omega]$ and $t \in [t_p + \tau_p, t_p + \omega + \tau_p]$, respectively.

For a signal that slowly increases in amplitude and then falls away rapidly, such as a gravitational wave inspiral, the choice of a forward integration will lead to a shift in time of the location of the maximum of the correlation integral compared to the location of the maximum amplitude of the signal. This may appear unusual in figs. 3.1–3.4, because the maximum correlation is found at a GPS time that is shifted to the left of the real coalescence time, by a quantity approximately equal to the used integration window. Both the residual correlation, and the difference between the strain correlation and the residual correlation, fall off before the reference coalescence time t_r, since with a forward integration large parts of the integrated strain beyond that point come from regions where the signal template is rapidly diminished. In spite of this issue, we choose here to keep a forward integration for our correlation formula (3.2.1), in order to enable easy comparison of our results with existing ones from the literature [196, 197, 199, 200].

With this choice we expect t_p to be around $t_r - \omega$, *i.e.* in the data segment preceding the signal's maximal strain (during the ringdown the amplitude of the signal is much weaker than in the late inspiral and merger phase). Our results fulfill this expectation (c.f. t_r and t_p in table [3.1] and table [3.2], which quotes the key quantities calculated in this section).

Figure 3.1 shows the correlation versus detector time around the event GW150914. The cross-correlation behaviour of this event is widely discussed in the literature [196, 197, 199, 200, 207]. We present it here for ease of comparison with previous results. We notice that, after subtracting the reconstructed signal, the correlation in

the time window $[t_p, t_p + \omega]$ is strongly reduced and the global peak of the correlation is no longer inside this window. The maximal variation between the cross-correlations before and after the subtraction is also outside of this time window, *i.e.* $t_d < t_p$. This is not surprising if after the subtraction of the model waveform from the original data, what remains is a pure noise correlation between the two detectors. The residual correlation, assuming a perfect subtraction of the signal waveform, may vary randomly in magnitude, as well as in sign, independently from the subtracted signal.

We have to emphasise however, that even though noise correlations and signal correlations are not linearly additive, they are still additive. Having a really low value of correlation difference after subtraction at the time t_*, therefore suggests that most of the correlations at said time were given by statistical fluctuations of the noise, which are indeed not the ones we are interested in this kind of analysis. We will see in particular in the case of GW151012, where the low signal-to-noise ratio (SNR) of the incoming wave allow the noise correlations to be comparable with the ones generated by genuine gravitational waves effects, that the first peak of maximum correlation found can be discarded due to the low significance difference of the correlations before after the subtraction. We detail the statistical compatibility of the residuals with the instrumental noise in Section sec. {3.3.3}.

In the top panel of fig. 3.1 after the merging time, there are still some slight differences between the original data correlation (in blue) and the residuals correlation (in orange). Since the model waveform is zero after the ringdown, one might expect there should be no difference between the correlations of the original data of fig. 3.1 and the residual data. However, the process of whitening applied both to the original data and the model waveform, introduces a small difference in both of the considered data (see the variation after the ringdown part of the model waveform in the bottom panel), that once integrated over the window ω to estimate the correlations will result in the small mismatching observable among the two. This feature of the analysis, is present in all of the reported figs. 3.1–3.4.

The analogous plots for the event GW151012 are presented in fig. 3.2. GW151012 is the event with the lowest SNR among the ones we investigate. The figure shows that we still obtain relatively high values of $|C|$, although not as high as for GW150914. As we will see later in this section, the significance of these values is also not as high as the ones for GW150914. This is qualitatively consistent with the interpretation of a lower amplitude signal due to a smaller mass system at a greater distance.

At $0.05\,\mathrm{s} \lesssim t - t_0 \lesssim 0.075\,\mathrm{s}$ the data correlation occasionally becomes positive, even though we expect that the effects of the incoming gravitational waves should result in an anticorrelation among the detectors. It has to be emphasized though, that the correlations of residuals and reconstructed waveforms are not linearly additive, hence this effect arises for this event due to the low amplitude of the gravitational wave signal in the detectors, compared to the noise, at times away from the coalescence. At

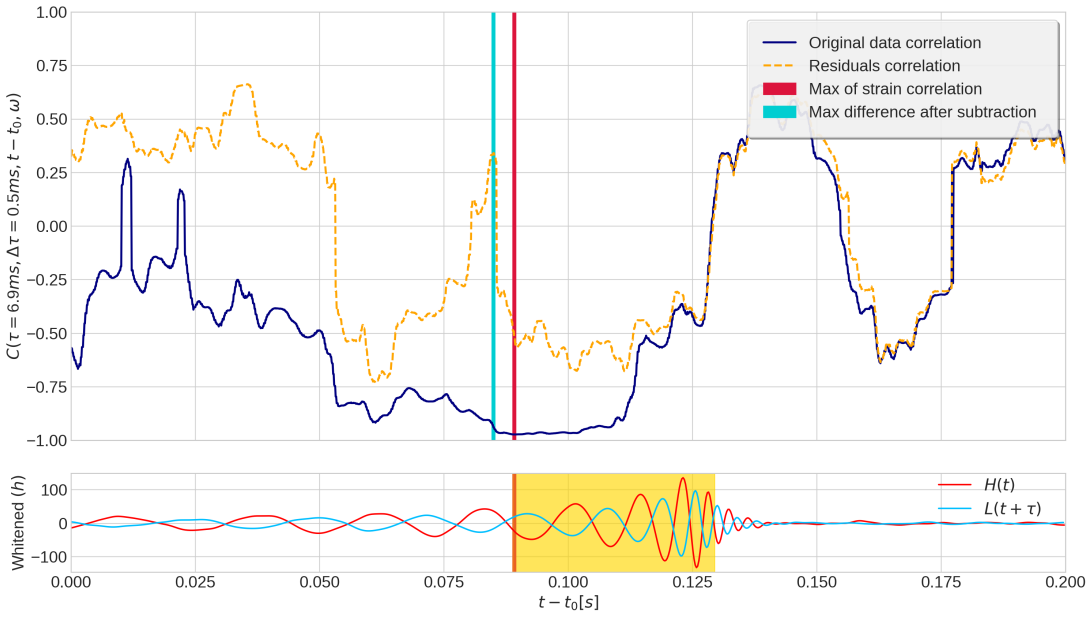

Figure 3.1. Top panel shows the correlations between Hanford and Livingston detector strain data for 200 ms of data around GW150914. The bottom panel shows the whitened model waveforms that are subtracted from the data to produce the residuals, where the time interval highlighted in yellow represents the part of the waveforms that was integrated in the estimation of the correlation at the time of maximum correlation t_p. The Livingston waveform is shifted in time relative to the Hanford waveform in order to highlight the anti-correlation between the two strains.

$t - t_0 \lesssim 0.010\,\mathrm{s}$ the signal dominates the noise in the detectors. Hence, even though the correlation of the residuals flips sign, the correlation in the data before the signal subtraction remains negative until it lines up with the residual strain after the coalescence time. Eventually, after the signal waveform fades out, no sizeable correlation remains.[5]

Furthermore, at $t - t_0 \lesssim 0.010\,\mathrm{s}$ a first maximum of strain correlation appears, however, as discussed previously this peak can be neglected because most of its anti-correlation is given by a statistical fluctuation of the noise. This fact may be further elucidated by observing the bottom panel of fig. 3.2, which clearly shows that in relation to the first peak we are not even including the merging part of the waveform in the correlation data. This event is the only one for which the correlations in the residual data are positive around the time of the signal merger, that is, in one forth of our events the residual exhibits a positive correlation, which seems statistically unremarkable to us.

[5]Our results do not confirm the late-time correlation found in ref. [190]. However our results are restricted to time lags τ consistent with the main event and are thus blind to correlations at other time lags, that could be interpreted as originating from other parts of the sky.

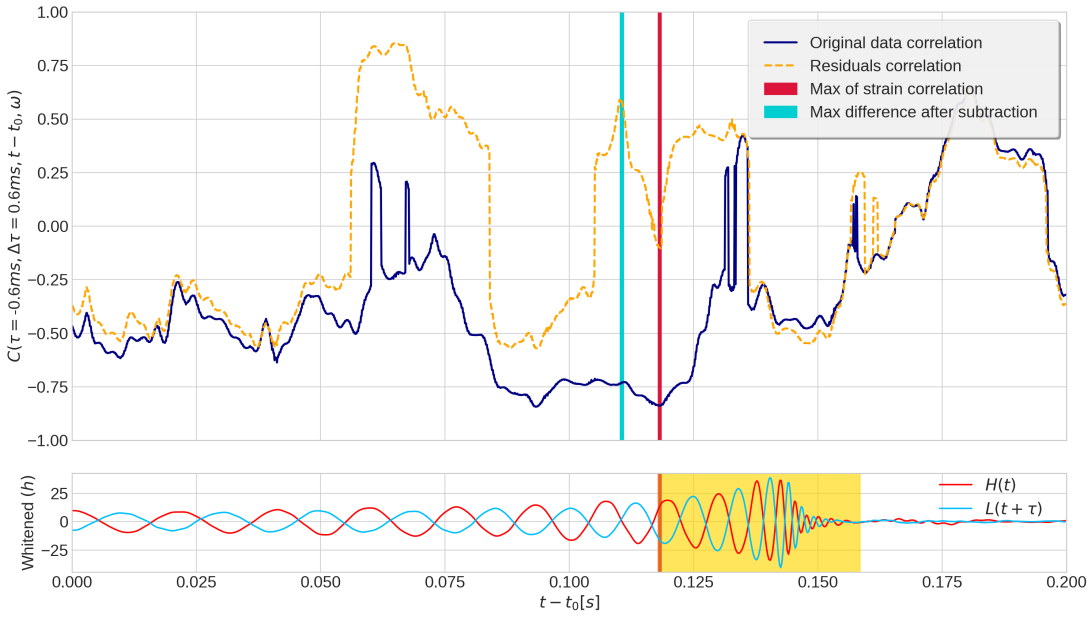

Figure 3.2. As fig. 3.1, but for the GW151012 event.

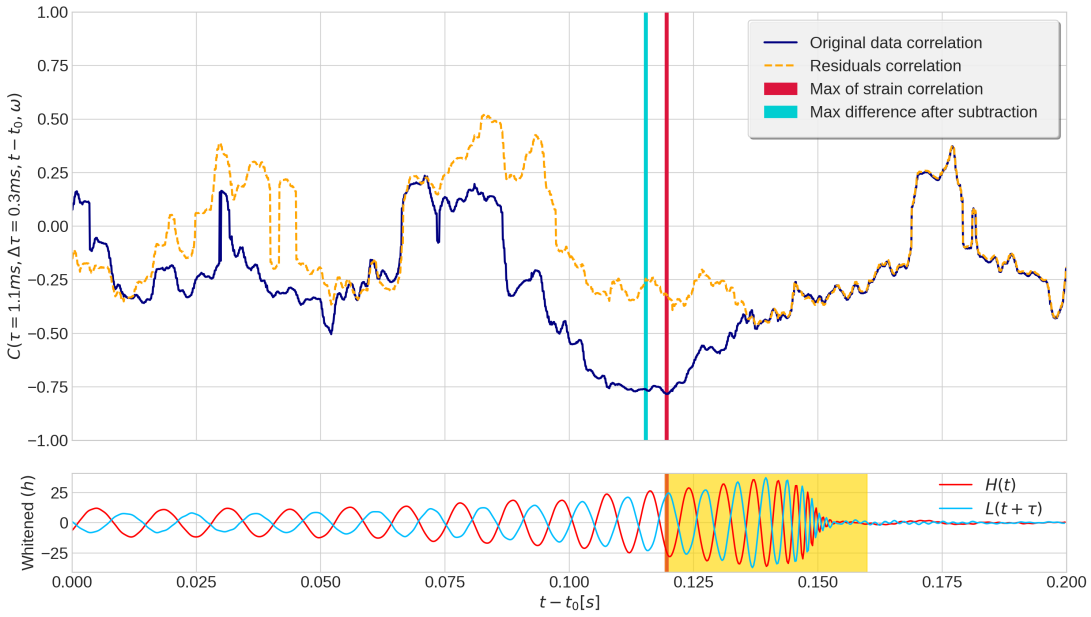

Figure 3.3. As fig. 3.1, but for the GW151226 event.

Concerning GW151226 and GW170104 (see figs. 3.3 and 3.4), the t dependence

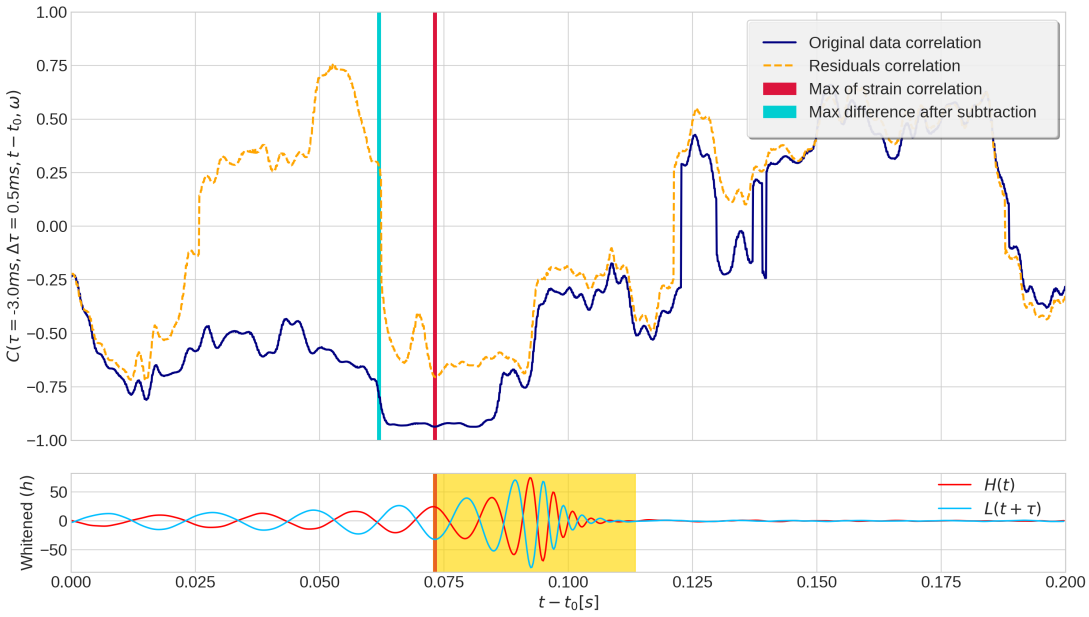

Figure 3.4. As fig. 3.1, but for the GW170104 event.

of C essentially presents no key qualitative features not already noted above for GW150914 and GW151012. The signal in GW151226 has a reconstructed total mass much smaller than the other three. The signal thus exhibits the largest gravitational wave frequency at the coalescence time, about 447 Hz [205], and the smallest relative strain around the coalescence time. The maximum of C is then the smallest in absolute value. The amplitude of the signal in GW170104 is instead much higher. Its source involves two highly massive black holes (of approximately 30 and 20 solar masses) and is the next to farthest among the four considered sources.

For binaries with masses inferred for GW170104 at the reconstructed luminosity distance, theory predicts that the gravitational wave signal has a peak strain amplitude at a frequency around 190 Hz, where the noise of the detectors is quite low. Thus the correlation of the data around this event peaks at a rather high value, almost as high as the one in GW150914.

The straight comparison between the values of the C peak in different events can be misleading. For instance, let us consider the case of GW150914 and GW170104. As just observed, C peaks at similar values in these two events. It is however known that the matched-filter SNR in GW150914 is almost twice as high as the matched-filter SNR in GW170104 [144], so it may seem that this observation is not compatible with the similar values of the correlation peaks. However, correlation values in and of themselves are not directly comparable without considering the different bandpass frequency ranges and length of data for which the correlations are calculated. We further investigate this aspect in sec. {3.3.3}.

For the four considered binary merger events, if one knows the time lag $\tau \pm \Delta\tau$ and has an indicative time data segment where to look in, $C(\tau, \Delta\tau, \omega, t)$ reaches large values in the proximity of the time frame where the inferred signal strength becomes high. In addition, running C on the residuals constitutes a valuable check of the signal model. In the case of our four events, if one subtracts the signal reconstructed assuming the theory of General Relativity, the correlation maximum (in absolute value) moves away from the time interval where C peaks. This is not yet a complete test of the model but it is certainly encouraging. We come back to this point after performing the consistency checks on the values of τ we have just adopted.

3.3.2 Cross-correlation: τ consistency check

We have determined t_p by assuming $\tau = \tau_p$ and $\Delta\tau = \Delta\tau_p$, with τ_p and $\Delta\tau_p$ taken from previous studies [197, 208]. Here we present the consistency checks. We test that $|C(\tau, 0, t_p, \omega)| < |C(\tau_p, \Delta\tau_p, t_p, \omega)|$ for $\tau \in [-10\,\mathrm{ms}, \tau_p - \Delta\tau_p] \cup [\tau_p + \Delta\tau_p, 10\,\mathrm{ms}]$, that is, no higher cross-correlations are found at $t = t_p$ for a time lag τ away from the strip $\tau_p \pm \Delta\tau_p$.

Figure 3.5 shows $C(\tau, \Delta\tau_p, t_p, \omega)$ as a function of τ, for $\Delta\tau_p$ and ω as in table [3.1]. The time is fixed at the values of t_p obtained from the t dependence analysis of C and reported in table [3.2]. Each panel corresponds to one of the four events we analyse. The grey band spans the time lag $\tau_p \pm \Delta\tau_p$. The figure highlights two remarkable facts. First of all, had we determined τ and $\Delta\tau$ independently of the previous results in the literature, this would have been estimated as the peak of correlations and its approximate width arising in the strain data before the signal subtraction (blue line). Such peaks turn out to be within the gray bands, which proves that the values of τ used in the previous section are consistent with the data treatment of our analysis. Secondly, the correlation in the residuals (pink line), obtained after the subtraction of the model waveform from the original data, does not necessarily peak in the grey zone. (In some cases the global peak for the residuals is close, but not inside, the grey zone. In some cases the global peak for the residuals is a positive correlation rather than a negative correlation.) This feature, together with the observation that the data and residual correlation peaks are well separated in figs. 3.1–3.4, sheds light on the precision of the subtracted waveform: If there was a sizeable discrepancy between signal and subtracted waveform during the merging phase, the cross-correlation in the residuals would have likely peaked within the grey band where the signal strain amplitude is larger.[6] A peaking of the residuals' correlation within the grey band is however not sufficient for there to be a problem with the subtracted waveforms. It can also happen by pure chance.

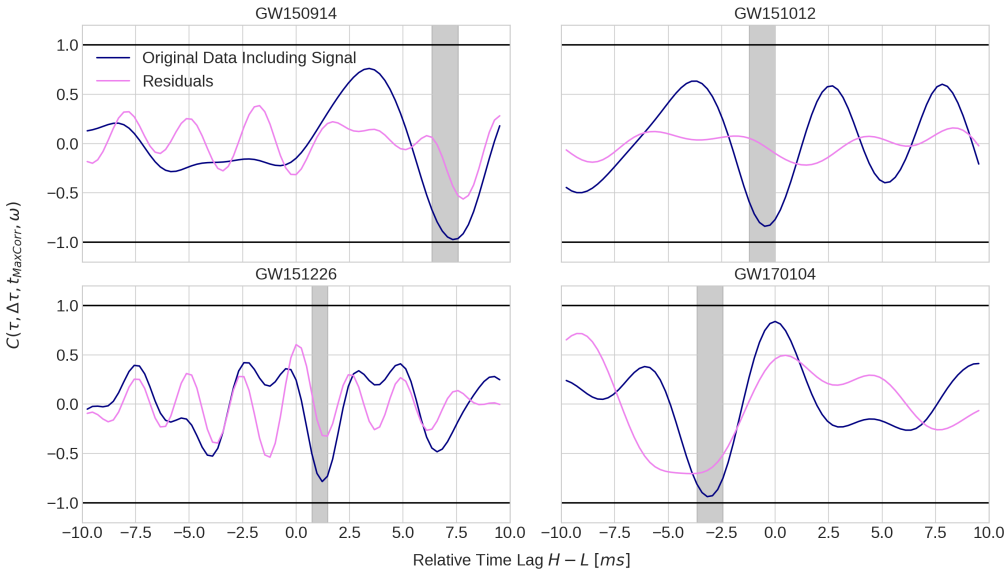

Figure 3.5. The cross-correlations as a function of τ at the time $t = t_p$. The gray bands correspond to the strips $\tau_p \pm \Delta\tau_p$ previously used to determine t_p.

3.3.3 Background cross-correlations and statistical interpretation

In order to determine the statistical significance of our computed cross-correlations, we run the C estimator over the aforementioned data sets of background, and count how often a given value of $|C|$ arises in pure noise data (preprocessed in the same way we preprocess the LIGO events that we analyze). From this we estimate the probability, in terms of a p-value, that a value at least as large as our observed cross-correlation value, would occur as a statistical fluctuation in pure noise.

Figure 3.6 reports the statistical significance of the cross-correlations arising in the four LIGO event data sets before and after subtracting the reconstructed signal waveform (dashed vertical lines in blue and pink, respectively).[7] The black and crimson curves show the p-value deduced from cross-correlations found in the off-source LIGO data sets and the simulated Gaussian noise data sets, respectively. The usage of these two different curves is complementary. The simulated Gaussian noise is guaranteed to be free of truly correlated signals while the off-source detector data more closely follows the noise distribution of the actual detectors. The close agreement of these curves however indicates that the true noise of the detectors is statistically indistinguishable from pure Gaussian noise at the level of this test for all the bandpass frequency ranges

[6] More details on this reasoning can be found in refs. [197, 199].

[7] To reduce the computational time, the code evaluates $R(\tau_p, t, \omega)$ instead of $C(\tau_p, \Delta\tau_p, t, \omega)$. The latter reproduces the former in the limit $\Delta\tau \to 0$ (cf. eqs. (3.2.1) and (3.2.2)). This leads to slightly overestimate the significance of the cross-correlations $C(\tau_p, \Delta\tau_p, t_p, \omega)$ obtained in Section {3.3.1}.

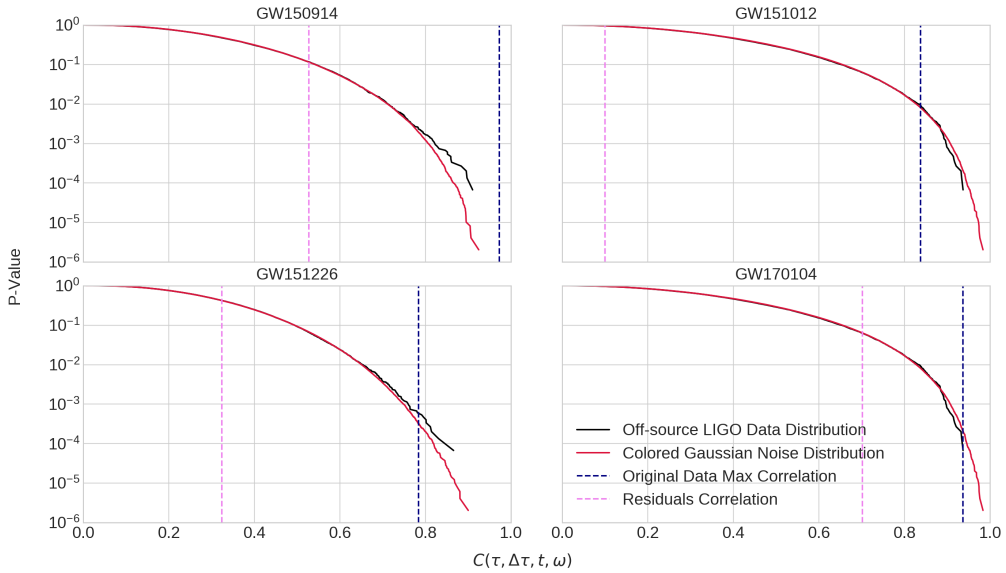

Figure 3.6. Comparison between the actual correlation values obtained for the events, and the frequency of occurrence of similar correlation values in the background of detector time away from events (black lines) and in simulated Gaussian noise (crimson lines). Here the same background values are used for the events GW151012 and GW170104, as the same frequency bandpass range was employed for these two events.

used in our analyses.

Although this procedure of estimating significance is different in several respects from that employed by the LVC, there is still qualitative agreement in the significance ranking of the four events. From fig. 3.6 the most significant event, in agreement with the LIGO results, is GW150914, with a p-value of approximately 10^{-5}. Moreover, the subtraction of the maximum likelihood waveform in the GW150914 data, makes $C(\tau_p, \Delta\tau_p, t, \omega)$ drop down four orders of magnitude. The GW151226 and GW170104 data before subtraction are the next most significant events of the four analyzed, with a p-values around 10^{-3} and 10^{-4} respectively. This similarity is unsurprising considering that both these events have a matched-filter SNR around 13 [144]. However, after the subtraction of the numerical waveform, the p-value of the residuals' cross-correlation for GW151226 is approximately 0.2, while for GW170104 it is around 0.08. This feature is a consequence of the fact that detector noise exists at all frequencies. With a bigger frequency range considered, a larger amount of noise is included in the data, making it harder to identify potential signals with a limited bandwidth. On the other hand, once the background is bandpassed and whitened, the dependence on the frequency range of the correlations is taken into account, hence the significance obtained for the various events, can be more easily compared between events. Lastly, in agreement with

Event Name	**Max corr. time t_p (s)**	**Max corr. var. time t_d (s)**	$C(\tau_p, \Delta\tau_p, t_p, \omega)$ **before subtr.**	$C(\tau_p, \Delta\tau_p, t_p, \omega)$ **in residuals**
GW150914	1126259462.39	0.0069 ± 0.0005	-0.97	-0.53
GW151012	1128678900.42	-0.0006 ± 0.0006	-0.84	-0.10
GW151226	1135136350.62	0.0011 ± 0.0003	-0.78	-0.32
GW170104	1167559936.57	-0.003 ± 0.0005	-0.94	-0.70

Table 3.2. Time of maximum correlation and obtained correlation values at that time for the four analysed events. Correlation values are rounded up to the second decimal value and denote the maximum magnitude of correlation found in the assumed time-lag intervals, both for the original data and after subtraction of a maximum likelihood waveform. To check the full precision results see ref. [209].

LVC results, GW151012[8] is the least significant event among the four. The p-value of its data before and after waveform subtraction is only around 10^{-2} and 1, showing that the maximum likelihood waveform still efficiently reduces the cross-correlation.

In general, fig. 3.6 shows that the cross-correlation method, combined with the present statistical interpretation, is a valid tool for complementary searches of signals and tests of their modelling.

3.4 Conclusions

Sensitivity to the unexpected is one of the main challenges of the modern experiments. Marvelous sensitivities often come at the expense of intricate data analysis techniques required to dig out weak signals from data largely contaminated by instrumental noise. Unfortunately, such techniques tend to rely on hidden or manifest assumptions, with the risk of overlooking signatures of new physics in the data. It is then worth developing alternative techniques to analyze data with a range of different assumptions and generality. In the present paper we have investigated one of these approaches, the so called Pearson cross-correlation method. Specifically, we have employed (a variation of) it to analyse the data of the four gravitational wave events GW150914, GW151012, GW151226 and GW170104, and scrutinize some claims made about them. The study has led to the following conclusions:

- Although the Pearson cross-correlation method is less sensitive than a matched-filter analysis, it is still able to recover the events at relatively low p-values, relative to both off-source detector data and simulated Gaussian noise.

- No significant cross-correlation arises at about 0.1 s after the end of each event if the Hanford and Livingston detector data are analysed with time lags consistent with the original events. No evidence of events such as echoes is then found with this method.

[8]There was a typo on the name of the event in the original article that is now corrected on this version.

- In all of the four events, the cross-correlations in the data after subtracting maximum likelihood general-relativity waveforms, is consistent with noise fluctuations. Specifically, such cross-correlations have p-values larger than 0.05. This is consistent with the residual analysis results of the LVC [21], and amply compatible with GR.

- The maximum peaks in the residual correlations do not typically occur at detector time lags consistent with the original events. This seems statistically natural in the case that the subtracted waveforms well fit the signal in the merging stage, which is the phase at which the binary signal strain is the largest and the Pearson cross-correlation method consequently reaches its highest sensitivity.

Several aspects however remain to be explored in more depth. With more computational resources dedicated to the study, it would be interesting to systematically investigate the performances of the Pearson cross-correlation method in the whole catalogue of LIGO events, and excise these data with a multivariational approach of the Pearson cross-correlation estimator (here we have run it by varying either the GPS detector time or the time lag). This is especially true of much lower mass systems such as the binary neutron star merger GW170817. While analysis of this event is beyond the scope of the present work, we see no fundamental reasons why the current techniques could not be applied there. The same method could also be adopted to test the quality of the multi-source fitting necessary to solve the "enchilada" problem in LISA data [210]. We plan to deal with some of these aspects in future investigations.

3.5 Aknowledgment

This work uses open-source code presented in ref. [199]. AN and FF thank the Max Planck Institute for Gravitational Physics in Hanover, Germany for support and hospitality during the initial stages of this project. G.N. is partly supported by the Research Council of Norway, ROMFORSK grant, project. no. 302640.

3.6 Appendix A : Maximum likelihood IMR waveform parameters

In this appendix, we report the values of the General Relativity model templates that we subtract from the detectors data for the four analyzed events. These values correspond to the maximum likelihood values reported in ref. [207]. They are constructed using the phenomenological inspiral-merger-ringdown waveform family IMRPhenomPv2 [211] which is freely available as part of LALSuite [212].

Parameter	Description	GW150914	GW151012	GW151226	GW170104
m_1	Mass of the larger black hole ($M_\odot$)	39	23	19	39
m_2	Mass of the smaller black hole ($M_\odot$)	32	19	7	21
a_1	Dimensionless spin of the larger BH	0.977	0.299	0.607	0.550
θ_1^a	Azth. angle of the larger BH spin (rad)	3.6	1.0	2.5	3.49
θ_1^p	Polar angle of the larger BH spin (rad)	1.6	2.30	1.2	2.39
a_2	Dimensionless spin of the smaller BH	0.189	0.067	0.938	0.553
θ_2^a	Azth. angle of the smaller BH spin (rad)	3.44	5.48	5.32	0.06
θ_2^p	Polar angle of the smaller BH spin (rad)	2.49	0.40	1.05	0.59
d_L	Luminosity distance (MPc)	480	750	380	530
α	Right ascension (rad)	1.57	0.65	1.85	0.89
δ	Declination (rad)	-1.27	0.07	0.99	-0.80
ψ	Polarization (rad)	5.99	5.64	2.76	5.69
f_0	Starting frequency of the waveform (Hz)	10	10	10	10
f_{ref}	Reference frequency (Hz)	20	20	20	20
i	Inclination of the binary at f_{ref} (rad)	2.91	2.32	0.66	1.09
ϕ_c	Reference phase at f_{ref}	0.69	4.44	$\emptyset$	$\emptyset$
$\Delta\phi$	Waveform's phase with respect to ϕ_c	-0.92	-0.91	-0.10	-1.80

Table 3.3. Table of the maximum likelihood parameters for the waveforms of the four events considered here. Values are rounded up to an arbitrary precision. The value of ϕ_c for GW151226 and GW170104 is not reported as it is not part of the maximum likelihood parameters reported by [207]. For the full precision results see ref. [209].

Chapter 4

Article: Stochastic Gravitational Wave Background from Stellar Origin Binary Black Holes in LISA

Published in JCAP 08 (2023) 034, DOI:10.1088/1475-7516/2023/08/034

Stanislav Babak,[a] Chiara Caprini,[b,c] Daniel G. Figueroa,[d] Nikolaos Karnesis,[e] Paolo Marcoccia,[a] Germano Nardini,[f] Mauro Pieroni,[c,1] Angelo Ricciardone,[g,l] Alberto Sesana,[h,i,j] and Jesús Torrado[l,m,1]

[a]Université de Paris, CNRS, Astroparticule et Cosmologie, 75013 Paris, France

[b]Université de Genève, Département de Physique Théorique and Centre for Astroparticle Physics, 24 quai Ernest-Ansermet, CH-1211 Genéve 4, Switzerland

[c]CERN, Theoretical Physics Department, 1 Esplanade des Particules, CH-1211 Genéve 23, Switzerland

[d]Instituto de Física Corpuscular (IFIC), Consejo Superior de Investigaciones Científicas (CSIC) and Universitat de València, 46980, Valencia, Spain

[e]Department of Physics, Aristotle University of Thessaloniki, Thessaloniki 54124, Greece

[f]Department of Mathematics and Physics, University of Stavanger, NO-4036 Stavanger, Norway

[h]Dipartimento di Fisica "G. Occhialini", Università degli Studi di Milano-Bicocca, Piazza della Scienza 3, I-20126 Milano, Italy

[i]INFN, Sezione di Milano-Bicocca, Piazza della Scienza 3, I-20126 Milano, Italy

[1]Corresponding authors

[g]Dipartimento di Fisica "E. Fermi", Università di Pisa, I-56127 Pisa, Italy
[j]INAF, Osservatorio Astronomico di Brera, Via E. Bianchi 46, 23807 Merate, Italy
[l]Dipartimento di Fisica e Astronomia "G. Galilei", Università degli Studi di Padova, via Marzolo 8, I–35131 Padova, Italy
[m]INFN, Sezione di Padova, via Marzolo 8, I–35131 Padova, Italy

E-mail: mauro.pieroni@cern.ch, jesus.torrado@pd.infn.it

Abstract. We use the latest constraints on the population of stellar origin binary black holes (SOBBH) from LIGO/Virgo/KAGRA (LVK) observations, to estimate the stochastic gravitational wave background (SGWB) they generate in the frequency band of LISA. In order to account for the faint and distant binaries, which contribute the most to the SGWB, we extend the merger rate at high redshift assuming that it tracks the star formation rate. We adopt different methods to compute the SGWB signal: we perform an analytical evaluation, we use Monte Carlo sums over the SOBBH population realisations, and we account for the role of the detector by simulating LISA data and iteratively removing the resolvable signals until only the confusion noise is left. The last method allows the extraction of both the expected SGWB and the number of resolvable SOBBHs. Since the latter are few for signal-to-noise ratio thresholds larger than five, we confirm that the spectral shape of the SGWB in the LISA band agrees with the analytical prediction of a single power law. We infer the probability distribution of the SGWB amplitude from the LVK GWTC-3 posterior of the binary population model: at the reference frequency of 0.003 Hz it has an interquartile range of $h^2\Omega_{\rm GW}(f = 3\times10^{-3}\,{\rm Hz}) \in [5.65,\, 11.5]\times10^{-13}$, in agreement with most previous estimates. We then perform a MC analysis to assess LISA's capability to detect and characterise this signal. Accounting for both the instrumental noise and the galactic binaries foreground, with four years of data, LISA will be able to detect the SOBBH SGWB with percent accuracy, narrowing down the uncertainty on the amplitude by one order of magnitude with respect to the range of possible amplitudes inferred from the population model. A measurement of this signal by LISA will help to break the degeneracy among some of the population parameters, and provide interesting constraints, in particular on the redshift evolution of the SOBBH merger rate.

4.1 Introduction

Stellar-origin binary black holes (SOBBHs) are among the targets of the Laser Interferometer Space Antenna (LISA) [213]. The emission of gravitational waves from these binaries crosses the mHz frequency band, probed by LISA, while they are still far from coalescence. Given the recent constraints from the LIGO/Virgo/KAGRA (LVK) collaboration after three observation runs, we expect a large population of such systems contributing to the LISA data stream [45]. At least a few of these binaries will be individually detected [214–219], while the bulk of them will form a *Stochastic Gravitational Wave Background*, as they are too faint/distant and/or because they produce long-lived overlapping time-domain signals. The characterization of both resolved and unresolved SOBBH sources is compelling since they are a source of confusion for other detectable sources in the LISA band. For example, the SOBBH SGWB contribution will act as a foreground for the detection of a possible signal of cosmological origin [220], see *e.g.* refs. [221–224] for prospects about the detectability of a cosmological SGWB in the presence of an SGWB of astrophysical origin.

Previous papers have estimated the expected level of the SOBBH background. This can be achieved via direct extrapolation of the LVK observed merger rate, supplemented by a simple modelling of the black-hole (BH) population and of the time delay between the binary formation and the merger taken from refs. [225–227], as done *e.g.* in refs. [214, 221, 228, 229]. In particular, refs. [221, 229] use the LVK observed event rate from the *Gravitational Wave Transient Catalog 2 (GWTC-2)* [230]. Alternatively, one can input more refined scenarios of BH formation from the evolution of different populations of stars, accounting for the cosmic chemical evolution, optical depth to reionisation, and metallicity of the interstellar medium, to evaluate the mass distribution of merging SOBBH and in turn the expected SGWB, as done *e.g.* in refs. [57, 231–235]. An estimate of the number of resolvable SOBBH in LISA using the GWTC-2 rate has been done *e.g.* in ref. [217].

In this paper, we employ several methods to estimate the SGWB in the LISA band, using the most recent population constraints from the *Gravitational Wave Transient Catalog 3 (GWTC-3)* [45]. We evaluate the impact, on the SGWB amplitude, of the observational uncertainty on the population parameters, taken from the posterior parameter sample of GWTC-3: we find that the SGWB amplitude can vary by as much as a factor of five. When considered independently, we show that the parameter whose marginalised 2σ error influences the most the SGWB level is the power-law index of the redshift dependence of the merger rate. We also assess LISA's capability to detect and characterise the predicted SOBBH SGWB via a Monte Carlo (MC) analysis of simulated data, including the SGWB, the galactic binary (GB) foreground component, and the instrumental noise. The maximal marginalised error on the SGWB amplitude by LISA is $\sim 5\%$, *i.e.* much smaller than the variation due to the present (GWTC-3)

observational uncertainty on the population parameters: this hints to the conclusion that LISA will have a role to play in constraining SOBBH population parameters via the SGWB measurement. Though future Earth-based GW detectors observations will improve on the GWTC-3 constraints by the time LISA flies, we expect that LISA will maintain an impactful constraining power, since the SGWB amplitude in the LISA band is influenced by the high-redshift behaviour of the merger rate, complementary to what will be accessible to ground-based detectors in the near future.

The paper is organised as follows. In sec. {4.2} we describe the population model that we use, and the assumptions we consider, to construct the SOBBH catalogues. In particular, we disregard eccentricity in the waveform, as well as any redshift dependence of the population parameters, and we adopt a uniform distribution for the time-to-coalescence in the detector frame (see sec. {4.2.1}). Faint and distant SOBBH contribute to the SGWB signal: we, therefore, need to complete the GWTC-3 merger rate, limited to low redshift, with a model for the star formation and evolution at higher redshift. As explained in sec. {4.2.2}, we assume that the merger rate tracks the cosmic star formation rate up to high redshift [130]. We evaluate the impact of a time-delay between the binary star formation and the BBH merger on the SGWB amplitude in sec. {4.4.2}. In sec. {4.2.3} we describe the other population parameters: for the mass distribution we adopt the Power Law + Peak model, and for the spin amplitudes a positive-exponents Beta distribution [230]; as for the remaining parameters, some of them are randomly generated (*i.e.* time-to-coalescence, initial phase, position in the sky, inclination, and polarization), whereas others are derived analytically (*e.g.* the initial frequency of the generated events, their distance...). We have also produced ten SOBBH catalogues at a benchmark fixed point in the population parameter space, that we use for consistency studies; their characteristics are presented in sec. {4.2.4}.

In sec. {4.3} we present the four methods we have used to compute the expected SOBBH background signal. In order of sophistication: (i) the first procedure is based on an analytic evaluation of the characteristic strain as an integral over the number density of inspirals, as first proposed by ref. [236] (sec. {4.3.1}); (ii) we then substitute the integral over the number density by an MC sum over a realisation of a population, (iia) first as a time-to-coalescence-averaged sum, (iib) and then taking into account the time-to-coalescence of individual events and binning them according to their corresponding emission frequencies (see sec. {4.3.2}); (iii) finally, in order to account for the actual detection process of the SOBBHs by LISA, we apply the iterative-subtraction method developed in ref. [237], for which at each step we compare the signal-to-noise ratio (SNR) of each source i (ρ_i) to an SNR threshold (ρ_0), and if $\rho_i > \rho_0$, the source is classified as resolvable and is subtracted from the data. The iterative subtraction is performed on realistic LISA data-streams produced by injecting the time domain, spinning wave-form signals of the events, one by one. The latter procedure, despite being computationally expensive, yields a very accurate representation of the LISA data and allows for the evaluation of both the residual SGWB level and the subtracted sources (which we analyse in a companion paper [238]).

In sec. {4.4} we present our results. We first check that the four methods give comparable SGWB levels (see sec. {4.4.1}): since the number of subtracted sources is small [233, 238], there is overall very good agreement. Method (i), *i.e.* the analytic integration of the background, while not capturing some detailed features of the signal, can safely be used to estimate the expected SGWB in the LISA band, for all points in the posterior parameter sample of the fiducial FIDLVK model: the results are given in sec. {4.4.2}. In sec. {4.4.3} we present the results of the MC analysis of simulated LISA data including the SOBBH SGWB, the galactic binary foreground, and the instrumental noise. We show that, also in presence of the GB foreground, with four years of data, LISA will be able to detect the SOBBH signal and reconstruct its amplitude and spectral index. Then, accounting for the estimated SOBBH signal and the GB foreground as extra noise contributions, in sec. {4.4.4} we build the LISA power-law sensitivity (PLS) [221, 239–241]. Finally, in sec. {4.4.5}, we analyse how the precise measurement of the SOBBH SGWB by LISA would impact the inference on population parameters, as put forward in refs. [242, 243]. We find that the effect is most promising for the merger rate parameters, *i.e.* amplitude, and power-law index. We conclude in sec. {4.5}.

4.2 SOBBH population model and use of GWTC-3 results

4.2.1 SOBBH population model

LISA is sensitive to the GW emission by SOBBHs in the inspiral phase. Within the timescale of the mission, which we assume of 4 years (*i.e.* 4.5 years with 89% duty cycle), the GW frequency emitted by most SOBBHs will slowly increase within the LISA frequency band, $f \in [10^{-4}, 0.1]\,\mathrm{Hz}$. A minority of SOBBHs will chirp (*i.e.* their GW emission will rapidly increase in frequency) and move throughout the band. Among the chirping SOBBHs, a fraction will be close to coalescence, so that the frequency of their GW emission will exit the LISA band and, shortly after, enter the ground-based detectors band, where they will merge. This opens up the possibility of multi-band observations and/or of archival analyses (*e.g.* refs. [214, 244–246]). On the other hand, no SOBBH entering the LISA band during the lifetime of the mission is statistically expected, as SOBBH with frequencies of the order of 10^{-4} Hz are practically monochromatic during the lifetime of the experiment.[1]

We aim at estimating the SGWB due to unresolved SOBBHs in LISA, accounting for the most recent population constraints from GWTC-3 [45]. For this aim, we generate catalogues of SOBBHs emitting in the LISA band, making some simplifying

[1] To give an example, by integrating the Newtonian relation $\mathrm{d}f_{\rm GW}/\mathrm{d}t = 96/5\,\pi^{8/3}(G\mathcal{M}/c^3)^{5/3} f_{\rm GW}^{11/3}$ one obtains that it takes about 10^8 years to shift the GW emission of an SOBBH with chirp mass $\mathcal{M} = 50 M_\odot$ from $2\cdot 10^{-5}$ Hz to 10^{-4} Hz, where it will still be about 10^6 years away from the merger; while the same binary will shift from 0.1 Hz to 1 Hz (where it will be about 16 minutes away from the merger) in about 5 days.

assumptions.

First of all, for simplicity, we neglect eccentricity in our analysis. LVK measurements poorly constrain the SOBBH eccentricities, but the eccentricity in the LISA band could be significant depending on the binary formation [247, 248]. In addition, we neglect a possible dependence on redshift of the population parameters, since there are no strong constraints on how the SOBBH parameter distributions should vary with redshift, and state-of-the-art studies based on observations have not found conclusive evidence on the presence of any redshift dependence [46, 243, 249] (this possibility has been explored *e.g.* in ref. [250]). Our methodology can incorporate a redshift dependence into the catalogue generation (albeit at a higher computational cost), if this will be constrained by future data.

Furthermore, we assume that the residual time to coalescence τ_c (*i.e.* the amount of time that an observer in the source frame must wait in order to see the binary merge) is statistically uniformly distributed across the SOBBH population. This amounts to assuming that the formation, and therefore the coalescence rates, are in a steady state. Indeed, any change in the demographics of the binaries happens on a cosmic time-scale of $\mathcal{O}(10^9)\,\mathrm{yrs}$, *i.e.* much longer than the LISA observation time, which is the typical time over which our catalogues are representative. Furthermore, the maximal τ_c that we consider in this analysis (c.f. sec. {4.2.3}) is $\tau_{c,\mathrm{max}}^{(\mathrm{det})} \sim \mathcal{O}(10^4)\,\mathrm{yrs}$ in the detector frame, also much smaller than the timescale over which the cosmic coalescence rate varies. We also neglect the possibility that the SOBBHs form on such a tight orbit that their GW emission at formation is already within the LISA band; this would indeed also break the uniform distribution hypothesis for τ_c.

The above assumptions allow us to model the SOBBH population as follows. We consider the binaries emitting in the LISA band and observed by the detector at a given instant t, *i.e.* the time at which LISA switches on. Note that for the sake of the argument, we take this time in the source frame. Among the intrinsic parameters (masses, spins, phase, polarisation...) and extrinsic ones (sky position, inclination...) of each SOBBH, we single out the time-to-coalescence $\tau_c = t_c - t$ in the source frame (where t_c denotes the time of coalescence of a given SOBBH) and the redshift of the source z, while $\vec{\xi}$ represents the remaining parameters. The population model parameterized in terms of some hyper-parameters $\vec{\theta}$ provides the statistical distributions $p(\vec{\xi}|\vec{\theta})$ of $\vec{\xi}$ (for simplicity we omit the vector symbol on ξ and θ from now on). The number of SOBBHs with given z, τ_c, ξ, whose signals reach the interferometer at time t, is

$$\frac{\mathrm{d}^3 N(z,\tau_c,\xi,\theta)}{\mathrm{d}\xi \mathrm{d}z \mathrm{d}\tau_c} = R(z,\tau_c)\left[\frac{\mathrm{d}V_c}{\mathrm{d}z}(z)\right] p(\xi|\theta)\,, \tag{4.2.1}$$

where V_c is the universe's comoving volume,[2] and

$$R(z, \tau_c) \equiv \frac{\mathrm{d}^2 N}{\mathrm{d}V_c \, \mathrm{d}\tau_c} \,. \tag{4.2.2}$$

Within our assumptions, all values of τ_c are equiprobable at any z: the rate density satisfies therefore $R(z, \tau_c) = R(z, \tau_c = 0)$, *i.e.* the one of *merging* SOBBHs. Moreover, in our population, the number of SOBBHs with given z and ξ that are received by the interferometer at the times t and $t + dt$, are precisely $N(z, \tau_c = 0, \xi)$ and $N(z, \tau_c = 0 + dt, \xi)$, so one can equivalently interchange $d\tau_c \leftrightarrow dt$ in eq. (4.2.2). All together, it follows $R(z, \tau_c) = \mathrm{d}^2 N(z, \tau_c = 0, \xi, \theta)/(\mathrm{d}V_c \, \mathrm{d}t)$, which is precisely the merger rate density in the form that LVK is constraining [46]. Hereafter, we drop the τ_c dependence in $R(z, \tau_c)$ as irrelevant.

Given our assumption that the merger rate $R(z)$ is in a steady state, we can readily apply LVK findings to it. In the next section, we explain how we use eq. (4.2.1) to generate SOBBH catalogues compatible with the latest population constraints from LVK GWTC-3. However, the merger-events-based LVK constraints on $R(z)$ are limited to small redshift, while we need to model sources also at high redshift, since they have a significant contribution to the SGWB. In order to simulate the high-redshift part of the SOBBH population, we therefore need to incorporate knowledge of the star formation and evolution at high redshift, as we will see below.

4.2.2 Implementing GWTC-3 posterior for the SOBBH population parameters

The SOBBH population model is determined by the merger rate $R(z)$ and the distribution function $p(\xi|\theta)$ in eq. (4.2.1). In ref. [46], the LVK collaboration has analysed a series of population models and produced inference on their parameters, finding that the most promising one to explain the SOBBH events gathered in GWTC-3 [45] is characterised by (a) a power-law dependence of the merger rate with redshift, $R(z) = R(0)(1 + z)^\kappa$; (b) a population mass model, known as Power Law + Peak mass model, combining an inverse power-law dependence on the largest BH mass, with a Gaussian peak at approximately 30–40 $M_\odot$, and a power-law distribution for the mass ratio of the binary; (c) a population spin model in which the amplitudes are independent and follow positive-exponent Beta distributions favouring intermediate-valued spins, and whose tilt distribution is a mixture of an isotropic distribution and a truncated Gaussian. The distributions for masses and spins are explained in more detail in app. {4.6.2}.

For the sake of convenience, we will call this combination FidLVK, and we will use it as the fiducial model in our analysis. We provide population-averaged predictions of the SGWB, based on the publicly-available population parameter posterior

[2] The redshift derivative of the comoving volume in eq. (4.2.1) accounts for the fact that spherical shells further from us enclose increasing amounts of volume and thus larger numbers of events for a given $R(z)$.

distribution [251] for the FIDLVK model conditioned to the SOBBH of GWTC-3 [46] (excluding low-mass-secondary GW190814 and likely-NSBHB GW190917, as per the fiducial approach by LVK). The parameters θ of the mass and spin distribution $p(\xi|\theta)$ are imported directly from the LVK results. On the other hand, the parameters of the merger rate $R(z)$ require a different treatment. Because of the interferometers frequency band, LVK probe the SOBBH population only at relatively low redshift, so the redshift dependence of the merger rate in LVK analyses is modelled as a power-law. Indeed, the GWTC-3 inferred merger rate posterior constrains the pivot rate $R(0)$ and the power-law exponent κ only for $z \lesssim 0.5$ [46]. In order to produce, from this posterior, SOBBH SGWB estimates valid in the LISA band, we need to extend the merger rate model towards higher redshift, since high redshift SOBBHs contribute significantly to the background.

For this purpose, we adopt a phenomenological approach and assume that the merger rate tracks the *Madau-Fragos SFR* [130], neglecting the presence of a time delay between the binary formation and merger. While in sec. {4.4.2} we discuss the impact on the SGWB amplitude of including time delays, in the rest of the paper we parameterize the merger rate as

$$R(z) = R_0 C \frac{(1+z)^\kappa}{1 + \frac{\kappa}{r}\left(\frac{1+z}{1+z_{\rm peak}}\right)^{\kappa+r}}\,, \tag{4.2.3}$$

where C ensures $R_0 \equiv R(z=0)$. The analysis of ref. [130] finds the following best fit values for the SFR parameters: $\kappa = 2.6$, $r = 3.6$ and $z_{\rm peak} = 2.04$ (note the difference in the definition of $z_{\rm peak}$ with respect to ref. [243]). At redshift $z \lesssim 1$, this behaves similarly to the $R(z) = R_0(1+z)^\kappa$ power law constrained by LVK, which finds a best fit $\kappa \approx 2.7$. Motivated by this agreement, we incorporate the LVK GWTC-3 posterior into eq. (4.6.1) by matching R_0 and κ for each point in the population parameter sample with the fixed fiducial values $r = 3.6$ and $z_{\rm peak} = 2.04$ from ref. [130]. The resulting posterior for the merger rate is by construction fully compatible with that of the low-redshift merger rate of LVK (see app. {4.6.1} for further discussion and in particular fig. 4.14).[3]

Finally, in order to keep consistency with LVK [46], we adopt the ΛCDM cosmological model with parameters fixed accordingly to the "Planck 2015 + external" data combination [252].[4] These correspond to $H_0 = h \times 100\,\mathrm{km/(s\,Mpc)}$, with $h = 0.678$

[3] In ref. [243], the LVK Collaboration also considers a similar high-redshift extension and finds mild constraints on r and $z_{\rm peak}$ (using a different definition of the latter, see app. {4.6.1}) by combining the population parameters inferred from GWTC-2 resolved mergers with the upper limits imposed by the non-detection of the SGWB. We verify a posteriori the compatibility of our results with the upper limits on the SGWB amplitude presented in ref. [243].

[4] Note that the ΛCDM parameter values used in ref. [46] correspond to the incomplete Planck 2015 data combination PLIKHM_TE (high-ℓ T×E spectrum data only) instead of the fiducial PLIKHM_TTTEEE+LOWTEB, which includes temperature-only and polarized data for the whole Planck multipole range. The difference is anyway negligible for the purposes of this paper.

being its dimensionless value, for the local Hubble rate, and $\Omega_m \approx 0.3$ and $\Omega_\Lambda \approx 0.7$ for the matter and cosmological-constant energy densities. The cosmological model enters in the differential comoving volume per unit redshift, $\mathrm{d}V_c(z)/\mathrm{d}z$, of eq. (4.2.1), and in the computation of the cosmological distances needed for the integration in sec. {4.3}.

4.2.3 SOBBH population synthesis

In sec. {4.3} we propose four different methods to compute the SGWB due to unresolved SOBBHs. The first method consists of an integration of the number density in eq. (4.2.1) [236]. The other three are based on the superposition of the GW signals from SOBBHs populations, with different levels of sophistication. The latter methods provide a more refined evaluation of the SGWB and of its spectral shape and are also important to assess the size of statistical effects (*e.g.* the uncertainty due to the population realisation) and the consequences of other choices inherent to the catalogue simulation, such as the value of the maximal time-to-coalescence $\tau_{c,\mathrm{max}}^{(\mathrm{det})}$, see below.

We thus need fast and reliable SOBBH population synthesis. We have written two independent population synthesis codes, which can be found in the following repositories: [253] and [254]. These have been also compared with ref. [25]. In these implementations, the masses and spins are drawn from the LVK GWTC-3 distributions, briefly revised in app. {4.6.2}.

The redshift of the binaries is generated independently as an inhomogeneous Poisson point process, according to the z-dependent terms in eq. (4.2.1), between $z_{\mathrm{min}} = 10^{-5}$ ($\approx 45\,\mathrm{kpc}$ of comoving distance, in order to exclude binaries within the Milky Way), and $z_{\mathrm{max}} = 5$, which is sufficient for an accurate SGWB computation, as we demonstrate in sec. {4.3.1}. Note that we will limit $z_{\mathrm{max}} = 1$ in the analyses based on catalogues whenever using a larger z_{max} would prove too costly from the computational point of view, c.f. sec. {4.3.3}.

The rest of the individual SOBBH parameters are generated from the priors presented in table [4.1], based on physical considerations: isotropy for the sky position, inclination, and polarization; and uniform time-to-coalescence in the detector frame, as discussed in sec. {4.2.1}. From the randomly-sampled parameters, we compute the derived quantities necessary for the problem at hand, such as the frequency at the start of the LISA runtime, the LISA in-band time, cosmological distances, and so on.

The upper limit for the population synthesis time-to-coalescence $\tau_{c,\mathrm{max}}^{(\mathrm{det})}$ needs to be high enough to give a faithful representation of the SOBBH SGWB signal in the LISA band (at least where it is the dominant contribution to the astrophysical-origin SGWBs), and at the same time it is conditioned by computational limitations. As discussed in app. {4.6.3}, $\tau_{c,\mathrm{max}}^{(\mathrm{det})} = 10^4\,\mathrm{yrs}$ provides a good balance between these requirements.

Parameter	Prior
Time-to-coalescence (source frame)	$U[0, \tau_{c,\max}^{(\mathrm{det})}/(1+z)]$ yrs
Ecliptic Longitude	$U[0, 2\pi]$ rad
Ecliptic Latitude	$\arcsin\left(U[-1,1]\right)$ rad
Inclination	$\arccos\left(U[-1,1]\right)$ rad
Polarization	$U[0, 2\pi]$ rad
Initial Phase	$U[0, 2\pi]$ rad

Table 4.1. Priors for the parameters of individual SOBBHs. The uniform prior for the time-to-coalescence, which is source-dependent, is justified in sec. {4.2.1}. The priors on the ecliptic coordinates and the inclination impose statistical isotropy in the positions and orientation of the binaries.

4.2.4 Benchmark fixed-point catalogues for consistency studies

In addition to probabilistic GWTC-3-posterior forecasts, we also single out a fixed point in the population parameter space, which we use as a benchmark to compare different SGWB computation methods and assess the size of statistical and numerical effects. For this fixed point, we use values close to the median of the GWTC-3 FIDLVK model posterior, indicated in table [4.2], with an important modification.

Rate of events $R(z)$	Mass distribution	Spin distribution
$R_{0.2} = 28.1\,\mathrm{Gpc}^{-3}\mathrm{yrs}^{-1}$	$[m_{\min}, m_{\max}] \in [2.5, 100]\,M_\odot$	$\mathrm{E}[a] = 0.25$
$\kappa = 2.7$	$\delta_{\min} = 7.8\,M_\odot$	$\mathrm{Var}[a] = 0.03$
$z_{\mathrm{peak}} = 2.04$	$\alpha = 3.4$	$\zeta = 0.66$
$r = 3.6$	$\lambda_{\mathrm{peak}} = 0.039$	$\sigma_t = 1.5$
	$\mu_m = 34\,M_\odot$	
	$\sigma_m = 5.1\,M_\odot$	
	$\beta_q = 1.1$	

Table 4.2. Population parameter values for the benchmark fixed-point. The other parameters in the population are set to their GWTC-3 posterior median values, given in apps. {4.6.1} and {4.6.2}. The mass range and mass smoothing parameter $\delta_{\min}$ have been modified to accommodate for the possibility of more extreme events in future data.

The determination of the mass range population parameters $m_{\min}$ and $m_{\max}$ in the LVK study [46] is sensitive to whether certain events from GWTC-3 (the extreme mass ratio binary GW190814 and the likely-NSBHB binary GW190917) are considered as outliers and excluded from the analysis. The inclusion of GW190814 suffices to push the lower mass bound down to $m_{\min} \approx 2.5\,M_\odot$.

Motivated by the possibility that such outliers may appear in future data, we enlarge the mass range for the benchmark fixed-point catalogues to $[2.5, 100]\,M_\odot$, also raising the upper bound up to the original prior boundary of the $m_{\max}$ population parameter, previous to GTWC-3 constraints. The modification in particular of the lower

mass boundary necessitates a further increase in the width of the low-mass smoothing function (see app. {4.6.2}), in order not to deviate strongly from the mean GWTC-3 mass probability density at masses $m \gg m_{\rm min}$. This is achieved by increasing the value of the $\delta_{\rm min}$ population parameter (nevertheless, we have found that the SGWB calculation is not very sensitive to this choice).

Though this fixed point in the population parameter space does not pertain to the GWTC-3 posterior, due to the modifications to the mass distribution, it leads to an SGWB in the LISA band which is compatible with our posterior-based evaluations. It is therefore useful as a benchmark to gauge the sensitivity of the SGWB predictions to different assumptions on the population model.

We have generated a sample of 10 catalogues with parameters set to this benchmark fixed-point. Since they will be used only to compare and validate population-based SGWB computation methods, we have limited their redshift range to $z_{\rm max} = 1$, to reduce computational cost. As stated before, we limit the time-to-coalescence in these catalogues to $\tau_{c,\rm max}^{(\rm det)} = 10^4\,$yrs. For the purposes of testing the sensitivity to different $\tau_{c,\rm max}^{(\rm det)}$ values (see sec. {4.3.3}), we have generated one catalogue with $\tau_{c,\rm max}^{(\rm det)} = 1.5 \times 10^4\,$yrs, and from it we have produced two sub-catalogues with $\tau_{c,\rm max}^{(\rm det)} = 1.0 \times 10^4$ and $5 \times 10^3\,$yrs. Setting $\tau_{c,\rm max}^{(\rm det)} = 10^4\,$yrs produces approximately 60 million binaries with inspiralling frequency within the LISA band. The number of events scales linearly with $\tau_{c,\rm max}^{(\rm det)}$.

4.3 Computation of the SOBBH signal in the LISA band

We adopt four different methods to evaluate the SOBBH SGWB which allow us, by their different nature, to capture different features of the signal. In the following sections, we describe them.

4.3.1 Method (i): analytical evaluation

In this section we provide a brief description of the formalism employed for the analytic evaluation of the SOBBH SGWB, following ref. [236]. The normalised SGWB energy density spectrum per logarithmic unit of frequency $\Omega_{\rm GW}(f)$ can be defined from the total GW energy density present in the Universe and emitted by the whole SOBBH population, expressed in the detector frame. Recalling eq. (4.2.1) this reads

$$\frac{\rho_{\rm GW}^{(\rm tot)}}{\rho_c} = \int_0^\infty \frac{{\rm d}f}{f}\,\Omega_{\rm GW}(f) = \int {\rm d}\xi \int {\rm d}V_c \int {\rm d}\tau_c \,\frac{{\rm d}^3 N(z,\tau_c,\xi,\theta)}{{\rm d}\xi {\rm d}V_c {\rm d}\tau_c}\,\frac{\rho_{\rm GW}^{(\rm event)}}{\rho_c}\,, \tag{4.3.1}$$

where $\rho_c = 3H_0^2 c^2/(8\pi G)$ is the Universe's critical energy density and $\rho_{\rm GW}^{(\rm event)} = t^{00}$ denotes the energy density associated to a single SOBBH event, at the detector. Using

ref. [31], one can derive

$$\frac{\rho_{\rm GW}^{\rm (event)}}{\rho_c} = \frac{c^2}{16\pi G\rho_c}\frac{\langle \dot{h}_+^2 + \dot{h}_\times^2\rangle}{(1+z)^4} = \\ = \frac{c^2}{16\pi G\rho_c(1+z)^4}\frac{32\pi^2}{a^2r^2}\Big(\frac{\pi}{c}\Big)^{4/3}\Big(\frac{G\mathcal{M}}{c^2}\Big)^{10/3} f_s(\tau_c)^{10/3}\Big[\Big(\frac{1+\cos^2\iota}{2}\Big)^2 + \cos^2\iota\Big]\,, \tag{4.3.2}$$

where all quantities are at the source: $\mathcal{M}$ is the SOBBH chirp mass, $a\cdot r$ its physical distance in the local wave zone, ι its orientation with respect to the detector, and $\omega_s = \pi f_s$ its orbital frequency. The second equality in eq. (4.3.2) has been obtained under the approximation of quasi circular motion for the binary $\dot{f}_s \ll f_s^2$, and we have averaged over the waveform phase. Substituting eq. (4.3.2) in eq. (4.3.1), expressing the differential comoving volume as $\mathrm{d}V_c = c\,d_M^2/H(z)\mathrm{d}\hat{\Omega}\mathrm{d}z$ where $d_M = a_0 r$ is the proper distance, $H(z) = H_0\sqrt{\Omega_m(1+z)^3+\Omega_\Lambda}$, and $\hat{\Omega}$ is the solid angle [255], and noting that $a^2r^2 = d_M^2/(1+z)^2$, one gets, after integration over the solid angle (giving a factor $16\pi/5$),

$$\frac{\rho_{\rm GW}^{\rm (tot)}}{\rho_c} = \frac{32}{5}\pi^{10/3}\frac{c^{5/3}}{G\,\rho_c}\int \mathrm{d}\xi \int \mathrm{d}z \int \mathrm{d}\tau_c \Big(\frac{G\mathcal{M}}{c^2}\Big)^{10/3}\frac{R(z)p(\xi|\theta)}{H(z)(1+z)^2} f_s(\tau_c)^{10/3}\,, \tag{4.3.3}$$

where we have also used definition eq. (4.2.1). One can change the integration variable from τ_c to f_s using the relation $\mathrm{d}f_s/\mathrm{d}\tau_c = 96/5\,\pi^{8/3}(G\mathcal{M}/c^3)^{5/3} f_s^{11/3}$, valid for quasi-circular binaries in the Newtonian approximation, then change to the frequency at the detector $f = f_s/(1+z)$, and equate the integrands in eq. (4.3.1), to obtain the SGWB energy density power spectrum:

$$\Omega_{\rm GW}(f) = \frac{8}{9}\pi^{5/3} f^{2/3}\int \mathrm{d}\xi \int \mathrm{d}z \frac{(G\mathcal{M})^{5/3}}{c^2 H_0^2}\frac{R(z)p(\xi|\theta)}{H(z)(1+z)^{4/3}}\,. \tag{4.3.4}$$

Among the set of binary parameters ξ, only the chirp mass is relevant within the Newtonian approximation. One can therefore express the SOBBH SGWB today as

$$h^2\Omega_{\rm GW}(f) = h^2\Omega_{\rm GW}(f_*)\left(\frac{f}{f_*}\right)^{2/3}\,, \tag{4.3.5}$$

with f_* an arbitrary pivot frequency, and

$$h^2\Omega_{\rm GW}(f_*) = \frac{(GM_\odot)^{5/3}}{c^2}\int \mathrm{d}m_1\mathrm{d}m_2\, p\,(m_1,m_2)\,(\mathcal{M}(m_1,m_2)[M_\odot])^{5/3} \\ \times \int_0^{z_{\rm max}} \mathrm{d}z\,\frac{R\,(z)}{(1+z)^{4/3}H(z)}\frac{f_*^{2/3}}{(1.32413\times10^{-18}\,\mathrm{Hz})^2}\,, \tag{4.3.6}$$

where we have used $(H_0/h)/\sqrt{8\pi^{5/3}/9} = 1.32413\times10^{-18}$ Hz. For the numerical evaluation of eq. (4.3.6), we have set $GM_\odot = 1.327\times10^{20}$ m^3/s^2 and $c = 2.9979246\times10^8$ m/s.

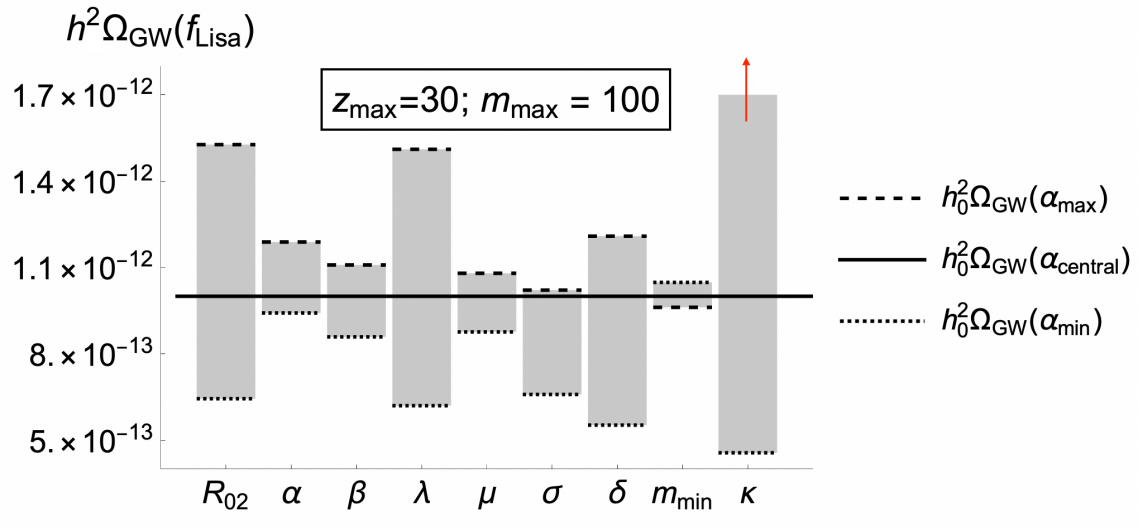

Figure 4.1. Amplitude $h^2\Omega_{\rm GW}(f_*)$ of the SOBBH SGWB at the pivot frequency $f_* = f_{\rm LISA} \equiv 0.003$ Hz, varying each parameter of the FIDLVK population model within the 5–95 percentile range of the GWTC-3 posterior, while maintaining all other parameters fixed to their central values. Dotted (dashed) lines represent the value of $h^2\Omega_{\rm GW}(f_*)$ evaluated at the 5 (95) percentile for a given parameter, whereas the horizontal solid line represents the amplitude of the signal when all parameters are fixed to the values in table [4.2]. The red arrow in κ indicates that the amplitude of the signal for $\kappa_{\rm max}$ ($h^2\Omega_{\rm GW}(f_*) \simeq 2.8\times10^{-12}$) is beyond the range of the plot. The signal amplitude grows with decreasing $m_{\rm min}$, contrary to all other parameters.

In fig. 4.1 we plot the amplitude of the expected background at the reference frequency $f_* = 0.003\,$Hz, close to LISA's peak sensitivity [256], evaluated from the integral in eq. (4.3.6). For the merger rate $R(z)$, we adopt the phenomenological parameterization described in sec. {4.2.2}. While in fig. 4.1 we consider $z_{\rm max} = 30$, as we do not expect active sources at higher redshifts, in fig. 4.2, in contrast, we analyse the relative difference of considering smaller values for $z_{\rm max}$. The only other population parameters that enter the analytic evaluation are the masses m_1, m_2 of the two compact objects, expressed in terms of the chirp mass: as previously stated, for their probability distribution $p\,(m_1, m_2)$, we adopt the POWER LAW + PEAK model. Naturally, the amplitude of the background depends on the choice of the parameters in $R(z)$ and $p(m_1, m_2)$: respectively, $(R_{02} \equiv R(z = 0.2), \kappa)$, and $(\alpha, \delta_{\rm min}, m_{\rm min}, m_{\rm max}, \lambda_{\rm peak}, \mu, \sigma, \beta)$, defined in apps. {4.6.1} and {4.6.2}. Following sec. {4.2.4}, we plot as a horizontal solid line the SGWB amplitude for the values indicated in table [4.2] for each of the population parameters ; we also show the range of SGWB amplitudes (grey bars) obtained when each of the parameters is varied within its 5–95 percentile range according to the GWTC-3 posterior (see apps. {4.6.1} and {4.6.2}), while the rest of the parameters stay fixed to their values of table [4.2]. This shows how the differ-

ent parameters in the model influence the SGWB amplitude when varied individually. Larger ranges for the SGWB amplitude translate into stronger constraining power from the measurement of the individual parameter; however, since this approach neglects degeneracies, large ranges for multiple parameters do not mean that these can be simultaneously constrained (the issue of SGWB-derived population parameter constraints will be further discussed in sec. {4.4.5}). Note that the signal amplitude grows with decreasing $m_{\rm min}$, contrary to its response to all other parameters. The population parameter with the largest impact on the SGWB amplitude is the power-law index of the merger rate κ, since its value controls the merger rate growth at intermediate redshift $1 < z < z_{\rm peak}$, which strongly influences the outcome of the redshift integration in eq. (4.3.6). The red arrow in fig. 4.1 indicates that the SGWB amplitude obtained for $\kappa_{\rm max}$, $h^2\Omega_{\rm GW}(f_*) \simeq 2.8 \times 10^{-12}$, is beyond the range of the plot.

In fig. 4.2 we plot the relative percentage change of the SGWB amplitude when varying $z_{\rm max}$ in eq. (4.3.6). Since the merger rate in eq. (4.6.1) decays at high redshift, the SGWB grows asymptotically towards a constant amplitude as we integrate over larger and larger redshift ranges. Taking $z_{\rm max} = 30$ as a reference, we plot $\Delta\Omega_{\rm GW}[\%] \equiv 100 \times (1 - \Omega_{\rm GW}(f_*)|_{z_{\rm max}}/\Omega_{\rm GW}(f_*)|_{z_{\rm max}=30})$ for different values of $z_{\rm max}$. The figure indicates that integrating up to $z_{\rm max} = 5$ already allows to obtain $\sim 1\%$ accuracy in the calculation of the SGWB amplitude. This is sufficient for the scope of this paper given that, as presented in sec. {4.4.3}, the typical error on the SGWB measurement by LISA is larger than that. The SGWB amplitude in fig. 4.2 has been evaluated adopting the parameter values corresponding to the benchmark fixed-point described in sec. {4.2.4}; the convergence trend is very similar when using the minimum or maximum values of a given parameter, keeping the others fixed to their central values.

4.3.2 Methods (iia) and (iib): Monte Carlo sum

An alternative method to compute the SGWB is to sum the GW signals, emitted by individual SOBBHs, over a realisation of the population drawn from the distribution represented by the number density. The simplest implementation consists in factoring out from eq. (4.3.4) the population number density of eq. (4.2.1), averaged over time-to-coalescence and sky-position, to obtain

$$\Omega_{\rm GW}(f) \approx \frac{2\pi^{2/3}}{9}\frac{G^{5/3}}{c^3 H_0^2}\frac{1}{\tau_{c,\rm max}^{(\rm det)}}\left(\sum_{i\in\rm pop}\frac{\mathcal{M}_i^{5/3}}{d_{M,i}^2(1+z_i)^{1/3}}\right) f^{2/3}\,, \tag{4.3.7}$$

where f is the observed frequency, and $\mathcal{M}_i$, z_i and $d_{M,i}$ are the chirp mass in the source frame, redshift and proper distance of the individual GW sources. The factor $1/\tau_{c,\rm max} = (1+z)/\tau_{c,\rm max}^{(\rm det)}$ comes from the time-averaging of the number density of eq. (4.2.1).

The SGWB amplitude resulting from the sum over a realisation of the SOBBH population is obviously realisation-dependent. We can assess its concordance, within

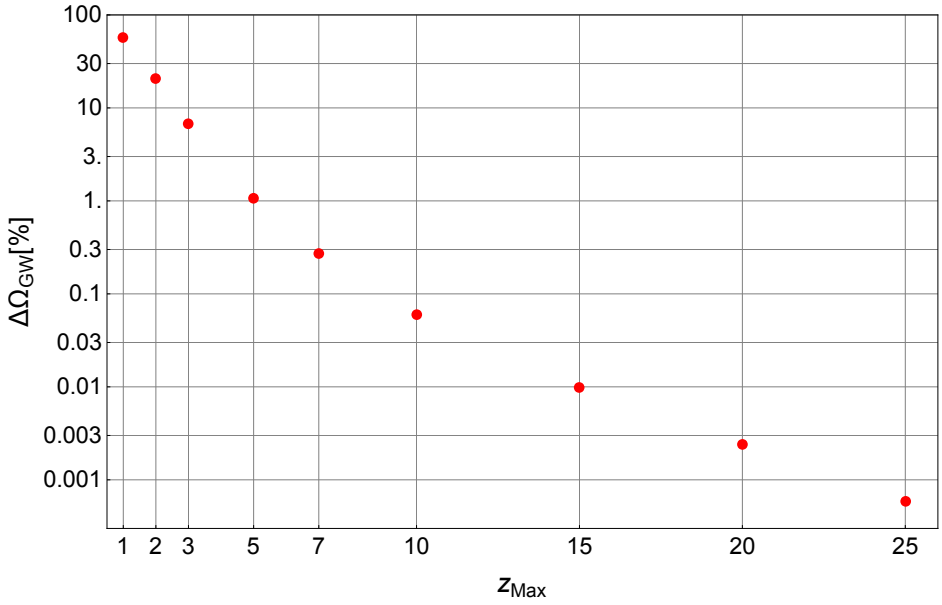

Figure 4.2. Relative percentage change of the signal amplitude $\Omega_{\rm GW}(f_*)$ evaluated at $f_* = 0.003\,\text{Hz}$ with respect to $\Omega_{\rm GW}(f_*)|_{z_{\rm max}=30}$, when varying $z_{\rm max}$ in eq. (4.3.6).

the variance due to the population draws, with the analytical computation of eq. (4.3.6) by evaluating eq. (4.3.7) for a large number of realisations. The result is shown in fig. 4.3, assuming population parameters fixed to the benchmark values described in sec. {4.2.4}, and setting $z_{\rm max} = 5$. The population variance in terms of the ratio of the interquartile range to the mean of the realisations' amplitudes amounts to 0.2% only.[5] The difference between the SGWB amplitude obtained by averaging the realisations, and the one obtained by the numerical integration of eq. (4.3.6), is much smaller than the population variance, highlighting the equivalence between the two methods. Furthermore, the population variance uncertainty is much smaller than both the expected integration error due to fixing $z_{\rm max} = 5$, and the forecasted precision of the LISA measurement (see sec. {4.4.3}).

A more refined approach to evaluating the SGWB can be obtained by summing the contribution of each SOBBH in the population, accounting for the actual frequency of emission of each source (while in eq. (4.3.7) only the chirp mass and the distance - equivalently redshift - pertain to the individual events). In order to do this, we rewrite the SGWB energy density starting from eq. (4.3.1), but re-expressing the number density as the number of events per unit of emission frequency f_s using the relation $\mathrm{d}f_s/\mathrm{d}\tau_c$ for quasi-circular Newtonian binaries, then changing the integration variable to the observed frequency, and equating the integrands in eq. (4.3.1) to single out the

[5] If one naively computes the realisation variance as that of the underlying Poisson point process (*i.e.* equal to the mean of the process, here the expected number of events), one would overestimate the realisation uncertainty by a very large factor since not all events contribute equally to the SGWB.

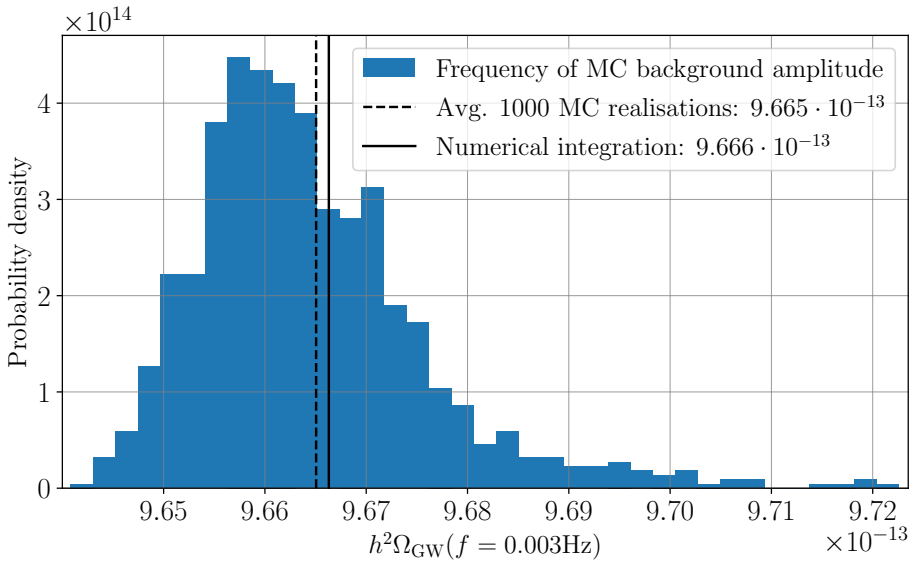

Figure 4.3. Comparison between the distribution of MC sums of eq. (4.3.7) over 1000 realisations sharing the same population parameters (see sec. {4.2.4}), and the numerical integration of eq. (4.3.6). The two methods are equivalent within the range of the population variance ($\sim 0.2\%$), which is in turn much smaller than the integration error due to the $z_{\max} = 5$ cut ($\sim 1\%$, see fig. 4.2). Such small effects will not be observable by LISA (see sec. {4.4.3}).

SGWB power spectrum:

$$\Omega_{\rm GW}(f) = \int \mathrm{d}\xi \int \mathrm{d}z \, \frac{\mathrm{d}^3 N(z,\xi,\theta)}{\mathrm{d}\xi \mathrm{d}z \, \mathrm{d}f} \, f \frac{1}{4\pi} \int \mathrm{d}\Omega \, \frac{\rho_{\rm GW}^{(\rm event)}}{\rho_c} \, . \tag{4.3.8}$$

We can now express the integral in the above equation as an MC sum, as done previously in eq. (4.3.7), but this time computing the sum of the GW energy density emitted by every SOBBH per (detector-frame) frequency bin, where the latter is defined using some frequency sampling δ_f as $[(j-1)\delta_f, j\delta_f]$, N_j being the subset of a population with emission frequencies (in detector frame) in bin j

$$\begin{aligned} \Omega_{\rm GW}(f) &\approx \frac{1}{\delta_f} \sum_{i \in N_j} f_i \frac{1}{4\pi} \int \mathrm{d}\Omega \, \frac{\rho_{\rm GW}^{(\rm event)}(z_i, \mathcal{M}_i, f_i)}{\rho_c} \\ &\approx \frac{64\pi^{10/3}}{15} \frac{G^{10/3}}{c^8 H_0^2} \frac{1}{\delta_f} \sum_{i \in N_j} \frac{(1+z_i)^{4/3}}{d_{M,i}^2} \mathcal{M}_i^{10/3} f_i^{13/3} \, , \end{aligned} \tag{4.3.9}$$

where the different powers of the per-source quantities with respect to eq. (4.3.7) can be explained by the frequency dependence of the number of sources in each bin.

This assumes monochromatic sources, ignoring frequency drifting during the life of the mission.[6] The largest contribution to the background is produced by sources with $f \in (10^{-3}, 10^{-2})$, whose frequency drifting is small; we can therefore choose *e.g.* the frequency with which they enter the LISA band (see sec. {4.6.3}). We will show the result of both MC integrations, eqs. (4.3.7) and (4.3.9), in sec. {4.4.1}.

4.3.3 Method (iii): iterative subtraction

The methods presented above are based on summing the signals of the SOBBH in the population, without accounting for the actual detection process, apart from restricting the maximal time-to-coalescence $\tau_{\rm c,max}^{\rm (det)}$ to a computationally manageable and detector-compatible value (for methods (iia) and (iib) of sec. {4.3.2}). However, we are ultimately interested in the SGWB signal in LISA, and the detector sensitivity can influence the SGWB spectral shape/amplitude. In order to consider such aspects, we also evaluate the SGWB following the methodology developed in ref. [237], using ideas first presented in refs. [258–260]. The procedure is based on generating LISA data-streams, by computing the waveform signals of all the events within the simulated population. Depending on the adopted waveform model, this can yield a very accurate representation of the LISA data, as far as SOBBHs are concerned. However, simulating millions of sources is computationally expensive, thus one has to allocate a considerable amount of computational resources to this task.

The procedure begins by fixing the mission duration $T_{\rm obs}$, here set to 4 years, and generating the signal to be measured by LISA. We compute the h_+ and $h_\times$ waveforms for each source of the simulated catalogue, and then we project them onto the LISA arms. We use the `IMRPhenomHM` model [261], which describes spinning, non-precessing binaries. It is based on the `IMRPhenomD` [262, 263] model, but it includes higher order modes. We use the `lisabeta` software [264, 265] for our computations. When generating each waveform, we also compute its SNR in isolation, $\rho_i^{\rm iso}$, with respect to the instrumental noise only, which will be used to reduce the computational requirements of the procedure, as explained below.

Next, we estimate the total power spectral density (PSD), $S_{\rm n,\,k}$, summing all the GW sources plus the instrumental noise. The index k refers to the iterative step. Since this PSD is very noisy, we compute its running median to produce a smoother version of it. We then evaluate the SNR ρ_i of each source i using the smoothed $S_{\rm n,\,k}$ as the total "noise" PSD. Note that, to speed up the computation, this is performed only on the subset of sources with sizable pre-computed SNR in isolation $\rho_i^{\rm iso}$ (see ref. [237]). The SNR ρ_i are then compared to a threshold SNR ρ_0: if $\rho_i > \rho_0$, the source is classified as resolvable, and is subtracted from the data. The smoothed residual PSD $S_{\rm n,\,k+1}$ is then re-evaluated after re-iterating through the catalogue of sources and subtracting the loud ones, and the procedure is repeated until the algorithm converges. Convergence is reached when all the sources are subtracted given the ρ_0 threshold, or

[6] We could easily extend this formula to account for drifting by summing each event over different bins with some weight proportional to the time spent emitting at the frequency of the bin [257].

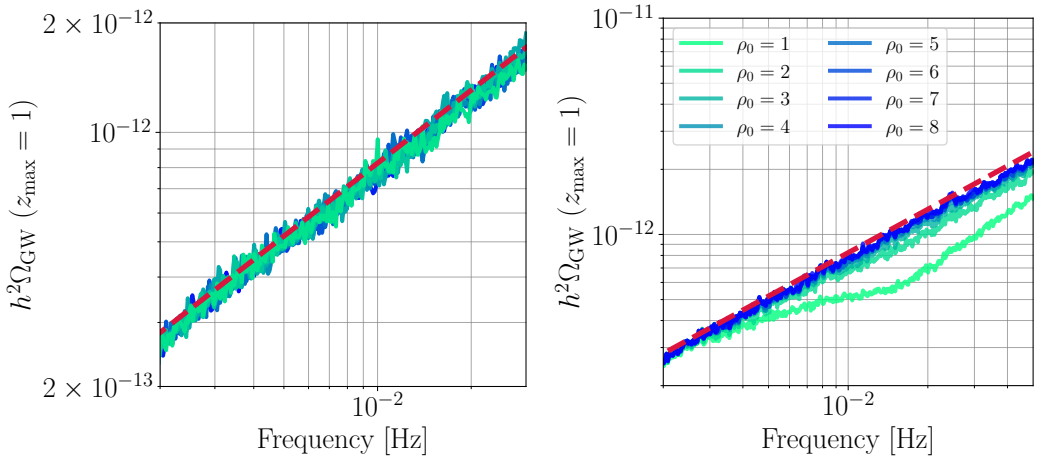

Figure 4.4. Left : Tests of the iterative-subtraction method: the SOBBH SGWB is shown in comparison with the analytical evaluation obtained integrating eq. (4.3.6) (red dashed line) for the benchmark population parameters described in sec. {4.2.4}, simulated, and integrated, up to $z_{\rm max} = 1$: the 10 realisations of the simulated population with equal parameters, set to the benchmark described in sec. {4.2.4}, yield the same level of stochastic signal; Right : the effect of different choices for the SNR threshold ρ_0 on the resulting stochastic signal: the smaller ρ_0, the more sources are classified as resolvable, generating a "dip" in the stochastic signal at high frequencies. The shape of this dip depends on both the astrophysical catalogue, and on the shape of the instrumental noise PSD.

if $S_{\rm n,\,k+1}$ and $S_{\rm n,\,k}$ are practically identical at all frequencies considered. At the end of the procedure, we compute the final SNR of the recovered sources, with respect to the final estimate of $S_{\rm n,\,k_{final}}$. Thus, as final products, we get both the SGWB due to the sources signal confusion, as well as the properties of the recovered sources (their number, waveform parameters, and final SNR).

Different realisations of the same population (with the same number density parameters) should yield different, though statistically compatible, sets of subtracted events, but a similar SGWB after smoothing. We have verified this statement by evaluating the SGWB from the 10 benchmark catalogues presented in sec. {4.2.4}; the result is shown in fig. 4.4.

The crucial parameter of the iterative method is ρ_0, the minimum SNR above which events are considered resolvable and thus subtracted from the total signal. We consider $\rho_0 = 8$ an appropriate choice [266, 267], assuming that stochastic methods to sample the sources parameter space, more efficient than grid-based methods [268], can be used to analyse the LISA data streams. Archival searches will allow to further reduce the SNR threshold down to $\rho_0 = 5$ [246, 267]. As can be appreciated from fig. 4.4, as long as $\rho_0 \gtrsim 5$, the number of detectable sources is too small to alter the shape and amplitude of the residual SGWB spectrum [214, 233] (see also ref. [238]). Our prediction for the SGWB level is therefore robust with respect to our choice of

setting $\rho_0 = 8$. On the other hand, if values of $\rho_0 \lesssim 4$ will be justified in the context of future improvements in data analysis methods, or of archival searches using future ground-based detector data [269], the residual SGWB spectral shape must be adapted: as can be seen in fig. 4.4, it no longer follows the analytical estimation of sec. {4.3.1}, which does not account the presence of the detector, but a dip on its amplitude appears at high frequencies.

Note that we have assumed uninterrupted measurement over the time frame $T_{\rm obs}$, and the instrumental noise, taken from ref. [256, 270], is assumed to be ideal, *i.e.* Gaussian and stationary. We also subtract each resolvable source from the data at its injection parameters, meaning that we generate "perfect residuals", or in other words, we neglect the uncertainty on the source parameters, which inevitably arises within the parameter estimation procedure. We, therefore, simulate an optimal case of the global fit scheme for the LISA SOBBHs. The above assumptions, while not totally realistic, allow us to simplify the analysis.

4.4 Results

4.4.1 Comparison between SGWB computation methods in the LISA band

In this section we show the effect of fixing a maximal time-to-coalescence for the simulated populations on the SGWB spectral shape, and compare the SGWB signals resulting from the four methods described in Sections sec. {4.3.1} to sec. {4.3.3}. As a benchmark, we use one of the fixed-point catalogues presented in sec. {4.2.4}. The redshift range is limited to $z \in [0, 1]$ (comoving distance up to ≈ 3 GPc) to guarantee the computational feasibility of the iterative-subtraction method. The amplitude of the SGWB signals shown in this section is therefore reduced (cf. sec. {4.4.2}), but this plays no role in the purpose of the tests performed here.

As discussed in Sections sec. {4.2.3} and sec. {4.2.4}, in order to limit computational costs, synthetic populations are generated including events up to a maximum time-to-coalescence, that we fix to $\tau^{(\rm det)}_{c,\rm max} = 10^4\,$yrs in the detector frame. In order to investigate the effect of this assumption, one of the catalogues among the benchmark ones has been generated with $\tau^{(\rm det)}_{c,\rm max} = 1.5 \times 10^4\,$yrs, and from it we have produced two sub-catalogues with $\tau^{(\rm det)}_{c,\rm max} = 1.0 \times 10^4$ and $5 \times 10^3\,$yrs. The SGWBs inferred from these catalogues via the iterative-subtraction method are shown in fig. 4.5: excluding all sources beyond a given $\tau^{(\rm det)}_{c,\rm max}$ (appropriately redshifted in the source frame), results in a non-physical bending of the SGWB at low frequencies, depending on the maximal time-to-coalescence (in agreement with ref. [237], see also app. {4.6.3}). It is therefore important to pick a value for $\tau^{(\rm det)}_{c,\rm max}$ ensuring a minimal loss of information while keeping the computational cost of generating the SGWB manageable: as discussed in app. {4.6.3}, we consider $\tau^{(\rm det)}_{c\rm max} = 10^4$ to be a good compromise.

In fig. 4.6 we show the SGWBs computed using the three methods based on population synthesis, presented in Sections sec. {4.3.2} and sec. {4.3.3}. The results are in

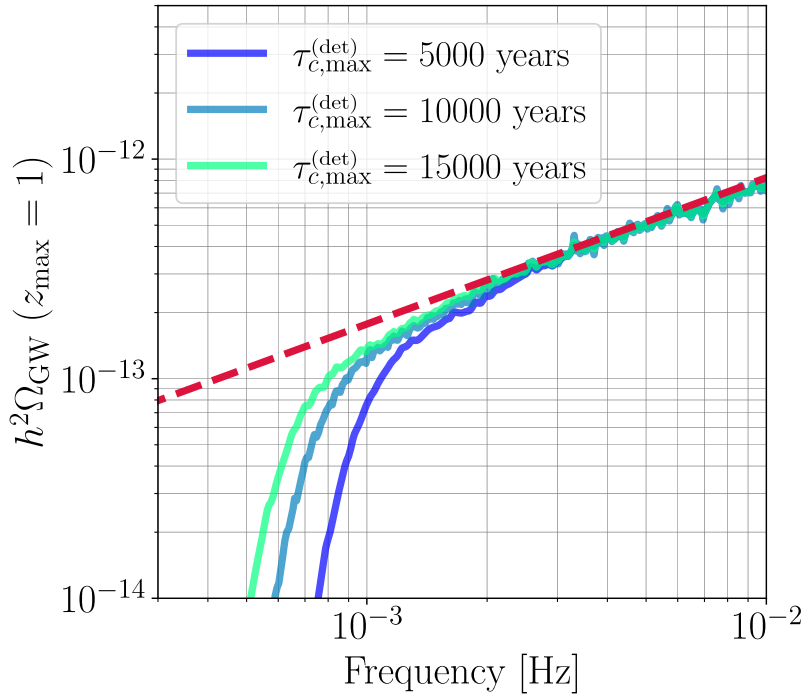

Figure 4.5. The effect of adopting different $\tau_{c,\max}^{(\mathrm{det})}$ values on the resulting stochastic signal, computed using the iterative subtraction (method (iii)). The red dashed line represents the analytical result (method (i)). Imposing a maximum time-to-coalescence in generating the synthetic populations suppresses early-phase inspirals, producing a cutoff in the SGWB at low frequencies. This is not a physical effect, but a limitation of the population synthesis: the spectrum tends towards the expected power law as the upper limit in time-to-coalescence grows.

very good agreement, for both the SGWB amplitude and spectral shape. In particular, those of the frequency-binned MC sum (method (iib)) and of the iterative subtraction (method (iii)) also follow the single power-law behaviour $f^{2/3}$ predicted by the analytical evaluation (eq. (4.3.4)), and taken over by the averaged power-law-like MC sum (eq. (4.3.7)). As far as the frequency-binned MC sum is concerned, this shows that our population catalogues are complete. As far as the iterative-subtraction method is concerned, instead, this is a consequence of the simulated detection process: the instrument sensitivity is such that the number of resolvable sources is too small, even at high frequencies, to alter the SGWB spectral shape, as already pointed out in ref. [233] (see also ref. [238]).

The signals from the frequency-binned MC sum and from the iterative subtraction share some features, especially at low frequencies, despite the fact that the former uses simplified waveform and does not account for frequency drifts. Both approaches also follow closely the averaged power-law-like MC sum, which is distributed around the analytical calculation of the background, from eq. (4.3.6) (see fig. 4.3).

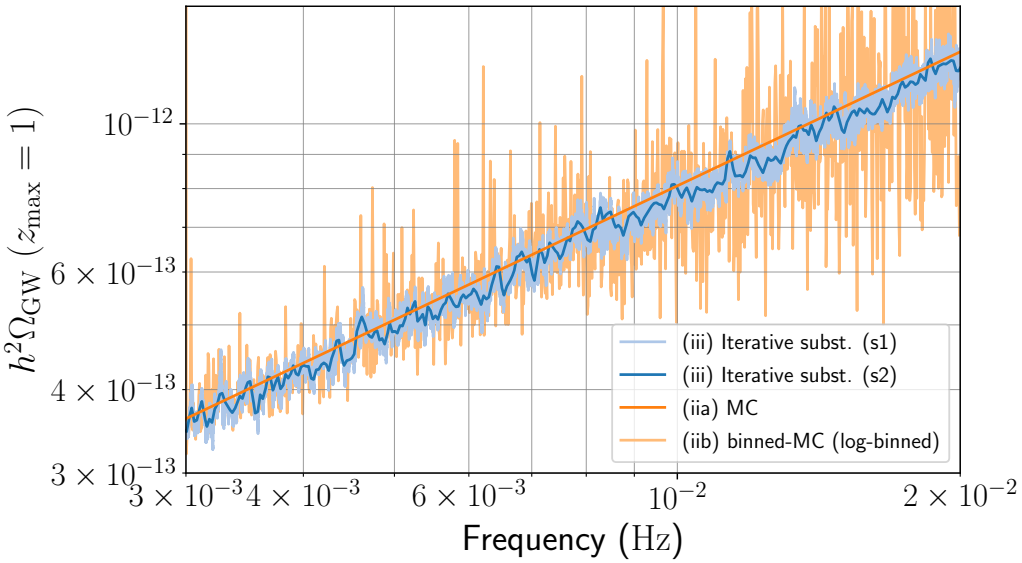

Figure 4.6. Comparison between the population synthesis-based methods presented in Sections sec. {4.3.2} and sec. {4.3.3}. The dark orange line shows the SGWB evaluated with the averaged MC sum (iia), and the light orange one the frequency-binned sum (iib). The blue curves show the SGWB evaluated with the iterative subtraction (iii), as explained in sec. {4.3.3}, for two different data smoothing methods: in s1 (light blue) we have performed a running median over the PSD data using a rolling window of 1000 points, whereas in s2 (dark blue) we apply an additional Gaussian filter. The signals from the frequency-binned MC sum and from the iterative subtraction share some features, especially at low frequencies, where the differences due to neglecting the drifting and using simplified waveforms are less important. Both follow closely the SGWB of the averaged, power-law-like MC sum.

4.4.2 Expected SOBBH signal in the LISA band from GWTC-3

Having established the consistency of the four methods, we turn to the actual computation of the expected SGWB in the LISA band, based on the present knowledge about the SOBBH population. To this purpose, we rely on eq. (4.3.5) and evaluate the SGWB amplitude by integrating eq. (4.3.6) for all points in the LVK posterior parameter sample that is publicly available [251] for the FIDLVK model [46], following the prescriptions described in sec. {4.2.2}. The distribution of the SGWB amplitude at the reference frequency $f = 3\times10^{-3}\,\mathrm{Hz}$ is shown in fig. 4.7 (blue solid line). On a logarithmic scale, it follows a lightly-right-skewed distribution with median $h^2\Omega_{\rm GW}(f = 3\times10^{-3}\,\mathrm{Hz}) = 7.87\times10^{-13}$, and has an interquartile range of $h^2\Omega_{\rm GW}(f = 3\times10^{-3}\,\mathrm{Hz}) \in [5.65,\ 11.5]\times10^{-13}$.

The computation of the SGWB amplitude has been performed under the assumption that the merger rate inherits the functional redshift dependence of the SFR, as in eq. (4.6.1). As discussed in sec. {4.2.1} and app. {4.6.1}, the agreement between the values of the merger rate parameters inferred from GW observations [46] with those of the SFR inferred from electromagnetic observations [130] supports this assumption at

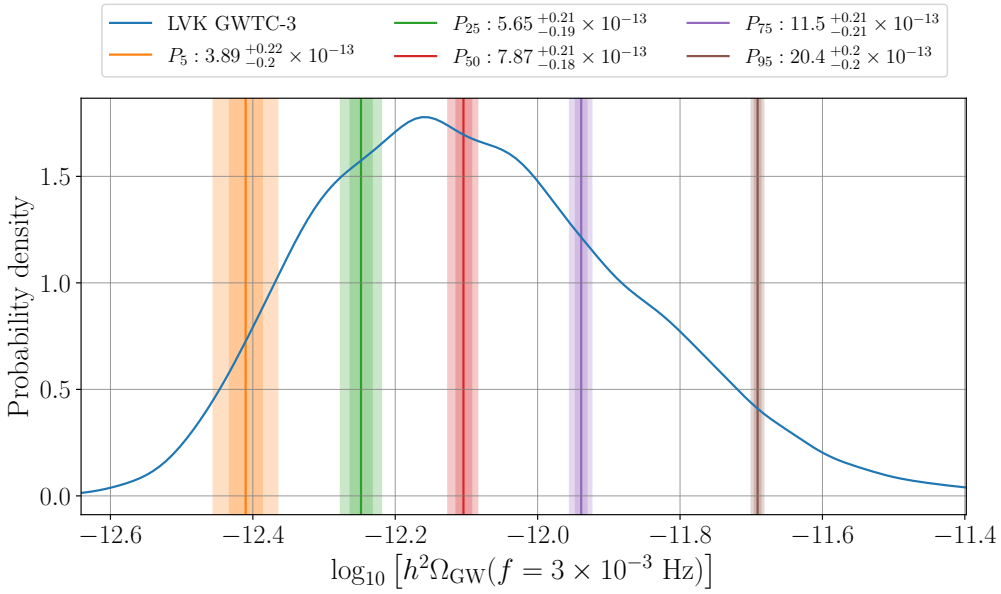

Figure 4.7. Posterior distribution of the SOBBH SGWB log-amplitude in the LISA band, from GWTC-3 (blue solid line). The coloured lines represent the percentiles 5, 25, 50, 75, and 95 (left to right) of the posterior, and their surrounding vertical bands represent the 68% (dark shading) and 95% (light shading) uncertainties on the corresponding SGWB amplitudes, forecasted from a LISA measurement (the uncertainties quoted in the legend correspond to the 68% error): as derived in sec. {4.4.3}, LISA will measure the SOBBH SGWB with an uncertainty on the amplitude one order of magnitude smaller than the present GWTC-3 prediction.

low redshift $z \lesssim 1.5$. However, the merger rate remains untested at higher redshifts, and it is therefore important to investigate how much this assumption influences the final SGWB result. We do so by analysing one example of a more refined model for the merger rate, introducing a time delay t_d between the formation of star binaries and their evolution into BBH systems. The merger rate is then given by the convolution of the SFR with the probability distribution of the time delay [126, 127, 231, 271]:

$$R(z) = \int_{t_{d,\rm min}}^{t_{d,\rm max}} R_{\rm SFR}\left(t(z) + t_d\right) p(t_d)\, {\rm d}t_d\,, \tag{4.4.1}$$

where $R_{\rm SFR}$ now denotes the rate of eq. (4.6.1) (with parameter values specified below that equation), and the probability distribution of the time delay is usually modelled as $p(t_d) \propto 1/t_d$. As a consequence, the minimum expected delay $t_{d,\rm min}$ plays the main role in determining the merger rate dependence on redshift. This parameter is expected to lay in the range 50 Myr–1 Gyr [231]: we therefore pick four values in this range, and compute the corresponding merger rates from eq. (4.4.1), further imposing that at $z = 0.2$ they are equal to the median value of the GWTC-3 constrain for the FIDLVK model, $R_{0.2} = 28.3\,{\rm Gpc}^{-3}{\rm yrs}^{-1}$ (see fig. 4.8) [46]. Looking at eq. (4.3.6), we see that (for redshift-independent mass models) the redshift-dependent contribution

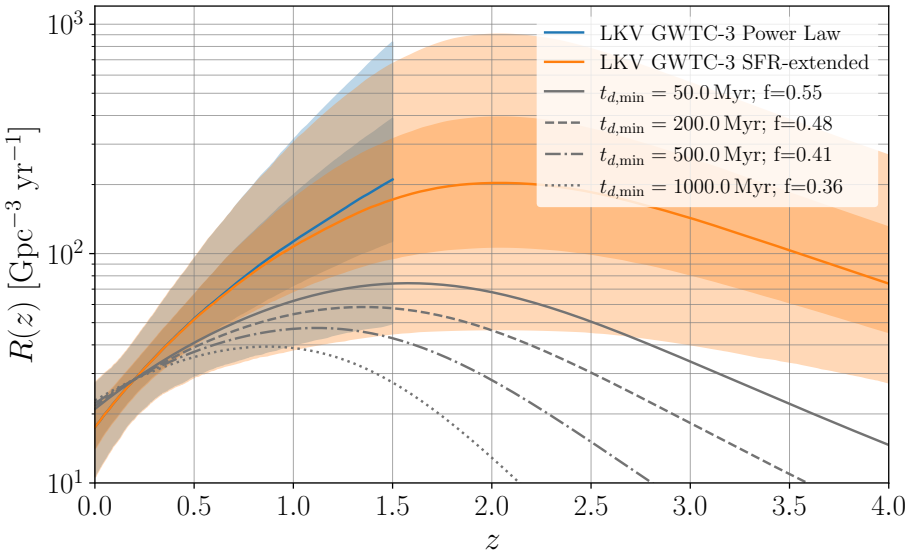

Figure 4.8. Blue: probability distribution (median, 25–75 and 5–95 percentile ranges) of the merger rate under the low-z power-law approximation $R(z) \propto (1+z)^{\kappa}$, according to the probability density obtained in ref. [230] for the FIDLVK model. Orange: its extension to high-z according to eq. (4.6.1), with fiducial values $z_{\rm peak} = 2.04$, $r = 3.6$. Gray lines: the SOBBH merger rate obtained by convolving the SFR with a time delay, for different values of the minimum time delay (see eq. (4.4.1)). For each case in the legend, f represents the fraction of the corresponding SGWB amplitude with respect to the median fiducial case (obtained using eq. (4.6.1) rather than eq. (4.4.1)).

to the background amplitude can be factored out. We can thus easily compute, for a given mass model, the ratio f between a time delayed model and our fiducial SRF case. For $t_{d,\min} = 50$ to 500 Myr, we find that they agree within 40%: accounting for the time delay, therefore, provides SGWB amplitudes close to the P_5 percentile of the median fiducial (SFR-extended) case (see fig. 4.7). The level of agreement drops to 36% for $t_{d,\min} = 1$ Gyr; however, from fig. 4.8, we can appreciate that the corresponding merger rate is rather in tension with LVK constraints.

Our results, in terms of translating the GWTC-3 population constraints into a forecast for the SOBBH SGWB in the LISA band, appear to be robust within one order of magnitude: the highest contribution to the background comes in fact from the SOBBH population at $z \lesssim 1.5$, for which the merger rate is well constrained by LVK GWTC-3. Note that all derived SGWB amplitudes fall well within LISA's detection capabilities (see sec. {4.4.3}). A more thorough study of the dependency of the SGWB amplitude on physically-motivated models for the merger rate and mass distribution can be found in ref. [272].

Our results are also compatible with the latest constraints on the SGWB amplitude by LVK [243]. The upper bound on a power-law SGWB with spectral index

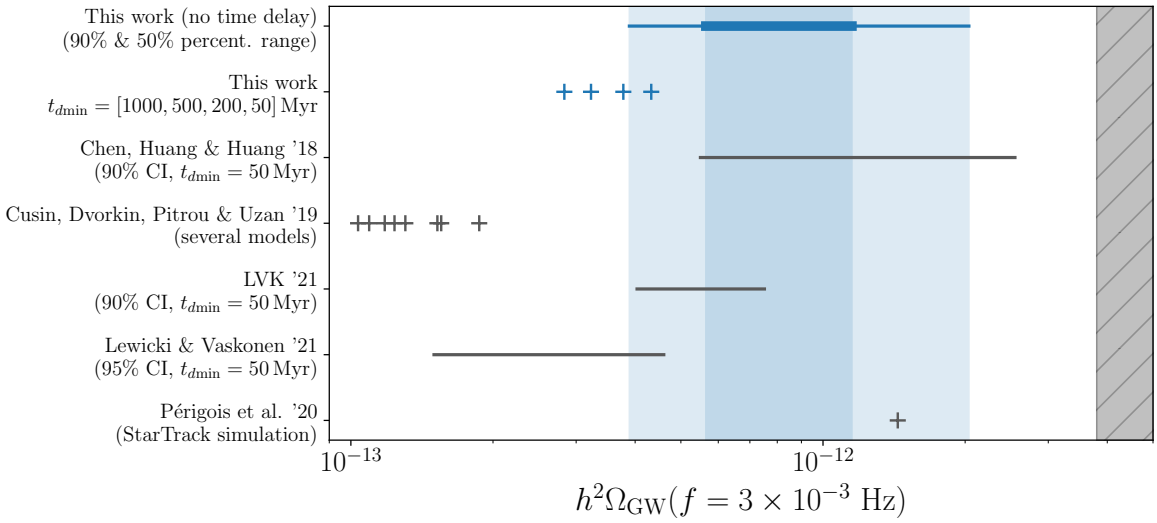

Figure 4.9. Comparison between the SGWB amplitude posterior from this work (blue shaded area, also shown in fig. 4.7), with the median SGWB value evaluated accounting for time-delays (blue crosses, left-to-right in decreasing value of $t_{d,\rm min}$, cf. fig. 4.8), and with other recent results from the literature (black lines and crosses). The grey band to the right represents the LVK upper bound, derived in ref. [243] for a power-law SGWB with index $\alpha = 2/3$.

2/3 at $f = 25\,\text{Hz}$ is, at 95% credible level, $3.4 \times 10^{-9} (1.2 \times 10^{-8})$, when using a log-uniform (uniform) prior, which becomes in the LISA band $h^2\Omega_{\rm GW}(f = 3 \times 10^{-3}\,\text{Hz}) < 3.8 \times 10^{-12}\,(1.3 \times 10^{-11})$. This upper bound applies to the total background, which contains other contributions together with the SOBBH confusion signal (for example the one from neutron star binaries). The actual limit on the SOBBH SGWB is therefore expected to be smaller. Nevertheless, the SGWB amplitude that we forecast remains compatible, being smaller than the LVK upper limit at 99% probability, with median amplitude being smaller by a factor of five (see fig. 4.7).

We also compare our results to a few other predictions for the SOBBH SGWB in the LISA band given in the literature, see fig. 4.9. In ref. [273], taking into account early LVK constraints (from the first 6 events) for the merger rate, a time delay distribution $p(t_d) \propto 1/t_d$ with $t_{d,\rm min} = 50\,\text{Myr}$, and a different fiducial model for the mass distribution from the one used here, it was found that $h^2\Omega_{\rm GW}(f = 3 \times 10^{-3}\,\text{Hz}) = 1.25^{+1.3}_{-0.7} \times 10^{-12}$ (90% credible level), which lies in the upper-half of our distribution (see fig. 4.7). In ref. [234], the authors compute both the isotropic SOBBH SGWB component and its anisotropy, and find a lower prediction than in our analysis: $h^2\Omega_{\rm GW}(f = 3 \times 10^{-3}\,\text{Hz}) \in [1.0, 1.9] \times 10^{-13}$, for a number of astrophysics-motivated models for the merger rate, adjusted to LVK GWTC-1 constraints. The latest LVK forecast [243], using the merger rate and the mass distribution inferred from GWTC-2, and the usual time-delay distribution, results in $h^2\Omega_{\rm GW}(f = 3 \times 10^{-3}\,\text{Hz}) = 5.6^{+1.9}_{-1.6} \times 10^{-13}$ (90% credible level), which is consistent with our results both when including and not including time delays. The analysis of ref. [221], also based on the LVK GWTC-

2 population model, uses power-law mass functions and the conventional time-delay distribution, and obtains $h^2\Omega_{\rm GW}(f = 3 \times 10^{-3}\,{\rm Hz}) = 2.9^{+1.7}_{-1.4} \times 10^{-13}$ (approx 95% credible level): this prediction is compatible with our results, but towards the low side of the distribution in fig. 4.7. In ref. [233], the authors use the population code Star-Track to model the binary formation, treating separately the contributions from population I/II and population III stars. The SGWB amplitude from SOBBHs formed by population I/II star is $h^2\Omega_{\rm GW}(f = 3 \times 10^{-3}\,{\rm Hz}) = 1.2 \times 10^{-12}$, which lays in the upper part of our probability distribution. Population III stars contribute an additional 2%, $h^2\Omega_{\rm GW}(f = 3 \times 10^{-3}\,{\rm Hz}) = 2.25 \times 10^{-13}$: since this is significantly larger than the expected uncertainty in LISA's measurement of the background (see sec. {4.4.3}), the presence of population III stars could be discriminated, provided that the population is known with sufficient certainty. Finally, in ref. [274] it is found that the contribution of SOBBH to the SGWB is even lower than what found in ref. [234], and subdominant in the LISA band with respect to the one from PBHs: $h^2\Omega_{\rm GW}(f = 3 \times 10^{-3}\,{\rm Hz}) \simeq 4.5 \times 10^{-14}$.

4.4.3 SGWB Parameter Estimation

In this section we assess LISA's capability to detect and characterise the SOBBH SGWB. We perform an MC analysis of simulated data containing the instrumental noise, the stochastic foreground from binaries in the Galaxy, and different levels of the SOBBH SGWB, corresponding to the percentiles presented in fig. 4.7. The SOBBH SGWB is modelled following eq. (4.3.5), but both the amplitude and the spectral tilt are left as free parameters in the analysis:

$$h^2\Omega_{\rm GW}(f) = 10^{\log_{10}(h^2\Omega_{\rm GW})(f_*)} \left(\frac{f}{f_*}\right)^{\alpha} . \tag{4.4.2}$$

We apply a pre-processing procedure similar to the one employed in refs. [241, 275], which we briefly summarize here: assuming a mission duration of 4 years, we chunk the data stream into N_c segments of 11.5 days each (corresponding to a frequency resolution $\Delta f \simeq 10^{-6}$ Hz); we generate data in the frequency domain for each segment, including the instrumental noise, the GB foreground, and the SOBBH SGWB, and we average over these segments to get the simulated measured spectrum. Using the noise as an estimate for the variance, we define a likelihood consisting of a sum of Gaussian and log-normal components (the latter accounting for the skewness of the exact likelihood), as discussed in ref. [241]. For the sake of speed and without loss of precision, this likelihood is applied to a coarse-grained version of the spectrum obtained by inverse variance weighting, the final data in frequency space being defined as

$$D^{th}_{ij}\left(f^k_{ij}\right) = h^2\Omega_{\rm GW}(f^k_{ij}, \vec{\theta}_s) + h^2\Omega_n(f^k_{ij}, \vec{\theta}_n)\,, \tag{4.4.3}$$

where f^k_{ij} and D^k_{ij} are respectively the coarse-grained frequency corresponding to bin k, and the data at that bin, for the combination of TDI channels i and j. $\Omega_{\rm GW}$ represents both the SOBBH component, with spectral shape defined by eq. (4.4.2), and the GB

foreground component, based on the model from ref. [237]. $\vec{\theta}_s$ is the vector of parameters of the signal: amplitude and spectral tilt of the SOBBH SGWB, while we reconstruct only the amplitude $h^2\Omega_{\rm Gal}$ of the GB foreground. Ω_n is the instrumental noise in omega units. We adopt a two-parameter noise model as typically done for LISA: the noise is characterized at low frequency by the acceleration component, parameterised by A, and at high frequency by displacements in the interferometry metrology system P [275]. The two noise parameters form the vector $\vec{\theta}_n$, and vary freely in our analysis. We sample over the joint $(\vec{\theta}_s, \vec{\theta}_n) = (\log_{10}[h^2\Omega_{\rm GW}(f = 3 \times 10^{-3}\,{\rm Hz})], \alpha, \log_{10}[h^2\Omega_{\rm Gal}], A, P)$ parameter space using the Nested Sampler `Polychord` [276, 277] via its interface with `Cobaya` [278].

In fig. 4.10 we show the MC contours (2-σ contours) on the SOBBH signal parameters $(\log_{10}(h^2\Omega_{\rm GW}(f_*)), \alpha)$, together with the parameters of the GB foreground and the noise $(\log_{10}(h^2\Omega_{\rm Gal}), A, P)$, obtained by injecting each of the SOBBH SGWB posterior percentiles shown in fig. 4.7. For all the injected SGWB amplitudes, the reconstruction of both the signals and the noise is accurate, with all parameters consistent with the injected values at 2-σ. In particular, the simultaneous reconstruction of the GB and SOBBH SGWB is achievable even when the amplitude of the latter is small, due to their different spectral shapes.

The uncertainty on the SOBBH SGWB amplitude from the LISA measurement is practically constant: $\Delta h^2\Omega_{\rm GW}(f = 3 \times 10^{-3}\,{\rm Hz}) \approx 4 \times 10^{-14}$ (68% CI), with relative uncertainties ranging from 5% for P_5, to 1% for P_{95}. Consequently, the $< 1\%$ computation error on the SGWB prediction due to limiting $z_{\rm max} = 5$ is acceptable for this study (cf. fig. 4.2). Moreover, LISA is insensitive to the $\approx 0.2\%$ population sample variance on the amplitude (cf. fig. 4.3).

Rather than sampling over the tilt α, as we did in the present background-detection study, in a realistic data analysis pipeline searching for the SOBBH SGWB, the tilt would be fixed to $\alpha = 2/3$. Thus, LISA's determination of the background amplitude could reveal more accurate, with respect to the tilt-marginalised errors presented here. On the other hand, realistic data would contain the contribution from all the other GW sources in the LISA band, which need to be extracted simultaneously to the SGWBs signals, possibly affecting the error on the SGWB amplitude compared to the simple MC evaluation performed here (*e.g.* ref. [279]).

As a sanity check, for the lowest value of the background amplitude, we have also performed a Fisher parameter estimation. In fig. 4.11 we present the comparison between the Fisher analysis and the corresponding MC result, showing that the two procedures are consistent in the reconstruction accuracy of the signal and noise parameters.

The results of this section show that LISA will be able to narrow down by one order of magnitude the current uncertainty on the SGWB amplitude due to the SOBBH

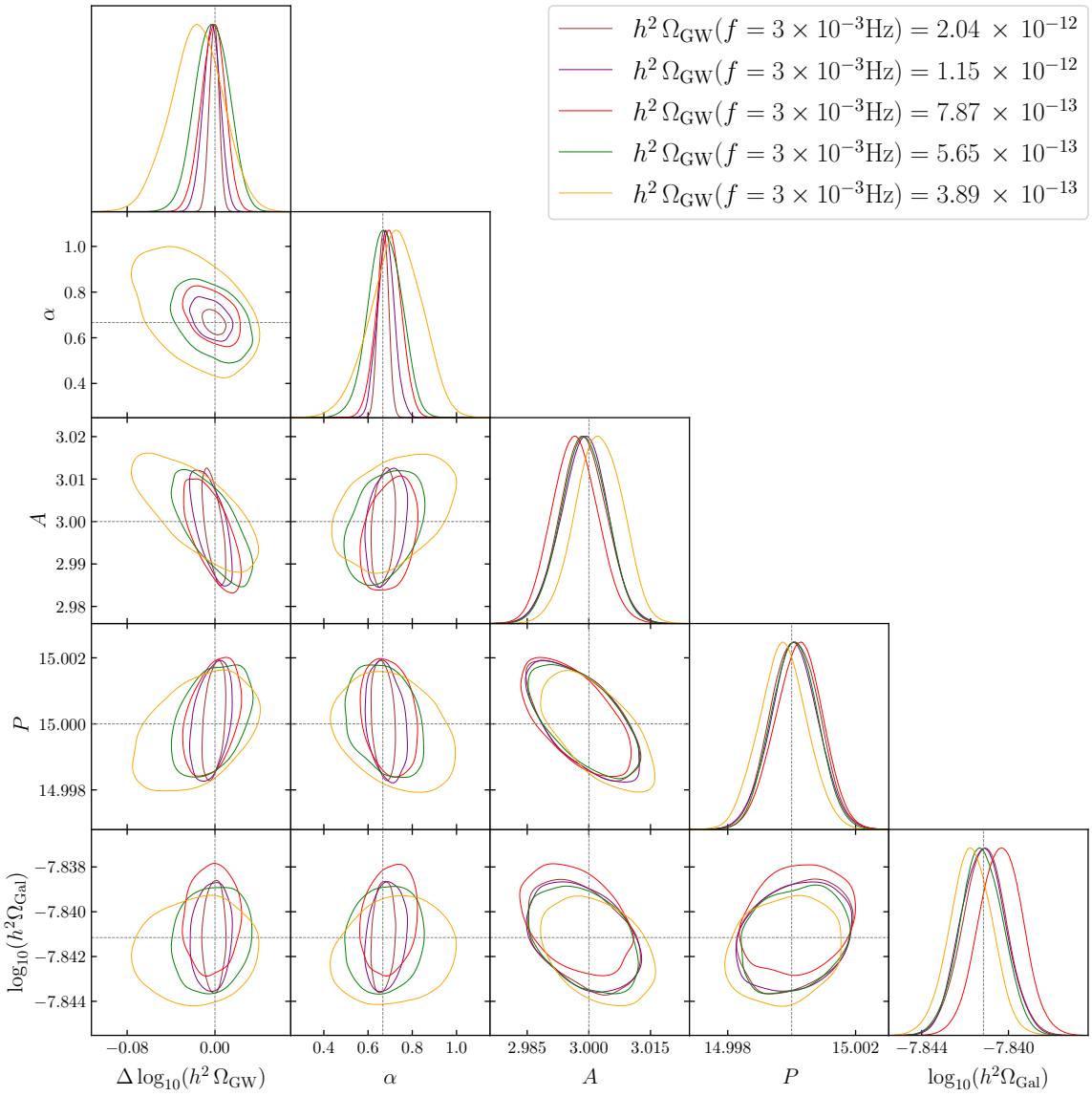

Figure 4.10. 2-σ MC contours on the SOBBH SGWB parameters ($h^2\Omega_{\rm GW}(f = 3 \times 10^{-3}\,{\rm Hz}), \alpha$), GB parameter $h^2\Omega_{\rm Gal}$, and instrumental noise parameters (A, P) for the five percentile levels of the SOBBH SGWB plotted in fig. 4.7.

population uncertainty inferred from GWTC-3 (see fig. 4.7). Moreover, we demonstrated that a clear detection of the SGWB is guaranteed, if the true signal falls within this uncertainty range. On the other hand, the lack of detection, or the detection of an SGWB outside the posterior prediction (likely lower), would indicate either that the population model needs to be changed, for example modifying the merger rate behaviour at high redshift, as discussed in sec. {4.4.2}, or possibly introducing a redshift-dependence in the mass probability density function; or, it could indicate that the nature of the SOBBHs is different from what assumed in this work, for example, they could have highly eccentric orbits. By the time LISA will perform the SGWB

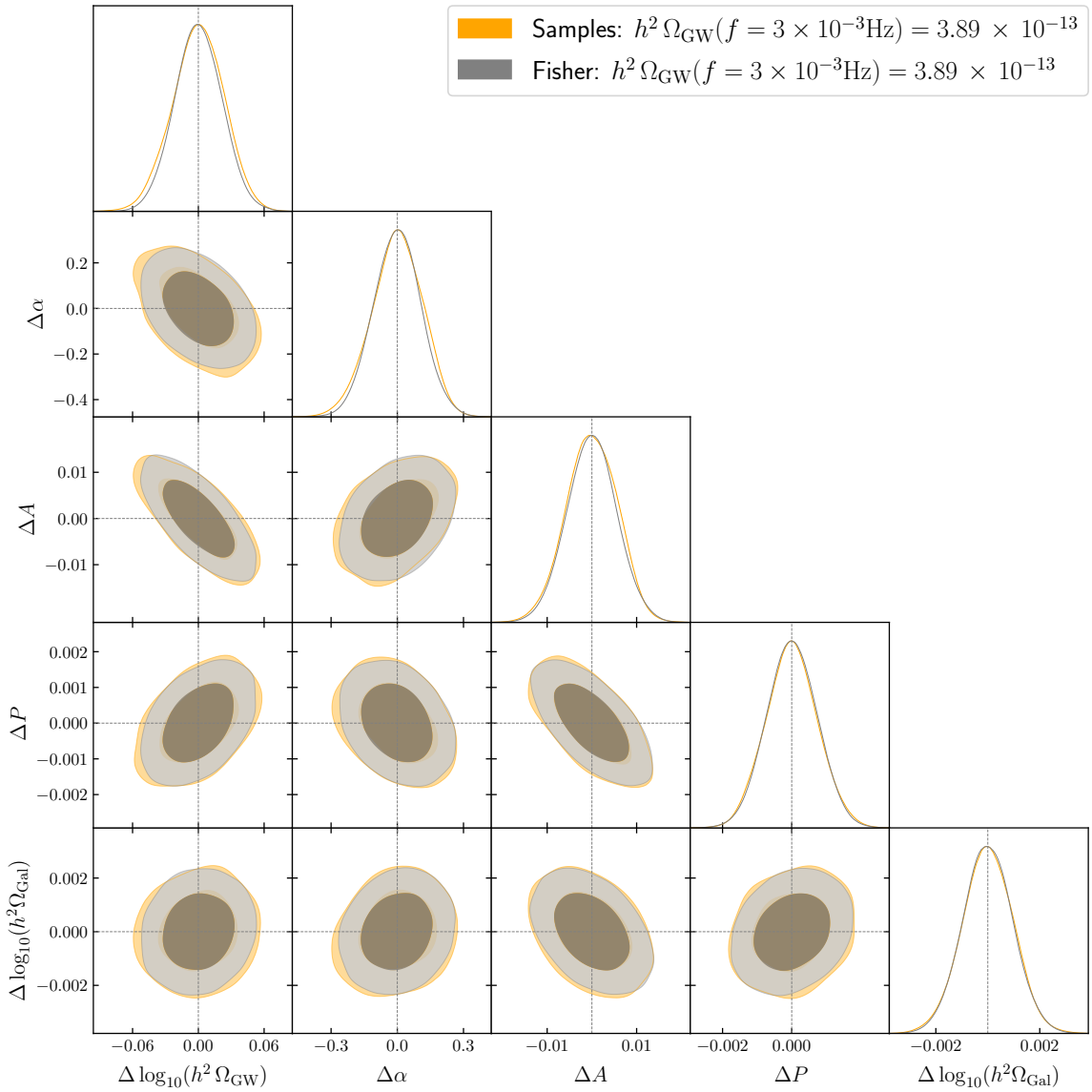

Figure 4.11. 1 and 2-σ contours from the Fisher analysis, compared with the MC ones, assuming the lowest value of the SGWB amplitude among the five percentile levels plotted in fig. 4.7.

measurement (or constraint), the SGWB amplitude posterior predicted from ground-based observations will probably have narrowed, if not a detection be made by either 2G or (more likely) 3G detectors. Nevertheless, the LISA measurement will provide further insight into the population of inspiralling SOBBH, by probing the population properties at high redshift and with low masses, and by testing the SGWB signal in a different frequency window.

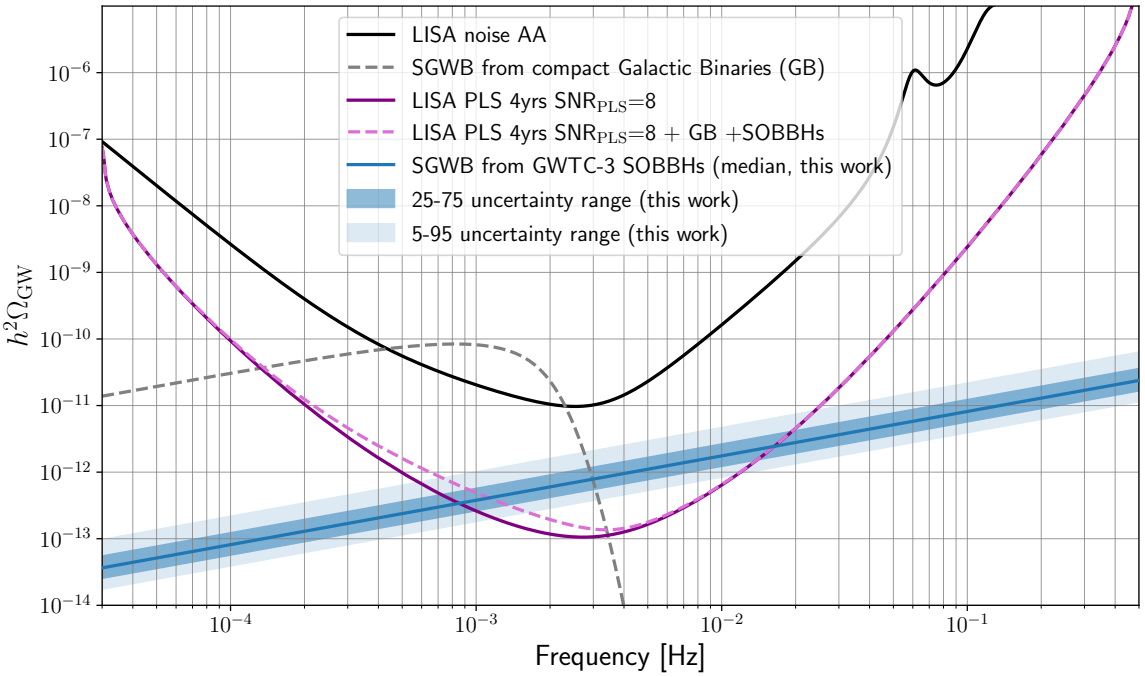

Figure 4.12. Effective, *i.e.*, averaged over all TDI channels, LISA PLS for 4 years of observations (with 100% efficiency), including (in dashed purple) and excluding (solid purple) the GBs and SOBBHs SGWB components. The black line shows the sensitivity of the AA TDI channel, and the dashed grey line shows the amplitude of the SGWB due to unresolved GBs. The median value for the SOBBH SGWB estimated in this work from GWTC-3 constraints on the SOBBH population (with 25-75 and 5-95 uncertainty ranges) is shown in blue.

4.4.4 Impact on the Power-Law Sensitivity

The PLS represents the standard tool to estimate the observability of a given power-law SGWB. The PLS is normally defined assuming that the only stochastic component affecting the SGWB measurement is the instrumental noise [239–241]. In fig. 4.12 we present an improved version of the LISA PLS including the confusion noises generated by GBs and by SOBBHs. For the GBs we adopt the analytical template of ref. [237] with all the parameters taken at their reference value; the SOBBH amplitude on the other hand is fixed to the median value evaluated in this analysis, see sec. {4.4.2}, and the tilt to 2/3.

The GB contribution mainly affects the low-frequency range, while the SOBBH contribution is relevant at higher frequencies: this effect is reflected in the PLS. The inclusion of the GB confusion noise slightly modifies the PLS at low frequencies, while the impact of the SOBBHs is nearly negligible. Note that fig. 4.12 corresponds to figure 2 of ref. [221], while figure 3 in the same reference is relative to a different treatment, meant to account for the effect of the SGWB amplitude uncertainty, evaluated from the GWTC-2 uncertainty on the merger rate at $z = 0$.

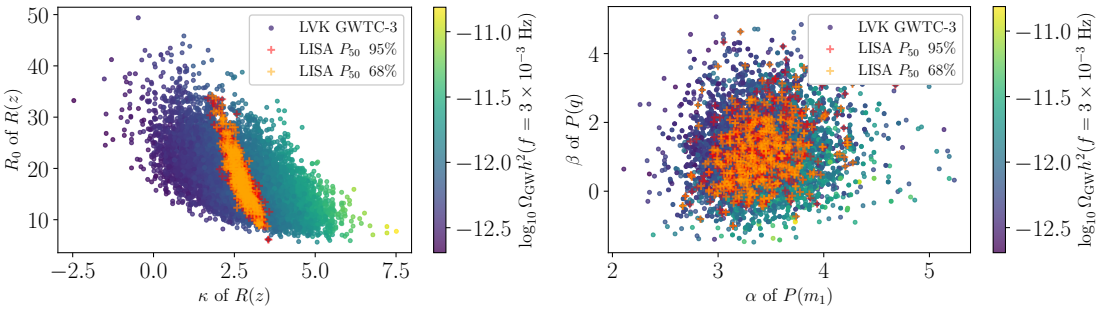

Figure 4.13. Impact, on the population parameters posterior inferred from GWTC-3, of the measurement by LISA of a SGWB with amplitude corresponding to the median value P_{50} of the amplitude distribution given in 4.7. The points coloured from blue to yellow represent the GWTC-3 posterior, and the color scale represents the corresponding SGWB amplitude. The points highlighted in yellow (red) represent the parameter values providing SGWB amplitudes within the 1-σ (2-σ) confidence region of the LISA measurement. Left panel: the initial merger rate R_0 versus its tilt κ. Right panel: the tilts (α, β) of the power-law distributions of m_1 and $q = m_2/m_1$ respectively. A measurement of the SOBBH SGWB would break the degeneracy coming from constraints based on individual mergers, and the credible intervals would shrink correspondingly, especially for the merger rate parameters. Had we not fixed the high-redshift behaviour of the merger rate, but treated it probabilistically, the improvement with respect to the GWTC-3 constraints would be smaller, but still significant.

4.4.5 SGWB detection and the SOBBH population parameters

Intuitively, one might expect the constraining power of a measurement of the SGWB on the SOBBH population model to be very limited, regardless of its precision, since it would reduce the dimensionality of the population parameter space at most by one, leading to a highly-degenerate posterior. On the other hand, this can still have an important impact if the degeneracy associated with the SGWB measurement does not align with the correlations in the population parameter posterior associated with the detection of individual events, the misalignment being due to the fact that the population parameters influence the SGWB amplitude differently from how they influence the characteristics of the population of individually resolvable events. Indeed, it has been demonstrated that a SGWB measurement (or even upper limit) by LVK, in combination with resolved merger events, can constrain the redshift evolution of their merger rate [242, 243] and possibly their mass distribution [280].

The high precision with which LISA is expected to measure the SOBBH background, as shown in sec. {4.4.3}, should render LISA especially suited to this task. In order to illustrate its potential constraining power, in fig. 4.13 we plot the GWTC-3 population parameters posterior sample as a scatter plot, highlighting the points compatible with a SGWB amplitude within the LISA 1- and 2-σ credible intervals, relative to a detection by LISA of a SGWB with amplitude corresponding to the median predicted SGWB level P_{50} (see fig. 4.10). One can appreciate that the two-dimensional posterior shrinks significantly, depending on the combination of population parameters.

In the left panel of fig. 4.13 we show the local merger rate R_0 versus its low-redshift tilt κ: the GWTC-3 posterior (points coloured in blue to yellow (for increasing SOBBH SGWB amplitude) presents a degeneracy due to the merger rate being best determined around $z \approx 0.2$. Since the value of the low-redshift tilt κ has a strong impact on the SGWB amplitude, the latter varies considerably along this degeneracy (colour scale from blue to yellow). Thus, a precise SGWB measurement, as performed by LISA, would break this degeneracy by leading to a posterior, in the (R_0, κ) parameter plane, almost perpendicular to the one inferred from the detection of individual SOBBH merger events by ground-based observatories.

The posterior distribution of the mass tilts (α, β), shown in the right panel, would also be significantly reduced.[7] Note that this could be further exploited by a measurement of the anisotropic component of the SOBBH background [281], since the relative amplitude of the anisotropic to the isotropic components appears to be correlated with the tilt of the mass distribution and with the maximal allowed mass [280].

The above results are valid within the assumptions of our analysis, in particular, that the merger rate at high redshift is fixed to the SFR as given in eq. (4.6.1), and that the LISA uncertainty on the SGWB amplitude is inferred from the MC analysis of a simulated data set containing exclusively the SOBBH SGWB, the GBs, and the instrumental noise. Allowing for variations in the high-redshift model of the merger rate, and/or performing a more realistic data analysis procedure accounting for the overlap of several categories of LISA sources, would likely reduce the potential of the SGWB measurement to shrink the population parameter posterior. However, these effects are not expected to alter the misalignment of the correlations in the posterior parameter space inferred from the measurements of individual events and from the measurement of the SGWB. Consequently, the latter will anyway retain, to some degree, its constraining power.

4.5 Conclusions

We have evaluated the SGWB expected in the LISA frequency band from SOBBHs, incorporating the most recent information on their mass function, spin distribution, and merger rate coming from LVK observations, in particular from the GWTC-3 posterior on the population parameters of the FIDLVK model.

[7] Figure 4.1 seemed to indicate that the effect on the SGWB amplitude of the parameters of the peak in the POWER LAW + PEAK m_1 distribution, (λ, σ), was larger than the effect of the tilts of the power laws in m_1 and $q = m_2/m_1$, *i.e.* (α, β). In this section we observe instead (see the right panel of fig. 4.13) that the latter would be more strongly constrained by a background amplitude measurement than the former, leading to an apparent contradiction. However one should notice that the analysis in sec. {4.3.1}, illustrated by fig. 4.1, does not take into account parameter degeneracies in the GTWC-3 posterior, overestimating the importance of some individual parameters, in particular (λ, σ).

The LVK observations only probe the SOBBH population at low redshift, while faint and distant SOBBHs contribute the most to the background signal. In order to properly evaluate the SGWB, we have therefore extended the GWTC-3 power-law merger rate by assuming that it follows the SFR [130], since the low-redshift expansion of the latter is coherent with the GWTC-3 constraints. With the aim of assessing the impact that this assumption has on the SGWB amplitude, we have also added a time delay in the SOBBHs formation and found that (under a simple model for the time delay distribution, and reasonable values for the minimal time delay) this reduces the SGWB amplitude by at most 40%, remaining within the uncertainty inherent to the GWTC-3 posterior. Though the current precision of the model is not sufficient, future ground-based observations of individual merger events, together with a detection of the SGWB by LISA, will allow to constrain the merger rate and possibly time delays in the future.

We have used four methods to estimate the SGWB. The first method is based on analytic considerations and consists of the integration, over the number density of binaries, of their GW emission in the quasi-circular Newtonian approximation, resulting in a power-law SGWB with slope $f^{2/3}$ [236]. The analytical approach has been used to evaluate the impact of each population parameter on the amplitude of the SOBBH background, accounting for its marginalized 95% confidence levels from the GWTC-3 posterior. The power-law index κ of the low-redshift expansion of the merger rate is the parameter influencing the most the SGWB amplitude. We have then calculated the relative percentage change induced in the latter by varying the redshift upper cutoff: we found that integrating up to $z_{\rm max} = 5$ is sufficient to obtain $\sim 1\%$ accuracy in the evaluation of the background amplitude, also well within the uncertainty induced by the GWTC-3 posterior.

The other three methods employed for the SGWB estimation, gradually increasing in complexity and accuracy, rely on synthetic SOBBH populations, which we have constructed following the GWTC-3 FIDLVK posterior distribution. The second method consists in replacing the integration of the analytical method with a MC sum over the masses and redshift of the SOBBHs in the synthetic population realisation, averaging over the time-to-coalescence and the sky-position; while in the third method, the MC sum is performed accounting for the time-to-coalescence of individual events and binning them according to their corresponding emission frequency. These methods allow establishing that the impact of the population variance over the SGWB amplitude is of the order of 0.2%, negligible with respect to the effect of the maximal redshift choice, which is in turn smaller than the uncertainty due to the GWTC-3 posterior.

The fourth method incorporates the actual LISA detection process and consists in simulating LISA data-streams containing the waveforms of all the SOBBHs within the simulated population, and iteratively subtracting the loudest ones until only the confusion noise remains [237]. The threshold SNR used to single out the resolvable GW sources is set to $\rho_0 = 8$, but we find that the saturation threshold, above which the

SOBBH signal is less sensitive to the choice of the threshold itself, is situated at $\rho_0 \approx 5$.

We have checked that the four methods provide consistent results for the SGWB amplitude: this is indeed the case at frequencies higher than about 2 mHz, this threshold being exclusively due to the computational limitation of our synthetic populations. The SNR threshold choice results in fact in a limited number of resolvable events, so that the SGWB in the LISA frequency band does not deviate from the analytical power law prediction, which is reproduced also by the three methods based on population synthesis. However, if sources with SNR lower than five will be resolvable in the future, thanks to improvements in data analysis techniques, or to archival searches using future ground-based detector observations, it will be necessary to take into account that the shape of the SGWB in the LISA band deviates from the power law behaviour. This clearly stresses the importance of a precise identification of the resolved sources and of their subtraction, which we present in a follow-up paper [238].

The distribution of the SGWB amplitude at the reference frequency of 3 mHz is evaluated using the analytical method, for all points in the GWTC-3 posterior parameter sample. The interquartile range of the distribution is $h^2\Omega_{\rm GW}(f = 3 \times 10^{-3}\,{\rm Hz}) \in [5.65,\, 11.5] \times 10^{-13}$. Our findings are in broad agreement with previous evaluations of the SOBBH stochastic signal and appear therefore to be robust with respect to assumptions such as the high-redshift behaviour of the merger rate and the mass distribution.

We have then performed a MC analysis of simulated LISA data to infer the parameters (*i.e.*, amplitude and spectral tilt) of the SOBBH SGWB in the presence of instrumental noise and of the stochastic signal from GBs. We have found that, with four years of data, the template-based reconstruction of the parameters of both signals and of the noise is accurate to the percent level, with all parameters consistent with their injected values at 2-σ. In this simplified setting where no other GW source is present, and the GB background is static, the SOBBH SGWB can therefore be distinguished from the GB one, despite their overlap at low frequency. We have also compared the MC analysis with a Fisher Information Matrix analysis, finding good agreement, and derived the PLS accounting for the SOBBH and GB backgrounds.

The precision with which LISA will measure the amplitude of the SOBBH SGWB goes from at best 1% (at 1-σ), for the amplitude value corresponding to the 95th percentile of its posterior distribution, up to 5% for the fifth percentile. LISA will therefore reduce by one order of magnitude the current uncertainty on the SGWB amplitude predicted from the GWTC-3 population model. The accuracy of this measurement opens interesting perspectives. We have shown that LISA has the potential to break the degeneracy between some population parameters, since the correlations in the posterior parameter space inferred from the measurements of individual events and of the SGWB, are almost orthogonal. In particular, we forecast an important impact on the merger rate parameters, since the SGWB detection by LISA probes the population

of inspiralling SOBBHs at high redshift, fully complementary to actual ground-based observations of low-redshift mergers.

Several extensions of our work are possible, tackling some of its underlying assumptions. First of all, including eccentricity and precession in the waveforms might have an important effect on the SGWB [282, 283]. While we have shown the effect of introducing a time delay between the star formation and the BHs mergers, the impact of the metallicity on the BH mass function has been neglected, see *e.g.* refs. [126, 127, 231, 271] for recent studies. A further layer of complexity can be added including the possibility of a redshift dependence of the mass function [46]. The LISA error on the SGWB parameters should be forecasted including other types of sources in the data stream, both resolved and of stochastic nature. Extra-galactic neutron star binaries, for example, generate a collective signal that, although lower in amplitude, is similar to the background from SOBBHs, and likely not negligible. Extreme mass ratio inspirals [284] also produce a background at mHz frequencies, although its amplitude is currently poorly constrained and its frequency dependence might not follow a simple power-law in the LISA band [257]. Finally, the effect of the SGWB measurement by LISA on the SOBBH population parameters demonstrated in this work should be properly evaluated via a joint analysis of simulated data from LISA and ground-based observatories, possibly 3G detectors which might be operative by the time LISA flies [285]. Such a joint analysis may also reveal deviations from the expected SOBBH SGWB spectrum, which could point towards a different origin for the BBHs (see *e.g.* ref. [286]).

Acknowledgments

The authors thank Léonard Lehoucq and Irina Dvorkin for useful discussions. C.C. thanks M. Vallisneri for enlightening discussions. D.G.F. thanks Androniki Dimitriou for tips on the numerical integration of the analytic evaluation of the SGWB. M.P. and A.R. thank E. Barausse for useful discussions on related topics. A.S. acknowledges the financial support provided under the European Union's H2020 ERC Consolidator Grant "Binary Massive Black Hole Astrophysics" (B Massive, Grant Agreement: 818691). D.G.F. (ORCID 0000-0002-4005-8915) is supported by a Ramón y Cajal contract with ref. RYC-2017-23493. This work was supported by Generalitat Valenciana grant PROMETEO/2021/083, and by Spanish Ministerio de Ciencia e Innovacion grant PID2020-113644GB-I00. G.N. is partly supported by the grant Project. No. 302640 funded by the Research Council of Norway. A.R. and J.T. acknowledge financial support from the Supporting TAlent in ReSearch@University of Padova (STARS@UNIPD) for the project "Constraining Cosmology and Astrophysics with Gravitational Waves, Cosmic Microwave Background and Large-Scale Structure cross-correlations".

4.6 Appendix A : Further information on the SOBBH population model

In this Appendix, we provide more detail on the SOBBH population model: we describe the characteristics of the probability distributions inferred from GWTC-3 observations [46], and justify some of our choices for the catalogues generation, in particular regarding the merger rate behaviour with redshift and the maximal time-to-coalescence.

4.6.1 Appendix A.1 : Redshift-dependent SOBBH rate

As discussed in sec. {4.2.2}, the GWTC-3 constraints on the SOBBH merger rate variation with redshift, assumed to be a power law $R(z) = R(0)(1+z)^{\kappa}$, are weak at $z \gtrsim 0.5$. Therefore, in order to produce accurate SGWB estimates, we need an Ansatz that extends the power law assumption towards higher redshift. We require $R(z)$ to follow the redshift profile of the *Madau-Fragos SFR* [130]:

$$R(z) = R_0 C \frac{(1+z)^{\kappa}}{1 + \frac{\kappa}{r}\left(\frac{1+z}{1+z_{\rm peak}}\right)^{\kappa+r}}\,, \tag{4.6.1}$$

with $r, \kappa > 0$ and $R_0 \equiv R(z=0)$, implying $C = 1 + (\kappa/r)\,(1+z_{\rm peak})^{-(\kappa+r)}$. Thus, along the evolution of the Universe, from high to low redshift, the SOBBH merger rate initially rises as z^{-r} as more stars are available, and eventually decreases as z^{κ} after the peak of stellar formation. Different from previous studies, *e.g.* ref. [243], we introduce the extra factor κ/r in the denominator of eq. (4.6.1) to guarantee that the function peaks precisely at redshift $z_{\rm peak}$; otherwise, the actual peak of the function would deviate from the value of the nominal $z_{\rm peak}$ parameter whenever $\kappa/r \neq 1$. Following this notation, the updated best fit values found in ref. [130] are $\kappa = 2.6$, $r = 3.6$, and $z_{\rm peak} = 2.04$.

In order for the merger rate $R(z)$ of eq. (4.6.1) to work as a reasonable high-redshift extension of the GWTC-3 low-redshift constraints, we require it to reproduce the profile that LVK obtains for the FiducialLVK fiducial model fitting the GWTC-3 data [46]. In that study, inference is performed on a low-redshift power law $R(z) \propto (1+z)^{\kappa}$, resulting in[8] $\kappa = 2.7^{+1.8}_{-1.9}$ and a pivot rate of $R_0 = 17.3^{+10.3}_{-6.7}\,\mathrm{Gpc^{-3}yrs^{-1}}$ at $z = 0$, or alternatively $R_{0.2} = 28.3^{+12.9}_{-9.0}\,\mathrm{Gpc^{-3}yrs^{-1}}$ at $z = 0.2$. These constraints are represented by the blue-shaded region in fig. 4.14. At low redshift, the median value for the spectral index κ coincides with that of the SFR [130]: in order to extend $R(z)$ at high redshift, we can therefore match the LVK posterior values for R_0, κ with some values for $r, z_{\rm peak}$. The latter could *e.g.* be drawn from some prior distribution; for the purposes of this paper (comparing LISA's sensitivity to SOBBH SGWB amplitudes approximately compatible with the GWTC-3 population inference), it is enough to fix $r, z_{\rm peak}$ to the SFR best fit values mentioned above [130]. The resulting, GWTC-3-compatible, high-redshift merger rate is displayed in fig. 4.14 in orange shading.

[8] All parameter ranges are given as median ± its respective differences with the percentiles 5 and 95, taken from the public population posterior sample of GTWC-3 for the fiducial FiducialLVK model.

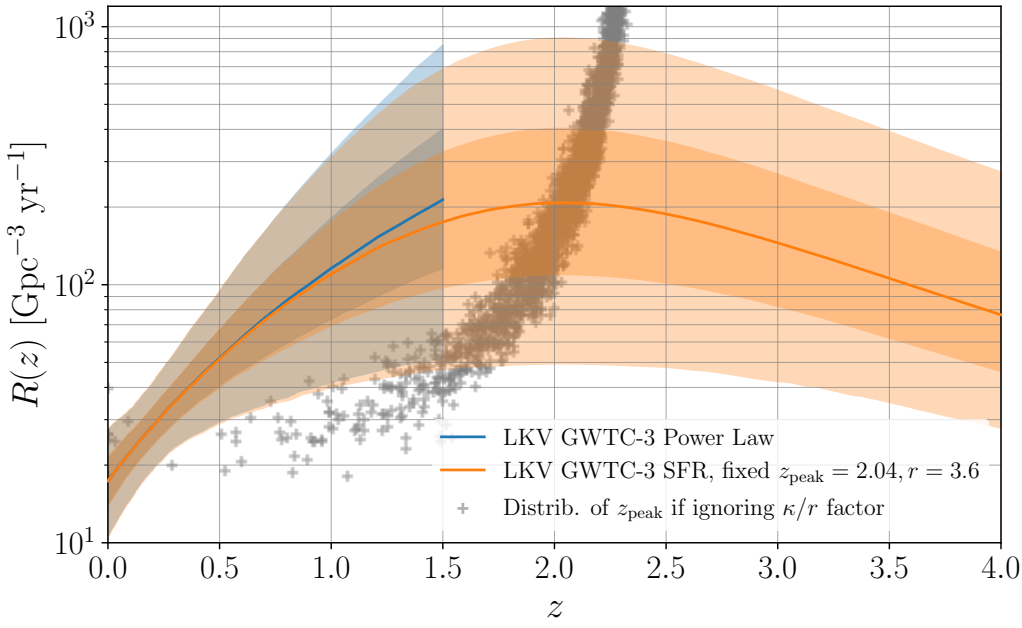

Figure 4.14. Distribution (median, 25–75 and 5–95 percentile ranges, with different levels of opacity) of the power-law merger rate $R(z) \propto (1+z)^{\kappa}$ (blue) according to the probability density obtained in ref. [46] for the FIDLVK model; and its extension to high-z beyond the low-redshift power-law behaviour, according to eq. (4.6.1) (orange), with fiducial values $z_{\rm peak} = 2.04$, $r = 3.6$. By construction, the two distributions are very similar in the redshift range probed by LVK, *i.e.* $z \lesssim 0.5$. The crosses (gray) represent a sample of positions of the ill-defined peak of $R(z)$, had we ignored the κ/r factor in eq. (4.6.1).

4.6.2 Appendix A.2 : Masses and spins density distributions

The probability distribution $p(\xi|\theta)$ of eq. (4.2.1) is taken from refs. [230, 287]. In the fiducial FIDLVK model, $p(\xi|\theta)$ is a separable probability density function, which can be split into a joint density function for the masses $m_{i=1,2}$ of the binary, and independent density functions for the spin amplitudes a_i and tilts t_i:

$$\begin{aligned} p(\xi|\theta) = {} & p(m_1, m_2|m_{\rm min}, m_{\rm max}, \delta_{\rm min}, \alpha, \lambda_{\rm peak}, \mu_m, \sigma_m, \beta_q) \\ & \times p(a_1|\alpha_a, \beta_a) \times p(a_2|\alpha_a, \beta_a) \times p(\cos(t_1), \cos(t_2)|\sigma_t, \zeta)\,. \end{aligned} \tag{4.6.2}$$

The separability of this distribution facilitates population synthesis since the parameters in the different components can be simulated independently (*e.g.* using *inverse transform sampling* in the single-parameter cases).[9]

The mass density function is usually given in terms of the mass of the heaviest

[9]The data in GWTC-3 suggest some correlations that would break this separability, such as that between high spin and mass asymmetry. For the level of the analysis in this paper, it is safe to ignore this finding.

binary, by convention m_1, and the mass ratio $q = m_2/m_1 \leq 1$:

$$p(m_1, m2) = \pi_1(m_1|m_{\rm min}, m_{\rm max}, \delta_{\rm min}, \alpha, \lambda_{\rm peak}, \mu_m, \sigma_m) \times \pi_2(q|m_1, m_{\rm min}, \delta_{\rm min}, \beta_q)\,, \tag{4.6.3}$$

where π_1 is a mixture density function, times a low-mass smoothing:

$$\begin{aligned}&\pi_1(m_1|m_{\rm min}, m_{\rm max}, \delta_{\rm min}, \alpha, \lambda_{\rm peak}, \mu_m, \sigma_m)\\ &\quad = C_1\left[(1-\lambda_{\rm peak})\,\mathfrak{P}_{[m_{\rm min},m_{\rm max}]}(m_1|-\alpha, m_{\rm min}, m_{\rm max}) + \lambda_{\rm peak} G_{[m_{\rm min},m_{\rm max}]}(m_1|\mu_m, \sigma_m)\right]\\ &\qquad \times S(m_1|m_{\rm min}, \delta_{\rm min})\,.\end{aligned} \tag{4.6.4}$$

Here $\mathfrak{P}_{[m_{\rm min},m_{\rm max}]}$ is a truncated power-law distribution with negative spectral index $-\alpha$, normalized within the $[m_{\rm min}, m_{\rm max}]$ range, $G_{[m_{\rm min},m_{\rm max}]}$ is a similarly-truncated Gaussian density function representing a possible mass pile-up of BBHs before the SN pair-instability gap [288], C_1 is an overall normalization factor (made necessary by the presence of the smoothing function), and S is a smooth cutoff for low masses that interpolates between 0 and 1 in the interval $[m_{\rm min}, m_{\rm min} + \delta_{\rm min}]$ as

$$S(m|m_{\rm min}, \delta_{\rm min}) = \begin{cases} 0 & \text{if } m < m_{\rm min} \\ [f(m - m_{\rm min}, \delta_{\rm min}) + 1]^{-1} & \text{if } m \in [m_{\rm min}, m_{\rm min} + \delta_{\rm min}]\,, \\ 1 & \text{if } m > m_{\rm min} + \delta_{\rm min} \end{cases} \tag{4.6.5}$$

with

$$f(m - m_{\rm min}, \delta_{\rm min}) = \exp\left(\frac{\delta_{\rm min}}{m - m_{\rm min}} + \frac{\delta_{\rm min}}{m - m_{\rm min} - \delta_{\rm min}}\right). \tag{4.6.6}$$

The probability density function π_2 for the mass ratio q in eq. (5.6.3) is

$$\pi_2(q|m_1, m_{\rm min}, \delta_{\rm min}, \beta_q) = C_q q^{\beta_q} S(q m_1|m_{\rm min}, \delta_{\rm min})\,, \tag{4.6.7}$$

where $C_q(m_1, m_{\rm min}, \delta_{\rm min}, \beta_q)$ is a normalization factor. The fact that C_q depends on m_1, in particular, makes the distribution in eq. (5.6.3) non-separable. It can be computed as

$$C_q^{-1}(m_1) = \frac{1}{m_1}\int_{m_{\rm min}}^{m_1} {\rm d}m_2\, q^{\beta_q}\, S(q m_1|m_{\rm min}, \delta_{\rm min})\,. \tag{4.6.8}$$

The LVK analysis with the latest GWTC-3 data constrains the boundaries of the mass range as $m_{\rm min} = 5.1^{+0.9}_{-1.5}\,M_\odot$, $m_{\rm max} = 86.9^{+11.4}_{-9.4}\,M_\odot$. The parameters of the larger-mass distribution are inferred as $\alpha = 3.40^{+0.58}_{-0.49}$, $\lambda_{\rm peak} = 0.039^{+0.058}_{-0.026}$, $\mu_m = 33.7^{+2.3}_{-3.8}\,M_\odot$, $\sigma_m = 3.6^{+4.6}_{-2.1}\,M_\odot$, the spectral index of the mass ratio as $\beta_q = 1.1^{+1.8}_{-1.3}$, and the single parameter of the smoothing function as $\delta_{\rm min} = 4.8^{+3.3}_{-3.2}\,M_\odot$.

The probability distribution of each of the spin amplitudes a_i in eq. (4.6.2) is a concave Beta distribution function in the amplitude interval (in natural units) $[0, 1]$, with parameters (α_a, β_a) [289]:

$$p(a_i|\alpha_a, \beta_a) = {\rm Beta}(a_i|\alpha_a, \beta_a)\,. \tag{4.6.9}$$

As in the LVK analysis, the subscript a stands for "amplitude" and α_a should not be confused with the parameter α of the mass distribution $p(m_1, m_2)$. The arguments $\alpha_a > 1$ and $\beta_a > 1$ of the Beta distribution are linked to the expected value and variance of the inferred amplitudes (*i.e.* all the inferred a_1 and a_2 joined into a single data set) via the relationships

$$\mathrm{E}[a] = \frac{\alpha_a}{\alpha_a+\beta_a}\,, \qquad \mathrm{Var}[a] = \frac{\alpha_a\beta_a}{(\alpha_a+\beta_a)^2(\alpha_a+\beta_a+1)}\,, \tag{4.6.10}$$

which the LVK analysis estimates to be $\mathrm{E}[a] = 0.25^{+0.09}_{-0.07}$ and $\mathrm{Var}[a] = 0.03^{+0.02}_{-0.01}$.

Lastly, the distribution for the spin tilts t_i are given by independent mixtures of an isotropic component and a truncated Gaussian component centered at perfect alignment [288]:

$$p\left(\cos(t_1), \cos(t_2)|\sigma_t, \zeta\right) = (1-\zeta)\left(\frac{1}{2}\right)^2 + \zeta\, G_{[-1,1]}(\cos(t_1)|1, \sigma_t)\, G_{[-1,1]}(\cos(t_2)|1, \sigma_t)\,. \tag{4.6.11}$$

For the values of this distribution, GWTC-3 infers $\zeta = 0.66^{+0.31}_{-0.52}$ and $\sigma_t = 1.5^{+2.0}_{-0.8}$.

4.6.3 Appendix A.3 : Time-to-coalescence and frequency of emission

Here we discuss the role of the residual time to coalescence for the population synthesis and the SGWB computation.

A correct prediction of the SOBBH SGWB in the LISA band implies catalogs that are complete enough to adequately simulate the signal. On the other hand, the only observational knowledge we have on these sources comes from LVK observations, which probe the population of merging SOBBHs. In sec. {4.2.1} we have shown that, under the hypothesis that the binaries formation, and therefore their coalescence rates, is in a steady state, the binary rate $R(z, \tau_c)$ in eq. (4.2.1) is indeed equivalent to the one of the merging binaries, constrained by LVK observations. This allows us to construct the catalogs and consequently, the SGWB estimation based on the LVK GWTC-3 posterior.

The hypothesis that the binary formation is in a steady state implies that we sample the time-to-coalescence of the binaries in the catalogs uniformly in the range $\tau_c^{(\mathrm{det})} \in [0, \tau_{c,\mathrm{max}}^{(\mathrm{det})}]$. We have imposed $\tau_{c,\mathrm{max}}^{(\mathrm{det})} = 10^4$ yrs, much smaller than the typical time over which the SOBBH population is expected to change, $\mathcal{O}(10^9)$ yrs. However, is this good enough to account for all the binaries emitting in the LISA band for the entire mission duration? In other words, are the simulated catalogs representative enough of the SOBBH population relevant for LISA? In what follows we demonstrate that, while not complete, our catalogs do indeed provide all the information necessary for a good characterization of the SOBBH SGWB, as far as our choices on the time-to-coalescence are concerned.

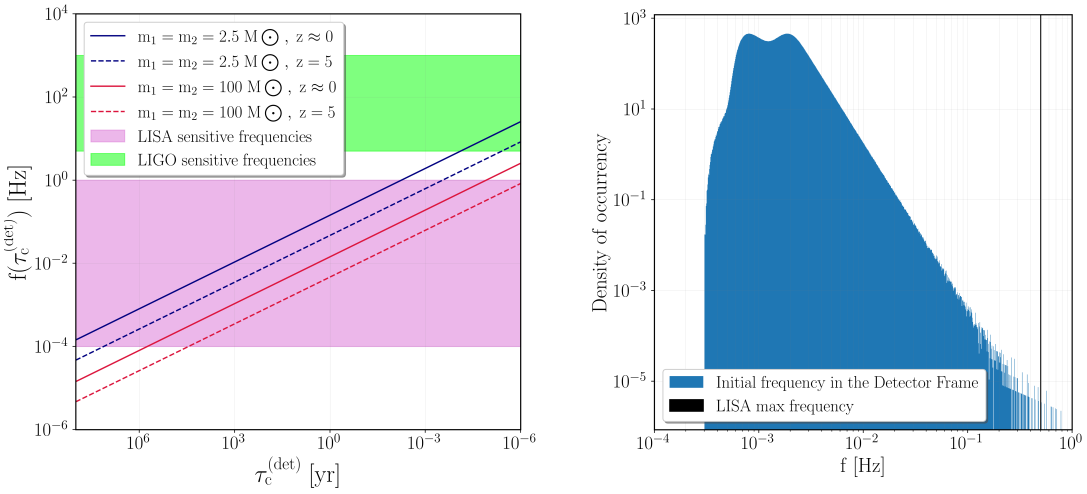

Figure 4.15. Left panel: Evolution of the frequency during the inspiral phase as a function of the time-to-coalescence for light, mid, and large mass SOBBHs. Pink and green bands represent the LISA and LIGO frequency bands. Right panel: The frequency distribution emerging in one of the benchmark catalogs, constructed with a flat τ_c prior.

The time interval over which we need to integrate the merger rate in order to obtain the appropriate number of observed events is

$$T_{\rm tot} = T_{\rm obs} + T_{\rm maxBand}, \tag{4.6.12}$$

where $T_{\rm obs}$ denotes the total detector observation time, while $T_{\rm maxBand}$ is the maximum, over all the binaries in the Universe, of the portion of each binary's lifetime (*i.e.* of τ_c) which is spent in the detector frequency range. While in the case of LVK $T_{\rm maxBand}$ is less than seconds, so that $T_{\rm tot} \simeq T_{\rm obs}$, LISA probes the SOBBH population at a different stage when they are still far from merging. Inserting the minimal LISA frequency $2 \cdot 10^{-5}$ Hz and the minimal mass in the catalogs $m_{\rm min} = 2.5\ M_\odot$ (see sec. {4.2.4}) in the Newtonian relation for circular orbits (here expressed at the detector, so that $\mathcal{M}_z$ is the redshifted chirp mass) [265]

$$f = \frac{1}{8\pi}\left[\frac{1}{5}\left(\frac{G\mathcal{M}_z}{c^3}\right)^{5/3}\tau_c^{(\rm det)}\right]^{-3/8}, \tag{4.6.13}$$

one obtains the maximal time-to-coalescence $\tau_c^{(\rm det)} \simeq 2 \cdot 10^{10}$ yrs in the worst case scenario of an equal mass binary at the minimal catalog redshift $z_{\rm min} = 10^{-5}$ (see sec. {4.2.3}). Therefore, in the case of LISA, $T_{\rm tot} \simeq T_{\rm maxBand}$, and setting $\tau_{c,\rm max}^{(\rm det)} = 10^4$ yrs appears inappropriate by as much as 6 orders of magnitude.

In reality, $\tau_{c,\rm max}^{(\rm det)} = 10^4$ yrs is a suitable choice that, while preserving computational feasibility, still provides all the relevant information for the SGWB evaluation. By cutting the time-to-coalescence sampling at $\tau_{c,\rm max}^{(\rm det)} = 5(10)[15] \times 10^3$ yrs, given the catalogues mass range $2.5\,M_\odot < m_2 < m_1 < 100\,M_\odot$ (see sec. {4.2.4}) and their redshift

range $10^{-5} < z < 5$ (see sec. {4.2.3}), according to eq. (4.6.13) one is disregarding some binaries with $f \lesssim 5.9(4.5)[3.9]\,\mathrm{mHz}$ and all binaries with $f \lesssim 0.19(0.15)[0.13]\,\mathrm{mHz}$, as illustrated in fig. 4.15. Figure 4.5 shows the aggregated effect of this suppression in the SGWB (note that this figure is produced setting $z_{\max} = 1$, as explained in sec. {4.2.4}): it is clear from this figure that the relevant spectral property of the SGWB signal, *i.e.* the power-law behavior in frequency, is still well captured by the signal produced via the simulated catalogs. The bending at low frequency is nonphysical and therefore irrelevant: the SGWB is expected to simply continue with the same power-law behavior at low frequencies for synthetic populations with much higher $\tau_{c,\max}$. Furthermore, in fig. 4.12, we can see that the GB foreground overcomes the SOBBH SGWB below 2–3 mHz. It is thus unlikely that an increase beyond $\tau_{c,\max} = 10^4\,\mathrm{yrs}$ would produce a noticeable effect in any realistic study. Given the growing computational cost of generating (and computing the SGWB of) synthetic populations with larger $\tau_{c,\max}$, we conclude that $\tau_{c,\max}^{(\mathrm{det})} = 10^4\,\mathrm{yrs}$ is a good compromise for the purposes of this study.

Chapter 5

Article: Probing primordial black holes at high redshift with future gravitational wave detectors

To Appear

Paolo Marcoccia,[a] Germano Nardini,[a] Mauro Pieroni[b]

[a]Department of Mathematics and Physics, University of Stavanger, NO-4036 Stavanger, Norway

[b]Department of Theoretical Physics, CERN, 1211 Geneva 23, Switzerland

E-mail: paolo.marcoccia@uis.no, germano.nardini@uis.no, mauro.pieroni@cern.ch

Abstract. We analyze the detection prospects for potential Primordial Black Hole Binary (PBHB) populations buried in the Stellar-Origin Black Hole Binary (SOBHB) population inferred by the LVK collaboration. We consider different PBHB population scenarios and several future Gravitational Wave (GW) detectors. To separate the PBHB component from the SOBHB one, we exploit the prediction that the PBHB merger rate does not decline as fast as the SOBHB one at high redshift. However, only a tiny fraction of PBHB events may be resolved individually, and the sub-threshold events may yield an undetectable Stochastic GW Background (SGWB). For this reason, we determine the statistical significance of the PBHB contributions in the number of resolvable events seen in future Earth-based detectors and the SGWB measured at LISA. We find that the synergy between these probes will consistently help assess whether or not a sizeable PBHB population is present.

5.1 Introduction

LIGO's first Gravitational Wave detection labeled GW150914 [44, 290] opened the gates to the world of GW astronomy. Since that detection, the sensitivity of LIGO detectors has increased considerably, and the Virgo [291] and KAGRA [292] experiments have also joined the network. At present, the LVK network has identified over ninety GW events involving Black Holes and Neutron Stars [45] and has started constraining the statistical properties of the *Stellar Mass Black Hole Binaries (SMBHB)* population, although some bounds remain loose. Primarily, these limitations arise from the current detector sensitivity, which only leads to a low number of events measured with high precision. The determination of the merger rate distribution at high redshift ($z \gtrsim 1$) is a striking example of these limitations. As a matter of fact, the properties of the population at $z \gtrsim 1$ are, currently, only guessed by using phenomenological models following the Star Formation Rate [56, 57, 130], leaving open space for the presence of both long time delays in the *Black Hole Binary (BHB)* formation [293] and a variety of subpopulations with different redshift behaviours [52, 294, 295] (see also refs. [182, 235, 243, 296, 297]). While this might be a reasonable assumption if all the events observed by current detectors are BHBs of Stellar Origin (SOBHBs), at least in principle, different scenarios are possible, leading to different high redshift behaviors.

An intriguing alternative for BH formation is the possibility for BHs to form due to some cosmological processes occurring in the early Universe. These objects are typically dubbed *Primordial Black Holes* to differentiate from BHs produced in some late-time astrophysical processes. PBHs might form when strong scalar perturbations, *e.g.*, generated by some inflationary model violating slow-roll, re-enter the Universe horizon, leading to the collapse of some regions of space [136, 137, 298, 299]. Such a mechanism would make PBHs, and in particular *PBH Binaries (PBHBs)*, completely independent of star formation processes. Different inflationary mechanisms and early-Universe histories can result, *e.g.*, in vastly different PBH abundances and mass distributions (see, *e.g.*, [16, 49, 132, 134, 300, 301] for reviews of PBH formation and constraints). Interestingly, depending on the formation scenario, PBHs can account for a substantial portion of the observed *Dark Matter (DM)* abundance [16, 133, 148, 301]. Furthermore, at least one of the two BHs in some SMBHBs might be of primordial origin, and, more in general, a PBHB population might contribute[1] to the events currently observed by LVK detector [302, 304–307]. In such a case, some statistical properties and observable signatures might radically differ from those arising when all SMBHBs are SOBHBs.

Despite their radically different origin and phenomenology, PBHs are elusive at current GW detectors. The challenge is partly rooted in the lack of unquestionable,

[1] Notice, however, that LVK observations put tight constraints on the fraction of DM in PBHs for BHs in the stellar mass range [52, 302, 303].

discriminating predictions at low redshift (see ref. [308] for a systematic procedure to assess the origin of BBHs). The predictions on PBHs and SOBHBs at low redshift are indeed loose due to the plethora of viable inflationary mechanisms and the numerous unknowns on the stellar-origin formation channels. On the contrary, a robust model-independent discrimination criterion exists at high redshift: at distances larger than the SFR peak ($z \simeq 2$), the SOBHB merger rate must fast decline, whereas the PBHB merger rate can keep growing [274, 294, 302, 306, 309, 310]. Remarkably, while the SFR peak is beyond the reach of the present LVK interferometers, it will be in the range[2] of future Earth-based detectors [55, 58, 285, 312–317]. In addition, the Laser Interferometer Space Antenna (LISA) [59], might look for imprints of PBHs in the milliHertz band from individual events [16, 318, 319] and the Stochastic Gravitational Wave Bacground [16, 146, 320–322]. Moreover, LISA will be sensitive to the SGWB due to the incoherent superposition of the weak signals from the SMBHB population, which, including the contribution of binaries at high-redshift, brings information on the behavior of the population above the SFR peak [182, 221, 233, 235, 273, 274].

In the present paper, we discuss the detection prospects for the PBHB population using its high-redshift behavior [316, 317, 323, 324]. Specifically, we study how future detectors might be able to identify PBHB populations beyond a certain *Fiducial Population* of SOBHB (based on ref. [182]), which is broadly compatible with the current LVK observations [45, 296]. For this purpose, we consider some well-established PBHB population models [274, 309] and we show how different detectors will complementarily probe their parameter spaces. In general, we expect our qualitative results to be independent of our fiducial population and PBHB models. However, the quantitative outcomes are contingent upon our population selections, so it will be worth repeating our analysis when the statistical properties of the SMBHB subpopulations become less uncertain than they are today.

The paper is structured as follows: In sec. {5.2}, we describe the PBHB subpopulation models, and in sec. {5.3}, we describe the methodology that we adopt. Our results are presented in sec. {5.4}, where we show how different PBHB subpopulations will be detectable with future Earth- and space-borne GW detectors. In particular, we demonstrate that the SGWB detection will give important complementary information on the presence of deviations from the fiducial model. We devote sec. {5.5} to our final remarks and conclusions, while we describe some technicalities of our analysis in apps. {5.6}, {5.7}, {5.8}, {5.9} and {5.10}.

5.2 Population models

In this section, we present the population models that we analyze in this work. Following refs. [182, 296], for a given population the number of expected sources in a given

[2]It is worth stressing, however, that while detecting high-redshift events will be possible with future detectors, accurately inferring their distances will not be trivial [311].

interval of redshift and parameter space is given by

$$\frac{\mathrm{d}^2 N(z,\theta,\xi)}{\mathrm{d}\theta \mathrm{d}z} = R(z)\left[\frac{\mathrm{d}V_c}{\mathrm{d}z}(z)\right]\frac{T_{\mathrm{Obs}}}{1+z}\,p(\theta|\xi)\,, \tag{5.2.1}$$

where T_{Obs} is the detector observation time, $\mathrm{d}V_c/\mathrm{d}z(z)$ is the differential comoving volume, $R(z)$ is the merger rate, and $p(\theta|\xi)$ is the *Probability Distribution Function (PDF)* for the source to have some specific values for the binary parameters (collectively denoted with θ) given some population hyperparameters (collectively denoted with ξ)[3]. Notice that since $p(\theta|\xi)$ is normalized, the number of events in a redshift interval $[z_m, z_M]$ is given by

$$\Delta N_{z_m,z_M} = \int_{z_{\mathrm{m}}}^{z_{\mathrm{M}}} \frac{\mathrm{d}N(z)}{\mathrm{d}z}\,\mathrm{d}z = T_{\mathrm{Obs}}\int_{z_{\mathrm{m}}}^{z_{\mathrm{M}}} \frac{R(z)}{1+z}\left[\frac{\mathrm{d}V_c}{\mathrm{d}z}(z)\right]. \tag{5.2.2}$$

More in detail, the PDF term $p(\theta|\xi)$ can be expressed as

$$p(\xi|\theta) = p(m_1, m_2|\xi_{\mathrm{Mass}}) \times p(\theta_{\mathrm{Angles}}|\xi_{\mathrm{Angles}}) \times p(\theta_{\mathrm{Spins}}|\xi_{\mathrm{Spins}})\,, \tag{5.2.3}$$

where m_1 and m_2 are the two masses, $p(m_1, m_2|\xi_{\mathrm{Mass}})$ is the mass function depending on some hyperparameters ξ_{Mass}, $p(\theta_{\mathrm{Angles}}|\xi_{\mathrm{Angles}})$ is the angle PDF, and $p(\theta_{\mathrm{Spins}}|\xi_{\mathrm{Spins}})$ is the spin PDF. The sources are assumed to be isotropic in the sky, with inclination and polarization uniformly distributed in their considered prior. Eccentricity in the orbit is neglected throughout this work. The spin PDF is further expanded as

$$p(\theta_{\mathrm{Spins}}|\xi_{\mathrm{Spins}}) = p(a_1, a_2|\xi_{\mathrm{Spin\,Amplitude}}) \times p(\cos(t_1), \cos(t_2)|\xi_{\mathrm{Spin\,Tilt}})\,, \tag{5.2.4}$$

where $p(a_1, a_2|\xi_{\mathrm{Spin\,Amplitude}})$ and $p(\cos(t_1), \cos(t_2)|\xi_{\mathrm{Spin\,Tilt}})$ are the spin amplitude and spin tilt PDFs, with a_i and t_i (with $i = 1, 2$) denoting the normalized spin amplitude and the angle between the binary angular momentum and the spin of the body i, respectively.

In our analysis, the SMBHB population consists of the sum of the SOBHB and PBHB subpopulations. We model each subpopulation using the framework outlined in eq. (5.2.1) and neglect binaries with mixed origins. For the SOBHB population, we consider a fiducial population model, utilizing *Probability Density Functions (PDFs)* derived from the most recent LVK studies. We set their hyperparameters to the best-fit values as determined by these studies [296]. We remind that the LVK data, which we refer to as GWTC-3, provide no direct constraint at $z \gtrsim 1$. To extend our analysis to the redshift range $1 \lesssim z \lesssim 10$, we assume that the SOBHB merger rate R_{SOBHB} tracks the SFR and that the PDFs remain redshift-independent. Specifically, we employ a phenomenological merger rate that closely follows the *Madau-Dickinson SFR* [56] with negligible time delay (see [225, 227, 325]). Appendix {5.6} provides further details

[3]Consistently with the most recent LVK analyses [230, 296], we are assuming the PDF to be separable. In particular, we assume all other parameters not to depend on the redshift.

about our approach.

Due to their early-universe origin, PBHBs have different statistical properties than SOBHBs, and, in particular, the PBHB merger rate is not expected to track the SFR. While several possibilities exist in the literature (see, *e.g.*, ref. [309]), for the PBHB merger rate we adopt [306, 310]

$$R_{\rm PBHB}(z) = \varepsilon R_0 \left[\frac{t(z)}{t(z=0)}\right]^{-34/37} \tag{5.2.5}$$

which corresponds to a power law in cosmic time $t(z)$ [274, 294], normalized so that in $z = 0$ it is ε-times smaller than the fiducial SOBBH merger rate R_0 at the same redshift. Figure 5.1 shows the fiducial SOBHB merger rate and the PBHB merger rate for some values of ε. As far as $\varepsilon \ll 1$, within the LVK horizon ($z \lesssim 1$) the PBHB population is subdominant and (up to a few outliers) the whole SMBHB population of GWTC-3 exhibits the SOBHB properties. On the other hand, most PBHB subpopulations become relevant after the peak of the SFR. This is particularly evident from the dashed lines in the right panel of fig. 5.1, which shows $\hat{N}_z^{\rm Pop}$ number of events redshift z predicted by population Pop, which is given by

$$\hat{N}_z^{\rm Pop} \equiv \frac{\Delta N^{\rm Pop}_{z_m,z_M}}{\Delta z}\,, \tag{5.2.6}$$

where $\Delta N^{\rm Pop}_{z_m,z_M}$ is defined in eq. (5.2.2) with the additional superscript specifying the considered population. By normalizing with $\Delta z = z_M - z_m$, we ensure that, for sufficiently small bin sizes, $\hat{N}_z^{\rm Pop}$ is independent of the specific binning scheme used in the analysis. The total PBH energy density normalized to the critical density $\Omega_{\rm PBH}$ is typically rescaled by the DM energy density parameter, $\Omega_{\rm DM}$, to get the fraction of DM in PBHs, $f_{\rm PBH} \equiv \Omega_{\rm PBH}/\Omega_{\rm DM}$. For techniques to relate the merger rate in eq. (5.2.5) to $f_{\rm PBH}$ see app. {5.7}.

For the PBHB mass distribution, we assume each of the two masses in the binary to be drawn from the same PDF[4], *i.e.*, $P(m_1) = P(m_2)$, which we set to be a *Log-Normal (LN)*

$$\Phi_{\rm LN}(m) = \frac{1}{\sqrt{2\pi m^2 \sigma_{\rm LN}^2}} \exp\left[-\frac{\ln^2(m/\mu_{\rm LN})}{2\sigma_{\rm LN}^2}\right]\,, \tag{5.2.7}$$

where $\mu_{\rm LN}$ and $\sigma_{\rm LN}$ are the hyperparameters setting the position and width of the peak.

Finally, we comment on the choices for the PDFs of the other variables. Since the PBHB spin PDF is still an argument of debate [327–329], we assume the PBHB

[4]This simplifying assumption doesn't include the effect of suppression terms in the mass function [55, 303, 306, 310, 326]. In the formalism of this paper, these effects are hidden in the definition of ε. For details see app. {5.7}.

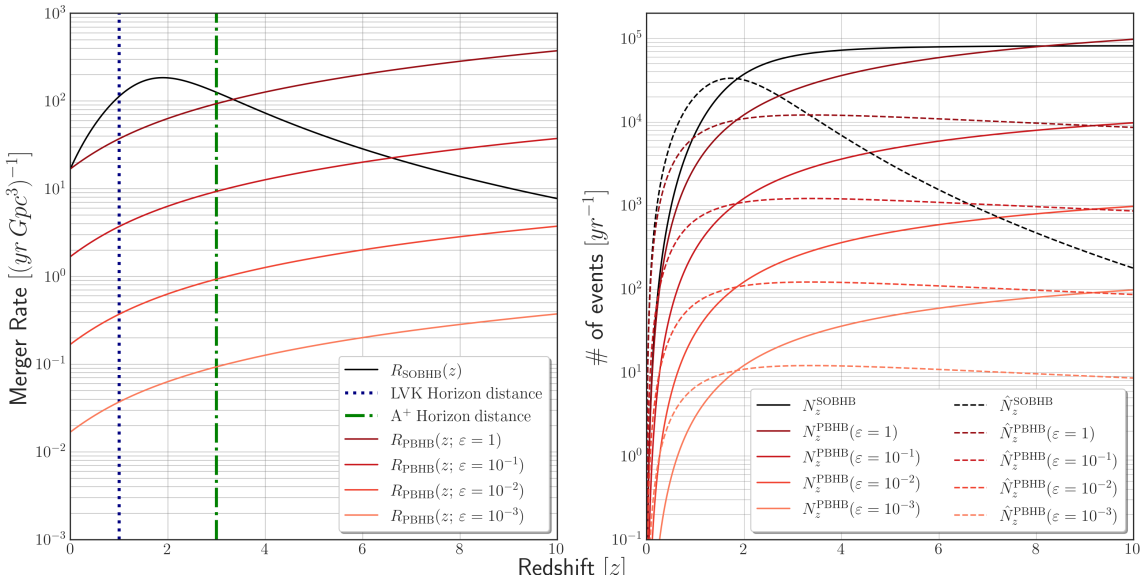

Figure 5.1. *Left panel:* Merger rate as a function of redshift for different populations (solid curves). The dashed, vertical lines mark the maximal horizon distances of LVK (dotted blue line) and LIGO A$^+$ (dash-dotted green line). *Right panel:* number of events per year within a redshift volume (solid lines) and number of events per year per redshift bin normalized by the bin width (dashed lines) as functions of redshift for different populations. In both panels, the quantities of the fiducial SOBHB population are marked in black, and those of the PBH population with varying ε are marked in red (dark to light for decreasing ε).

spin distribution to be the same as the SOBHB one (see app. {5.6} and, in particular, table [5.4]). Similarly, we assume all the angular variables (including the phase of the binary) to follow the same distribution of SOBHBs.

5.3 Methodology

This section describes our methodology to identify a PBHB population component on top of the fiducial population consistent with GWTC-3. Our analysis studies the detectability of individual sources and SGWB with future GW detectors. Specifically, we consider LIGO A$^+$ and ET, with either 1 or 10 years of observations, for the measurement of individual sources, and LISA, assuming either 4 or 10 years of observations, for the SGWB detection and characterization. While our analysis concerns the PBHB population models presented in sec. {5.2}, a similar methodology could be applied to other PBH scenarios and GW detectors. For details on the detector characteristics and our numerical codes, see app. {5.9} and the repository [330], respectively.

5.3.1 Resolvable sources analysis

Our analysis of individually resolvable sources relies on measurements performed with Earth-based detectors. In particular, we check whether the presence of the PBHB subpopulation increases the expected number of detectable sources by more than $3\,\sigma$

beyond the number predicted by the fiducial population. For this purpose, hereafter we define an event as "detectable" when its Signal-to-Noise Ratio (SNR) (see definition in eq. (5.3.3)) is larger than some threshold value $\mathrm{SNR}_{\mathrm{Thr}}$, which we set to 8.

Let us start by briefly reviewing the methods to evaluate the SNR associated with a GW signal. The signal, h, measured by any GW detector is expressed as

$$h = F_{ij}^{+} h_{ij}^{+} + F_{ij}^{\times} h_{ij}^{\times} \,, \tag{5.3.1}$$

where h_{ij}^{+} and $h_{ij}^{\times}$ denote the two GW polarization modes, while F_{ij}^{+} and $F_{ij}^{\times}$ are the detector pattern functions (for details, see *e.g.*, ref. [331]). The two GW modes can be further expanded as a combination of polarization tensors e_{ij}^{+}, $\mathrm{e}_{ij}^{\times}$, and a waveform depending on the source parameters. In our study, we employ the IMRPhenomXHM waveform [173], a phenomenological waveform from the IMRPhenom family [171, 172, 332–334], offering a good compromise between quality and computation speed. With this choice, the signal depends on the parameters

$$m_1, m_2, d_L, \phi_0, \tau_c, \theta, \phi, \iota, \psi, \chi_1, \chi_2 \,, \tag{5.3.2}$$

where m_1 and m_2 are the masses of the two BHs in the detector frame, d_L is the luminosity distance, ϕ_0 is the binary's initial phase, τ_c is the coalescence time, θ and ϕ are the binary's latitude and longitude, ι is the angle between the binary's angular momentum and the line of sight, ψ is the orientation, and χ_1 and χ_2 are the two (dimensionless) spin amplitudes projected on the orbital plane. Finally, the SNR for a given source and a given detector is defined as [335]

$$\mathrm{SNR}^2 = 4 \int_{f_{\mathrm{m}}}^{f_{\mathrm{M}}} \frac{\mathrm{Re}[h^* h]}{S_n(f)} \, \mathrm{d}f \,, \tag{5.3.3}$$

where $S_n(f)$ is the detector strain sensitivity (see sec. {5.9}), while f_{m} and f_{M} are the minimal and maximal detector frequencies. Notice that in this equation, h depends on all the parameters listed in eq. (5.3.2) but, for a large sample of sources, only their average values matter in our analyses, at least at the leading order. This is why in several evaluations, *e.g.*, the analytical estimates, we can average over both the spins (χ_1, χ_2) and angular $(\theta, \phi, \iota, \psi)$ variables; we dub this approximated SNR as $\mathrm{SNR}_{\mathrm{avg}}$. However, as a check of robustness, in a few cases, we test our averaged-based results with those obtained without the average approximation, and we indicate the result of this precise evaluation simply as SNR (*i.e.*, without any subscript).

As a first step, to fast probe the PBHB detectability in a broad part of their parameter space, we perform a semi-analytical analysis. For this purpose, we modify eq. (5.2.6) by including a selection effect. Specifically, we define the expected number of resolvable sources at redshift z for the population Pop as

$$\hat{N}_z^{\mathrm{Res,Pop}} \equiv \frac{\Delta N_{z_m, z_M}^{\mathrm{Res,Pop}}}{\Delta z} = \frac{T_{\mathrm{Obs}}}{\Delta z} \int_{z_m}^{z_M} \frac{R^{\mathrm{Pop}}(z)}{1+z} \left[\frac{\mathrm{d}V_c}{\mathrm{d}z}(z) \right] \int p^{\mathrm{Pop}}(\xi|\theta) \, \theta_{\mathrm{SNR}_{\mathrm{avg}}}(\xi) \, \mathrm{d}\xi \, \mathrm{d}z \,, \tag{5.3.4}$$

where, for any given detector, the selection function $\theta_{\mathrm{SNR_{avg}}}(\xi)$ is a *Heaviside* Θ *function* filtering the sources with $\mathrm{SNR_{avg}}$ larger than $\mathrm{SNR_{Thr}} = 8$. The integrals in eq. (5.3.4) are carried out numerically. Notice that due to the presence of the selection function, the integration over the ξ variables has to be computed explicitly.

We use eq. (5.3.4) to set our (analytic) criterion for the identification of the PBHB component via resolvable sources at Earth-based detectors. We define the PBH contribution to be visible if, in a given bin in z, it satisfies the condition

$$\hat{N}_z^{\mathrm{Res,PBHB}} > 3\Delta_z^{\mathrm{Res,Fid}} \equiv 3\sqrt{\hat{N}_z^{\mathrm{Res,Fid}}}\,. \tag{5.3.5}$$

In other words, the PBHB component can be separated from the fiducial SOBBH component if there exists a bin in z, in which the number of resolvable sources, $\hat{N}_z^{\mathrm{Res,PBHB}}$, exceeds the number of resolvable SOBHB sources, $\hat{N}_z^{\mathrm{Res,SOBHB}}$, by $3\,\sigma$. In our case, the error comes from a Poissonian distribution, and this is why we have $\Delta_z^{\mathrm{Res,Fid}} = \sqrt{\hat{N}_z^{\mathrm{Res,Fid}}}$.

The semi-analytic analysis is fast but disregards two effects: the populations' realization dependence and the impact of the angular and spin variables on the SNR. We quantify these effects by running a more sophisticated analysis on some PBHB population benchmarks. Specifically, we use the code in ref. [253] to sample over the PDF in eq. (5.2.1) and generate $n_{\mathrm{r}} = 100$ catalogs of the SOBBH fiducial population and one catalog per PBHB benchmark population. Then, for every merger event predicted in the catalogs, we compute $\mathrm{SNR_{avg}}$ and the exact SNR. We define as $\Delta\hat{\mathcal{N}}_{z_{\mathrm{m}},z_{\mathrm{M}}}^{\mathrm{Res,Pop}}$ the number of events with $\mathrm{SNR_{avg}} > \mathrm{SNR_{Thr}}$ in a given redshift interval $z_{\mathrm{m}} \leq z \leq z_{\mathrm{M}}$ for the catalogue i of the population Pop. Similarly, we define as $\Delta\overline{\mathcal{N}}_{z_{\mathrm{m}},z_{\mathrm{M,i}}}^{\mathrm{Res,Pop}}$ the analogous quantity obtained with the detectability condition $\mathrm{SNR} > \mathrm{SNR_{Thr}}$. For convenience, we also introduce

$$\hat{\mathcal{N}}_{z,i}^{\mathrm{Res,Pop}} \equiv \Delta\hat{\mathcal{N}}_{z_{\mathrm{m}},z_{\mathrm{M}},i}^{\mathrm{Res,Pop}}/\Delta z\,, \qquad \overline{\mathcal{N}}_{z,i}^{\mathrm{Res,Pop}} \equiv \Delta\overline{\mathcal{N}}_{z_{\mathrm{m}},z_{\mathrm{M}},i}^{\mathrm{Res,Pop}}/\Delta z\,. \tag{5.3.6}$$

The mismatches between $\hat{\mathcal{N}}_{z,i}^{\mathrm{Res,Pop}}$ and $\hat{N}_z^{\mathrm{Res,Pop}}$ highlight the effect of the realization dependence that our semi-analytic results neglect. However, we expect the mismatch to be statistically within the Poisson deviation from the mean, *i.e.*,

$$\left|\hat{\mathcal{N}}_{z,i}^{\mathrm{Res,Pop}} - \mu_z^{\mathrm{Res,Pop}}\right| < 3\,\sigma_z^{\mathrm{Pop,Res}} \qquad \text{at } 95\%\text{ C.L.}\,, \tag{5.3.7}$$

where

$$\hat{\mu}_z^{\mathrm{Res,Pop}} \equiv \frac{\Delta\hat{\mu}_{z_{\mathrm{m}},z_{\mathrm{M}}}^{\mathrm{Res,Pop}}}{\Delta z} \equiv \frac{1}{n}\sum_{i=1}^{n}\frac{\Delta\hat{\mathcal{N}}_{z_{\mathrm{m}},z_{\mathrm{M}},i}^{\mathrm{Res,Pop}}}{\Delta z}\,, \tag{5.3.8}$$

$$\hat{\sigma}_z^{\mathrm{Pop,Res}} = \sqrt{\frac{1}{\Delta z}\sum_{i=1}^{n}\frac{\left[\Delta\hat{\mathcal{N}}_{z_{\mathrm{m}},z_{\mathrm{M}},i}^{\mathrm{Res,Pop}} - \Delta\hat{\mu}_{z_{\mathrm{m}},z_{\mathrm{M}}}^{\mathrm{Res,Pop}}\right]^2}{n-1}}\,. \tag{5.3.9}$$

Here the index i runs over n, the number of realizations of each population scenario. Since we produce multiple realizations only of our fiducial population (namely $n = n_r = 100$), we focus on the realizations of this population to test eq. (5.3.7). This allows us to prove $\sigma_z^{\rm Res,Pop} \simeq \Delta_z^{\rm Res,Pop}$ and, in turn, to use $\Delta_z^{\rm Res,Pop}$ as a proxy of the realization dependences in our PBHB benchmarks.

The quantities $\overline{\mathcal{N}}^{\rm Res,Pop}_{z_{\rm m},z_{\rm M},i}$ are useful to investigate the impact of the approximation $\rm SNR_{avg}$, in which the SNR is computed by averaging over the angles and spin. For this purpose, we calculate the quantities $\overline{\mu}_z^{\rm Res,Pop}$ and $\overline{\sigma}_z^{\rm Pop,Res}$, given as in eqs. (5.3.8) and (5.3.9) but with the hat symbol replaced by the bar one. In the parameter regions where the approximation is satisfactory, $\hat{\mu}_z^{\rm Res,Pop}$ and $\overline{\mu}_z^{\rm Res,Pop}$ are expected to be practically equal[5].

All these quantities can be computed for different values of $T_{\rm Obs}$ and several detector sensitivities. For concreteness, we consider LIGO $\rm A^+$ and ET, assuming $T_{\rm Obs} = 1, 10\,\rm yr$ of data. Moreover, to simplify the notation, hereafter we drop all the z subscripts in all these quantities and refer to the quantity, say q, as $q^{\rm Res,Pop}$.

Let us comment on the assumptions of our analysis. The most relevant assumption resides in the procedure to evaluate the right-hand side of eq. (5.3.5). In particular, while a consistent analysis should account for both the realization error and the uncertainty in the model parameters, we evaluate eq. (5.3.5) using the central values for all the fiducial population parameters without including their uncertainties. There are three main reasons behind this choice:

1. The main message of this work is to stress the synergy between Earth-based and space-based GW detectors for what concerns assessing the presence of populations of high-redshift SMBBHs beyond our fiducial population. Thus, including further uncertainties in the analysis will quantitatively affect our results, but it will not change the message of the present work.

2. Current GW detections have only probed the Universe at $z \lesssim 1$ so that the peak in the SOBHB population directly descends from imposing the population to follow the SFR at high redshift. Moreover, we have no information on the possible presence of time delays, which might shift the SOBHB peak position. All these uncertainties should also be included to perform a consistent analysis.

3. With more measurements to come in the next few years (with improved sensitivity and possibly with more detectors joining the existing network), the determination of the model parameters will improve significantly. Currently, we

[5] In principle, it is possible to replace the whole semi-analytic approach with the much more time-consuming method based on realizations and precise SNR evaluation. In this case, the detection criterion for a PBH population realization would be $\overline{\mathcal{N}}_z^{\rm Res,Benchmark} > 3\,\overline{\sigma}_z^{\rm Fid,Res}$ instead of eq. (5.3.5).

have no reliable information on the errors in the measured values of the fiducial population parameters at the end of the next LVK runs[6].

For these reasons, we restrict ourselves to the case where the main uncertainty on $\hat{N}^{\rm Res,Pop}$ comes from the Poissonian error and postpone the more accurate, though more involved analyses, to future studies.

5.3.2 SGWB analysis

The SGWB from to the fiducial population, and its variation due to the PBHB subpopulations, is evaluated using the analytical approach introduced in ref. [236] (for details, see app. {5.10}). In this framework, the SGWB due to each population is parametrized as a simple power-law:

$$h^2\Omega^{\rm Pop}_{\rm GW}(f) = 10^{\alpha_{\rm Pop}} \left(\frac{f}{f_*}\right)^{\beta} , \tag{5.3.10}$$

where β is the tilt of the GW power spectrum and $\alpha_{\rm Pop}$ is the ($\log_{10}$ of) the amplitude at a reference (irrelevant) pivot frequency f_*. This parameterization assumes each frequency bin to be highly populated by the GW signals due to binaries in circular orbits, with negligible environmental effects, and emitting GWs only. If all these assumptions are satisfied, the template in eq. (5.3.10) can be further simplified by imposing $\beta = 2/3$ [235, 238, 274, 297]. Dropping any of these assumptions might induce modifications in this behavior[7]. Since in the following, we are interested in evaluating the SGWB at LISA scales, with frequencies in the range $f \in \{3\times10^{-5}\,, 0.5\}\,$Hz, we set $f_* = 0.01\,$Hz. To compute the amplitude of the SOBHB component, we integrate the SOBHB population up to $z \approx 10$, which provides an estimate that is accurate to within 1% error in the SGWB amplitude [182]. With these assumptions, we have $\alpha_{\rm SOBHB} = -12.0246$ at $f_* = 0.01$Hz. We follow the same procedure to compute $\alpha_{\rm PBH}$ predicted by a PBH population with a given set of hyperparameter values. However, the (unresolved) PBHB signals do not die off as fast as the SOBHB ones. For this contribution, we set the cut-off at $z = 100$ corresponding to a $\sim 10\%$ accuracy in the SGWB evaluation[8].

To assess the significance of the PBHB subpopulation in the SMBHB SGWB signal at LISA, we perform an analysis based on the Fisher Information Matrix (FIM) formalism. Given some data $\tilde{d}(f)$, containing signal $\tilde{s}(f)$ and noise $\tilde{n}(f)$, which we

[6] Data for the O4 run, which has both longer acquisition time and better sensitivity compared to O3, will be released in the next couple of years [336, 337], leading to significant improvement in the determination of all the population parameters. The parameter determination will improve even further with O5.

[7] Also the eccentricity of the orbit, astrophysical uncertainties, or individual source subtraction might affect the shape of the SGWB generated by a population of compact objects [182, 237, 282, 283, 338–342].

[8] To achieve the 1% accuracy level in the computation of $\alpha_{\rm PBH}$, one would have to integrate much higher values of z. Given the theoretical uncertainties on the distribution of PBHB at such high redshifts, we choose a cut-off that reasonably compromises between numerical and theoretical uncertainties [16].

assume to be Gaussian, with zero means, and characterized only by their variances[9], the (log-)likelihood can be written as

$$-\log\mathcal{L}(\tilde{d}|\vec{\theta}) \propto T\int_{f_{\rm min}}^{f_{\rm max}}\left\{\ln\left[D(f,\vec{\theta})\right]+\frac{\tilde{d}(f)\tilde{d}^*(f)}{D(f,\vec{\theta})}\right\}\,{\rm d}f\ , \tag{5.3.11}$$

where $f_{\rm min}$ and $f_{\rm max}$ are the minimal and maximal frequencies measured by the detector, T is the total observation time, and $D(f,\vec{\theta})$ is the model for the variance of the data, depending on some (signal and noise) parameters $\vec{\theta}$. The best-fit parameters $\vec{\theta}_0$ are defined to maximize $\log\mathcal{L}$:

$$\left.\frac{\partial\log\mathcal{L}}{\partial\theta^\alpha}\right|_{\vec{\theta}=\vec{\theta}_0} \propto T\int_{f_{\rm min}}^{f_{\rm max}}\frac{\partial\ln D(f,\vec{\theta})}{\partial\theta^\alpha}\left[1-\frac{\tilde{d}(f)\tilde{d}^*(f)}{D(f,\vec{\theta})}\right]=0\ , \tag{5.3.12}$$

which is clearly solved by $D(f,\vec{\theta}_0)=\tilde{d}(f)\tilde{d}^*(f)$. Then, the FIM $F_{\alpha\beta}$ is given by

$$F_{\alpha\beta}\equiv-\left.\frac{\partial^2\log\mathcal{L}}{\partial\theta^\alpha\partial\theta^\beta}\right|_{\vec{\theta}=\vec{\theta}_0}=T\int_{f_{\rm min}}^{f_{\rm max}}\frac{\partial\log D(f,\vec{\theta})}{\partial\theta^\alpha}\frac{\partial\log D(f,\vec{\theta})}{\partial\theta^\beta}\,{\rm d}f\ . \tag{5.3.13}$$

By definition, the FIM $F_{\alpha\beta}$ is the inverse of the covariance matrix $C_{\alpha\beta}$. As a consequence, estimates of the errors on the model parameters $\vec{\theta}$ are obtained by computing $\sqrt{{\rm diag}(C_{\alpha\beta})}=\sqrt{{\rm diag}(F^{-1}_{\alpha\beta})}$.

Notice that these forecasts match the real measurement errors only in the limit where the (log-)likelihood is sufficiently Gaussian around the best fit. When this condition is violated, the errors estimated with the FIM formalism might deviate significantly from the real errors. As a final comment on the procedure to compute our forecast, we stress that LISA will measure three data streams. Under some simplifying assumptions, these data streams can assumed to be independent in the AET TDI basis (see app. {5.9}), and the total Fisher matrix is given by

$$F^{\rm Tot}_{\alpha\beta}\equiv F^{\rm AA}_{\alpha\beta}+F^{\rm EE}_{\alpha\beta}+F^{\rm TT}_{\alpha\beta}=2F^{\rm AA}_{\alpha\beta}+F^{\rm TT}_{\alpha\beta}\ . \tag{5.3.14}$$

For what concerns the observation time we assume 100% efficiency and impose $T^{\rm LISA}_{\rm Obs}=$ 4yrs, and for reference, we show how results improve if the mission lifetime is extended to 10yrs.

Let us assume that the data are expressed in Ω units, and we have factored the detector response out (for details, see app. {5.9}), then, the variance $D(f,\vec{\theta})$ can be expanded as

$$D(f,\vec{\theta})=h^2\Omega_{\rm GW}(f,\vec{\theta}_s)+h^2\Omega_n(f,\vec{\theta}_n)\ , \tag{5.3.15}$$

[9]In reality, the resolution Δf is finite and given by $1/T$. As long as this frequency is much smaller than $f_{\rm min}$, we can effectively replace the discrete sums with integrals.

where $\Omega_{\rm GW}(f,\vec{\theta}_s)$ is the model for the signal, as a function of the frequency and some signal parameters $\vec{\theta}_s$, and $\Omega_n(f,\vec{\theta}_n)$ is the noise model, depending on the noise parameters $\vec{\theta}_n$. For what concerns the noise, we use the analytical two-parameter model commonly used in the literature (for details, see app. {5.9}). On the other hand, for the signal, we assume the model to consist of the sum of two contributions, one for the Fiducial population, and one for the PBHB subpopulation, each described by the template in eq. (5.3.10). Given the complete degeneracy between these two components, we will not attempt to measure them independently, but, rather, we will only forecast the precision on the determination of the overall amplitude, which in the pivot frequency is simply given by $\alpha_{\rm Tot} = \log_{10}(10^{\alpha_{\rm Fid}} + 10^{\alpha_{\rm PBH}})$. To assess the significance of the PBHB contribution, for each PBHB subpopulation, we will check whether the value of $\alpha_{\rm Fid}$, with its error band, is not compatible at some σ-level (from 1 to 3) with $\alpha_{\rm Tot}$, *i.e.*:

$$\alpha_{\rm Tot} - n\,\sigma_{\alpha,\rm Tot} > \alpha_{\rm Fid} + n\,\sigma_{\alpha,\rm Fid}\ , \tag{5.3.16}$$

where $\sigma_{\alpha,\rm Tot}$, $\sigma_{\alpha,\rm Fid}$ are the FIM errors on $\alpha_{\rm Tot}$, $\alpha_{\rm Fid}$, respectively and $n \in \{1,2,3\}$. For reference, we report that for $\alpha_{\rm Fid} = \alpha_{\rm SOBHB} = -12.0246$ at $f_* = 0.01$Hz, we have $\sigma^{\rm 4yr}_{\alpha,\rm Fid} \simeq 8.44\times10^{-3}$ and $\sigma^{\rm 10yr}_{\alpha,\rm Fid} \simeq 5.34\times10^{-3}$ at 68% confidence level after marginalizing over the error on β.

As in the previous section, we conclude by discussing the limitations of our analysis. Analogously to Earth-based detectors and following similar lines of reasoning, we did not include the uncertainties in the population parameters in our analyses[10]. Beyond that, the main assumption in our analyses is that the FIM formalism gives accurate estimates for the uncertainties in determining the model parameters. This approximation holds in the limit where the log-likelihood for the model parameters is sufficiently Gaussian around $\vec{\theta}_0$, which should be quite accurate for the specific injections considered in this work [182].

5.4 Results and discussion

Parameter	Range
R_0 fraction	$\varepsilon \in [10^{-3}, 1]$
Mass PDF central parameter	$\mu_{\rm LN} \in [0, 100]$
Mass PDF standard deviation	$\sigma_{\rm LN} = [0.1, 0.5, 1, 2.5]$
Integrated mass range	$m \in [0, 150]$
Earth-based integrated redshift range	$z \in [0, 10]$
SGWB integrated redshift range	$z \in [0, 10^2]$

Table 5.1. The range of parameter values used for the LN PDF in the semi-analytic analysis.

[10] A detailed study on how these uncertainties would affect the SGWB signal at LISA, can be found in ref. [182].

In this section, we present the results obtained by applying the methodology presented in sec. {5.3}. We start by discussing, in sec. {5.4.1}, the results we obtain with the LIGO A$^+$ detector. In particular, we will show results for 1 and 10 years of continuous observations compared with the constraints obtained with 4 and 10 years of measurements with LISA. The range of values considered both for the merger rate and LN mass function are summarized in table [5.1]. The same analysis for the ET detector is presented in sec. {5.4.2}. Given these results, we choose a set of benchmark points to assess the robustness of the analysis upon the inclusion of spin and sky localization parameters. Moreover, by explicitly generating some realizations of the populations, we test the impact of low statistics on the results of secs. {5.4.1} and {5.4.2}. This analysis is presented in sec. {5.4.3}.

5.4.1 Detectability of PBHB subpopulations using LISA and LIGO A$^+$

Let us discuss the results obtained with the LIGO A$^+$ detector, which are shown in fig. 5.2 when assuming either $T_{\rm Obs} = 1,\, 10\,$yrs of data (top and bottom subfigure, respectively). Each panel of these subfigures corresponds to a different value for $\sigma_{\rm LN}$ introduced in eq. (5.2.7). On the other hand, the x axes of these plots span different values for $\mu_{\rm LN}$, and the y axes correspond to different values of ε defined in eq. (5.2.5). For each point in the parameter space, we compute the integral in eq. (5.3.4) and look for the smallest value of z, say $\bar{z}$, such that the condition in eq. (5.3.5) is satisfied. The value of $\bar{z}$ sets the color in all these plots. Colorless areas correspond to injections that do not satisfy the condition in eq. (5.3.5) for any value of z. The magenta and light brown lines are defined by evaluation of the condition in eq. (5.3.16), for different values of $T_{\rm Obs}$ and $n \in \{1, 2, 3\}$. The gray area, typically appearing in the top right corner of some of these plots, represents the upper bound on the SGWB amplitude set by LVK detectors [243]. Finally, the numbered points are benchmarks that will be considered for the analysis in sec. {5.4.3}.

First of all, by analyzing the results in fig. 5.2, we observe that LIGO A$^+$ will only be able to observe events from the PBHB subpopulations up $z \lesssim 2$. This is both a consequence of the averaging over the spin and angular variables and the detector's sensitivity (which only allows for detecting events up to $z \lesssim 3$, see the horizon distance plots in fig. 5.13). Thus, LIGO A$^+$ will not be able to resolve events in the range where the PBHB subpopulation naturally dominates over the fiducial population, *i.e.*, at redshift higher than the peak of the SFR. As a consequence, either the fraction ε of the PBHB subpopulation is relatively high at low redshift, or LIGO A$^+$ will not be able to detect its presence. The additional information provided by the SGWB amplitude measured by LISA SGWB might provide an invaluable tool to break the degeneracy among different population models. In particular, the SGWB proves to be quite effective for probing models predicting very narrow peaks at low masses or very broad peaks with small values of ε.

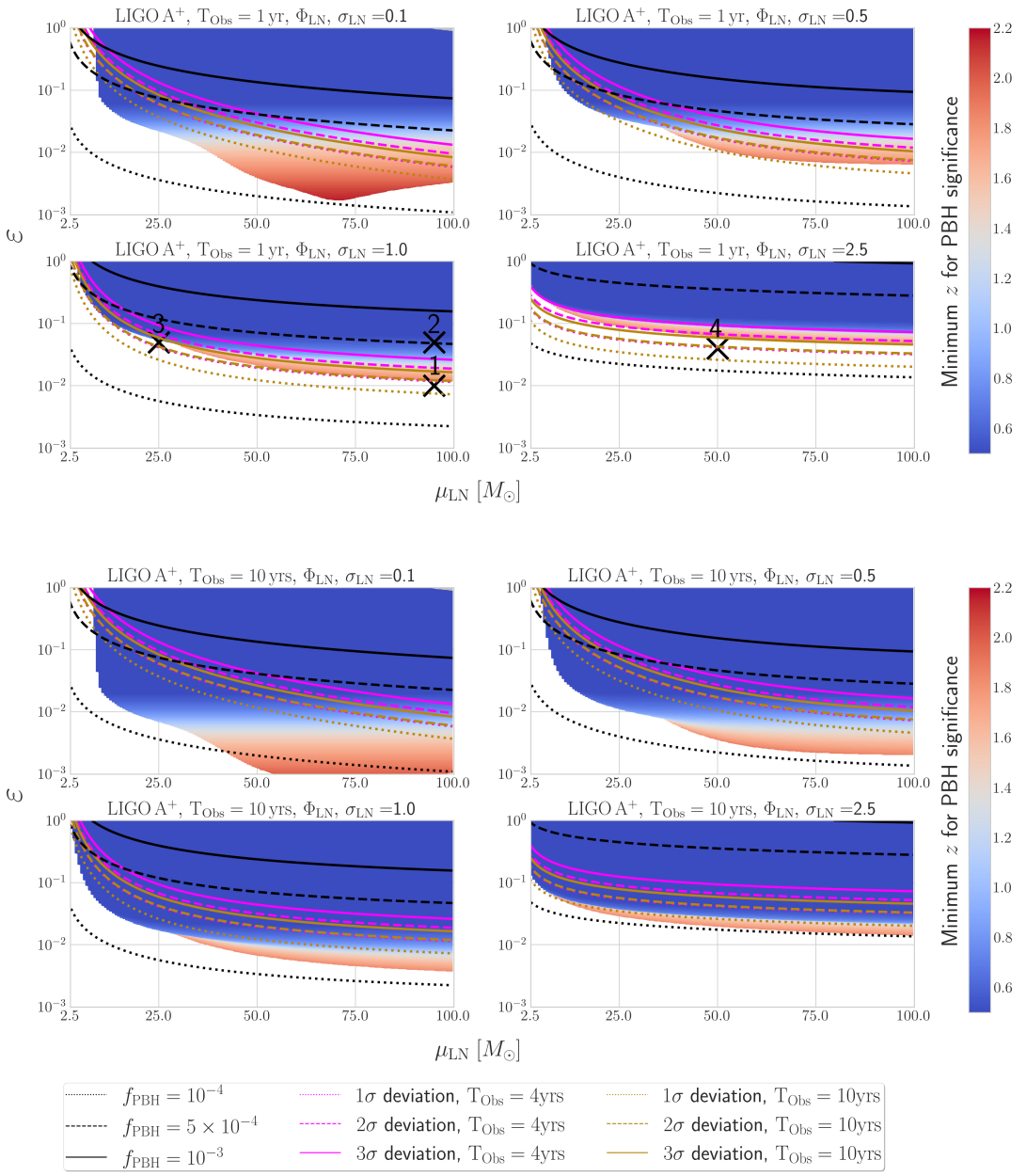

Figure 5.2. Analysis of the parameter spaces of PBHB subpopulations with LN mass function using either 1 (top subfigure) or 10 (bottom subfigure) years of LIGO A$^+$ observations. Each sub-plot corresponds to a different value of $\sigma_{\rm LN}$, and it spans over values of ε and $\mu_{\rm LN}$. The black lines correspond to different values of $f_{\rm PBH}$. For all the points in the region above the magenta (light brown) dotted (dash-dotted/solid) line, the variation in the SGWB amplitude w.r.t the fiducial model as measured by LISA with 4 (10) years of observations would be detectable at 1(2/3) σ level. The color map is set by the minimal value of z such that the condition in eq. (5.3.5) is satisfied. Crosses indicate the benchmark points used in the following subsections.

We also notice that, in general, for sufficiently large values of $\mu_{\rm LN}$, subpopulations with narrow mass distributions are more easily detectable with Earth-based detectors. The motivation is that the SNR decreases for increasing mass ratio ($q = m_1/m_2$). For narrow mass distributions, the two PBHs are more likely to have similar masses, which, on average, increases the typical event SNR. Notice that subpopulations with extremely narrow mass distributions, located at either too small or too large masses, will not be detectable since they generate too feeble signals (the GW amplitude grows with the mass of the binary) or signals outside the detector's frequency band (higher masses generally coalesce at lower frequencies). Examples of these effects are visible, *e.g.*, in the two top panels in the top subfigure in fig. 5.2. Indeed, the presence of a minimum at $\mu_{\rm LN} \simeq 70 M_\odot$ in the colorful area in the top left panel of said figure originates from the interplay between these two effects. Notice also that the structure in the colored region before such minimum tracks the behavior of the fiducial mass function, which, as discussed in app. {5.6}, is assumed to be a *power-law + peak model* [296]. All these effects get smoothed out by increasing the spread of the PBH mass function. We notice also that for peaked PBH mass functions, centered around masses that maximize the SNR, values of ε of the order of 10^{-3} are within reach of LIGO A^+. While this quickly degrades as the PBH mass function broadens, we stress that this behavior is not as marked for the prospect of SGWB detection with LISA. As a consequence, parts of the parameter space that might be hardly probed with Earth-based detectors might still be accessed with LISA.

We conclude this section by comparing the results obtained when $T_{\rm Obs} = 1$ year (top subfigure) with the results obtained with $T_{\rm Obs} = 10$ years (bottom subfigure), which are shown in fig. 5.2. Firstly, we notice that, for Earth-based detectors and LISA, increasing the effective observation time will generally move the detectable regions at smaller values of ε but will not significantly affect the qualitative behavior of the results. Indeed, for Earth-based detectors, increasing the observation time does not affect the detections of the single events, but rather, it only increases their number, improving the overall statistic. Similarly, for LISA, increasing the observation time will not affect the overall SGWB amplitude[11], but rather, the accuracy of its measurement.

5.4.2 Detectability of PBHB subpopulations using LISA and ET

We proceed by discussing the results using the ET detector. As in sec. {5.4.1}, we assume either $T_{\rm Obs} = 1\,{\rm yr}$ or $T_{\rm Obs} = 10\,{\rm yrs}$. The results for the LN mass distributions are presented in the top and bottom subfigure in fig. 5.3, respectively. For reference, in fig. 5.3 we also show the benchmark points identified in the previous section to highlight their detectability with ET.

ET will resolve events up to $z \gtrsim 10$, *i.e.*, well beyond the SFR peak, where the SOBHB population quickly drops. As a consequence, ET has way better prospects

[11] As already mentioned in the footnote 7, this might not be true, as by increasing the observation time, and with archival searches, the individual source subtraction will improve, leading to changes both in the amplitude and shape of the SGWB.

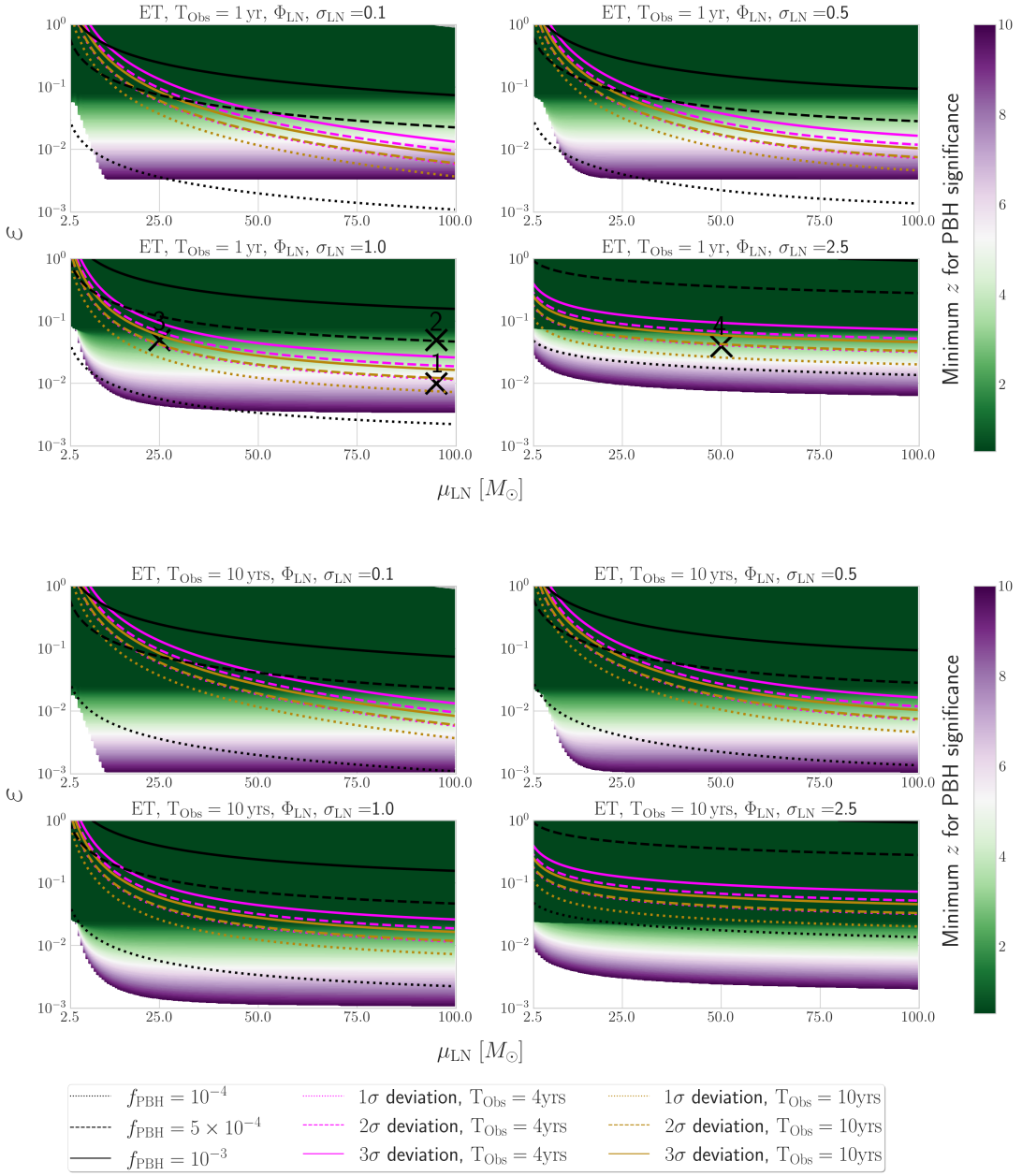

Figure 5.3. Analysis of the parameter spaces of PBHB subpopulations with LN mass distribution using either 1 (top subfigure) or 10 (bottom subfigure) years of ET observations. Plot structure as in fig. 5.2.

of identifying PBHB subpopulations beyond the LVK fiducial model. Moreover, by looking at fig. 5.3, we notice less dependency, compared to LIGO A$^+$, of the results on the position of the mass peak. This effect originates from the improved sensitivity, which, for the mass and redshift ranges considered in the present work, leads to less pronounced selection effects in ET compared to LIGO A$^+$. Indeed, all figures in this

LN Point N.	1	2	3	4
$\mu_{\rm LN}\,[M_\odot]$	95.0	95.0	25.0	50.0
$\sigma_{\rm LN}$	1.0	1.0	1.0	2.5
ε	0.01	0.05	0.05	0.04
LIGO A$^+$ (1 yr)	N.D.	$z\sim 1$	N.D.	N.D.
ET (1 yr)	$z\sim 6$	$z\sim 2$	$z\sim 2$	$z\sim 3$
LISA (4 yrs)	$\sim 1\sigma$	$>> 3\sigma$	$\lesssim 2\sigma$	$\gtrsim 1\sigma$

Table 5.2. Description of the benchmark LN PBHB subpopulations. The acronym N.D. stands for non-detectable for a particular benchmark/detector combination.

subsection show that selection effects due to the mass of the binary only affect the very low end of the mass range. We can thus conclude that, as long as the PBHB subpopulation will produce a sufficiently large number of events (*i.e.*, larger than the Poissonian 3σ expected for the fiducial population) at high redshift, ET will measure a significant excess in the number of events. Despite the great increase in the detection ability of ET compared to LIGO A$^+$, the SGWB measured by LISA will still bring additional information. The main motivation for this claim is that events with very large masses (which are cut in our plots) would merge at too low frequencies to be detected with ET, but would still contribute to the SGWB amplitude. However, a similar argument could also hold for different redshift distributions predicting a few events at low redshift and many more events at very high redshift. Hence, we stress, once again, the synergy between individual events and SGWB for constraining population models.

While, beyond the improvements discussed in the previous paragraphs, most of the discussion of the previous section remains valid for ET, we remark that following the methodology introduced in sec. {5.3.1}, there are some regions where the PBHB subpopulation might be detectable with smaller values of ε in LIGO A$^+$ compared to ET, which might seem counter-intuitive, given that ET has better sensitivity. Indeed, this is an artifact of our choice for the detectability criterion, introduced in eq. (5.3.5) and of the selection function for the different GW detectors. With our approach, if the fiducial population produces fewer resolvable events at a given redshift, fewer events are required from the PBHB subpopulation to satisfy eq. (5.3.5). In particular, since LIGO A$^+$ selects very few events from the fiducial population, it might be easier for a PBHB subpopulation with suitable properties (*i.e.*, with a narrow mass function centered at the right value to optimize the SNR at LIGO A$^+$) to satisfy eq. (5.3.5). However, a proper population analysis, similar to ref. [52], keeping track of both the redshift and mass distribution would reveal this feature.

5.4.3 Analysis of the subpopulation benchmark points

In this section, we perform a more accurate analysis of the resolvable sources with LIGO A$^+$ and ET using the benchmark points shown in figs. 5.2 and 5.3. Part of this analysis will include all the waveform parameters we have averaged over in the previous

sections. Let us start by commenting on the choice of our benchmark points. While details are summarized in table [5.2], qualitatively these points are chosen such that:

- Given Point 2, Points 1 and 3 have the same ε but smaller $\mu_{\rm LN}$, and the same $\mu_{\rm LN}$ but smaller ε, respectively. While Point 2 leads to signatures in LISA, LIGO A$^+$, and ET, Points 1 and 3, being marginally detectable with LISA and LIGO A$^+$, are testable with ET only.

- Given the large value of $\sigma_{\rm LN}$, Point 4 is almost a flat mass function in the range of interest. This point is visible for ET, barely visible for LISA, but not visible by LIGO A$^+$.

The results obtained on these benchmark points using LIGO A$^+$ and ET are shown in fig. 5.4. The left columns of these figures analyze benchmark points for the LN subpopulations on the LIGO A$^+$ detector, while the right columns refer to the results on the ET detector. The three rows correspond to three different techniques (with increasing levels of accuracy) for the evaluation of the (expected) number of resolvable sources for a given population. The lines in the top row are computed using the method described in sec. {5.3}, and, in particular, by evaluating eq. (5.2.6). The error bands are estimated from these numbers assuming Poisson distribution. Since this procedure matches the one used to generate the maps in fig. 5.2 (and the predicted PBHB distributions of fig. 5.5), the results agree perfectly. For reference, in fig. 5.5, we show the analytical predictions (and the corresponding Poissonian uncertainties) for the distribution of resolvable sources at the LIGO A$^+$ and ET detectors for the 4 benchmark points compared with $\Delta_z^{\rm Res,Fid}$ (at 1 and 3 σ-level) for the fiducial population. The central row uses the generated catalogs, but the SNR for each source is evaluated using the sky and spin-averaged expression. This is the same prescription we use to get the top-row results, by comparing the top and middle-row figures we can assess the impact of realization dependence on our results. As expected, we find consistency in regions with a large number of resolvable sources (small z) and deviations in the low-statistics regime (large z). Finally, the bottom row shows the results obtained using the catalogs and the complete expression for the SNR, consistently including all waveform variables. Deviations between top and bottom-row results manifest at higher redshift. This behavior is expected since small differences in the source parameters can move borderline sources inside or outside the detection threshold. Thus, including all parameters in the SNR evaluation makes results more dependent on the realization effects in the low-statistics regime. The figures show clearly that this effect is more pronounced for LIGO A$^+$, which has less resolvable sources, than for ET. Despite this effect, generically, we observe good agreement between numerical and semi-analytical results.

We conclude this section by showing, in fig. 5.6, the relative differences between the semi-analytical estimates of the number of resolvable sources $\hat{N}^{\rm Res,Fid}$ (and its standard deviation $\sqrt{\hat{N}^{\rm Res,Fid}}$) and its value estimated using the generated catalogs

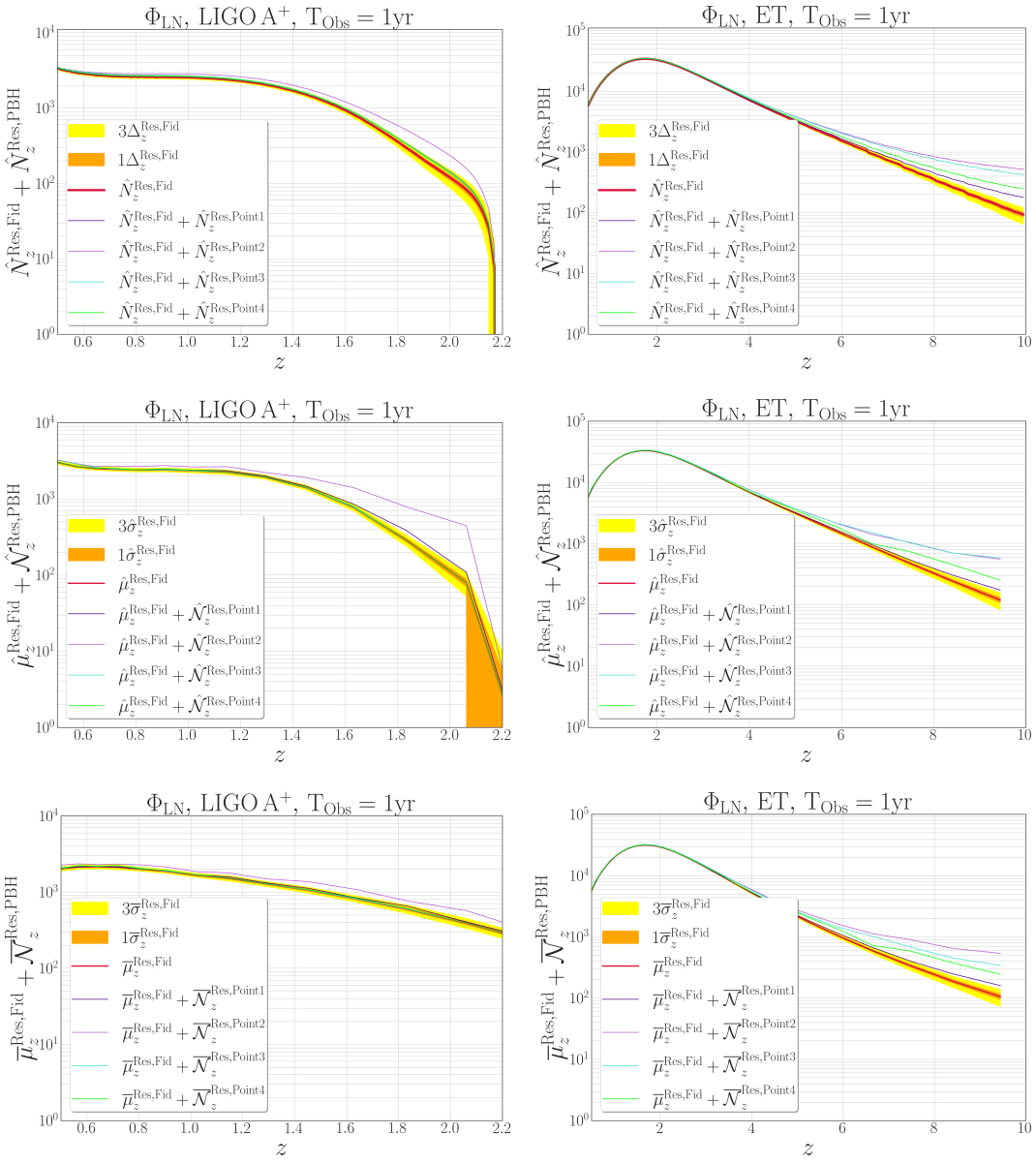

Figure 5.4. Comparison between the analytical predictions of sec. {5.3} (top row) and SNR evaluations on the generated catalog with (middle row) and without (bottom row) sky and spin-averaging. Each panel shows the number of events in the fiducial population (red line), with 1 (orange band) and 3σ (yellow band) compared with the number of events for the fiducial population plus one of the subpopulations (fixed by the benchmark points). All the results shown in this plot are obtained assuming 1 year of either LIGO A$^+$ (left panels) or ET (right panels) measurements.

$\mu^{\rm Res,Fid}$ and (and its standard deviation $\sigma^{\rm Res,Fid}$) defined as

$$\rho_{\mu,z} = \frac{|\mu_z^{\rm Res,Fid} - \hat{N}_z^{\rm Res,Fid}|}{\mu_z^{\rm Res,Fid}}\,, \qquad \rho_{\sigma,z} = \frac{|\sigma_z^{\rm Fid,Res} - \sqrt{\hat{N}_z^{\rm Fid,Res}}|}{\sigma_z^{\rm Fid,Res}}\,. \tag{5.4.1}$$

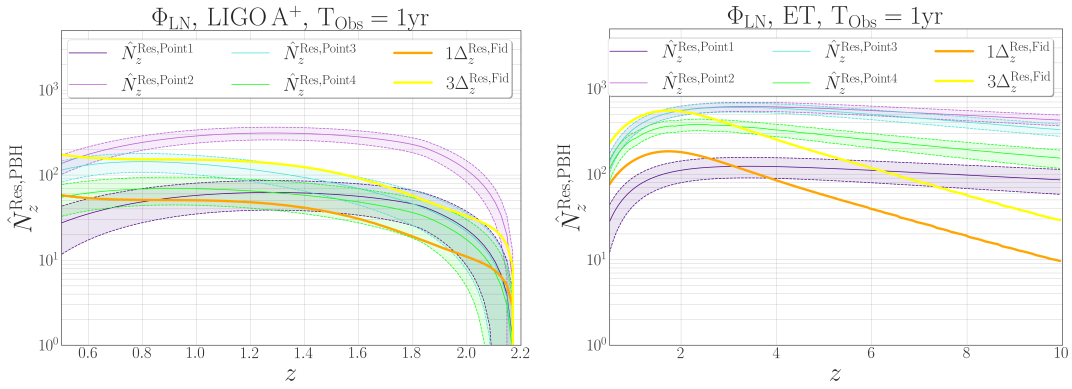

Figure 5.5. Analytical predictions for the benchmark points of sec. {5.3} compared with the analytical estimate for the Poissonian error on the fiducial population. The dashed lines delimit the $3\Delta_z^{\rm Res,Point\,i}$ region for the i-th benchmark point. The LIGO A$^+$ (ET) results for 1yr of observations are shown in the left (right) panel.

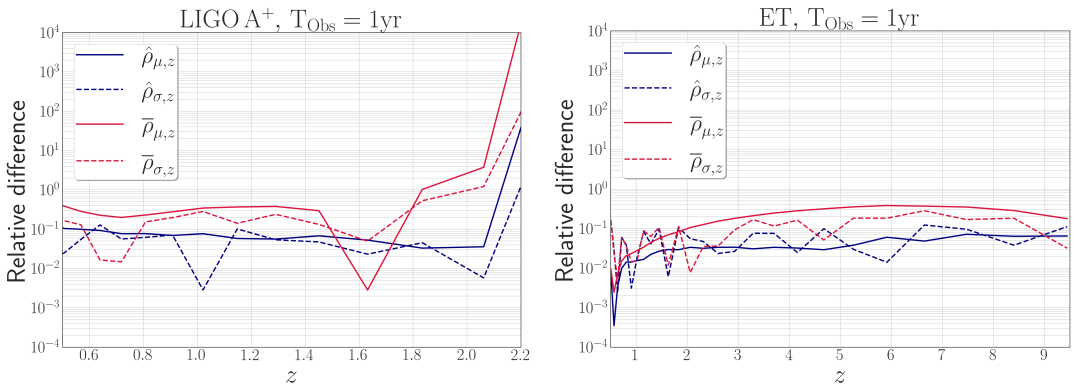

Figure 5.6. Plots of ρ_μ (solid lines) and ρ_σ (dashed lines) as defined in eq. (5.4.1), for LIGO A$^+$ (left panel) and ET (right panel). The blue (red) curves use the sky and spin-averaged (full) expression for the SNR.

The blue curves in fig. 5.6 use the value of $\hat{\mu}^{\rm Res,Fid}$ and $\hat{\sigma}^{\rm Res,Fid}$ computed assuming the sky and spin-averaged version of the SNR. We see that before reaching the low-statistics regime these curves are always smaller than 10% for both LIGO A$^+$ and ET. This proves a quite good agreement between the semi-analytical approach and the generated catalogs. On the other hand, the red curves use the value of $\overline{\mu}^{\rm Res,Fid}$ and $\overline{\sigma}^{\rm Res,Fid}$ evaluated using the full expression for the SNR. While we notice some level of degradation with respect to the blue curves (the relative difference is up to $\simeq 30/40\%$), we still find quite good agreement between the results.

5.5 Conclusions

In this paper, we have discussed the prospects of detecting potential PBHB subpopulations with future GW detectors. For this purpose, we have assumed a fiducial population in agreement with the GWTC-3 results and added PBHB subpopulations with different merger rates and mass distributions to test whether these would lead to observable signatures in LIGO A^+, ET, or LISA. Using Earth-based detectors, we have checked how the number of resolvable events changes in the presence of PBHB subpopulations. In particular, we have evaluated this analytically and tested our results by simulating event catalogs to assess the impact of low statistics on the analytic results. We have generally found good agreement between our semi-analytical and numerical results. Beyond that, we have evaluated the increase in the amplitude of the SGWB arising from the PBH contribution and tested its detectability with LISA using a FIM approach. We found that the information LISA will bring might be significant to test whether the SGWB is due to SOBHBs only.

For all models considered in this work, we have found sizable regions of the parameter spaces where the PBHB subpopulations will lead to significant variations in the number of detectable events in LIGO A^+ and ET (with ET performing better in most cases) with respect to SOBHB expectations. However, it is worth stressing that detecting events at high redshift does not imply that it will always be possible to infer their redshift accurately [311]. Moreover, we have found that for all models considered in this work, there are sizable parts of the parameter spaces leading to an increase in the SGWB amplitude that would be detectable with LISA. Interestingly, since the SGWB integrates over all masses, the SGWB measurement can also test subpopulations with very low and very large masses, generating signals beyond the reach of future Earth-based detectors. Indeed, different GW detectors probe complementarily distinct parts of the parameter space. In particular, our results highlight three different regimes:

- **Signatures in Earth-based detectors and LISA:** This can happen if the PBH population becomes abundant (but still statistically marginal in present LVK observations) around (or after) the SFR peak so that the number of individual events does not decline at $z \simeq 2$. Simultaneously, the SGWB at LISA exceeds the SOBHB prediction.

- **Signatures in Earth-based detectors only:** The PBH population grows very slowly with z and becomes sizable only at high redshifts. In this case, the signals from unresolved sources are faint, and their contribution to the SGWB at LISA is not sufficiently strong to modify the SOBHB prediction significantly. While deviations in the merger rate might be appreciated, their statistical significance might not be sufficient to pin down the presence of a secondary population unless some additional features are found in, *e.g.*, the mass distribution of the observed population.

- **Signatures in LISA only:** The PBH population has very small or very large masses, and the signals are not detectable with Earth-based detectors. LISA observes an SGWB amplitude incompatible with the value predicted using the SOBHB population measured by Earth-based detectors.

Overall, we conclude that the considered measurements from Earth-based detectors and LISA will generally be complementary, and our understanding of the BH population that we observe in our Universe will improve if we use their synergy. This conclusion comes with no surprise, knowing the underlying differences between the properties of the signals these detectors will probe. Furthermore, we generally observe that the dependency of the LISA SGWB on the subpopulation parameters scales differently than the distribution of resolvable sources that Earth-based interferometers will detect. This fact implies that, in general, SGWB measurements will help Earth-based detectors improve the constraints on the BH population parameters that we observe in our Universe.

As discussed in sec. {5.3}, our analysis does not include errors on the fiducial population parameter, which are currently quite broad on some of the most influencing parameters and would impact our results significantly if extrapolated to the volume that LIGO A^+ and ET detector will probe. However, the open codes presented in our GitHub repository [330] can be readily updated when the new results of future inference papers, *e.g.*, by the LVK collaboration, come out. With improvements in the LVK network, we expect more (and more accurate) detections, which will reduce the uncertainties on the population parameters, making the analysis much more reliable.

The present study assumes that the two populations do not interact with one another, *i.e.*, mergers only involve BHs drawn from the same population. This assumption impacts both the number of mergers and their properties. By dropping this assumption and assuming the two populations to have sufficiently different mass ranges, it would be possible to enhance the number of Extreme Mass Ratio Inspirals (EMRIs) [12] in the LISA band significantly [343, 348–350]. Thus, determining the abundance of these objects can also be used to further constrain the eventual presence of PBHB subpopulations on GW detectors with LISA-like frequency range. Moreover, keeping track of the number of resolvable sources in different frequency bands (*e.g.*, BHs with masses higher than the ones considered in the present work would merge in the LISA frequency band) could also provide a possible tracer for the presence of PBHB subpopulation. Finally, even the analysis of the SGWB on the Earth-based detectors frequency range can further improve the results presented in this study. On one hand, detecting the SGWB at different frequency bands will decrease the uncertainties on its amplitude, hence improving our chance to detect variations in the expected value. On the other hand, if the PBH mass distribution is narrow, and peaked in the stellar-mass BH range, it could result in deviations of the SGWB shape from the standard power-law behavior in the LVK/ET frequency range, which could be used as a further

[12] For SGWB predictions and cosmological constraints with EMRIs, see, *e.g.*, [343–347].

constraint on the PBH sub-population properties [54, 273, 274, 351].

We conclude by commenting on alternative methods to assess the detectability of PBHB subpopulations beyond the ones considered in this work for both Earth-based and Space-based detectors. It would be possible, in principle, to adopt other criteria, similar to the one we have introduced. For example, since we expect PBHBs to become relevant at high redshift, variations on the cumulative number of resolvable sources predicted after a given redshift could provide a viable alternative. While maintaining less information on the source distribution, this approach would be less sensitive to the error in the inference of the source distance [311]. Finally, a fully consistent population analysis based on hierarchical Bayesian modeling would provide a robust and more accurate alternative to the criteria discussed here. Thus, we deem it worth exploring these (and possibly other) methodologies in future works.

Acknowledgments

We thank Gabriele Franciolini for several useful comments on a draft of this work. MP acknowledges the hospitality of Imperial College London, which provided office space during some parts of this project. PM acknowledges the Cost action CA16104 for financing the STSM to London that led to the start of this work. GN is partly supported by the grant Project. No. 302640 funded by the Research Council of Norway.

5.6 Appendix A : The SOBHB fiducial population

In this appendix, we detail the fiducial SOBHB population model we adopt throughout the analysis. In most aspects, we follow the approach of ref. [182] and rely on the master equation in eq. (5.2.1). We proceed by clarifying the functional forms of the quantities appearing in such an equation.

As already discussed in the main text, the current LVK data put tight bounds on the SMBHB population properties up to $z \sim 0.5$ [45]. Few events have been detected at redshift $0.5 \lesssim z \lesssim 1$, but they are too rare and/or poorly reconstructed to impose strong constraints [352, 353]. Despite these caveats, current data are compatible with a population of SOBHBs with a merger rate behaving as

$$R(z) = R_0(1+z)^{\kappa} \tag{5.6.1}$$

for $z \lesssim 0.5$, with $R(z=0.2) = 28.3^{+13.9}_{-9.1}\mathrm{Gpc}^{-3}\mathrm{yr}^{-1}$ and $\kappa = 2.9^{+1.7}_{-1.8}$ [45, 354]. At higher redshift, $R(z)$ has to keep track of the stellar-formation origin of the binaries and, to some degree, resemble the SFR. Thus, consistently with [182], we choose the *Madau-Dickinson phenomenological profile* [56, 57] with a negligible time delay[13]. Such

[13]Other choices [225, 227, 231, 293, 325, 355, 356] are possible and might qualitatively change the results, but not the rationale, of our analysis.

a choice leads to

$$R_{\rm SOBHB}(z) = R_0 \frac{(1+z)^\kappa}{1+((1+z)/2.9)^{\kappa+2.9}}\,, \tag{5.6.2}$$

where R_0 is set so that $R(z=0.2)$ matches the measured value.

For what concerns the mass distribution, we adopt the *power law + peak* scenario [45, 354]

$$\begin{aligned} p(m_1, m_2|m_m, m_M, \alpha, \beta_q, \mu_m, \sigma_m, \delta_m, \lambda_{\rm peak}) = \\ C_{\rm mass}\, \pi_1(m_1|\alpha, \mu_m, \sigma_m, m_m, m_M, \delta_m, \lambda_{\rm peak})\, \pi_2(q|\beta_q, m_1, m_m, \delta_m)\,, \end{aligned} \tag{5.6.3}$$

with $C_{\rm mass}$ being a normalization constant and q being the mass ratio $q = m_2/m_1$. The functions π_1 and π_2 read as

$$\begin{aligned} \pi_1(m_1|\alpha, \mu_m, \sigma_m, m_m, m_M, \delta_m, \lambda_{\rm peak}) = \\ [(1-\lambda_{\rm peak})\mathfrak{P}(m1|-\alpha, m_M) + \lambda_{\rm peak}\mathfrak{G}(m_1|\mu_m, \sigma_m)]\, \mathfrak{S}(m1|m_m, \delta_m) \end{aligned} \tag{5.6.4}$$

and

$$\pi_2(q|\beta_q, m_1, m_m, \delta_m) = C_q(m_1)\, q^{\beta_q}\, \mathfrak{S}(m2|m_m, \delta_m)\,, \tag{5.6.5}$$

where $C_q(m_1)$ is a normalization function, $\mathfrak{S}$ is a smoothing function for the low mass cutoff, and $\mathfrak{P}$ and $\mathfrak{G}$ are respectively a normalized power law and a normalized Gaussian distribution

$$\mathfrak{P} = C_{\rm PL} m^{-\alpha}\,, \tag{5.6.6}$$

$$\mathfrak{G} = \frac{C_m}{\sqrt{2\pi\sigma_m^2}} \exp\left[-\frac{1}{2}\left(\frac{m-\mu_m}{\sigma_m}\right)^2\right]\,, \tag{5.6.7}$$

with α being the spectral index of the power law, μ_m and σ_m being the mean and width of the Gaussian, and $C_{\rm PL}$ and C_m being normalization. The smoothing function $\mathfrak{S}$ imposes a smooth cutoff for low masses, rising from 0 to 1 in the interval $[m_m, m_m+\delta_m]$

$$\mathfrak{S} = \begin{cases} 0, & \text{if } m < m_m \\ [f(m-m_m, \delta_m)+1]^{-1}, & \text{if } m \in [m_m, m_m+\delta_m] \\ 1, & \text{if } m > m_m + \delta_m \end{cases}\,, \tag{5.6.8}$$

with

$$f(m', \delta_m) = \exp\left(\frac{\delta_m}{m'} + \frac{\delta_m}{m'-\delta_m}\right)\,, \tag{5.6.9}$$

so that, by construction, we have $m \geq m_m$. The high end of the mass range doesn't have an explicit cutoff but large masses are statistically suppressed. In practice, we set $m_M = 100 M_\odot$, which is slightly higher than the values used in the LVK analysis [296], to take into account possible higher mass events of astrophysical origin[14]. All the hyperparameters entering the mass distribution eq. (5.6.3) are fixed at the central

$m_m\,[M_\odot]$	$m_M\,[M_\odot]$	$\delta_m\,[M_\odot]$	$\lambda_{\rm peak}$	α	β_q	μ_m	σ_m
$5.0^{+0.86}_{-1.7}$	100	$4.9^{+3.4}_{-3.2}$	$0.038^{+0.058}_{-0.026}$	$3.5^{+0.6}_{-0.56}$	$1.1^{+1.7}_{-1.3}$	$34^{+2.6}_{-4.0}$	$5.69^{+4.28}_{-4.34}$

Table 5.3. Fiducial values (with 1σ C.L.) for the mass function hyperparameters [296].

Coefficients	a_M	E[a]	Var[a]	ζ	σ_1	σ_2
Value	1	$0.26^{+0.09}_{-0.07}$	$0.02^{+0.02}_{-0.01}$	$0.76^{+0.22}_{-0.45}$	$0.87^{+1.08}_{-0.45}$	$0.87^{+1.08}_{-0.45}$

Table 5.4. Fiducial values (with 1σ C.L.) for the spin amplitude and spin tilt hyperparameters [296].

values of the LVK analysis outcome reported in table [5.3].

The spin distribution is a product of two different PDFs, one for the spin amplitudes and one for the spin tilts. The former reads as [45, 354]:

$$p(a_i|\alpha_a,\beta_a) = \frac{a_i^{\alpha_a-1}(1-a_i^{\beta_a-1})}{B(\alpha_a,\beta_a)}\,, \tag{5.6.10}$$

where $B(\alpha_a,\beta_a)$ is a Beta function that guarantees the appropriate normalization of the PDF. The α_a and β_a are positive constants defined through

$$\begin{aligned} \mathrm{E}[a] &= \tfrac{\alpha_a}{\alpha_a+\beta_a} \\ \mathrm{Var}[a] &= \tfrac{\alpha_a\beta_a}{(\alpha_a+\beta_a)^2(\alpha_a+\beta_a+1)} \end{aligned}\,, \tag{5.6.11}$$

where $E[a]$ and $Var[a]$ are set in table [5.4]. We stress that the spin amplitudes of the two black holes are independent of one another. On the other hand, the PDF spin tilt distribution reads

$$p(\cos(t_1),\cos(t_2)|\sigma_1,\sigma_2,\zeta) = \frac{1-\zeta}{4} + \frac{2\zeta}{\pi}\prod_{i\in 1,2}\frac{\exp\left\{-\left[1-\cos(t_i)\right]^2/(2\sigma_i^2)\right\}}{\sigma_i\,\mathrm{erf}(\sqrt{2}/\sigma_i)}\,, \tag{5.6.12}$$

which is a mixture between an isotropic and a truncated Gaussian distribution centered in $\cos(t_i)\approx 1$. The σ_i, and ζ parameters are specified in table [5.4].

Finally, for cosmology we assume the ΛCDM model where the Hubble parameter is $H_0 = h\times 100\,\mathrm{km/(s\,Mpc)}$, with $h=0.678$ being its dimensionless value, and $\Omega_m = 0.3$ and $\Omega_\Lambda = 0.7$.

5.7 Appendix B : PBH contribution to the Dark Matter relic abundance

While PBHs behave as cold DM and could, at least in principle constitute a sizable amount of the presently observed DM, their abundance in the stellar mass range is

[14] We test that other choices would not practically change our results. For *e.g.*, $m_M = 150M_\odot$, no masses above 100 $M_\odot$ appear in our catalog realizations due to the PDF suppression.

tightly constrained [133, 134, 141–143, 302, 357, 358]. We define $f_{\rm PBH} \equiv \Omega_{\rm PBH}/\Omega_{\rm DM}$, the ratio between today's PBH and DM energy densities in the Universe. For a given PBH population model, the parameters ε and $f_{\rm PBH}$ can be explicitly related. We obtain their relationship in the case that our PBH population, which we derive from phenomenological models, is dominated by binaries that gravitationally decoupled from the Hubble flow before the matter–radiation equality [16, 55, 294].

In eq. (5.2.5), we modulate the PBHB merger rate $R_{\rm PBHB}(z)$ through the parameter ε. An alternative way to write $R_{\rm PBHB}(z)$ is [55, 294]

$$R_{\rm PBHB}(z) = \frac{1.6\times10^6}{\rm Gpc^3\,yr} f_{\rm PBH}^{53/37} \left[\frac{t(z)}{t(z=0)}\right]^{-\frac{34}{37}} \int {\rm d}m_1 \int {\rm d}m_2 \left[\left(\frac{m_1+m_2}{M_\odot}\right)^{-\frac{32}{37}} \eta^{-\frac{34}{37}} \mathcal{S}\right], \tag{5.7.1}$$

where $\eta = m_1 m_2/(m_1+m_2)^2$ and $\mathcal{S} = \Phi_{\rm LN}(m_1)\,\Phi_{\rm LN}(m_2) S$. The function $\Phi_{\rm LN}$ is given in eq. (5.2.7). The function S is a suppression factor accounting for environmental effects that slow down the binary formation or favor their disruption. It can be approximated as[15]

$$S_1 \approx 1.42 \left(\frac{\langle m^2\rangle / \langle m\rangle^2}{\bar{N}(m_1, m_2, f_{\rm PBH}) + C} + \frac{\sigma_{\rm M}^2}{f_{\rm PBH}^2}\right) e^{-\bar{T}}\,, \tag{5.7.2}$$

with

$$\bar{T} = \frac{m_1+m_2}{\langle m\rangle}\left(\frac{f_{\rm PBH}}{f_{\rm PBH}+\sigma_{\rm M}}\right), \tag{5.7.3}$$

$$C = \frac{\langle m^2\rangle}{\sigma_{\rm M}^2 \langle m\rangle^2} \frac{f_{\rm PBH}^2}{\left[\frac{\Gamma(29/37)}{\sqrt{\pi}} U\left(\frac{21}{74}, \frac{1}{2}, \frac{5 f_{\rm PBH}^2}{6\sigma_{\rm M}^2}\right)\right]^{-74/21} - 1}\,. \tag{5.7.4}$$

Here $\sigma_{\rm M} \approx 0.004$ represents the rescaled variance of matter density perturbations at the time the binaries form, Γ denotes the Euler gamma function, $U(a,b,z)$ is the confluent hypergeometric function, while $\langle m\rangle$ and $\langle m^2\rangle$ are the first and second momenta of the PBH mass PDF.

The comparison of eq. (5.2.5) to eq. (5.7.1) yields

$$\varepsilon = \frac{1.6\times10^6}{R_0} f_{\rm PBH}^{53/37} \int {\rm d}m_1 \int {\rm d}m_2 \left[\left(\frac{m_1+m_2}{M_\odot}\right)^{-\frac{32}{37}} \eta^{-\frac{34}{37}} \mathcal{S}\right]. \tag{5.7.5}$$

Figure 5.7 shows the values of $f_{\rm PBH}$ that arise in the parameter regions of the PBH models considered in our analysis.

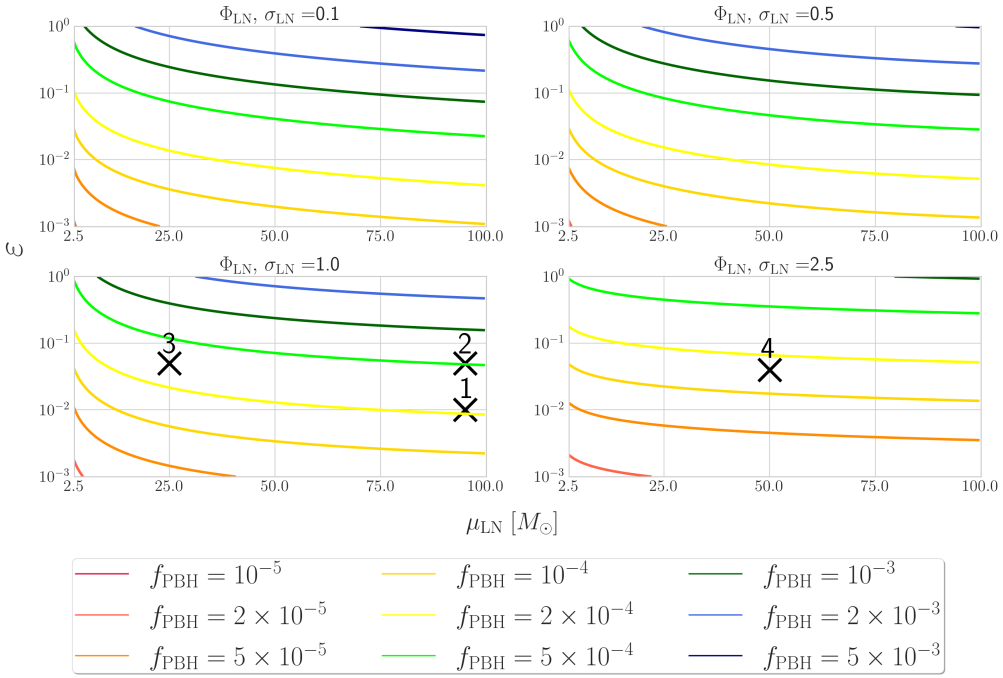

Figure 5.7. Conversion maps from ε to $f_{\rm PBH}$ of the parameter spaces of PBHB subpopulations with LN mass function. Each sub-plot corresponds to a different value of $\sigma_{\rm LN}$, and it spans over values of ε and $\mu_{\rm LN}$. Crosses indicate the benchmark points used in the following subsections.

Parameter	Range
R_0 fraction	$\varepsilon \in [10^{-3}, 1]$
Mass PDF central parameter	$\mu_{\rm G} \in [0, 100]$
Mass PDF standard deviation	$\sigma_{\rm G} = [1, 5, 10, 15]$
Integrated mass range	$m \in [0, 150]$
Earth-based integrated redshift range	$z \in [0, 10]$
SGWB integrated redshift range	$z \in [0, 10^2]$

Table 5.5. The range of parameter values used for the Gaussian PDF in the semi-analytic analysis.

5.8 Appendix C : Results for a Gaussian mass distribution

To further analyze the qualitative results presented in sec. {5.4}, we perform the same analysis when considering a *Gaussian Mass Distribution* function as in [359]:

$$\Phi_{\rm G}(m) = \frac{1}{\sqrt{2\pi\sigma_{\rm G}^2}} \exp\left[-\frac{1}{2}\left(\frac{m-\mu_{\rm G}}{\sigma_{\rm G}}\right)^2\right], \tag{5.8.1}$$

with $\mu_{\rm G}$ and $\sigma_{\rm G}$ the hyperparameters setting the position and width of the peak. Even for this study, we will adopt a merger rate in the form of eq. (5.2.5). The range of parameters considered, for both the merger rate and Gaussian mass function, are summarized in table [5.5].

Following the procedure described in app. {5.7} (where we replace the mass distribution and momenta with the Gaussian ones), we start by presenting the conversion maps from ε to $f_{\rm PBH}$ for the considered Gaussian parameter space in fig. 5.8. The detectability of the considered Gaussian PBHB subpopulations on the LIGO A$^+$ and ET detector is then described in figs. 5.9 and 5.10 respectively. In the aforementioned figures, we present the results when assuming either $T_{\rm Obs} = 1\,{\rm yr}$ (top subfigure) or $T_{\rm Obs} = 10\,{\rm yrs}$ (bottom subfigure) of data. Each panel of these subfigures corresponds to a different value for $\sigma_{\rm G}$. On the other hand, the x axes of these plots span different values for $\mu_{\rm G}$, and the y axes correspond to different values of ε defined in eq. (5.2.5). We generally observe that all the discussion of sec. {5.4} holds up even when considering a Gaussian PDF. In particular, the selection features that appear for narrow mass functions on the LIGO A$^+$ detector discussed in sec. {5.4.1} are even further highlighted on the top panels of fig. 5.9, thanks to the choice of $\sigma_{\rm G}$.

As done in sec. {5.4.3}, we then proceed by performing a more accurate analysis of the resolvable sources with LIGO A$^+$ and ET using the benchmark points shown in figs. 5.9 and 5.10. While details are summarized in table [5.6], qualitatively these points are chosen such that:

- Point 5 is chosen to be detectable with LIGO A$^+$, but not detectable with LISA/ET, according to the methodology assumed in this work.
- Points 6, 7, and 8 are chosen analogously to Points 1, 2, and 3 but with the Gaussian mass function instead of the LN distribution.

The analytical predictions (together with their Poissonian uncertainties) for the distribution of resolvable sources of the Gaussian benchmark points on the LIGO A+ (left panel) and ET (right panel) detectors are presented in fig. 5.11. In said figure, for comparison we also report the expected analytical $\Delta_z^{\rm Res,Fid}$ at 1σ and 3σ level for the fiducial population. We then synthesize some populations for both the fiducial and

[15] In general, in $\mathcal{S}$ contains an extra suppression factor, which introduces redshift dependence at small z. Such a term is negligible for $f_{\rm PBHB} \simeq 10^{-3}$ [55, 294], which is the region of parameter space relevant parts for most models considered in this work. As a consequence, we neglect this factor.

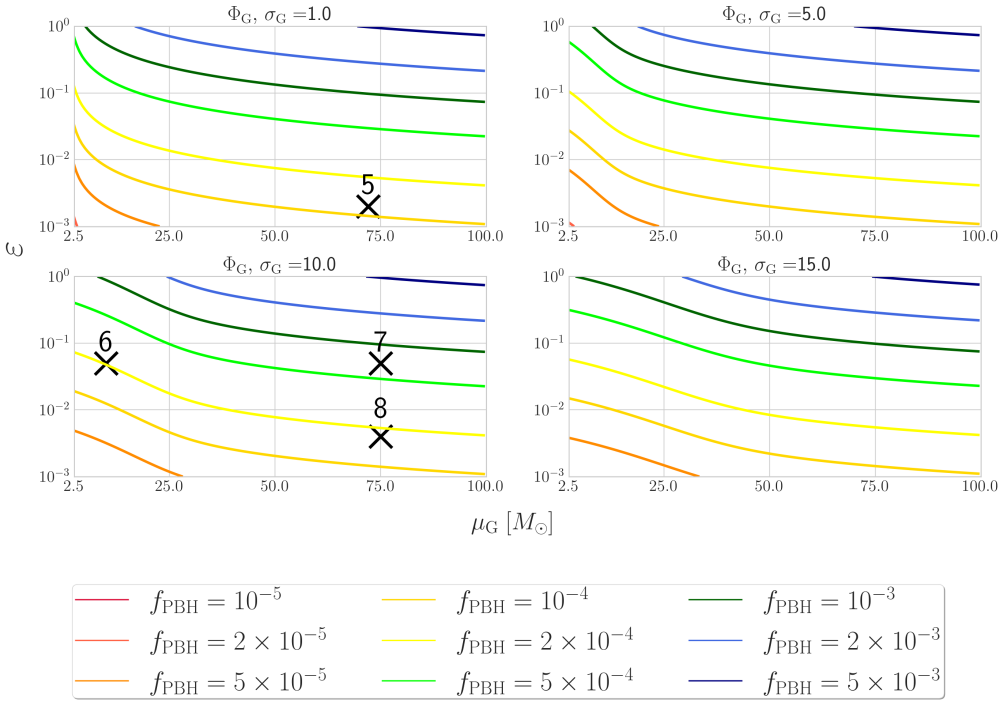

Figure 5.8. Conversion maps from ε to $f_{\rm PBH}$ of the parameter spaces of PBHB subpopulations with Gaussian mass function. Each sub-plot corresponds to a different value of $\sigma_{\rm G}$, and it spans over values of ε and $\mu_{\rm G}$. Crosses indicate the benchmark points chosen for further analysis.

Gaussian Point N.	5	6	7	8
$\mu_{\rm G}\,[M_\odot]$	72.0	10.0	75.0	75.0
$\sigma_{\rm G}$	$1.0M_\odot$	$10.0M_\odot$	$10.0M_\odot$	$10.0M_\odot$
ε	0.002	0.05	0.05	0.004
LIGO A$^+$ (1 yr)	$z \sim 2$	N.D.	$z \sim 1$	$z \sim 2$
ET (1 yr)	N.D.	$z \sim 2$	$z \sim 2$	$z \sim 10$
LISA (4 yrs)	N.D.	N.D.	$>> 3\sigma$	N.D.

Table 5.6. Description of the benchmark Gaussian PBHB subpopulations. The acronym N.D. stands for non-detectable for a particular benchmark/detector combination.

PBHB benchmarks, and analyze the numerical results using different levels of complexity, as done in sec. {5.4.3}. Despite the variations arising due to low statistics and underlying differences among the three different approaches, in general, we observe good agreement between numerical and semi-analytical results. The only exceptions we find in this case are for Point 5 and Point 8 which, due to the low value of $\varepsilon \approx 10^{-3}$, generate very few sources ($\lesssim 100$/yr by comparing with fig. 5.1) and are hence more likely to not reach the necessary realization statistic.

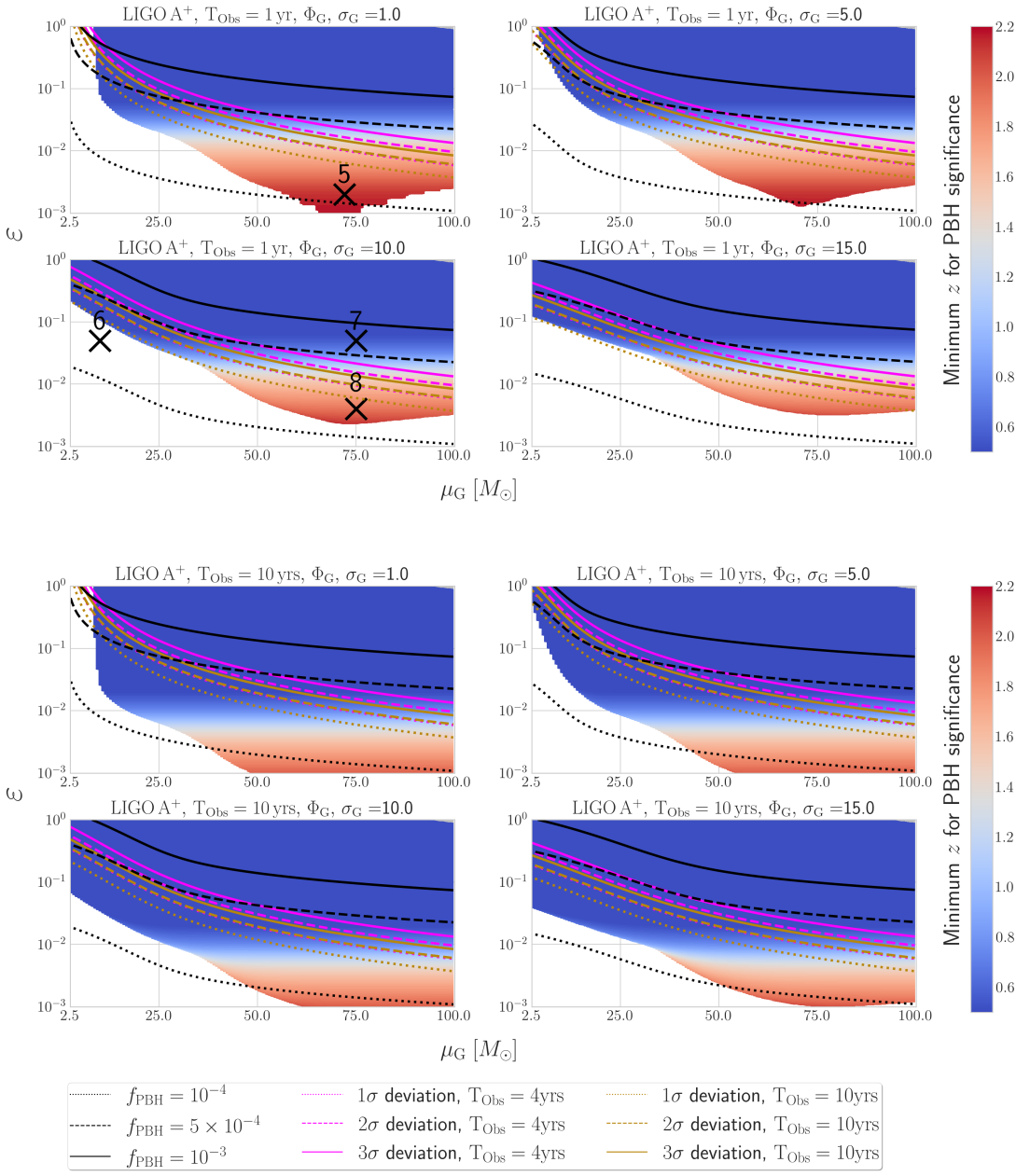

Figure 5.9. Analysis of the parameter spaces of PBHB subpopulations with Gaussian mass function using either 1 (top subfigure) or 10 (bottom subfigure) years of LIGO A$^+$ observations. Plot structure as in fig. 5.2

.

5.9 Appendix D : Detector characteristics

In this study, we consider LIGO A$^+$ and ET as representatives of upcoming and future Earth-based interferometers and LISA as a reference for the first generation of space-based GW detectors. The precise timeline and operational durations of these

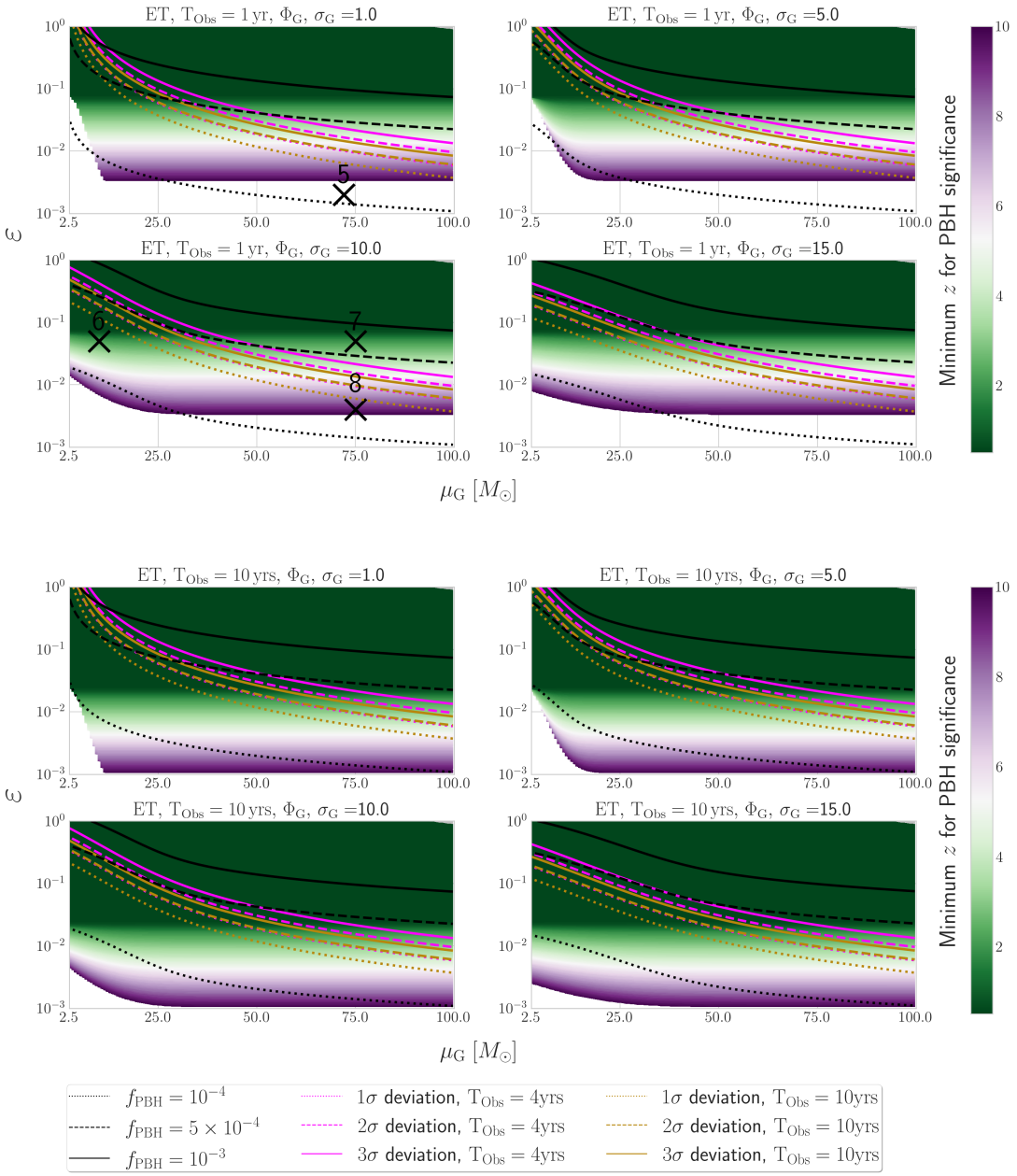

Figure 5.10. Analysis of the parameter spaces of PBHB subpopulations with Gaussian mass distribution using using either 1 (top subfigure) or 10 (bottom subfigure) years of ET observations. Plot structure as in fig. 5.9

.

instruments are uncertain. Nevertheless, it is reasonable to anticipate that LIGO A$^+$ will operate for several years before the early/mid-2030s when ET and LISA are expected to commence to acquire data. In the lack of a well-defined progress plan, we consider a couple of somewhat extreme timeline scenarios, believing that the actual

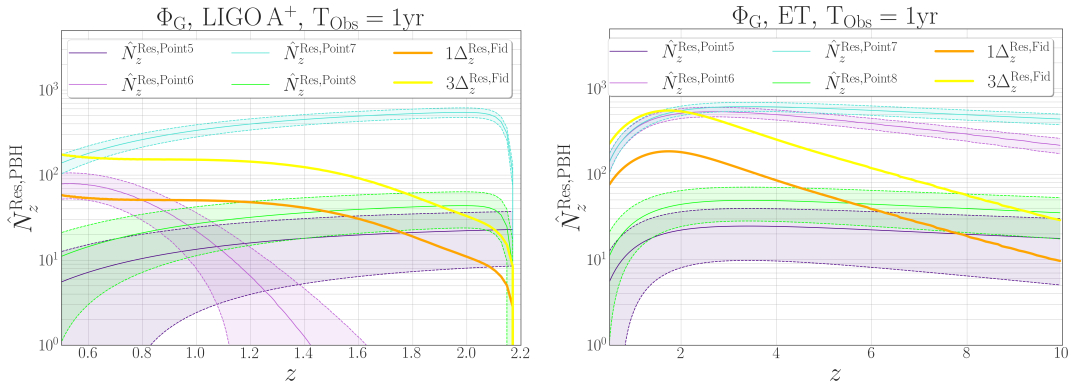

Figure 5.11. Analytical predictions for the benchmark points resolvable source distribution of sec. {5.3} w.r.t. the expected Poissonian error predicted for the analytical fiducial population. The dashed lines delimit the $3\Delta_z^{\text{Res,Point i}}$ region for the i-th benchmark point. We present the results predicted for benchmarks on the LIGO A$^+$(ET) on the left (right) panels of the figure. To conclude, all the results shown in this plot are obtained assuming 1 year of either LIGO A$^+$ or ET measurements.

future will likely fall somewhere in between. Concretely, we analyze 1 and 10 years of data for LIGO A$^+$ and ET, and 4 and 10 for LISA. We leave it to the knowledge of the future reader to estimate which scenario the future will tend to and in which order each detector and its measurements will arrive.

Earth-based interferomenters The location of the two LIGO A$^+$ detectors are set to be in the Livingston (N 30°330′, W 90°460′) and Hanford (N 46°270′, W 119°240′) sites. Regarding the sensitivity, we use the curve described in ref. [360], with frequency range $[5, 5000]$ Hz. For ET, we assume the location proposed in the Sos Enattos mine in the Lula area (N 40°260′, E 9°260′) with the ET-D-sum sensitivity in the frequency range $[0.1, 10^4]$ Hz [361, 362]. However, our resolvable event analysis is nearly independent of the precise detector sites. The expected horizon distance for these detector configurations, w.r.t the BHB populations considered in this paper, is presented in fig. 5.13.

LISA LISA will be the first interferometer in space. The detector will consist of three satellites orbiting around the Lagrange point L5. For our analysis, we assume mission adoption sensitivity in the frequency range $[3 \times 10^{-5}, 0.5]$ Hz [363]. In the following, we describe the 2-parameters instrument noise model [59, 364] based on the results of the LISA Pathfinder mission, as well as the latest laboratory test. In particular, we report the LISA sensitivity in the *Time Delay Interferometry (TDI)* channels A and T[16]. For

[16]TDI is a technique designed for LISA to suppress the otherwise dominant (and several orders of magnitude larger than the required noise levels) primary noises. TDI consists of combining interferometric measurements performed at different times. It can be shown that for a fully symmetric LISA configuration, it is possible to introduce an orthogonal (*i.e.*, noise in the different channels is

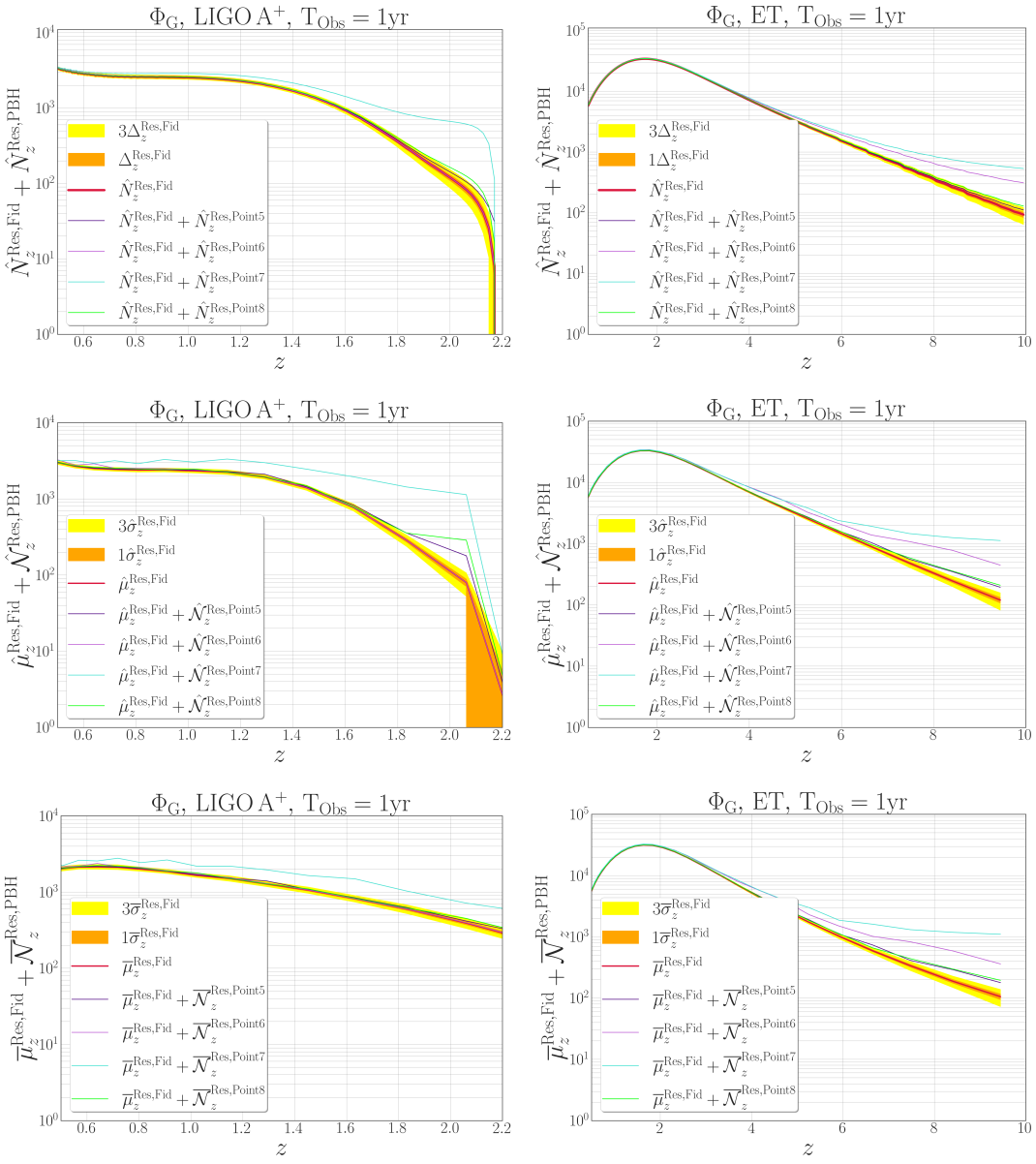

Figure 5.12. Comparison between the analytical predictions of sec. {5.3} (top row) and SNR evaluations on the generated catalog with (middle row) and without (bottom row) sky and spin-averaging. Each panel shows the number of events in the fiducial population (red line), with 1 (orange band) and 3σ (yellow band) compared with the number of events for the fiducial population plus one of the subpopulations (fixed by the benchmark points). All the results shown in this plot are obtained assuming 1 year of either LIGO A$^+$ (left panels) or ET (right panels) measurements.

more details on the noise model and the TDI construction, see *e.g.*, ref. [241, 372].

uncorrelated) TDI basis, typically dubbed AET. See, *e.g.*, refs. [365–371] for details.

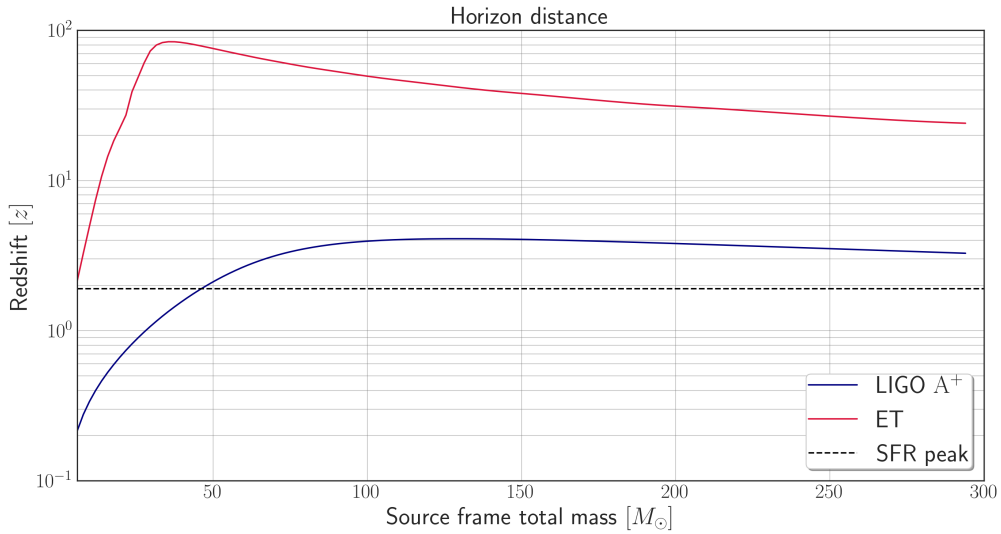

Figure 5.13. Horizon distance for the LIGO A$^+$ (blue) and ET (red) detectors as a function of the total mass that we consider for the populations of this analysis. The black dashed line corresponds to the value of the peak of the SFR (when no time delays are not considered) that we obtain for the fiducial SOBHB population that we assumed in this paper.

The noise in LISA is a combination of two main components: Test Mass (TM) acceleration noise and Optical Metrology System (OMS) noise. The power spectra $P_{\rm TM}$, $P_{\rm OMS}$, for these two components are

$$\begin{aligned} P_{\rm TM}(f,A) &= A^2 \frac{\rm fm^2}{s^4 \rm Hz}\left[1+\left(\frac{0.4\rm mHz}{f}\right)^2\right]\left[1+\left(\frac{f}{8\rm mHz}\right)^4\right]\left(\frac{1}{2\pi f}\right)^4\left(\frac{2\pi f}{c}\right)^2, \\ P_{\rm OMS}(f,P) &= P^2 \frac{\rm pm^2}{\rm Hz}\left[1+\left(\frac{2\rm mHz}{f}\right)^4\right]\left(\frac{2\pi f}{c}\right)^2, \end{aligned} \tag{5.9.1}$$

where c is the light speed and the two noise parameters A and P control the amplitudes of the TM and OMS components, respectively. The total noise spectral densities in the TDI A and T channels read

$$\begin{aligned} N_{\rm AA}(f,A,P) = 8\sin^2\left(\frac{2\pi f L}{c}\right)\Bigg\{4\left[1+\cos\left(\frac{2\pi f L}{c}\right)+\cos^2\left(\frac{2\pi f L}{c}\right)\right]P_{\rm TM}(f,A)+ \\ +\left[2+\cos\left(\frac{2\pi f L}{c}\right)\right]P_{\rm OMS}(f,P)\Bigg\}, \end{aligned} \tag{5.9.2}$$

$$\begin{aligned} N_{\rm TT}(f,A,P) = 16\sin^2\left(\frac{2\pi f L}{c}\right)\Bigg\{2\left[1-\cos\left(\frac{2\pi f L}{c}\right)\right]^2 P_{\rm TM}(f,A)+ \\ +\left[1-\cos\left(\frac{2\pi f L}{c}\right)\right]P_{\rm OMS}(f,P)\Bigg\}, \end{aligned} \tag{5.9.3}$$

with $L = 2.5 \times 10^9$m is the LISA armlength.

Given the noise power spectra, the strain sensitivity (for a generical channel ij) is defined as

$$S_{n,ij}(f, A, P) = \frac{N_{ij}(f, A, P)}{R_{ij}(f)} = \frac{N_{ij}(f, A, P)}{16 \sin^2\left(\frac{2\pi f L}{c}\right)\left(\frac{2\pi f L}{c}\right)^2 \tilde{R}_{ij}(f)}\,, \tag{5.9.4}$$

where $R_{ij}(f)$ is the (quadratic) response function, mapping incoming GW signals onto the TDI data stream. The response can be further expanded as a purely geometrical factor, $\tilde{R}_{ij}(f)$, times TDI-dependent terms. While $\tilde{R}_{ij}(f)$ should be evaluated, approximate expressions for the A and T channels read

$$\tilde{R}_{\rm AA}(f) = \frac{9}{20}\frac{1}{1 + 0.7\left(\frac{2\pi f L}{c}\right)^2}\,, \qquad \tilde{R}_{\rm TT}(f) = \frac{9}{20}\frac{\left(\frac{2\pi f L}{c}\right)^6}{1.8 \times 10^3 + 0.7\left(\frac{2\pi f L}{c}\right)^8}\,. \tag{5.9.5}$$

Since $\tilde{R}_{\rm TT}$ is strongly suppressed at low frequencies with respect to $\tilde{R}_{\rm AA}$, the T channel is typically assumed to be signal insensitive. It is customary to express the noise in Ω units using

$$h^2 \tilde{\Omega}_{n,ij}(f, A, P) = \frac{4\pi^2 f^3}{3(H_0/h)^2} S_{n,ij}(f, A, P)\,. \tag{5.9.6}$$

In the analyses presented in this work, we assume the face values for the noise parameters to be $A = 3$, $P = 15$ with 20% Gaussian priors.

5.10 Appendix E : Analytical derivation of the SGWB from a population of merging objects

In this last appendix, we are going to present briefly the analytical derivation of the SGWB. Further details on said derivations, can be found on refs. [236, 373]. The result presented will be computed in the framework of the LISA detector, for which we know that the circular orbit approximation works well and the number of resolvable sources is small enough (~ 10 for $\mathrm{SNR}_{\rm tresh} = 8$) to prevent dampenings in the high-frequency region of the SGWB signal (see ref. [182] for further details).

Following the approach of refs. [236, 374] the characteristic spectral strain of the SGWB is hence defined as

$$h_c^2(f) = \frac{4G}{\pi c^2 f^2}\int_0^\infty dz \frac{\mathrm{d}n}{\mathrm{d}z}\frac{1}{1+z} f_r \frac{\mathrm{d}E_{\rm GW}}{\mathrm{d}f_r}\bigg|_{f_r = f(1+z)}\,, \tag{5.10.1}$$

where $\mathrm{d}n/\mathrm{d}z$ is the comoving number density and the $\mathrm{d}E_{\rm GW}/\mathrm{d}f_r$ represents the (redshifted) energy each event produced per log frequency interval. By assuming a waveform, which in the case of LISA can be approximated using the circular-orbit assumption, we can write the redshifted energy emitted per frequency interval as follows:

$$\frac{\mathrm{d}E_{\rm GW}}{\mathrm{d}f_r} = \frac{\pi}{3G}\frac{(G\mathcal{M})^{5/3}}{(\pi f_r)^{1/3}}\bigg|_{f_r = f(1+z)}\,, \tag{5.10.2}$$

with $\mathcal{M}$ the Chirp Mass for the considered event.

If we now wish to compute the SGWB for a generical population model, the comoving number density as a function of the chosen population may be rewritten as

$$\frac{\mathrm{d}n}{\mathrm{d}z} = \int_0^\infty \mathrm{d}\mathcal{M} \frac{\mathrm{d}^2 n}{\mathrm{d}z \mathrm{d}\mathcal{M}} = \int_0^\infty \mathrm{d}\mathcal{M} R(z) P(\mathcal{M}(m_1, m_2)) \frac{\mathrm{d}t_r}{\mathrm{d}z} \,. \tag{5.10.3}$$

In the last equation, we defined with $R(z)$ the model merger rate for the considered BH population, $P(\mathcal{M}(m_1, m_2))$ is the probability of having a Chirp Mass $\mathcal{M}(m_1, m_2)$ given the mass PDF of the population for m_1, m_2, and $\mathrm{d}t_r/\mathrm{d}z$ is a drift term defined as

$$\frac{\mathrm{d}t_r}{\mathrm{d}z} = \frac{1}{H_0(1+z)\sqrt{\Omega_m(1+z)^3 + \Omega_\Lambda}} \,. \tag{5.10.4}$$

We can finally define the analytical SGWB for a given BH population in Ω units as follows:

$$\Omega_{\mathrm{GW}}(f) = \frac{2(\pi f h_c(f))^2}{3H_0^2} \,, \tag{5.10.5}$$

where $h_c(f)$ is given by

$$h_c^2(f) = \frac{4G^{5/3}}{3c^2\pi^{1/3} f^{4/3}} \int_0^\infty \mathrm{d}z \int_{m_m}^{m_M} \mathrm{d}m_1 \int_{m_m}^{m_M} \mathrm{d}m_2 R(z) p(m_1, m_2) \frac{M(m_1, m_2)^{5/3}}{(1+z)^{1/3}} \frac{\mathrm{d}t_r}{\mathrm{d}z} \,. \tag{5.10.6}$$

Chapter 6

Summary of the results and conclusions

In this document, we have investigated the signal generated by gravitational waves on present-stage, and next-generation detectors. We started by analyzing the real detector strain of the first four events observed by the LIGO collaboration, and we tested the detection claims using a different approach compared to the matched filtering used by LIGO. Even though it is well-known in the literature that matched filtering is the optimal approach to detect gravitational waves if the noise is Gaussian [185–187], this method relies on comparing the detector data with a template bank that contains a class of signals determined in a specified theory. This technique is hence robust and very sensitive only when the noise can be well approximated with Gaussian noise, the template bank is complete enough to describe the expected signals on the detector, and the source waveform is accurately predicted from theory. The discovery of residual signal on the LIGO detector strain after the subtraction of the waveform model by refs. [196, 197, 200] consequently raised questions about the reliability and significance of the LIGO detections claims. These questions were partially answered in ref. [199], which found that the residual signal in the detector strain was due to discrepancies in the best-fit waveforms that were used by the LIGO collaboration. The exact size of the statistical significance, however, was still left unanswered and led to further debate [200, 201]. We hence followed the approach of refs. [199, 200] and used maximum-likelihood waveforms inferred by refs. [206, 207], to perform a blind search with a Pearson cross-correlation analysis in correspondence of the first four LIGO detection claims. In the paper, we demonstrated that even though this approach is less-sensitive compared to the matched filtering adopted by LIGO, all the detection claims are able to be reproduced with statistical significance comparable to the latter even when adopting this highly agnostic approach. We further showed that by using waveforms obtained through maximum likelihood, the residual noise in the detector strain after the subtraction of the signal goes back to values that are not statistically significant. This proved that the residual noise found in the detector strain after the subtraction was only caused by a non-optimal choice of the waveforms, and is not a problem caused by the theory in itself. One point of remark of this article is that

the Pearson cross-correlation, despite not being as sensitive as the matched filtering when looking for gravitational wave signals, can still be used to easily test non-trivial theories on detection claims. In particular, the information that is left by the residual after the subtraction can in principle be used to evaluate the description quality of a theory over another. The last claim, however, still has to be properly tested and is left as an open question for further research works.

For our second paper, we moved from single events on real data to multiple events on simulated data. This was a necessary choice in order to analyze the SGWB on the LISA detector. We hence used the latest results from the LVK inference paper [46] to generate a BBH population in our universe, some modifications to these results were however needed in order to account for intrinsic differences among the two detectors and analysis. First of all, as the main objective was to study the SGWB on LISA, we needed to describe clearly also the population of non-resolvable sources that naturally extends to higher values of redshift compared to the LVK observable volume of universe. We hence adopted a phenomenological merger rate that follows the Star Formation Rate as done in refs. [56, 130]. This allowed us to extend the validity range of the LIGO inferred merger rate after the currently detected farthest away events ($z \lesssim 1$). Another difference that needed to be taken into account when computing populations for the LISA detector, is the difference in the sensitive frequency range among the two detectors. This difference implies that while SOBHB on the LIGO detector frequency range only spend a few milliseconds before coalescing, on the LISA frequency range they can in principle keep inspiraling for several millions of years. Compared to the LIGO detector, the strain on the LISA detector will hence be composed mainly of sources that are already inspiralling once the LISA detector will be turned on, with only a few sources drifting in and out of its frequency range during the mission time. In order to account for this factor, we hence replaced the detector observation time in the equation describing the differential number of BBH events (see eq. (4.2.1)) with a cutoff value for the maximum observed residual time to coalescence by the LISA detector. The previously mentioned equation will then move from asking "How many events can I observe drifting on my detector in x years of observation" to "How many events that are closer than x years away from coalescence will be in my detector frequency range". Events that will drift outside the LISA frequency range during the mission time will be described by a residual time to coalescence smaller than the assumed mission time. The events that will drift inside the LISA frequency range during the assumed mission time, instead, can be ignored as long as the maximum value for the residual time to coalescence is high enough to take into account all the events relevant for the observables we are interested in. After choosing cutoff values for the maximum redshift and residual time to coalescence that were both computationally efficient and exhaustive for the analysis, we computed the SGWB in LISA using four different methods with increasing levels of complexity. We started with a simple analytical evaluation, this method is indeed the fastest but doesn't take into account potential effects arising from the population realization errors or signal processing on the detector strain. We then performed a semi-analytic calculation of

the SGWB by replacing the integrals of the analytical evaluation with a summation over the events coming from a synthesized population. Lastly, we analyzed the real strain on the LISA detector generated by a synthesized population, and estimated the SGWB by iteratively subtracting the resolvable sources. This method is indeed computationally expensive, but allow us to both obtain the resolvable sources on LISA, and analyze the effects on the SGWB shape due to event subtraction as a function of the SNR threshold. We found that for SNR thresholds bigger than 8, all the methods are well in agreement with each other. When not considering the possible effects of archival searches on the detector strain (see refs. [246, 267]), we can hence use the analytical approximation to quickly estimate the SGWB without a large loss of precision. The results obtained for the resolvable sources achieved by using the iterative subtraction method will also be used for a future companion paper that is going to appear in the next months (see ref. [238]). By analyzing the detectability of the predicted SGWB level, we also hinted that due to the high level of precision that we will achieve on its amplitude reconstruction, we can use this measure to break the degeneracy on the Earth-based population parameters estimation. In particular, this result was then used in the third paper presented in this document (see Chapter {5}) to study the BH population outside the ground-based detectors observable range, and search for the potential presence of PBH populations outside the detectors observed volume.

To conclude, in the third paper presented, we considered the possibility of different BH formation channels [52, 294, 295, 315] on the detector strain. In particular, we studied the case of a subpopulation coming from a primordial origin over a fiducial astrophysical SOBBH population. This configuration was already deeply explored in literature, *e.g.* ref. [323] searched for single detections outside the region where we expect astrophysical events to be, refs. [52, 294] analyzed this assumption by looking at features in the mass spectrum of the LVK fiducial model, ref. [274] instead used the SGWB to assess for a PBH component in the high-redshift non-resolvable volume of our universe. Further analysis can also be found in refs. [134, 359] (see also refs. [16, 308] for a detailed procedure on how to identify PBHB). The main motivation that led us to perform this study, instead, resides in the difference in the high redshift behavior between populations of astrophysical and primordial origin [316, 317, 324]. While we know that astrophysical BHs are supposed to follow the cosmic history of our universe, and hence have a merger rate that closely follows the SFR (up to some potential time delays) [56, 57, 130], the PBH merger rate is expected to grow as a function of redshift [16, 274, 294]. Due to this main difference among the two formation channels, we expect the SOBHB population to slowly die at redshift higher than the peak of the SFR, while the PBHB population is supposed to dominate in the high redshift regime. We hence decided to study the potential impact of PBHB subpopulations over the astrophysical SOBHB population in said high redshift regime. To this extent, again we assumed a fiducial population that follows the LVK GWTC-3 results [46], and we extended its regime of validity by means of a phenomenological merger rate in the form of refs. [56, 130, 182]. We then studied the impact of the PBHB subpopulations by considering both the distribution of resolvable sources as a function of

redshift, and the amplitude variation on the LISA SGWB. As we are mainly interested in the high-redshift distribution of resolvable sources, which is hardly accessible by our present-stage GW detectors, we forecasted our results in the next generation of ground-based GW detectors [312, 315]. In particular, we computed our results both for the A^+ LIGO [58] and ET [55, 361] detectors. The value of the SGWB on the LISA detector was instead computed by following the analytical approach described in Chapter {4}. We then presented our results for several different combinations of the PBH merger rate and mass PDF, and we concluded that the three considered detectors work synergistically when this type of study is performed. The amplitude of the SGWB, in particular, always proved to be a useful complementary tool to the information that may be obtained with the resolvable sources on ground-based detectors. This is well expected knowing that by definition, the SGWB is the confusion noise generated by the superposition of the signal of all the non-resolvable sources on the detector strain. It has to be emphasized, however, that in order to compute our results we neglected potential merger among BHs of the two considered channels, as well as the impact of the current uncertainties on the GWTC-3 inferred parameters. The second assumption, in particular, is motivated by the fact that the current uncertainties are so large ($\sim 50\%$) that they would dominate our results when forecasted on the next generation of GWs detectors, for which we expect these uncertainties to become much smaller in the next years. While without taking care of the aforementioned assumptions our results are merely indicative, the codes that we presented in our GitHub repository [330] can easily be adapted to future LVK inference results. This study, which in the presented paper can be taken as a proof of concept, can hence be easily performed with the tools provided when the quality of our observations, and hence the errors on the inference, will improve. We expect that the presented analysis, together with the others discussed at the beginning of this paragraph, will improve our constraints on the PBH component of our universe deeply when the next generation of detectors will be running.

Bibliography

[1] E. Barausse *et al.*, "Prospects for Fundamental Physics with LISA," *Gen. Rel. Grav.*, vol. 52, no. 8, p. 81, 2020.

[2] P. A. Seoane *et al.*, "The effect of mission duration on LISA science objectives," *Gen. Rel. Grav.*, vol. 54, no. 1, p. 3, 2022.

[3] A. Einstein, "Zur Allgemeinen Relativitätstheorie," *Sitzungsber. Preuss. Akad. Wiss. Berlin (Math. Phys.)*, vol. 1915, pp. 778–786, 1915. [Addendum: Sitzungsber.Preuss.Akad.Wiss.Berlin (Math.Phys.) 1915, 799–801 (1915)].

[4] A. Einstein, "Näherungsweise Integration der Feldgleichungen der Gravitation," *Sitzungsberichte der Königlich Preussischen Akademie der Wissenschaften*, pp. 688–696, Jan. 1916.

[5] A. Einstein, "Über Gravitationswellen," *Sitzungsber. Preuss. Akad. Wiss. Berlin (Math. Phys.)*, vol. 1918, pp. 154–167, 1918.

[6] A. Einstein, *Die Grundlage der allgemeinen Relativitätstheorie*, pp. 81–124. Wiesbaden: Vieweg+Teubner Verlag, 1923.

[7] B. Schutz, *A First Course in General Relativity*. Cambridge University Press, 2 ed., 2009.

[8] V. Ferrari, L. Gualtieri, and P. Pani, *General Relativity and its Applications*. CRC Press, Taylor & Francis Group, 2020.

[9] H. Grote and D. H. Reitze, "First-Generation Interferometric Gravitational-Wave Detectors," in *46th Rencontres de Moriond on Gravitational Waves and Experimental Gravity*, (Paris, France), pp. 5–18, Moriond, 2011.

[10] M. Pitkin, S. Reid, S. Rowan, and J. Hough, "Gravitational Wave Detection by Interferometry (Ground and Space)," *Living Rev. Rel.*, vol. 14, p. 5, 2011.

[11] S. Kroker and R. Nawrodt, "The Einstein telescope," *IEEE Instrum. Measur. Mag.*, vol. 18, no. 3, pp. 4–8, 2015.

[12] J. Baker *et al.*, "The Laser Interferometer Space Antenna: Unveiling the Millihertz Gravitational Wave Sky," 7 2019.

[13] K. Schwarzschild, "On the gravitational field of a mass point according to Einstein's theory," *Sitzungsber. Preuss. Akad. Wiss. Berlin (Math. Phys.)*, vol. 1916, pp. 189–196, 1916.

[14] K. Schwarzschild, "On the gravitational field of a sphere of incompressible fluid

according to Einstein's theory," *Sitzungsber. Preuss. Akad. Wiss. Berlin (Math. Phys.)*, vol. 1916, pp. 424–434, 1916.

[15] L. Barack *et al.*, "Black holes, gravitational waves and fundamental physics: a roadmap," *Class. Quant. Grav.*, vol. 36, no. 14, p. 143001, 2019.

[16] E. Bagui *et al.*, "Primordial black holes and their gravitational-wave signatures," 10 2023.

[17] P. Marcoccia and G. Montani, "Weakly Inhomogeneous models for the Low-Redshift Universe," 8 2018.

[18] R. C. Nunes, "Structure formation in $f(T)$ gravity and a solution for H_0 tension," *JCAP*, vol. 05, p. 052, 2018.

[19] S. Banerjee, M. Petronikolou, and E. N. Saridakis, "Alleviating H_0 Tension with New Gravitational Scalar Tensor Theories," 9 2022.

[20] C. M. Will, "The Confrontation between General Relativity and Experiment," *Living Rev. Rel.*, vol. 17, p. 4, 2014.

[21] B. Abbott *et al.*, "Tests of General Relativity with the Binary Black Hole Signals from the LIGO-Virgo Catalog GWTC-1," *Phys. Rev. D*, vol. 100, no. 10, p. 104036, 2019.

[22] A. A. Shoom, P. K. Gupta, B. Krishnan, A. B. Nielsen, and C. D. Capano, "Testing GR with the Gravitational Wave Inspiral Signal GW170817," 5 2021.

[23] C. D. Capano, J. Abedi, S. Kastha, A. H. Nitz, J. Westerweck, Y.-F. Wang, M. Cabero, A. B. Nielsen, and B. Krishnan, "Statistical validation of the detection of a sub-dominant quasi-normal mode in GW190521," 9 2022.

[24] P. R. Capelo, *Astrophysical black holes*. 2019.

[25] M. Pieroni, A. Ricciardone, and E. Barausse, "Detectability and parameter estimation of stellar origin black hole binaries with next generation gravitational wave detectors," *Sci. Rep.*, vol. 12, no. 1, p. 17940, 2022.

[26] E. Poisson, "The Motion of point particles in curved space-time," *Living Rev. Rel.*, vol. 7, p. 6, 2004.

[27] L. Tu, *An Introduction to Manifolds*. Universitext, Springer New York, 2010.

[28] J. Smith, *Introduction to Special Relativity*. Dover Books on Physics, Dover Publications, 2016.

[29] A. Friedmann, "Über die Krümmung des Raumes," *Zeitschrift fur Physik*, vol. 10, pp. 377–386, Jan. 1922.

[30] B. F. Schutz, *A FIRST COURSE IN GENERAL RELATIVITY*. Cambridge, UK: Cambridge Univ. Pr., 1985.

[31] M. Maggiore, *Gravitational Waves. Vol. 1: Theory and Experiments*. Oxford Master Series in Physics, Oxford University Press, 2007.

[32] P. J. E. Peebles, *Principles of physical cosmology*. 1994.

[33] G. Montani, M. V. Battisti, R. Benini, and G. Imponente, *Primordial cosmology*. Singapore: World Scientific, 2009.

[34] L. D. Landau and E. M. Lifshitz, *Mechanics, Third Edition: Volume 1 (Course of Theoretical Physics)*. Butterworth-Heinemann, 3 ed., Jan. 1976.

[35] I. Newton, *Philosophiæ Naturalis Principia Mathematica*. 1687.

[36] R. Casadio, "What is the Schwarzschild radius of a quantum mechanical particle?," *Springer Proc. Phys.*, vol. 170, pp. 225–231, 2016.

[37] S. Chandrasekhar, *The mathematical theory of black holes*. 1985.

[38] R. P. Kerr, "Gravitational field of a spinning mass as an example of algebraically special metrics," *Phys. Rev. Lett.*, vol. 11, pp. 237–238, Sep 1963.

[39] M. Visser, "The Kerr spacetime: A Brief introduction," in *Kerr Fest: Black Holes in Astrophysics, General Relativity and Quantum Gravity*, 6 2007.

[40] D. L. Wiltshire, M. Visser, and S. M. Scott, *The Kerr spacetime: Rotating black holes in general relativity*. Cambridge University Press, 1 2009.

[41] T. A. Callister, S. J. Miller, K. Chatziioannou, and W. M. Farr, "No Evidence that the Majority of Black Holes in Binaries Have Zero Spin," *Astrophys. J. Lett.*, vol. 937, no. 1, p. L13, 2022.

[42] N. Gürlebeck, "No-hair theorem for Black Holes in Astrophysical Environments," *Phys. Rev. Lett.*, vol. 114, no. 15, p. 151102, 2015.

[43] V. Cardoso and L. Gualtieri, "Testing the black hole 'no-hair' hypothesis," *Class. Quant. Grav.*, vol. 33, no. 17, p. 174001, 2016.

[44] B. Abbott *et al.*, "Observation of Gravitational Waves from a Binary Black Hole Merger," *Phys. Rev. Lett.*, vol. 116, no. 6, p. 061102, 2016.

[45] R. Abbott *et al.*, "GWTC-3: Compact Binary Coalescences Observed by LIGO and Virgo During the Second Part of the Third Observing Run," 11 2021.

[46] R. Abbott *et al.*, "The population of merging compact binaries inferred using gravitational waves through GWTC-3," 11 2021.

[47] M. Mapelli, *Formation Channels of Single and Binary Stellar-Mass Black Holes*. 2021.

[48] A. C. Fabian and A. N. Lasenby, "Astrophysical Black Holes," 11 2019.

[49] M. Y. Khlopov, "Primordial Black Holes," *Res. Astron. Astrophys.*, vol. 10, pp. 495–528, 2010.

[50] B. Carr, K. Kohri, Y. Sendouda, and J. Yokoyama, "Constraints on primordial black holes," *Reports on Progress in Physics*, vol. 84, p. 116902, 11 2021.

[51] V. De Luca, G. Franciolini, P. Pani, and A. Riotto, "Primordial Black Holes Confront LIGO/Virgo data: Current situation," *JCAP*, vol. 06, p. 044, 2020.

[52] G. Franciolini, V. Baibhav, V. De Luca, K. K. Y. Ng, K. W. K. Wong, E. Berti, P. Pani, A. Riotto, and S. Vitale, "Searching for a subpopulation of primordial black holes in LIGO-Virgo gravitational-wave data," *Phys. Rev. D*, vol. 105, no. 8, p. 083526, 2022.

[53] K. Breivik, C. L. Rodriguez, S. L. Larson, V. Kalogera, and F. A. Rasio, "Distinguishing Between Formation Channels for Binary Black Holes with LISA," *Astrophys. J. Lett.*, vol. 830, no. 1, p. L18, 2016.

[54] G. Franciolini and P. Pani, "Stochastic gravitational-wave background at 3G detectors as a smoking gun for microscopic dark matter relics," 4 2023.

[55] G. Franciolini, F. Iacovelli, M. Mancarella, M. Maggiore, P. Pani, and A. Riotto, "Searching for Primordial Black Holes with the Einstein Telescope: impact of design and systematics," 4 2023.

[56] P. Madau and M. Dickinson, "Cosmic Star Formation History," *Ann. Rev. Astron. Astrophys.*, vol. 52, pp. 415–486, 2014.

[57] A. Mangiagli, M. Bonetti, A. Sesana, and M. Colpi, "Merger rate of stellar black hole binaries above the pair instability mass gap," *Astrophys. J. Lett.*, vol. 883, no. 1, p. L27, 2019.

[58] M. L. Barsotti, L. McCuller and P. Fritschel, "The a+ design curve," 2018.

[59] P. Amaro-Seoane *et al.*, "Laser Interferometer Space Antenna," 2 2017.

[60] S. Hild and A. Freise, "Et sensitivities," 2009.

[61] F. LeBlanc, *An Introduction to Stellar Astrophysics*. 2010.

[62] N. Langer, "Presupernova evolution of massive single and binary stars," *Annual Review of Astronomy and Astrophysics*, vol. 50, no. 1, pp. 107–164, 2012.

[63] S. Ekström, C. Georgy, P. Eggenberger, G. Meynet, N. Mowlavi, A. Wyttenbach, A. Granada, T. Decressin, R. Hirschi, U. Frischknecht, C. Charbonnel, and A. Maeder, "Grids of stellar models with rotation. I. Models from 0.8 to 120 $M_\odot$ at solar metallicity (Z = 0.014)," , vol. 537, p. A146, Jan. 2012.

[64] A. Heger, B. Müller, and I. Mandel, "Chapter 3: Black Holes as the End State of Stellar Evolution: Theory and Simulations," pp. 61–111, 2023.

[65] S.-C. Yoon, S. E. Woosley, and N. Langer, "Type ib/c supernovae in binary systems. i. evolution and properties of the progenitor stars," *The Astrophysical Journal*, vol. 725, p. 940, nov 2010.

[66] B. Paxton *et al.*, "Modules for Experiments in Stellar Astrophysics (MESA): Binaries, Pulsations, and Explosions," *Astrophys. J. Suppl.*, vol. 220, no. 1, p. 15, 2015.

[67] K. Belczynski, T. Ryu, R. Perna, E. Berti, T. L. Tanaka, and T. Bulik, "On the likelihood of detecting gravitational waves from Population III compact object binaries," *Mon. Not. Roy. Astron. Soc.*, vol. 471, no. 4, pp. 4702–4721, 2017.

[68] A. Vigna-Gómez, S. Toonen, E. Ramirez-Ruiz, N. W. C. Leigh, J. Riley, and C.-J. Haster, "Massive Stellar Triples Leading to Sequential Binary Black-Hole Mergers in the Field," *Astrophys. J. Lett.*, vol. 907, no. 1, p. L19, 2021.

[69] F. Antonini, S. Toonen, and A. S. Hamers, "Binary black hole mergers from field triples: properties, rates and the impact of stellar evolution," *Astrophys. J.*, vol. 841, no. 2, p. 77, 2017.

[70] T. Ryu, S. de Mink, R. Farmer, R. Pakmor, R. Perna, and V. Springel, "Close Encounters of Star - Black Hole Binaries with Single Stars," 7 2023.

[71] K. Omukai, T. Tsuribe, R. Schneider, and A. Ferrara, "Thermal and fragmentation properties of star-forming clouds in low-metallicity environments," *Astrophys. J.*, vol. 626, pp. 627–643, 2005.

[72] M. L. Norman, "Population III Star Formation and IMF," *AIP Conf. Proc.*, vol. 990, no. 1, pp. 3–15, 2008.

[73] A. Tanikawa, T. Yoshida, T. Kinugawa, A. A. Trani, T. Hosokawa, H. Susa, and K. Omukai, "Merger Rate Density of Binary Black Holes through Isolated Population I, II, III and Extremely Metal-poor Binary Star Evolution," *Astrophys. J.*, vol. 926, no. 1, p. 83, 2022.

[74] T. Kaczmarek, C. Olczak, and S. Pfalzner, "Evolution of the binary population in young dense star clusters," *Astronomy & Astrophysics*, vol. 528, p. A144, 2011.

[75] G. D. Quinlan and S. L. Shapiro, "The Dynamical Evolution of Dense Star Clusters in Galactic Nuclei," , vol. 356, p. 483, June 1990.

[76] N. Leigh, N. Stone, J. Webb, and W. Lyra, "The thermodynamics of stellar multiplicity: dynamical evolution of binary star populations in dense stellar environments," *arXiv preprint arXiv:2205.15351*, 2022.

[77] J. Kaler, "Stellar evolution," *McGraw-Hill Encyclopedia of Science and Technology, eleventh ed., McGraw-Hill*, 2012. https://www.accessscience.com/content/article/a654000.

[78] D. J. Whalen, M. Surace, C. Bernhardt, E. Zackrisson, F. Pacucci, B. L. Ziegler, and M. Hirschmann, "Finding Direct-Collapse Black Holes at Birth," *Astrophys. J. Lett.*, vol. 897, no. 1, p. L16, 2020.

[79] M. A. Latif, S. Khochfar, and D. Whalen, "The Birth of Binary Direct-Collapse Black Holes," *Astrophys. J. Lett.*, vol. 892, no. 1, p. L4, 2020.

[80] M. Chruslinska and G. Nelemans, "Metallicity of stars formed throughout the cosmic history based on the observational properties of star-forming galaxies," , vol. 488, pp. 5300–5326, Oct. 2019.

[81] L. Amard and S. P. Matt, "The Impact of Metallicity on the Evolution of the Rotation and Magnetic Activity of Sun-like Stars," , vol. 889, p. 108, Feb. 2020.

[82] M. Mapelli and A. Bressan, "Impact of metallicity on the evolution of young star clusters," *Monthly Notices of the Royal Astronomical Society*, vol. 430, no. 4, pp. 3120–3127, 2013.

[83] L. Gehrig, T. Steindl, E. I. Vorobyov, R. Guadarrama, and K. Zwintz, "The influence of metallicity on a combined stellar and disk evolution," , vol. 669, p. A84, Jan. 2023.

[84] J. S. Vink and A. de Koter, "On the metallicity dependence of Wolf-Rayet winds," *Astron. Astrophys.*, vol. 442, p. 587, 2005.

[85] A. A. Trani, M. Mapelli, and A. Bressan, "The impact of metallicity-dependent mass-loss versus dynamical heating on the early evolution of star clusters," *Monthly Notices of the Royal Astronomical Society*, vol. 445, no. 2, pp. 1967–1976, 2014.

[86] J. S. Vink, "Very Massive Stars: a metallicity-dependent upper-mass limit, slow winds, and the self-enrichment of Globular Clusters," *Astron. Astrophys.*, vol. 615, p. A119, 2018.

[87] J. S. Vink and A. A. C. Sander, "Metallicity-dependent wind parameter predictions for OB stars," *Mon. Not. Roy. Astron. Soc.*, vol. 504, no. 2, pp. 2051–2061, 2021.

[88] A. Gallazzi, S. Charlot, J. Brinchmann, S. D. M. White, and C. A. Tremonti, "The Ages and metallicities of galaxies in the local Universe," *Mon. Not. Roy. Astron. Soc.*, vol. 362, pp. 41–58, 2005.

[89] M. M. Larkin, R. Gerasimov, and A. J. Burgasser, "Characterization of Population III Stars with Stellar Atmosphere and Evolutionary Modeling and Predictions of their Observability with the JWST," , vol. 165, p. 2, Jan. 2023.

[90] A. Heger and S. E. Woosley, "The nucleosynthetic signature of population III," *Astrophys. J.*, vol. 567, pp. 532–543, 2002.

[91] T. Chantavat, S. Chongchitnan, and J. Silk, "The most massive Population III stars," *Mon. Not. Roy. Astron. Soc.*, vol. 522, no. 3, pp. 3256–3262, 2023.

[92] F. Santoliquido, M. Mapelli, G. Iorio, G. Costa, S. C. O. Glover, T. Hartwig, R. S. Klessen, and L. Merli, "Binary black hole mergers from Population III stars: uncertainties from star formation and binary star properties," 3 2023.

[93] U. Maio, B. Ciardi, K. Dolag, L. Tornatore, and S. Khochfar, "The transition from population III to population II-I star formation," , vol. 407, pp. 1003–1015, Sept. 2010.

[94] T. J. Dupuy and A. L. Kraus, "Distances, Luminosities, and Temperatures of the Coldest Known Substellar Objects," *Science*, vol. 341, pp. 1492–1495, Sept. 2013.

[95] H. Sana, S. E. de Mink, A. de Koter, N. Langer, C. J. Evans, M. Gieles, E. Gosset, R. G. Izzard, J. B. Le Bouquin, and F. R. N. Schneider, "Binary Interaction Dominates the Evolution of Massive Stars," *Science*, vol. 337, p. 444, July 2012.

[96] S. Rao, C. Pezzotti, G. Meynet, P. Eggenberger, G. Buldgen, C. Mordasini, V. Bourrier, S. Ekström, and C. Georgy, "Star-planet interactions. VI. Tides, stellar activity, and planetary evaporation," , vol. 651, p. A50, July 2021.

[97] D. Kushnir, M. Zaldarriaga, J. A. Kollmeier, and R. Waldman, "GW150914: spin-based constraints on the merger time of the progenitor system," *Monthly Notices of the Royal Astronomical Society*, vol. 462, pp. 844–849, 07 2016.

[98] H. M. Boffin, "Mass transfer by stellar wind," in *Ecology of Blue Straggler Stars*, pp. 153–178, Springer, 2014.

[99] J. Ziółkowski and A. A. Zdziarski, "Non-conservative mass transfer in stellar evolution and the case of V404 Cyg/GS 2023+338," *Mon. Not. Roy. Astron. Soc.*, vol. 480, no. 2, pp. 1580–1586, 2018.

[100] T. L. S. Wong and L. Bildsten, "Mass Transfer and Stellar Evolution of the White Dwarfs in AM CVn Binaries," *Astrophys. J.*, vol. 923, no. 1, p. 125, 2021.

[101] N. Ivanova, S. Justham, X. Chen, O. De Marco, C. L. Fryer, E. Gaburov, H. Ge, E. Glebbeek, Z. Han, X. D. Li, G. Lu, T. Marsh, P. Podsiadlowski, A. Potter, N. Soker, R. Taam, T. M. Tauris, E. P. J. van den Heuvel, and R. F. Webbink, "Common envelope evolution: where we stand and how we can move forward," , vol. 21, p. 59, Feb. 2013.

[102] D. Jones, "Observational Constraints on the Common Envelope Phase," in *Reviews in Frontiers of Modern Astrophysics; From Space Debris to Cosmology*, pp. 123–153, 2020.

[103] R. Hirai and I. Mandel, "A Two-stage Formalism for Common-envelope Phases of Massive Stars," *Astrophys. J. Lett.*, vol. 937, no. 2, p. L42, 2022.

[104] M. Mapelli, "Binary Black Hole Mergers: Formation and Populations," *Front. Astron. Space Sci.*, vol. 7, p. 38, 2020.

[105] P. Marchant, K. M. W. Pappas, M. Gallegos-Garcia, C. P. L. Berry, R. E. Taam, V. Kalogera, and P. Podsiadlowski, "The role of mass transfer and common envelope evolution in the formation of merging binary black holes," *Astron. Astrophys.*, vol. 650, p. A107, 2021.

[106] P. Podsiadlowski, P. C. Joss, and J. J. L. Hsu, "Presupernova Evolution in Massive Interacting Binaries," , vol. 391, p. 246, May 1992.

[107] S. Wellstein and N. Langer, "Implications of massive close binaries for black hole formation and supernovae," *Astron. Astrophys.*, vol. 350, p. 148, 1999.

[108] M. R. Krumholz, C. F. McKee, and J. Bland-Hawthorn, "Star clusters across cosmic time," *Annual Review of Astronomy and Astrophysics*, vol. 57, pp. 227–303, 2019.

[109] A. P. Milone and A. F. Marino, "Multiple populations in star clusters," *Universe*, vol. 8, no. 7, p. 359, 2022.

[110] C. Olczak, S. Pfalzner, and A. Eckart, "Stellar interactions in dense and sparse star clusters," *Astronomy & Astrophysics*, vol. 509, p. A63, 2010.

[111] S. Khoperskov, A. Mastrobuono-Battisti, P. Di Matteo, and M. Haywood, "Mergers, tidal interactions, and mass exchange in a population of disc globular clusters," *Astron. Astrophys.*, vol. 620, p. A154, 2018.

[112] A. Bahramian, C. O. Heinke, G. R. Sivakoff, and J. C. Gladstone, "Stellar Encounter Rate in Galactic Globular Clusters," *Astrophys. J.*, vol. 766, p. 136, 2013.

[113] A. M. Geller and N. W. Leigh, "Interrupted stellar encounters in star clusters," *The Astrophysical Journal Letters*, vol. 808, no. 1, p. L25, 2015.

[114] S. Dib, S. Schmeja, and R. J. Parker, "Structure and mass segregation in galactic stellar clusters," *Monthly Notices of the Royal Astronomical Society*, vol. 473, no. 1, pp. 849–859, 2018.

[115] R. De Grijs, C. Li, and A. M. Geller, "The dynamical importance of binary systems in young massive star clusters," *Proceedings of the International Astronomical Union*, vol. 12, no. S316, pp. 222–227, 2015.

[116] S. Torniamenti, A. Ballone, M. Mapelli, N. Gaspari, U. N. Di Carlo, S. Rastello, N. Giacobbo, and M. Pasquato, "The impact of binaries on the evolution of star clusters from turbulent molecular clouds," *Monthly Notices of the Royal Astronomical Society*, vol. 507, no. 2, pp. 2253–2266, 2021.

[117] A. J. Dittmann, M. Cantiello, and A. S. Jermyn, "Accretion onto Stars in the Disks of Active Galactic Nuclei," *Astrophys. J.*, vol. 916, no. 1, p. 48, 2021.

[118] M. Cantiello, A. S. Jermyn, and D. N. C. Lin, "Stellar Evolution in AGN Disks," , vol. 910, p. 94, Apr. 2021.

[119] F. Özel, D. Psaltis, R. Narayan, and J. E. McClintock, "The Black Hole Mass Distribution in the Galaxy," , vol. 725, pp. 1918–1927, Dec. 2010.

[120] W. M. Farr, N. Sravan, A. Cantrell, L. Kreidberg, C. D. Bailyn, I. Mandel, and V. Kalogera, "The Mass Distribution of Stellar-mass Black Holes," , vol. 741, p. 103, Nov. 2011.

[121] S. E. Woosley, "The Progenitor of Gw150914," *Astrophys. J. Lett.*, vol. 824, no. 1, p. L10, 2016.

[122] V. CASTELLANI, "L'astrofisica stellare," *Nuncius*, vol. 17, no. 2, pp. 423 – 446, 2002.

[123] H. J. Lamers and E. M. Levesque, *Understanding Stellar Evolution*. 2514-3433, IOP Publishing, 2017.

[124] S. C. Yoon, S. E. Woosley, and N. Langer, "Type Ib/c Supernovae in Binary Systems. I. Evolution and Properties of the Progenitor Stars," , vol. 725, pp. 940–954, Dec. 2010.

[125] J. H. Groh, S. Ekström, C. Georgy, G. Meynet, A. Choplin, P. Eggenberger, R. Hirschi, A. Maeder, L. J. Murphy, I. Boian, and E. J. Farrell, "Grids of stellar models with rotation. IV. Models from 1.7 to 120 $M_{\odot}$ at a metallicity Z = 0.0004," , vol. 627, p. A24, July 2019.

[126] M. Fishbach and V. Kalogera, "The time delay distribution and formation metallicity of LIGO-virgo's binary black holes," *The Astrophysical Journal Letters*, vol. 914, p. L30, jun 2021.

[127] L. A. C. van Son, S. E. de Mink, T. Callister, S. Justham, M. Renzo, T. Wagg, F. S. Broekgaarden, F. Kummer, R. Pakmor, and I. Mandel, "The redshift evolution of the binary black hole merger rate: A weighty matter," *The Astrophysical Journal*, vol. 931, p. 17, may 2022.

[128] P. Madau, L. Pozzetti, and M. Dickinson, "The Star formation history of field galaxies," *Astrophys. J.*, vol. 498, p. 106, 1998.

[129] L. Hernquist and V. Springel, "An analytical model for the history of cosmic star formation," *Monthly Notices of the Royal Astronomical Society*, vol. 341, pp. 1253–1267, 06 2003.

[130] P. Madau and T. Fragos, "Radiation Backgrounds at Cosmic Dawn: X-Rays from Compact Binaries," *Astrophys. J.*, vol. 840, no. 1, p. 39, 2017.

[131] J. Garcia-Bellido, S. Clesse, and P. Fleury, "Primordial black holes survive SN lensing constraints," *Phys. Dark Univ.*, vol. 20, pp. 95–100, 2018.

[132] M. Sasaki, T. Suyama, T. Tanaka, and S. Yokoyama, "Primordial black holes—perspectives in gravitational wave astronomy," *Class. Quant. Grav.*, vol. 35, no. 6, p. 063001, 2018.

[133] P. Villanueva-Domingo, O. Mena, and S. Palomares-Ruiz, "A brief review on primordial black holes as dark matter," *Front. Astron. Space Sci.*, vol. 8, p. 87, 2021.

[134] J. García-Bellido, "Massive primordial black holes as dark matter and their detection with gravitational waves," *Journal of Physics: Conference Series*, vol. 840, p. 012032, may 2017.

[135] Y. B. Zel'dovich and I. D. Novikov, "The Hypothesis of Cores Retarded during Expansion and the Hot Cosmological Model," *Soviet Astron. AJ (Engl. Transl.),*, vol. 10, p. 602, 1967.

[136] S. Hawking, "Gravitationally collapsed objects of very low mass," *Mon. Not. Roy. Astron. Soc.*, vol. 152, p. 75, 1971.

[137] B. J. Carr and S. W. Hawking, "Black holes in the early Universe," *Mon. Not. Roy. Astron. Soc.*, vol. 168, pp. 399–415, 1974.

[138] G. F. Chapline, "Cosmological effects of primordial black holes," *Nature*, vol. 253, no. 5489, pp. 251–252, 1975.

[139] E. Aubourg *et al.*, "Evidence for gravitational microlensing by dark objects in the galactic halo," *Nature*, vol. 365, pp. 623–625, 1993.

[140] C. Alcock *et al.*, "The MACHO project LMC microlensing results from the first two years and the nature of the galactic dark halo," *Astrophys. J.*, vol. 486, pp. 697–726, 1997.

[141] P. Tisserand *et al.*, "Limits on the Macho Content of the Galactic Halo from the EROS-2 Survey of the Magellanic Clouds," *Astron. Astrophys.*, vol. 469, pp. 387–404, 2007.

[142] L. Wyrzykowski, J. Skowron, S. Kozłowski, A. Udalski, M. K. Szymań ski, M. Kubiak, G. Pietrzyński, I. Soszyński, O. Szewczyk, K. Ulaczyk, R. Poleski, and P. Tisserand, "The OGLE view of microlensing towards the magellanic clouds - IV. OGLE-III SMC data and final conclusions on MACHOs72," *Monthly Notices of the Royal Astronomical Society*, vol. 416, pp. 2949–2961, aug 2011.

[143] M. Ricotti, J. P. Ostriker, and K. J. Mack, "Effect of primordial black holes on the cosmic microwave background and cosmological parameter estimates," *The Astrophysical Journal*, vol. 680, p. 829, jun 2008.

[144] B. Abbott *et al.*, "GWTC-1: A Gravitational-Wave Transient Catalog of Compact Binary Mergers Observed by LIGO and Virgo during the First and Second Observing Runs," *Phys. Rev. X*, vol. 9, no. 3, p. 031040, 2019.

[145] K. Ando, K. Inomata, M. Kawasaki, K. Mukaida, and T. T. Yanagida, "Primordial black holes for the LIGO events in the axionlike curvaton model," *Phys. Rev. D*, vol. 97, no. 12, p. 123512, 2018.

[146] J. Garcia-Bellido, M. Peloso, and C. Unal, "Gravitational Wave signatures of inflationary models from Primordial Black Hole Dark Matter," *JCAP*, vol. 09, p. 013, 2017.

[147] Z. Arzoumanian *et al.*, "The NANOGrav 12.5 yr Data Set: Search for an Isotropic Stochastic Gravitational-wave Background," *Astrophys. J. Lett.*, vol. 905, no. 2, p. L34, 2020.

[148] B. Carr and F. Kuhnel, "Primordial Black Holes as Dark Matter: Recent Developments," *Ann. Rev. Nucl. Part. Sci.*, vol. 70, pp. 355–394, 2020.

[149] K. Enqvist, "Lemaitre-Tolman-Bondi model and accelerating expansion," *Gen. Rel. Grav.*, vol. 40, pp. 451–466, 2008.

[150] A. G. Polnarev and I. Musco, "Curvature profiles as initial conditions for primordial black hole formation," *Class. Quant. Grav.*, vol. 24, pp. 1405–1432, 2007.

[151] D. S. Salopek and J. R. Bond, "Nonlinear evolution of long wavelength metric fluctuations in inflationary models," *Phys. Rev. D*, vol. 42, pp. 3936–3962, 1990.

[152] C.-M. Yoo, T. Harada, J. Garriga, and K. Kohri, "Primordial black hole abundance from random Gaussian curvature perturbations and a local density threshold," *PTEP*, vol. 2018, no. 12, p. 123E01, 2018.

[153] I. Musco, "Threshold for primordial black holes: Dependence on the shape of the cosmological perturbations," *Phys. Rev. D*, vol. 100, no. 12, p. 123524, 2019.

[154] M. Shibata and M. Sasaki, "Black hole formation in the friedmann universe: Formulation and computation in numerical relativity," *Phys. Rev. D*, vol. 60, p. 084002, Sep 1999.

[155] C. W. Misner and D. H. Sharp, "Relativistic equations for adiabatic, spherically symmetric gravitational collapse," *Phys. Rev.*, vol. 136, pp. B571–B576, Oct 1964.

[156] A. B. Nielsen and D.-h. Yeom, "Spherically symmetric trapping horizons, the Misner-Sharp mass and black hole evaporation," *Int. J. Mod. Phys. A*, vol. 24, pp. 5261–5285, 2009.

[157] A. Escrivà, C. Germani, and R. K. Sheth, "Universal threshold for primordial black hole formation," *Phys. Rev. D*, vol. 101, p. 044022, Feb 2020.

[158] V. De Luca, G. Franciolini, A. Kehagias, M. Peloso, A. Riotto, and C. Ünal, "The Ineludible non-Gaussianity of the Primordial Black Hole Abundance," *JCAP*, vol. 07, p. 048, 2019.

[159] S. Young, I. Musco, and C. T. Byrnes, "Primordial black hole formation and abundance: contribution from the non-linear relation between the density and curvature perturbation," *JCAP*, vol. 11, p. 012, 2019.

[160] V. D. Luca, G. Franciolini, P. Pani, and A. Riotto, "The evolution of primordial black holes and their final observable spins," *Journal of Cosmology and Astroparticle Physics*, vol. 2020, p. 052, apr 2020.

[161] V. Desjacques and A. Riotto, "Spatial clustering of primordial black holes," *Phys. Rev. D*, vol. 98, no. 12, p. 123533, 2018.

[162] V. De Luca, V. Desjacques, G. Franciolini, and A. Riotto, "The clustering evolution of primordial black holes," *JCAP*, vol. 11, p. 028, 2020.

[163] K. S. Thorne, "Multipole expansions of gravitational radiation," *Rev. Mod. Phys.*, vol. 52, pp. 299–339, Apr 1980.

[164] L. Collaboration, "Calculating gravitational waveforms: examples," 1 2021. https://dcc.ligo.org/public/0097/T1200476/002/GW_examples.pdf.

[165] B. J. Owen and B. S. Sathyaprakash, "Matched filtering of gravitational waves from inspiraling compact binaries: Computational cost and template placement," *Phys. Rev. D*, vol. 60, p. 022002, 1999.

[166] S. Babak, R. Balasubramanian, D. Churches, T. Cokelaer, and B. S. Sathyaprakash, "A Template bank to search for gravitational waves from inspiralling compact binaries. I. Physical models," *Class. Quant. Grav.*, vol. 23, pp. 5477–5504, 2006.

[167] S. Babak, "Building a stochastic template bank for detecting massive black hole binaries," *Class. Quant. Grav.*, vol. 25, p. 195011, 2008.

[168] N. Indik, K. Haris, T. Dal Canton, H. Fehrmann, B. Krishnan, A. Lundgren, A. B. Nielsen, and A. Pai, "Stochastic template bank for gravitational wave searches for precessing neutron-star–black-hole coalescence events," *Phys. Rev. D*, vol. 95, no. 6, p. 064056, 2017.

[169] N. Indik, H. Fehrmann, F. Harke, B. Krishnan, and A. B. Nielsen, "Reducing the number of templates for aligned-spin compact binary coalescence gravitational wave searches using metric-agnostic template nudging," *Phys. Rev. D*, vol. 97, no. 12, p. 124008, 2018.

[170] T. Dal Canton and I. W. Harry, "Designing a template bank to observe compact binary coalescences in Advanced LIGO's second observing run," 5 2017.

[171] S. Khan, S. Husa, M. Hannam, F. Ohme, M. Pürrer, X. Jiménez Forteza, and A. Bohé, "Frequency-domain gravitational waves from nonprecessing black-hole binaries. II. A phenomenological model for the advanced detector era," *Phys. Rev. D*, vol. 93, no. 4, p. 044007, 2016.

[172] S. Husa, S. Khan, M. Hannam, M. Pürrer, F. Ohme, X. Jiménez Forteza, and A. Bohé, "Frequency-domain gravitational waves from nonprecessing black-hole binaries. I. New numerical waveforms and anatomy of the signal," *Phys. Rev. D*, vol. 93, no. 4, p. 044006, 2016.

[173] G. Pratten *et al.*, "Computationally efficient models for the dominant and subdominant harmonic modes of precessing binary black holes," *Phys. Rev. D*, vol. 103, no. 10, p. 104056, 2021.

[174] A. Maselli, L. Gualtieri, V. Ferrari, and F. Pannarale, "On the validity of the adiabatic approximation in compact binary inspirals," in *13th Marcel Grossmann Meeting on Recent Developments in Theoretical and Experimental General Relativity, Astrophysics, and Relativistic Field Theories*, pp. 951–953, 2015.

[175] J. M. Antelis, J. M. Hernández, and C. Moreno, "Post-newtonian approximation of gravitational waves from the inspiral phase," *Journal of Physics: Conference Series*, vol. 1030, p. 012005, may 2018.

[176] X.-J. Zhu, E. Howell, T. Regimbau, D. Blair, and Z.-H. Zhu, "Stochastic Gravitational Wave Background from Coalescing Binary Black Holes," *Astrophys. J.*, vol. 739, p. 86, 2011.

[177] A. Celletti, *Stability and Chaos in Celestial Mechanics*. 01 2010.

[178] R. Fitzpatrick, *Bibliography*. Cambridge University Press, 2012.

[179] R. A. Hulse and J. H. Taylor, "Discovery of a pulsar in a binary system," *Astrophys. J. Lett.*, vol. 195, pp. L51–L53, 1975.

[180] M. Bramanti, C. D. Pagani, and S. Salsa, "Analisi matematica 2," 2009.

[181] V. Serov, "Fourier series, fourier transform and their applications to mathematical physics," 2017.

[182] S. Babak, C. Caprini, D. G. Figueroa, N. Karnesis, P. Marcoccia, G. Nardini, M. Pieroni, A. Ricciardone, A. Sesana, and J. Torrado, "Stochastic gravitational wave background from stellar origin binary black holes in LISA," 4 2023.

[183] B. Abbott *et al.*, "GW150914: The Advanced LIGO Detectors in the Era of First Discoveries," *Phys. Rev. Lett.*, vol. 116, no. 13, p. 131103, 2016.

[184] B. Brügmann, "Fundamentals of numerical relativity for gravitational wave sources," *Science*, vol. 361, no. 6400, pp. 366–371, 2018.

[185] B. Allen, W. G. Anderson, P. R. Brady, D. A. Brown, and J. D. Creighton, "FINDCHIRP: An Algorithm for detection of gravitational waves from inspiraling compact binaries," *Phys. Rev. D*, vol. 85, p. 122006, 2012.

[186] S. A. Usman *et al.*, "The PyCBC search for gravitational waves from compact binary coalescence," *Class. Quant. Grav.*, vol. 33, no. 21, p. 215004, 2016.

[187] S. Sachdev *et al.*, "The GstLAL Search Analysis Methods for Compact Binary Mergers in Advanced LIGO's Second and Advanced Virgo's First Observing Runs," 1 2019.

[188] S. Klimenko *et al.*, "Method for detection and reconstruction of gravitational wave transients with networks of advanced detectors," *Phys. Rev. D*, vol. 93, no. 4, p. 042004, 2016.

[189] R. Lynch, S. Vitale, R. Essick, E. Katsavounidis, and F. Robinet, "Information-theoretic approach to the gravitational-wave burst detection problem," *Phys. Rev. D*, vol. 95, no. 10, p. 104046, 2017.

[190] F. Salemi, E. Milotti, G. Prodi, G. Vedovato, C. Lazzaro, S. Tiwari, S. Vinciguerra, M. Drago, and S. Klimenko, "Wider look at the gravitational-wave transients from GWTC-1 using an unmodeled reconstruction method," *Phys. Rev. D*, vol. 100, no. 4, p. 042003, 2019.

[191] K. W. Tsang, A. Ghosh, A. Samajdar, K. Chatziioannou, S. Mastrogiovanni, M. Agathos, and C. Van Den Broeck, "A morphology-independent search for gravitational wave echoes in data from the first and second observing runs of Advanced LIGO and Advanced Virgo," *Phys. Rev. D*, vol. 101, no. 6, p. 064012, 2020.

[192] B. Edelman *et al.*, "Constraining Unmodeled Physics with Compact Binary Mergers from GWTC-1," *arXiv:2008.06436*.

[193] B. Abbott *et al.*, "Gravitational Waves and Gamma-rays from a Binary Neutron Star Merger: GW170817 and GRB 170817A," *Astrophys. J. Lett.*, vol. 848, no. 2, p. L13, 2017.

[194] B. Abbott *et al.*, "GW190425: Observation of a Compact Binary Coalescence with Total Mass $\sim 3.4 M_{\odot}$," *Astrophys. J. Lett.*, vol. 892, no. 1, p. L3, 2020.

[195] E. Barausse, V. Cardoso, and P. Pani, "Can environmental effects spoil precision gravitational-wave astrophysics?," *Phys. Rev. D*, vol. 89, no. 10, p. 104059, 2014.

[196] H. Liu and A. D. Jackson, "Possible associated signal with GW150914 in the LIGO data," *JCAP*, vol. 1610, no. 10, p. 014, 2016.

[197] J. Creswell, S. von Hausegger, A. D. Jackson, H. Liu, and P. Naselsky, "On the time lags of the LIGO signals," *JCAP*, vol. 08, p. 013, 2017.

[198] H. Liu, J. Creswell, S. von Hausegger, A. D. Jackson, and P. Naselsky, "A blind search for a common signal in gravitational wave detectors," *JCAP*, vol. 02, p. 013, 2018.

[199] A. B. Nielsen, A. H. Nitz, C. D. Capano, and D. A. Brown, "Investigating the noise residuals around the gravitational wave event GW150914," *JCAP*, vol. 02, p. 019, 2019.

[200] A. D. Jackson, H. Liu, and P. Naselsky, "Noise residuals for GW150914 using maximum likelihood and numerical relativity templates," *JCAP*, vol. 1905, p. 014, 2019.

[201] R. Maroju, S. R. Dyuthi, A. Sukrutha, and S. Desai, "Looking for ancillary signals around GW150914," *JCAP*, vol. 04, p. 007, 2019.

[202] B. P. Abbott *et al.*, "A guide to LIGO–Virgo detector noise and extraction of transient gravitational-wave signals," *Class. Quant. Grav.*, vol. 37, no. 5, p. 055002, 2020.

[203] A. H. Nitz, C. Capano, A. B. Nielsen, S. Reyes, R. White, D. A. Brown, and B. Krishnan, "1-OGC: The first open gravitational-wave catalog of binary mergers from analysis of public Advanced LIGO data," *Astrophys. J.*, vol. 872, no. 2, p. 195, 2019.

[204] T. Venumadhav, B. Zackay, J. Roulet, L. Dai, and M. Zaldarriaga, "New search pipeline for compact binary mergers: Results for binary black holes in the first observing run of Advanced LIGO," *Phys. Rev. D*, vol. 100, no. 2, p. 023011, 2019.

[205] M. Vallisneri, J. Kanner, R. Williams, A. Weinstein, and B. Stephens, "The LIGO Open Science Center," *J. Phys. Conf. Ser.*, vol. 610, no. 1, p. 012021, 2015.

[206] S. De, C. M. Biwer, C. D. Capano, A. H. Nitz, and D. A. Brown, "Posterior samples of the parameters of binary black holes from Advanced LIGO, Virgo's second observing run," 11 2018.

[207] C. Biwer, C. D. Capano, S. De, M. Cabero, D. A. Brown, A. H. Nitz, and V. Raymond, "PyCBC Inference: A Python-based parameter estimation toolkit for compact binary coalescence signals," *Publ. Astron. Soc. Pac.*, vol. 131, no. 996, p. 024503, 2019.

[208] B. Abbott *et al.*, "Binary Black Hole Mergers in the first Advanced LIGO Observing Run," *Phys. Rev. X*, vol. 6, no. 4, p. 041015, 2016. [Erratum: Phys.Rev.X 8, 039903 (2018)].

[209] P. Marcoccia. https://github.com/GravWaves-IMF/Correlation-Method-first-2019.

[210] S. Babak, ""Enchilada" is back on the menu," *J. Phys. Conf. Ser.*, vol. 840, no. 1, p. 012026, 2017.

[211] M. Hannam, P. Schmidt, A. Bohé, L. Haegel, S. Husa, F. Ohme, G. Pratten, and M. Pürrer, "Simple Model of Complete Precessing Black-Hole-Binary Gravitational Waveforms," *Phys. Rev. Lett.*, vol. 113, no. 15, p. 151101, 2014.

[212] R. A. Mercer *et al.*, "Ligo algorithm library v6.49.," 2018. https://git.ligo.org/lscsoft/lalsuite.

[213] P. Amaro-Seoane, H. Audley, S. Babak, J. Baker, E. Barausse, P. Bender, E. Berti, P. Binetruy, M. Born, D. Bortoluzzi, *et al.*, "Laser interferometer space antenna," *arXiv preprint arXiv:1702.00786*, 2017.

[214] A. Sesana, "Prospects for Multiband Gravitational-Wave Astronomy after GW150914," *Phys. Rev. Lett.*, vol. 116, no. 23, p. 231102, 2016.

[215] K. Kyutoku and N. Seto, "Concise estimate of the expected number of detections for stellar-mass binary black holes by eLISA," *Mon. Not. Roy. Astron. Soc.*, vol. 462, no. 2, pp. 2177–2183, 2016.

[216] D. Gerosa, S. Ma, K. W. K. Wong, E. Berti, R. O'Shaughnessy, Y. Chen, and K. Belczynski, "Multiband gravitational-wave event rates and stellar physics," *Phys. Rev. D*, vol. 99, no. 10, p. 103004, 2019.

[217] N. Seto and K. Kyutoku, "How many extragalactic stellar mass binary black holes will be detected by space gravitational-wave interferometers?," *Mon. Not. Roy. Astron. Soc.*, vol. 514, no. 4, pp. 4669–4675, 2022.

[218] K. Kremer *et al.*, "Post-Newtonian Dynamics in Dense Star Clusters: Binary Black Holes in the LISA Band," *Phys. Rev. D*, vol. 99, no. 6, p. 063003, 2019.

[219] A. Sesana, A. Lamberts, and A. Petiteau, "Finding binary black holes in the Milky Way with LISA," *Mon. Not. Roy. Astron. Soc.*, vol. 494, no. 1, pp. L75–L80, 2020.

[220] C. Caprini and D. G. Figueroa, "Cosmological Backgrounds of Gravitational Waves," *Class. Quant. Grav.*, vol. 35, no. 16, p. 163001, 2018.

[221] M. Lewicki and V. Vaskonen, "Impact of LIGO-Virgo black hole binaries on gravitational wave background searches," *Eur. Phys. J. C*, vol. 83, no. 2, p. 168, 2023.

[222] G. Boileau, N. Christensen, R. Meyer, and N. Cornish, "Spectral separation of the stochastic gravitational-wave background for lisa: Observing both cosmological and astrophysical backgrounds," *Physical Review D*, vol. 103, 05 2021.

[223] G. Boileau, A. Lamberts, N. Christensen, N. J. Cornish, and R. Meyer, "Spectral separation of the stochastic gravitational-wave background for LISA: galactic, cosmological and astrophysical backgrounds," in *55th Rencontres de Moriond on QCD and High Energy Interactions*, 5 2021.

[224] M. Pieroni and E. Barausse, "Foreground cleaning and template-free stochastic background extraction for LISA," *JCAP*, vol. 07, p. 021, 2020. [Erratum: JCAP 09, E01 (2020)].

[225] M. Dominik, K. Belczynski, C. Fryer, D. Holz, E. Berti, T. Bulik, I. Mandel, and R. O'Shaughnessy, "Double Compact Objects I: The Significance of the Common Envelope on Merger Rates," *Astrophys. J.*, vol. 759, p. 52, 2012.

[226] C. J. Neijssel, A. Vigna-Gómez, S. Stevenson, J. W. Barrett, S. M. Gaebel, F. S. Broekgaarden, S. E. de Mink, D. Szécsi, S. Vinciguerra, and I. Mandel, "The effect of the metallicity-specific star formation history on double compact object mergers," *Monthly Notices of the Royal Astronomical Society*, vol. 490, no. 3, pp. 3740–3759, 2019.

[227] M. Mapelli, N. Giacobbo, E. Ripamonti, and M. Spera, "The cosmic merger rate of stellar black hole binaries from the Illustris simulation," *Mon. Not. Roy. Astron. Soc.*, vol. 472, no. 2, pp. 2422–2435, 2017.

[228] A. C. Jenkins, M. Sakellariadou, T. Regimbau, and E. Slezak, "Anisotropies in the astrophysical gravitational-wave background: Predictions for the detection of compact binaries by LIGO and Virgo," *Phys. Rev. D*, vol. 98, no. 6, p. 063501, 2018.

[229] S. Mukherjee and J. Silk, "Can we distinguish astrophysical from primordial black holes via the stochastic gravitational wave background?," *Mon. Not. Roy. Astron. Soc.*, vol. 506, no. 3, pp. 3977–3985, 2021.

[230] R. Abbott *et al.*, "Population Properties of Compact Objects from the Second LIGO-Virgo Gravitational-Wave Transient Catalog," *Astrophys. J. Lett.*, vol. 913, no. 1, p. L7, 2021.

[231] I. Dvorkin, E. Vangioni, J. Silk, J.-P. Uzan, and K. A. Olive, "Metallicity-constrained merger rates of binary black holes and the stochastic gravitational wave background," *Mon. Not. Roy. Astron. Soc.*, vol. 461, no. 4, pp. 3877–3885, 2016.

[232] K. Nakazato, Y. Niino, and N. Sago, "Gravitational-Wave Background from Binary Mergers and Metallicity Evolution of Galaxies," *Astrophys. J.*, vol. 832, no. 2, p. 146, 2016.

[233] C. Périgois, C. Belczynski, T. Bulik, and T. Regimbau, "StarTrack predictions of the stochastic gravitational-wave background from compact binary mergers," *Phys. Rev. D*, vol. 103, no. 4, p. 043002, 2021.

[234] G. Cusin, I. Dvorkin, C. Pitrou, and J.-P. Uzan, "Properties of the stochastic astrophysical gravitational wave background: astrophysical sources dependencies," *Phys. Rev. D*, vol. 100, no. 6, p. 063004, 2019.

[235] G. Cusin, I. Dvorkin, C. Pitrou, and J.-P. Uzan, "Stochastic gravitational wave background anisotropies in the mHz band: astrophysical dependencies," *Mon. Not. Roy. Astron. Soc.*, vol. 493, no. 1, pp. L1–L5, 2020.

[236] E. S. Phinney, "A Practical theorem on gravitational wave backgrounds," 7 2001.

[237] N. Karnesis, S. Babak, M. Pieroni, N. Cornish, and T. Littenberg, "Characterization of the stochastic signal originating from compact binary populations as measured by LISA," *Phys. Rev. D*, vol. 104, no. 4, p. 043019, 2021.

[238] S. Babak *et al.*, "To appear.,"

[239] E. Thrane and J. D. Romano, "Sensitivity curves for searches for gravitational-wave backgrounds," *Phys. Rev. D*, vol. 88, no. 12, p. 124032, 2013.

[240] C. Caprini *et al.*, "Detecting gravitational waves from cosmological phase transitions with LISA: an update," *JCAP*, vol. 03, p. 024, 2020.

[241] R. Flauger, N. Karnesis, G. Nardini, M. Pieroni, A. Ricciardone, and J. Torrado, "Improved reconstruction of a stochastic gravitational wave background with LISA," *JCAP*, vol. 01, p. 059, 2021.

[242] T. Callister, M. Fishbach, D. Holz, and W. Farr, "Shouts and Murmurs: Combining Individual Gravitational-Wave Sources with the Stochastic Background to Measure the History of Binary Black Hole Mergers," *Astrophys. J. Lett.*, vol. 896, no. 2, p. L32, 2020.

[243] R. Abbott *et al.*, "Upper limits on the isotropic gravitational-wave background from Advanced LIGO and Advanced Virgo's third observing run," *Phys. Rev. D*, vol. 104, no. 2, p. 022004, 2021.

[244] C. Cutler *et al.*, "What we can learn from multi-band observations of black hole binaries," 3 2019.

[245] B. Ewing, S. Sachdev, S. Borhanian, and B. S. Sathyaprakash, "Archival searches for stellar-mass binary black holes in LISA data," *Phys. Rev. D*, vol. 103, no. 2, p. 023025, 2021.

[246] K. W. K. Wong, E. D. Kovetz, C. Cutler, and E. Berti, "Expanding the LISA Horizon from the Ground," *Phys. Rev. Lett.*, vol. 121, no. 25, p. 251102, 2018.

[247] A. Nishizawa, A. Sesana, E. Berti, and A. Klein, "Constraining stellar binary black hole formation scenarios with eLISA eccentricity measurements," *Mon. Not. Roy. Astron. Soc.*, vol. 465, no. 4, pp. 4375–4380, 2017.

[248] J. Samsing and D. J. D'Orazio, "Black Hole Mergers From Globular Clusters Observable by LISA I: Eccentric Sources Originating From Relativistic N-body Dynamics," *Mon. Not. Roy. Astron. Soc.*, vol. 481, no. 4, pp. 5445–5450, 2018.

[249] M. Mapelli, N. Giacobbo, F. Santoliquido, and M. C. Artale, "The properties of merging black holes and neutron stars across cosmic time," *Monthly Notices of the Royal Astronomical Society*, vol. 487, pp. 2–13, 04 2019.

[250] C. Karathanasis, S. Mukherjee, and S. Mastrogiovanni, "Binary black holes population and cosmology in new lights: Signature of PISN mass and formation channel in GWTC-3," 4 2022.

[251] V. C. L.S. Collaboration, V.C.S. Collaboration and K. Collaboration, "The population of merging compact binaries inferred using gravitational waves through GWTC-3 - Data release," 11 2021.

[252] P. A. R. Ade *et al.*, "Planck 2015 results. XIII. Cosmological parameters," *Astron. Astrophys.*, vol. 594, p. A13, 2016.

[253] P. Marcoccia, "Generating a bh merging catalogue," 2023. https://github.com/KuZa91/Generating-a-BH-Merging-Catalogue.

[254] J. Torrado, "EXTRAPOPS: fast simulation and analysis of extra-galactic binary gw sources," 2023. https://github.com/JesusTorrado/extrapops.

[255] D. W. Hogg, "Distance measures in cosmology," 5 1999.

[256] S. Babak, A. Petiteau, and M. Hewitson, "LISA Sensitivity and SNR Calculations," 8 2021.

[257] M. Bonetti and A. Sesana, "Gravitational wave background from extreme mass ratio inspirals," *Phys. Rev. D*, vol. 102, no. 10, p. 103023, 2020.

[258] S. E. Timpano, L. J. Rubbo, and N. J. Cornish, "Characterizing the galactic gravitational wave background with lisa," *Phys. Rev. D*, vol. 73, p. 122001, Jun 2006.

[259] J. Crowder and N. J. Cornish, "Solution to the galactic foreground problem for lisa," *Phys. Rev. D*, vol. 75, p. 043008, Feb 2007.

[260] S. Nissanke, M. Vallisneri, G. Nelemans, and T. A. Prince, "Gravitational-wave emission from compact Galactic binaries," , vol. 758, p. 131, 2012.

[261] L. London, S. Khan, E. Fauchon-Jones, C. García, M. Hannam, S. Husa, X. Jiménez-Forteza, C. Kalaghatgi, F. Ohme, and F. Pannarale, "First higher-multipole model of gravitational waves from spinning and coalescing black-hole binaries," *Phys. Rev. Lett.*, vol. 120, no. 16, p. 161102, 2018.

[262] S. Husa, S. Khan, M. Hannam, M. Pürrer, F. Ohme, X. J. Forteza, and A. Bohé, "Frequency-domain gravitational waves from nonprecessing black-hole binaries. I. New numerical waveforms and anatomy of the signal," , vol. 93, p. 044006, Feb. 2016.

[263] S. Khan, S. Husa, M. Hannam, F. Ohme, M. Pürrer, X. J. Forteza, and A. Bohé, "Frequency-domain gravitational waves from nonprecessing black-hole binaries. II. A phenomenological model for the advanced detector era," , vol. 93, p. 044007, Feb. 2016.

[264] J. S. Marsat, "*lisabeta*," 2020.

[265] S. Marsat and J. G. Baker, "Fourier-domain modulations and delays of gravitational-wave signals," 6 2018.

[266] R. Buscicchio, A. Klein, E. Roebber, C. J. Moore, D. Gerosa, E. Finch, and A. Vecchio, "Bayesian parameter estimation of stellar-mass black-hole binaries with LISA," *Phys. Rev. D*, vol. 104, no. 4, p. 044065, 2021.

[267] A. Toubiana, S. Babak, S. Marsat, and S. Ossokine, "Detectability and parameter estimation of GWTC-3 events with LISA," *Phys. Rev. D*, vol. 106, no. 10, p. 104034, 2022.

[268] C. J. Moore, D. Gerosa, and A. Klein, "Are stellar-mass black-hole binaries too quiet for LISA?," *Mon. Not. Roy. Astron. Soc.*, vol. 488, no. 1, pp. L94–L98, 2019.

[269] T. Regimbau, M. Evans, N. Christensen, E. Katsavounidis, B. Sathyaprakash, and S. Vitale, "Digging deeper: Observing primordial gravitational waves below the binary black hole produced stochastic background," *Phys. Rev. Lett.*, vol. 118, no. 15, p. 151105, 2017.

[270] LISA Science Study Team, "LISA Science Requirements Document, ESA-L3-EST-SCI-RS-001," Tech. Rep. 1.0, ESA, May 2018. https://www.cosmos.esa.int/web/lisa/lisa-documents/.

[271] F. Santoliquido, M. Mapelli, Y. Bouffanais, N. Giacobbo, U. N. D. Carlo, S. Rastello, M. C. Artale, and A. Ballone, "The cosmic merger rate density evolution of compact binaries formed in young star clusters and in isolated binaries," *The Astrophysical Journal*, vol. 898, p. 152, aug 2020.

[272] L. Lehoucq and I. Dvorkin, "To appear.,"

[273] Z.-C. Chen, F. Huang, and Q.-G. Huang, "Stochastic Gravitational-wave Background from Binary Black Holes and Binary Neutron Stars and Implications for LISA," *Astrophys. J.*, vol. 871, no. 1, p. 97, 2019.

[274] S. S. Bavera, G. Franciolini, G. Cusin, A. Riotto, M. Zevin, and T. Fragos, "Stochastic gravitational-wave background as a tool for investigating multi-channel astrophysical and primordial black-hole mergers," *Astron. Astrophys.*, vol. 660, p. A26, 2022.

[275] C. Caprini, D. G. Figueroa, R. Flauger, G. Nardini, M. Peloso, M. Pieroni, A. Ricciardone, and G. Tasinato, "Reconstructing the spectral shape of a stochastic gravitational wave background with LISA," *JCAP*, vol. 11, p. 017, 2019.

[276] W. J. Handley, M. P. Hobson, and A. N. Lasenby, "PolyChord: nested sampling for cosmology," *Mon. Not. Roy. Astron. Soc.*, vol. 450, no. 1, pp. L61–L65, 2015.

[277] W. Handley, M. Hobson, and A. Lasenby, "Polychord: next-generation nested sampling," *Monthly Notices of the Royal Astronomical Society*, vol. 453, no. 4, pp. 4384–4398, 2015.

[278] J. Torrado and A. Lewis, "Cobaya: Code for Bayesian Analysis of hierarchical physical models," *JCAP*, vol. 05, p. 057, 2021.

[279] T. B. Littenberg and N. J. Cornish, "Prototype global analysis of LISA data with multiple source types," *Phys. Rev. D*, vol. 107, no. 6, p. 063004, 2023.

[280] A. C. Jenkins, R. O'Shaughnessy, M. Sakellariadou, and D. Wysocki, "Anisotropies in the astrophysical gravitational-wave background: The impact of black hole distributions," *Phys. Rev. Lett.*, vol. 122, no. 11, p. 111101, 2019.

[281] N. Bartolo *et al.*, "Probing anisotropies of the Stochastic Gravitational Wave Background with LISA," *JCAP*, vol. 11, p. 009, 2022.

[282] D. J. D'Orazio and J. Samsing, "Black Hole Mergers From Globular Clusters Observable by LISA II: Resolved Eccentric Sources and the Gravitational Wave Background," *Mon. Not. Roy. Astron. Soc.*, vol. 481, no. 4, pp. 4775–4785, 2018.

[283] Y. Zhao and Y. Lu, "Stochastic Gravitational Wave Background and Eccentric Stellar Compact Binaries," *Mon. Not. Roy. Astron. Soc.*, vol. 500, no. 1, pp. 1421–1436, 2020.

[284] P. Amaro-Seoane, J. R. Gair, M. Freitag, M. Coleman Miller, I. Mandel, C. J. Cutler, and S. Babak, "Astrophysics, detection and science applications of intermediate- and extreme mass-ratio inspirals," *Class. Quant. Grav.*, vol. 24, pp. R113–R169, 2007.

[285] M. Branchesi *et al.*, "Science with the Einstein Telescope: a comparison of different designs," 3 2023.

[286] M. Braglia, J. Garcia-Bellido, and S. Kuroyanagi, "Testing Primordial Black Holes with multi-band observations of the stochastic gravitational wave background," *JCAP*, vol. 12, no. 12, p. 012, 2021.

[287] B. Abbott *et al.*, "Binary Black Hole Population Properties Inferred from the First and Second Observing Runs of Advanced LIGO and Advanced Virgo," *Astrophys. J. Lett.*, vol. 882, no. 2, p. L24, 2019.

[288] C. Talbot and E. Thrane, "Determining the population properties of spinning black holes," *Phys. Rev. D*, vol. 96, no. 2, p. 023012, 2017.

[289] D. Wysocki, J. Lange, and R. O'Shaughnessy, "Reconstructing phenomenological distributions of compact binaries via gravitational wave observations," *Phys. Rev. D*, vol. 100, no. 4, p. 043012, 2019.

[290] B. P. Abbott *et al.*, "GW150914: The Advanced LIGO Detectors in the Era of First Discoveries," *Phys. Rev. Lett.*, vol. 116, no. 13, p. 131103, 2016.

[291] F. Acernese *et al.*, "Virgo Detector Characterization and Data Quality during the O3 run," 5 2022.

[292] T. Akutsu *et al.*, "Overview of KAGRA : KAGRA science," 8 2020.

[293] M. Fishbach and V. Kalogera, "The Time Delay Distribution and Formation Metallicity of LIGO-Virgo's Binary Black Holes," *Astrophys. J. Lett.*, vol. 914, no. 2, p. L30, 2021.

[294] G. Hütsi, M. Raidal, V. Vaskonen, and H. Veermäe, "Two populations of LIGO-Virgo black holes," *JCAP*, vol. 03, p. 068, 2021.

[295] A. Antonelli, K. Kritos, K. K. Y. Ng, R. Cotesta, and E. Berti, "Classifying the generation and formation channels of individual LIGO-Virgo-KAGRA observations from dynamically formed binaries," 6 2023.

[296] R. Abbott *et al.*, "Population of Merging Compact Binaries Inferred Using Gravitational Waves through GWTC-3," *Phys. Rev. X*, vol. 13, no. 1, p. 011048, 2023.

[297] C. Périgois, C. Belczynski, T. Bulik, and T. Regimbau, "startrack predictions of the stochastic gravitational-wave background from compact binary mergers," *Phys. Rev. D*, vol. 103, p. 043002, Feb 2021.

[298] Y. B. Zel'dovich and I. D. Novikov, "The Hypothesis of Cores Retarded during Expansion and the Hot Cosmological Model," *Soviet Astronomy*, vol. 10, p. 602, Feb. 1967.

[299] B. J. Carr, "The Primordial black hole mass spectrum," *Astrophys. J.*, vol. 201, pp. 1–19, 1975.

[300] B. J. Carr, K. Kohri, Y. Sendouda, and J. Yokoyama, "New cosmological constraints on primordial black holes," *Phys. Rev. D*, vol. 81, p. 104019, 2010.

[301] B. Carr, K. Kohri, Y. Sendouda, and J. Yokoyama, "Constraints on primordial black holes," *Rept. Prog. Phys.*, vol. 84, no. 11, p. 116902, 2021.

[302] Y. Ali-Haïmoud, E. D. Kovetz, and M. Kamionkowski, "Merger rate of primordial black-hole binaries," *Phys. Rev. D*, vol. 96, no. 12, p. 123523, 2017.

[303] G. Franciolini, I. Musco, P. Pani, and A. Urbano, "From inflation to black hole mergers and back again: Gravitational-wave data-driven constraints on inflationary scenarios with a first-principle model of primordial black holes across the QCD epoch," *Phys. Rev. D*, vol. 106, no. 12, p. 123526, 2022.

[304] S. Bird, I. Cholis, J. B. Muñoz, Y. Ali-Haïmoud, M. Kamionkowski, E. D. Kovetz, A. Raccanelli, and A. G. Riess, "Did LIGO detect dark matter?," *Phys. Rev. Lett.*, vol. 116, no. 20, p. 201301, 2016.

[305] S. Clesse and J. García-Bellido, "The clustering of massive Primordial Black Holes as Dark Matter: measuring their mass distribution with Advanced LIGO," *Phys. Dark Univ.*, vol. 15, pp. 142–147, 2017.

[306] M. Raidal, C. Spethmann, V. Vaskonen, and H. Veermäe, "Formation and Evolution of Primordial Black Hole Binaries in the Early Universe," *JCAP*, vol. 02, p. 018, 2019.

[307] A. Hall, A. D. Gow, and C. T. Byrnes, "Bayesian analysis of LIGO-Virgo mergers: Primordial vs. astrophysical black hole populations," *Phys. Rev. D*, vol. 102, p. 123524, 2020.

[308] G. Franciolini, R. Cotesta, N. Loutrel, E. Berti, P. Pani, and A. Riotto, "How to assess the primordial origin of single gravitational-wave events with mass, spin, eccentricity, and deformability measurements," *Phys. Rev. D*, vol. 105, no. 6, p. 063510, 2022.

[309] V. Atal, J. J. Blanco-Pillado, A. Sanglas, and N. Triantafyllou, "Constraining changes in the merger history of (P)BH binaries with the stochastic gravitational wave background," 1 2022.

[310] S. Young and C. T. Byrnes, "Initial clustering and the primordial black hole merger rate," *JCAP*, vol. 03, p. 004, 2020.

[311] M. Mancarella, F. Iacovelli, and D. Gerosa, "Inferring, not just detecting: Metrics for high-redshift sources observed with third-generation gravitational-wave detectors," *Phys. Rev. D*, vol. 107, no. 10, p. L101302, 2023.

[312] S. M. Koushiappas and A. Loeb, "Maximum redshift of gravitational wave merger events," *Phys. Rev. Lett.*, vol. 119, no. 22, p. 221104, 2017.

[313] V. De Luca, G. Franciolini, P. Pani, and A. Riotto, "The minimum testable abundance of primordial black holes at future gravitational-wave detectors," *JCAP*, vol. 11, p. 039, 2021.

[314] M. Maggiore *et al.*, "Science Case for the Einstein Telescope," *JCAP*, vol. 03, p. 050, 2020.

[315] K. K. Y. Ng, S. Vitale, W. M. Farr, and C. L. Rodriguez, "Probing multiple populations of compact binaries with third-generation gravitational-wave detectors," *Astrophys. J. Lett.*, vol. 913, no. 1, p. L5, 2021.

[316] K. K. Y. Ng *et al.*, "Measuring properties of primordial black hole mergers at cosmological distances: Effect of higher order modes in gravitational waves," *Phys. Rev. D*, vol. 107, no. 2, p. 024041, 2023.

[317] M. Martinelli, F. Scarcella, N. B. Hogg, B. J. Kavanagh, D. Gaggero, and P. Fleury, "Dancing in the dark: detecting a population of distant primordial black holes," *JCAP*, vol. 08, no. 08, p. 006, 2022.

[318] H.-K. Guo, J. Shu, and Y. Zhao, "Using LISA-like Gravitational Wave Detectors to Search for Primordial Black Holes," *Phys. Rev. D*, vol. 99, no. 2, p. 023001, 2019.

[319] P. Auclair *et al.*, "Cosmology with the Laser Interferometer Space Antenna," *Living Rev. Rel.*, vol. 26, no. 1, p. 5, 2023.

[320] R.-g. Cai, S. Pi, and M. Sasaki, "Gravitational Waves Induced by non-Gaussian Scalar Perturbations," *Phys. Rev. Lett.*, vol. 122, no. 20, p. 201101, 2019.

[321] N. Bartolo, V. De Luca, G. Franciolini, A. Lewis, M. Peloso, and A. Riotto, "Primordial Black Hole Dark Matter: LISA Serendipity," *Phys. Rev. Lett.*, vol. 122, no. 21, p. 211301, 2019.

[322] C. Unal, "Imprints of Primordial Non-Gaussianity on Gravitational Wave Spectrum," *Phys. Rev. D*, vol. 99, no. 4, p. 041301, 2019.

[323] K. K. Y. Ng, S. Chen, B. Goncharov, U. Dupletsa, S. Borhanian, M. Branchesi, J. Harms, M. Maggiore, B. S. Sathyaprakash, and S. Vitale, "On the Single-event-based Identification of Primordial Black Hole Mergers at Cosmological Distances," *Astrophys. J. Lett.*, vol. 931, no. 1, p. L12, 2022.

[324] K. K. Y. Ng, G. Franciolini, E. Berti, P. Pani, A. Riotto, and S. Vitale, "Constraining High-redshift Stellar-mass Primordial Black Holes with Next-generation Ground-based Gravitational-wave Detectors," *Astrophys. J. Lett.*, vol. 933, no. 2, p. L41, 2022.

[325] C. J. Neijssel, A. Vigna-Gómez, S. Stevenson, J. W. Barrett, S. M. Gaebel, F. S. Broekgaarden, S. E. de Mink, D. Szécsi, S. Vinciguerra, and I. Mandel, "The effect of the metallicity-specific star formation history on double compact object mergers,"

Monthly Notices of the Royal Astronomical Society, vol. 490, no. 3, pp. 3740–3759, 2019.

[326] V. Vaskonen and H. Veermäe, "Lower bound on the primordial black hole merger rate," *Phys. Rev. D*, vol. 101, no. 4, p. 043015, 2020.

[327] V. De Luca, V. Desjacques, G. Franciolini, A. Malhotra, and A. Riotto, "The initial spin probability distribution of primordial black holes," *JCAP*, vol. 05, p. 018, 2019.

[328] M. M. Flores and A. Kusenko, "Spins of primordial black holes formed in different cosmological scenarios," *Phys. Rev. D*, vol. 104, p. 063008, Sep 2021.

[329] D. Saito, T. Harada, Y. Koga, and C.-M. Yoo, "Spins of primordial black holes formed with a soft equation of state," *JCAP*, vol. 07, p. 030, 2023.

[330] P. Marcoccia, "PBH sub-populations effects analysis." https://github.com/KuZa91/PBH_subpopulations_effects_analysis, 2023.

[331] M. Maggiore, "Gravitational wave experiments and early universe cosmology," *Phys. Rept.*, vol. 331, pp. 283–367, 2000.

[332] P. Ajith *et al.*, "A Template bank for gravitational waveforms from coalescing binary black holes. I. Non-spinning binaries," *Phys. Rev. D*, vol. 77, p. 104017, 2008. [Erratum: Phys.Rev.D 79, 129901 (2009)].

[333] P. Ajith *et al.*, "Phenomenological template family for black-hole coalescence waveforms," *Class. Quant. Grav.*, vol. 24, pp. S689–S700, 2007.

[334] L. Santamaria *et al.*, "Matching post-Newtonian and numerical relativity waveforms: systematic errors and a new phenomenological model for non-precessing black hole binaries," *Phys. Rev. D*, vol. 82, p. 064016, 2010.

[335] C. Cutler and E. E. Flanagan, "Gravitational waves from merging compact binaries: How accurately can one extract the binary's parameters from the inspiral wave form?," *Phys. Rev. D*, vol. 49, pp. 2658–2697, 1994.

[336] C. Cahillane and G. Mansell, "Review of the Advanced LIGO Gravitational Wave Observatories Leading to Observing Run Four," *Galaxies*, vol. 10, no. 1, p. 36, 2022.

[337] R. W. Kiendrebeogo *et al.*, "Updated observing scenarios and multi-messenger implications for the International Gravitational-wave Network's O4 and O5," 6 2023.

[338] M. Rajagopal and R. W. Romani, "Ultralow frequency gravitational radiation from massive black hole binaries," *Astrophys. J.*, vol. 446, pp. 543–549, 1995.

[339] A. H. Jaffe and D. C. Backer, "Gravitational waves probe the coalescence rate of massive black hole binaries," *Astrophys. J.*, vol. 583, pp. 616–631, 2003.

[340] J. S. B. Wyithe and A. Loeb, "Low-frequency gravitational waves from massive black hole binaries: Predictions for lisa and pulsar timing arrays," *The Astrophysical Journal*, vol. 590, p. 691, jun 2003.

[341] N. Cornish and T. Robson, "Galactic binary science with the new LISA design," *J. Phys. Conf. Ser.*, vol. 840, no. 1, p. 012024, 2017.

[342] L. Lehoucq, I. Dvorkin, R. Srinivasan, C. Pellouin, and A. Lamberts, "Astrophysical uncertainties in the gravitational-wave background from stellar-mass compact binary mergers," *Mon. Not. Roy. Astron. Soc.*, vol. 526, no. 3, pp. 4378–4387, 2023.

[343] S. Babak, J. Gair, A. Sesana, E. Barausse, C. F. Sopuerta, C. P. L. Berry, E. Berti, P. Amaro-Seoane, A. Petiteau, and A. Klein, "Science with the space-based interferometer LISA. V: Extreme mass-ratio inspirals," *Phys. Rev. D*, vol. 95, no. 10, p. 103012, 2017.

[344] X. Chen, Y. Qiu, S. Li, and F. K. Liu, "Milli-Hertz Gravitational-wave Background Produced by Quasiperiodic Eruptions," *Astrophys. J.*, vol. 930, no. 2, p. 122, 2022.

[345] D. Laghi, N. Tamanini, W. Del Pozzo, A. Sesana, J. Gair, S. Babak, and D. Izquierdo-Villalba, "Gravitational-wave cosmology with extreme mass-ratio inspirals," *Mon. Not. Roy. Astron. Soc.*, vol. 508, no. 3, pp. 4512–4531, 2021.

[346] F. Pozzoli, S. Babak, A. Sesana, M. Bonetti, and N. Karnesis, "Computation of stochastic background from extreme mass ratio inspiral populations for LISA," 2 2023.

[347] C. Liu, D. Laghi, and N. Tamanini, "Probing modified gravitational-wave propagation with extreme mass-ratio inspirals," 10 2023.

[348] J. R. Gair, S. Babak, A. Sesana, P. Amaro-Seoane, E. Barausse, C. P. L. Berry, E. Berti, and C. Sopuerta, "Prospects for observing extreme-mass-ratio inspirals with LISA," *J. Phys. Conf. Ser.*, vol. 840, no. 1, p. 012021, 2017.

[349] H.-K. Guo and A. Miller, "Searching for Mini Extreme Mass Ratio Inspirals with Gravitational-Wave Detectors," 5 2022.

[350] G. Mazzolari, M. Bonetti, A. Sesana, R. M. Colombo, M. Dotti, G. Lodato, and D. Izquierdo-Villalba, "Extreme mass ratio inspirals triggered by massive black hole binaries: from relativistic dynamics to cosmological rates," *Mon. Not. Roy. Astron. Soc.*, vol. 516, no. 2, pp. 1959–1976, 2022.

[351] S. J. Kapadia, K. L. Pandey, T. Suyama, and P. Ajith, "Prospects for probing ultralight primordial black holes using the stochastic gravitational-wave background induced by primordial curvature perturbations," *Phys. Rev. D*, vol. 101, no. 12, p. 123535, 2020.

[352] R. Abbott *et al.*, "GW190521: A Binary Black Hole Merger with a Total Mass of $150M_{\odot}$," *Phys. Rev. Lett.*, vol. 125, no. 10, p. 101102, 2020.

[353] B. O'Brien, M. Szczepanczyk, V. Gayathri, I. Bartos, G. Vedovato, G. Prodi, G. Mitselmakher, and S. Klimenko, "Detection of LIGO-Virgo binary black holes in the pair-instability mass gap," *Phys. Rev. D*, vol. 104, no. 8, p. 082003, 2021.

[354] R. Abbott *et al.*, "Population Properties of Compact Objects from the Second LIGO-Virgo Gravitational-Wave Transient Catalog," 10 2020.

[355] F. Santoliquido, M. Mapelli, Y. Bouffanais, N. Giacobbo, U. N. Di Carlo, S. Rastello, M. C. Artale, and A. Ballone, "The cosmic merger rate density evolution of compact binaries formed in young star clusters and in isolated binaries," *Astrophys. J.*, vol. 898, no. 2, p. 152, 2020.

[356] L. A. C. van Son, S. E. de Mink, T. Callister, S. Justham, M. Renzo, T. Wagg, F. S. Broekgaarden, F. Kummer, R. Pakmor, and I. Mandel, "The redshift evolution of the binary black hole merger rate: a weighty matter," 10 2021.

[357] T. Nakamura, M. Sasaki, T. Tanaka, and K. S. Thorne, "Gravitational waves from

coalescing black hole MACHO binaries," *Astrophys. J. Lett.*, vol. 487, pp. L139–L142, 1997.

[358] K. Ioka, T. Chiba, T. Tanaka, and T. Nakamura, "Black hole binary formation in the expanding universe: Three body problem approximation," *Phys. Rev. D*, vol. 58, p. 063003, 1998.

[359] U. Mukhopadhyay, D. Majumdar, and A. Halder, "Constraining pbh mass distributions from 21cm brightness temperature results and an analytical mapping between probability distribution of 21cm signal and pbh masses," *Journal of Cosmology and Astroparticle Physics*, vol. 2022, p. 099, oct 2022.

[360] L. I. G. O. Collaboration, "The a^+ design sensitivity curve." https://dcc.ligo.org/public/0149/T1800042/005/AplusDesign.txt, 2018.

[361] S. Hild *et al.*, "Sensitivity studies for third-generation gravitational wave observatories," *Classical and Quantum Gravity*, vol. 28, p. 094013, apr 2011.

[362] E. T. Collaboration, "Et design sensitivity curve." https://apps.et-gw.eu/tds/?content=3&r=14065, 2018.

[363] ESA, "LISA Science Requirements Document." https://www.cosmos.esa.int/documents/678316/1700384/SciRD.pdf, 2018.

[364] S. Babak, A. Petiteau, and M. Hewitson, "LISA Sensitivity and SNR Calculations," 8 2021.

[365] J. W. Armstrong, F. B. Estabrook, and M. Tinto, "Time-delay interferometry for space-based gravitational wave searches," *The Astrophysical Journal*, vol. 527, pp. 814–826, dec 1999.

[366] M. Tinto and J. W. Armstrong, "Cancellation of laser noise in an unequal-arm interferometer detector of gravitational radiation," *Phys. Rev. D*, vol. 59, p. 102003, 1999.

[367] F. B. Estabrook, M. Tinto, and J. W. Armstrong, "Time delay analysis of LISA gravitational wave data: Elimination of spacecraft motion effects," *Phys. Rev. D*, vol. 62, p. 042002, 2000.

[368] M. Tinto and S. V. Dhurandhar, "Time-delay interferometry," *Living Rev. Rel.*, vol. 24, no. 1, p. 1, 2021.

[369] T. A. Prince, M. Tinto, S. L. Larson, and J. W. Armstrong, "The LISA optimal sensitivity," *Phys. Rev. D*, vol. 66, p. 122002, 2002.

[370] D. A. Shaddock, M. Tinto, F. B. Estabrook, and J. W. Armstrong, "Data combinations accounting for LISA spacecraft motion," *Phys. Rev. D*, vol. 68, p. 061303, 2003.

[371] M. Tinto, F. B. Estabrook, and J. W. Armstrong, "Time delay interferometry with moving spacecraft arrays," *Phys. Rev. D*, vol. 69, p. 082001, 2004.

[372] O. Hartwig, M. Lilley, M. Muratore, and M. Pieroni, "Stochastic gravitational wave background reconstruction for a nonequilateral and unequal-noise LISA constellation," *Phys. Rev. D*, vol. 107, no. 12, p. 123531, 2023.

[373] A. Sesana, A. Vecchio, and C. N. Colacino, "The stochastic gravitational-wave background from massive black hole binary systems: implications for observations with Pulsar Timing Arrays," *Mon. Not. Roy. Astron. Soc.*, vol. 390, p. 192, 2008.

[374] S. W. Hawking and W. Israel, *Three Hundred Years of Gravitation*. 1989.